MODELING VOLCANIC UNREST BY DATA ASSIMILATION

BY

YAN ZHAN

DISSERTATION

Submitted in partial fulfillment of the requirements
for the degree of Doctor of Philosophy in Geology
in the Graduate College of the
University of Illinois at Urbana-Champaign, 2020

Urbana, Illinois

Doctoral Committee:

Assistant Professor Patricia M. Gregg, Chair and Director of Research
Associate Professor Lijun Liu
Professor Stephen Marshak
Professor Craig Lundstrom

ABSTRACT

Volcanic activity may lead to potential volcanic eruptions, but it also provides critical information for understanding the physical processes within a volcanic system. Combining multiple observations and advanced physical models allows us to explore the response of the surrounding host rock to changes in the physical condition in a magmatic system. This work focuses on developing and applying a robust data-model fusion framework to investigate the mechanisms involved in volcanic unrest, such as deformation, failure, and pore fluid migration. First, using a series of tests based on the synthetic data, I optimize a data assimilation technique, Ensemble Kalman Filter (EnKF), to improve its performance in forecasting volcanic unrests with multiple geodetic observations. Then, the robustness of the EnKF is confirmed in application to the unrest and 2009 eruption of Kerinci volcano, Indonesia. To understand the effects of uncertain rheology on our model results, I conduct a systematic sensitivity study to determine the impact of rheology on the host-rock failure prediction. With a better understanding of the uncertainties in my models, I establish numerical models by integrating multiple observations to investigate the magma reservoir dynamics, crustal stress, failure-related seismicity, and hydrological interactions of two different magmatic systems, Laguna del Maule in the Andes, Chile, and Atka in the Aleutian, USA. In both systems, the pre-existing structures and pore fluids play critical roles in catalyzing seismicity, redistributing masses, and delaying/trigger eruptions.

ACKNOWLEDGMENTS

First, I want to say thank you to my advisor, Trish Gregg. Since my first day in graduate school, Trish has treated me as a family and given me endless support. Without her calm patience, constant enthusiasm, continuous encouragement, generosity, and persistent advocacy, I cannot finish this odyssey for a Ph.D. in a foreign country. Her insight and wisdom are always the best examples for me to follow, to become a better scientist and an independent thinker.

Besides my advisor, I would like to thank the rest of my dissertation committee members, Lijun Liu, Steve Marshak, Craig Lundstrom, and Cory Pettijohn, for their great support and invaluable advice. Lijun has been a constant, positive presence throughout my Ph.D. life. I have learned a lot by having conversions with him, and from his inspiring courses (e.g., Geodynamics and Subduction Zone). Steve is always a wise elder and an idol as a structural geologist to me. His wealthy knowledge, skillful teaching strategy, and vivid illustration benefit me a lot. My understanding of geoscience can hardly be comprehensive without numerous discussions with Craig. His thoughts on petrology and geochemistry have greatly deepened my thesis. Cory has shared with me tons of experience within or beyond research. I benefit a lot from his help during my Ph.D. research.

There is no scientific research without collaborations. Many thanks to Estelle Chaussard and Yosuke Aoki for sharing the data and ideas in my Kerinci volcano project. In this project, my newly developed workflow has been successfully tested for the first time. Thanks also to Hélène Le Mével, Craig A. Miller, Carlos Cardona, Brad Singer, Clifford Thurber, and Kurt Feigl for introducing me to the project of Laguna del Maule volcano. My understanding of the mechanism of volcanic unrest deepened a lot from this project. Many thanks to Zhong Lu, John

Power, Michelle Coombs, and Jeff Freymueller for guiding me around the scientific questions from Aleutian volcanos. Thanks also to Mike Poland, Kyle Anderson, Josef Dufek, Diana Roman, Terry Plank, Emily Montgomery-Brown, and Falk Amelung for their advice during my research.

The scientific community of UIUC has played a critical role in my scientific growth. Many thanks to Michael Stewart. The field trip to Scotland was fantastic. Many thanks to Tom Johnson for lots of positive feedback and advice. Thanks to Xiaodong Song for his instruction in seismology, and also for his mentoring as "old ginger" (in Chinese, "old ginger" means people with more experience, so they have insights). Thanks also to Alison Anders and Jim Best for guiding me into the world of earth's surface and landscape evolution. Thanks also to Rob Sanford for sharing numerous experiences within and beyond scientific research. Many thanks to Willy Guenthner for his advice during my qualification exam. Thanks also to Roman Makhnenko, Arif Masud, Jennifer Druhan, Jessica Conroy, and many other faculties in the UIUC for their instructions, which greatly broaden my eyesight. Many thanks to Robert Brunner for helping me to run numerical simulations on the Bluewater Supercomputer. Thanks also to Kenneth Patten, Michael Savage, and David Wojtowicz for the supports on my projects using the Keeling Cluster.

I am also very proud to work with my nice, brilliant, and brave colleagues and friends. Many thanks to my group colleagues, Haley Cabaniss, Jack Albright, Robby Goldman, and Valentina Romano. I have got tons of inspiration from the discussion with them. Thanks also to Jingtao Lai, Mingfei Chen, Ching Chang, and Julia Cisneros for their supports and optimism during my hours in the NHB and UB. Thanks to all graduate students, without them, my life in UIUC will lose a lot of brightness and colors.

Special thanks to Lana Holben. As a geology mon, she has taken care of everything from big to small. Thanks also to Chandré Johnson, Susie Zukoshy, and Rachel Davidson for all help and support.

It is hard to express my gratefulness to my mon, Lijun Miao, and dad, Minqian Zhan. As said by a great poet of ancient China, “Can the gratitude like an inch-long grass repay the warmth of the sun in spring?” Finally, I offer my gratitude to my wife, Li Zhang. Without her, I cannot get so far here.

FUNDING SOURCES

NASA Earth and Space Science Fellowship

Evergreen Match Fellowship

Provost Match Fellowship

NCSA Faculty Fellowship

For my wife Li Zhang who helped me in all things great and small.

TABLE OF CONTENTS

CHAPTER 1: INTRODUCTION

Volcanic unrest is defined as the deviated behavior of a volcano from its baseline or background (e.g., Phillipson et al., 2013; Acocella, 2014). Some unrest may lead to volcanic eruptions (e.g., Sparks, 2003; Moran et al., 2011), whereas often it does not (e.g., Biggs et al., 2014). Understanding the mechanisms of volcanic unrest helps scientists to determine whether and when activity will be followed by an eruption. To quantify the stability of a volcanic system, we need to combine volcanic monitoring data such as geodesy (e.g., InSAR, GNSS) and seismology (e.g., broadband seismometer), with models including experimental, analytical, and numerical models (Sparks et al., 2012). Data assimilation techniques based on Bayesian Markov chain Monte Carlo method allow us to utilize volcanic monitoring data to obtain probabilistic estimates of model parameters, and to forecast future behavior. A recently developed, advanced data assimilation technique, Ensemble Kalman Filter (EnKF) (Evensen, 1994), has the power to handle highly nonlinear models, which has been widely used in hydrologic, physical oceanography, and climate modeling (e.g., vanLeeuwen and Evensen, 1996; Allen et al., 2003), and starts to show its potential in volcanology (Gregg and Pettijohn, 2016).

The primary focus of this Ph.D. thesis is (1) developing a robust data assimilation technique for volcano modeling based on the EnKF, and (2) utilizing this technique to investigate the physical process, such as deformation, failure, pore fluid migration, and so on, during the volcanic unrest. Chapter 2 establishes a robust data assimilation workflow by a series of tests based on synthetic data, which optimizes the application of the EnKF in modeling complex volcanic deformation. In Chapter 3, I use a single type of observation, InSAR, from a real volcanic system to test the performance of the EnKF in exploring the volcanic unrest. Since,

in previous tests, the effects of uncertainties in the rock properties have not been discussed, In Chapter 4, I conduct a series of sensitivity tests to determine that under which condition the impact of the rheological uncertainties on failure prediction is not negligible. Therefore, In Chapters 5 and 6, model implementations based on inferred rheological structure from geophysical observation are used to investigate restless behaviors during periods of volcanic unrest for two different volcanic systems. The brief description and primary conclusions of each chapter are presented as follows.

In Chapter 2, I establish a new 3-dimensional EnKF framework, which significantly expands the usage of this data assimilation method in volcanology (Zhan and Gregg, 2017). Then, I introduce an iterative EnKF algorithm to enhance the traditional EnKF framework, which is more effective in highly non-linear problems. Third, I add synthetic noise to both synthetic GPS and InSAR signals to test the ability of EnKF when dealing with more realistic data. Fourth, I simulate defects which are inevitable in real measurements such as gaps in data coverage and continuity. Finally, I conduct systematic sensitivity tests to exam the EnKF analysis results affected by prescribed model setup conditions. These tests not only provide information for using the EnKF analysis to enhance our modeling techniques but also give insights into data collection optimization. From these tests, I optimize the utilizing of the EnKF to improve its effectiveness and efficiency in assimilating multiple geodetic observations to forecast volcanic unrest.

In Chapter 3, I apply the EnKF to investigate the surface deformation leading up to the 2009 eruption of the Kerinci volcano, Central Sumatra along the Sunda Arc, Indonesia (Zhan et al., 2017). I use InSAR timeseries data during 2007-2011 from the ALOS-1 satellite to track the dynamics of a shallow magma storage system before and after the eruption. I apply a two-step

EnKF analysis to determine the two pressure sources which present an inflating shallow, spherical pressure source and a deflating, dike-like source feeding the shallower one. The ensemble mean values of the parameters are used to predict the stress state of the system leading up to the 2009 eruption. The stress model suggests that the shallow magma reservoir is close to the failure threshold prior to the 2009 eruption, which may explain the eruption.

In Chapter 4, I conduct a series of sensitivity tests using 2-dimensional, axisymmetric models to evaluate the impact of the uncertainties in assumed rheological parameters (Zhan and Gregg, 2019). It is essential to understand whether significant uncertainties in rock properties will preclude the ability of models to predict reservoir failure before we can use date assimilation to forecast volcanic unrest. The tests show that predictions of the onset magma chamber failure are more sensitive to Young's modulus than other elastic properties. Displacement at the onset of magma reservoir failure is not sensitive to variations in Young's modulus for stiff host rocks (E>40 GPa). Longer precursory volcano-tectonic events may occur in weak host-rock (E <40 GPa) due to well-developed Coulomb failure prior to dike propagation.

In Chapter 5, I investigate the recent (2008-2017) restless behaviors at the Laguna del Maule (LdM) magmatic system, Chile, by integrating reservoir dynamics, crustal stress, and multiple observations (Zhan et al., 2019). I use a series of 3D FEM models to simulate the volcanic deformation of at LdM revealed by multi-band InSAR data. The model results are compared with seismic tomography, gravity, and magnetotelluric data to indicating the magma reservoir architecture. To explain the seismicity and gravity change data, I test the effects of a pre-existing weak zone (i.e., the Troncoso fault). The results illustrate that the permeability of the fault zone can increase due to an inflating magma reservoir, allowing pore fluid to inject into the dilatant places of the fault, then triggering earthquakes, and finally causing microgravity

changes. This “hydrofracturing” process may release some accumulated stress along the magma reservoir to delay potential eruptions.

In Chapter 6, I investigate previous volcanic unrest (2006-2007) of the Atka volcanic center, Alaska, to evaluate whether the acceleration of uplift and seismicity triggered the phreatic eruption 5-km far away from focus of unrest. I use 3-D finite element models with data assimilation by the InSAR data to investigate the pressure source of the surface displacement, mechanism of the volcano-tectonic (VT) earthquakes, and triggering of the phreatic eruption. The results show that a migrating pressure source can best explain the surface deformation, indicating the melt connectivity in a magma reservoir dominated by crystal mush can evolve without a dramatic change in the overpressure of the magma reservoir. Further, the dilatancy in a pre-existing weak zone caused by the pressure source may open channels for pore fluid to inject into and to trigger VT earthquakes. Consequently, the water table may drop due to increased capability of the fault, to drain the crater lake at Korovin, and to trigger the phreatic eruption.1.1

1.1 References

Acocella V. (2014) Structural control on magmatism along divergent and convergent plate boundaries: Overview, model, problems. Earth-Science Reviews 136, 226–288.

Allen J. I., Eknes M. and Evensen G. (2003) An Ensemble Kalman Filter with a complex marine ecosystem model: hindcasting phytoplankton in the Cretan Sea. Ann. Geophys. 21, 399–411.

Biggs J., Ebmeier S. K., Aspinall W. P., Lu Z., Pritchard M. E., Sparks R. S. J. and Mather T. A. (2014) Global link between deformation and volcanic eruption quantified by satellite imagery. Nature Communications 5, 1–7.

Evensen G. (1994) Sequential data assimilation with a nonlinear quasi-geostrophic model using

Monte Carlo methods to forecast error statistics. J. Geophys. Res. 99, 10143–10162.

Gregg P. M. and Pettijohn J. C. (2016) A multi-data stream assimilation framework for the assessment of volcanic unrest. Journal of Volcanology and Geothermal Research 309, 63–77.

Moran S. C., Newhall C. and Roman D. C. (2011) Failed magmatic eruptions: late-stage cessation of magma ascent. Bulletin of Volcanology 73, 115–122.

Phillipson G., Sobradelo R. and Gottsmann J. (2013) Global volcanic unrest in the 21st century: An analysis of the first decade. Journal of Volcanology and Geothermal Research 264, 183–196.

Sparks R. S. J. (2003) Forecasting volcanic eruptions. Earth and Planetary Science Letters 210, 1–15.

Sparks R. S. J., Biggs J. and Neuberg J. W. (2012) Monitoring Volcanoes. Science 335, 1310–1311.

vanLeeuwen P. J. and Evensen G. (1996) Data assimilation and inverse methods in terms of a probabilistic formulation. Mon. Weather Rev. 124, 2898–2913.

Zhan Y. and Gregg P. M. (2017) Data assimilation strategies for volcano geodesy. Journal of Volcanology and Geothermal Research 344, 13–25.

Zhan Y. and Gregg P. M. (2019) How Accurately Can We Model Magma Reservoir Failure With Uncertainties in Host Rock Rheology? Journal of Geophysical Research: Solid Earth 124, 8030–8042.

Zhan Y., Gregg P. M., Chaussard E. and Aoki Y. (2017) Sequential Assimilation of Volcanic Monitoring Data to Quantify Eruption Potential: Application to Kerinci Volcano, Sumatra. Front. Earth Sci. 5. Available at:

https://www.frontiersin.org/articles/10.3389/feart.2017.00108/full.

Zhan Y., Gregg P. M., Mével H. L., Miller C. A. and Cardona C. (2019) Integrating Reservoir Dynamics, Crustal Stress, and Geophysical Observations of the Laguna del Maule Magmatic System by FEM Models and Data Assimilation. Journal of Geophysical Research: Solid Earth 124, 13547–13562.

CHAPTER 2: DATA ASSIMILATION STRATEGIES FOR VOLCANO GEODESY[1]

Abstract

Ground deformation observed using near-real time geodetic methods, such as InSAR and GPS, can provide critical information about the evolution of a magma chamber prior to volcanic eruption. Rapid advancement in numerical modeling capabilities has resulted in a number of finite element models targeted at better understanding the connection between surface uplift associated with magma chamber pressurization and the potential for volcanic eruption. Robust model-data fusion techniques are necessary to take full advantage of the numerical models and the volcano monitoring observations currently available. In this study, we develop a 3D data assimilation framework using the Ensemble Kalman Filter (EnKF) approach in order to combine geodetic observations of surface deformation with geodynamic models to investigate volcanic unrest. The EnKF sequential assimilation method utilizes disparate data sets as they become available to update geodynamic models of magma reservoir evolution. While the EnKF has been widely applied in hydrologic and climate modeling, the adaptation for volcano monitoring is in its initial stages. As such, our investigation focuses on conducting a series of sensitivity tests to optimize the EnKF for volcano applications and on developing specific strategies for assimilation of geodetic data. Our numerical experiments illustrate that the EnKF is able to adapt well to the spatial limitations posed by GPS data and the temporal limitations of InSAR, and that specific strategies can be adopted to enhance EnKF performance to improve model forecasts. Specifically, our numerical experiments indicate that: (1) incorporating additional iterations of

[1] Published as: Zhan Y. and Gregg P. M. (2017) Data assimilation strategies for volcano geodesy. Journal of Volcanology and Geothermal Research 344, 13–25.

the EnKF analysis step is more efficient than increasing the number of ensemble members; (2) the accuracy of the EnKF results are not affected by initial parameter assumptions; (3) GPS observations near the center of uplift improve the quality of model forecasts; (4) occasionally shifting continuous GPS stations to provide variability in the locations of observations results in better model predictions than utilizing fixed locations when the number of available instruments is limited; (5) spotty InSAR data coverage on the flanks of a volcano due to topographic shadows and/or atmospheric interference does not adversely impact the effectiveness of EnKF if the available coverage is > 50%; and (6) snow or glacial obstruction in the center of uplift can adversely impact EnKF forecasts. By utilizing these strategies, we conclude that the EnKF is an effective sequential model-data fusion technique for assimilating multiple geodetic observations to forecast volcanic activity at restless volcanoes.

2.1 Introduction

Assessing the unrest of volcanic systems around the world requires a multi-disciplinary approach that utilizes disparate datasets to analyze volcano observations. Over the past decades, significant effort has been expended to develop monitoring strategies to mitigate potential disasters for vulnerable populations living in the shadows of active volcanoes. Geodetic monitoring methods, including Global Positioning System (GPS) (e.g. Beauducel and Cornet, 1999; Bevis and Foster, 2000; Bonforte and Puglisi, 2003, 2006; Rivet et al., 2014) and Interferometric Synthetic Aperture Radar (InSAR) (Massonnet and Feigl, 1998; Sigmundsson et al., 1999; Lu et al., 2000; Chaussard et al., 2013; Papoutsis et al., 2013; Pinel et al., 2014; Le Mével et al., 2015; Morales Rivera et al., 2015; Masterlark et al., 2016a), provide 4D surface deformation observations of volcanoes experiencing unrest, and give insight into the dynamic evolution of the magma systems below. Advancements in geodetic data collection and analysis

have shown the capability to detect volcano inflation and provide early warning of volcanic unrest sometimes years in advance of measurable seismicity (Lu et al., 2010; Chaussard and Amelung, 2012; Chaussard et al., 2013; Biggs et al., 2014).

To analyze surface deformation observations, classic inversion and joint inversion strategies have been developed using analytical solutions such as the elastic Mogi (1958) model and its derivatives (McTigue, 1987; Massonnet and Feigl, 1998; M. Battaglia et al., 2003; M Battaglia et al., 2003; Nooner and Chadwick, 2009; Newman et al., 2012; Parks et al., 2015). To adapt static analytical approximations of volcano evolution into time-forward models, the evolution of static models can be solved as a function of time (Newman et al., 2006). Alternatively, time-dependent kinematic models can be used in a model-data fusion framework to provide the temporal variation (Desmarais and Segall, 2007; Anderson and Segall, 2013). The strength of analytical and kinematic solutions is that they provide first order solutions with relative computational ease. However, they are limited in their ability to solve complex multiphysics problems.

Thermomechanical numerical models offer an additional means to decipher observations of deformation and investigate precursory signals for eruptions (e.g. Currenti et al., 2007; Gregg et al., 2012, 2013; Ronchin et al., 2013; Cannavò et al., 2015), and may be used to invert geodetic observations through optimization schemes (Carbone et al., 2007; Hickey et al., 2013). The integration of geodetic measurements into multiphysics dynamic models has been shown to provide advanced understanding of how highly non-linear volcano systems evolve in time (Cianetti et al., 2012; Gregg et al., 2013; Alparone et al., 2013; Hickey et al., 2015). While these inversion approaches work well for combining one or potentially two data streams with numerical models, they are static assessments of the system state and do not provide updates or forecasts. Unlike their kinematic modeling counter parts (e.g., Anderson and Segall, 2013),

robust time-sequential data assimilation strategies that link sophisticated numerical models with observations have not been widely used in volcano studies and must be developed to fully realize the potential of numerical modeling approaches.

To work towards the goal of a multi-data stream forecasting method for volcanic application, Gregg and Pettijohn (2016) developed a 2D data assimilation framework based on the Ensemble Kalman Filter (EnKF) method (Fig. 2.1). Widely applied in hydrologic, physical oceanography, and climate modeling (vanLeeuwen and Evensen, 1996; Allen et al., 2003; Bertino et al., 2003; Brusdal et al., 2003; Natvik and Evensen, 2003; Lisaeter et al., 2007; Skjervheim et al., 2007; Evensen, 2009a, 2009b; Seiler et al., 2010; Wilson et al., 2010; Wilson and Özkan-Haller, 2012; Wilson et al., 2014), the EnKF has been shown to be a powerful forecasting tool for assimilating highly disparate observations into complex dynamic models. The EnKF method has proven to be a more efficient and computationally economical approach than the traditional Kalman Filter (Kalman, 1960) and the Extended Kalman Filter (Schmidt, 1966) because the covariance matrix in the EnKF analysis is estimated using a Markov Chain Monte Carlo (MCMC) approach allowing for updates of both the model state and model parameters concurrently (Evensen, 2003, 2009a). The MCMC approach utilized by the EnKF has a proven track record (Evensen, 2003, 2009a) for performing well with highly nonlinear systems where the traditional Kalman Filter and pseudo non-linear Extended Kalman Filter may perform suboptimally (Julier et al., 2000). Furthermore, the ensemble based method enables users to swap in model advancements without making major adjustments to the data assimilation procedure (Evensen, 2003, 2009a). By assimilating surface deformation data, the EnKF is able to swiftly update the parameters for the magma reservoir by matching new measurements with the numerical model forecasting (Gregg and Pettijohn, 2016).

Although this study focuses on utilizing synthetic data to explore the usage of the Ensemble Kalman Filter in volcanology, it offers several critical advancements over the implementation of Gregg and Pettijohn (2016). First, we establish a new 3-dimensional EnKF framework, which significantly expands the use of this data assimilation method in volcanology. The ability to assimilate data into a 3D models is critical for analyzing the inherent 3D nature of volcanic systems, such as asymmetric magma reservoirs, topography, faults, and host rock heterogeneities (e.g. Cannavò et al., 2015; Hickey et al., 2015). Second, this study introduces an important improvement in the EnKF algorithm itself. As an enhancement to the traditional EnKF framework (Evensen, 2003, 2009a; Gregg and Pettijohn, 2016), we develop and apply an iterative EnKF algorithm, which, as we illustrate, is more effective in highly non-linear problems such as volcanic unrest. Third, instead of using idealized synthetic data (Gregg and Pettijohn, 2016), we add synthetic noise to both synthetic GPS and InSAR signals. Testing more realistic error models (e.g. Mao et al., 1999; Williams et al., 2004; Lohman and Simons, 2005; Fattahi and Amelung, 2015) allows us optimize the EnKF analysis more wisely, test whether this strategy will be able to effectively analyze real data in the future. Fourth, in addition to utilizing more realistic noise models to mimic real data errors, we also simulate defects which are inevitable in real measurements such as gaps in data coverage and continuity. These tests not only provide information for using the EnKF analysis to enhance our modeling techniques, but also give insights into data collection optimization. Finally, this study conducts systematic sensitivity tests to exam the EnKF analysis results affected by prescribed model setup conditions such as the number of ensemble members, the number of iterations, and the initial guess of model parameters in order to improve the EnKF performance while minimizing computational costs.

2.2 Methods

2.2.1 Magma reservoir finite element model

We use a 3D viscoelastic finite element model (FEM) to create a time series of surface deformation to provide synthetic GPS and InSAR datasets for the data assimilation. The numerical approach was modified after previous 2D and 3D finite element models for magma reservoirs (Grosfils, 2007; Del Negro et al., 2009; Gregg et al., 2012, 2013; Gregg and Pettijohn, 2015; Grosfils et al., 2015). The crust surrounding a magma reservoir is simulated by a box with a spherical void, which is loaded from within to create an inflating volume change, ΔV (Fig. 2.2). The size of the box is $60\ km \times 60\ km \times 20\ km$, consistent with the common scale of terrestrial volcanic systems (Gregg and Pettijohn, 2016). The sides and bottom of the box are defined by roller boundary conditions. A constant gravity (g = *9.8 m/s2*) and an initial isostatic stress are balanced to maintain the lithostatic state of the system (Fig. 2.2b):

$$\sigma_1^{initial} = \sigma_2^{initial} = \sigma_3^{initial} = \rho g z \tag{2.1}$$

where $\sigma_k^{initial}$ is the initial principle stress, *z* is the depth, and $\rho = 2700 kg/m^3$ is the density of the host rocks.

COMSOL Multiphysics 5.1® is utilized to calculate the model mesh. The mesh grids are coarse within the outer domain far away from the volcano and refined in the inner box close to the center of the magma chamber (Fig. 2.2a). We apply a linear viscoelastic stress-strain relation with Maxwell model to calculate stress and strain resulting from an applied load, following:

$$\dot{\varepsilon} \propto \frac{\sigma}{\eta} + \frac{\dot{\sigma}}{G} \tag{2.2}$$

where $\dot{\varepsilon}$ is strain rate, σ is stress, $\dot{\sigma}$ is stress rate, η and G are constants. The viscosity η is defined as $2 \times 10^{16}\ Pa \cdot s$ and the shear modulus is defined by $G = E/2(1+\nu)$, where the Young's modules *E* is 75 *GPa* and Poisson ratio ν is 0.25. The material properties are defined to

simulate synthetic terrestrial volcano. However, future data assimilation efforts on natural systems will allow for estimating variations in material properties from geophysical observations such as tomography.

The predicted surface deformation from the 3D numerical approach is consistent with the viscoelastic analytical solution of Gregg et al. (2012) modified from Del Negro et al. (2009) (Fig. 2.3). The volume changes ΔV, due to the expansion of the magma reservoir, is defined as a function of time (Fig. 2.2b). During the first and the third year, continuous inflation mimics possible magma injection. The inflation ceases in the second year approximating a volcanically silent period between injections.

2.2.2 Synthetic data

The synthetic data created by the FEM described in section 2.2.1 are utilized to systematically investigate the performance of the EnKF. The synthetic datasets, including single component line of sight (LOS) "InSAR", and multi-component "GPS", are calculated based on defined parameters (Table 2.1), which the EnKF analysis attempts to find.

The synthetic InSAR LOS data are created by calculating the surface deformation difference between two sequential time steps, collected every 60 days in a 10 km × 10 km grid with a lateral resolution of 20 m. All the synthetic LOS data are composed of both signal and noise (Fig. 2.4a). We followed Lohman and Simons (2005) to create synthetic distance-correlated noise, n_c, which exhibits a power law behavior mainly correlated to atmospheric structures (Agram and Simons, 2015; Fattahi and Amelung, 2015). The distance-correlated noise, n_c is derived from a predetermined covariance matrix, C_d (Lohman and Simons, 2005):

$$C_d^{ij} = e^{-L^{ij}/L_c} \tag{2.3}$$

$$n_c = \mathcal{L} \times n_n \tag{2.4}$$

where L^{ij} is distance between the *i*th and *j*th points, and L_c is the window size. $\mathcal{L}$ is the lower triangular matrix derived from C_d by Cholesky decomposition, and n_n is the uncorrelated noise matrix. Although many previous studies revealed that other factors like topography also contribute to the LOS delay (e.g. Jónsson et al., 2002; Emardson et al., 2003), we neglect those effects and only consider a spatially stationary and isotropic noise model, since the purpose of this paper is discussing the performance of the Ensemble Kalman Filter.

Applying the full "InSAR" dataset is prohibitively computationally expensive as full resolution interferograms contain more than one million points. Therefore, we reduce the InSAR sampling points from ~10_6 to ~800 (Fig. 2.4d), through a root-mean-square-error (RMSE) based quadtree algorithm (e.g., Jónsson et al., 2002).

The synthetic GPS observations are collected every day at 20 synthetic GPS stations whose locations are shown in the supporting information in Zhan and Gregg (2017). The "GPS" data are composed of three components east-west, north-south, and up-down. The three components are directly interpolated from the finite element model output. In addition, we add noise to the signal to create a more realistic synthetic GPS data. We utilize a combination of white and flicker noise model (e.g. Zhang et al., 1997; Mao et al., 1999; Williams et al., 2004; Dmitrieva et al., 2015) as the uncertainty of the "GPS" data. Since he uncertainty of the up-down component is obvious higher than other two components (Mao et al., 1999), we assume 1 mm/yr of uncertainty in the horizontal components and 5 mm/yr in vertical one (Fig. 2.4c). Before the synthetic data are utilized in EnKF analysis, the full signal, with noise, is smoothed by a low pass filter (Fig. 2.4c).

2.2.3 Ensemble Kalman Filter

The Ensemble Kalman Filter (EnKF) is a data assimilation method built upon the traditional Kalman Filter (KF) approach (Kalman, 1960). The EnKF utilizes a Markov chain of Monte

Carlo (MCMC) method to solve the time evolution of the probability density function of the model. This update overcomes the limitations of the Kalman Filter and Extended Kalman Filter methods, such as computational expensive, storage issues, and poor performance with highly nonlinear problems (Evensen, 2009). We follow the EnKF analysis scheme described by Evensen (2003) and Gregg and Pettijohn (2016) (Fig. 2.1), which we briefly describe below.

The forecast ensemble members $\psi_i \in \mathbb{R}^{Ndim}$, composed by both parameters and solutions, are stored in

$$\boldsymbol{A} = (\psi_1, \psi_2, \cdots, \psi_{Nens}) \in \mathbb{R}^{Ndim \times Nens}, \tag{2.5}$$

where $Ndim$ is the number of the parameters and measurements and $Nens$ is the number of ensemble members. In the first step, the initial ensemble members are calculated based on an initial guess of the model parameters. For the magma reservoir models in this study, unknown parameters include the geometry, location, and volume change, while the rheological properties of the host rock are assumed. Thus, an initial parameter space is built by Monte Carlo methods to derive the initial solution space according to the equation of the Mogi (1958) model.

The ensemble perturbation matrix is defined as

$$\boldsymbol{A'} = \boldsymbol{A}(\boldsymbol{I} - \mathbf{1}_{Nens}), \tag{2.6}$$

where $\boldsymbol{I}$ is an $Nens \times Nens$ identity matrix and $\mathbf{1}_{Nens} \in \mathbb{R}^{Nens \times Nens}$ is a matrix where every element equals to $1/Nens$.

The covariance matrix is calculated by:

$$\boldsymbol{P}_e = \frac{\boldsymbol{A'}\left(\boldsymbol{A'}\right)^T}{Nens-1}. \tag{2.7}$$

The EnKF analysis requires measurements to update the model parameters. In this study, we apply the synthetic observations generated by the FEM described in section 2.2.1. The measurements d with their perturbation δd_j are given as:

$$d_j = d + \delta d_j, \tag{2.8}$$

where we assume 10 % random perturbation for the measurements. The measurement matrix is then defined as

$$\boldsymbol{D} = (d_1, d_2, \cdots, d_{Nmes}) \in \mathbb{R}^{Nmes \times Nens}, \tag{2.9}$$

and the ensembles of measurement perturbations, $\boldsymbol{\delta d}$, is:

$$\boldsymbol{\delta d} = (\delta d_1, \delta d_2, \cdots, \delta d_{Nens}), \tag{2.10}$$

from which the covariance matrix for measurements, $\boldsymbol{R}_e$, is represented by:

$$\boldsymbol{R}_e = \frac{\boldsymbol{\delta d}(\boldsymbol{\delta d})^T}{Nens-1}. \tag{2.11}$$

Finally, the EnKF analysis step combines the models and data to provide a matrix of updated model parameters:

$$\boldsymbol{A}^a = \boldsymbol{A} + \boldsymbol{P}_e\boldsymbol{H}^T(\boldsymbol{H}\boldsymbol{P}_e\boldsymbol{H}^T + \boldsymbol{R}_e)^{-1}(\boldsymbol{D} - \boldsymbol{H}\boldsymbol{A}), \tag{2.12}$$

where $\boldsymbol{H}$ is the mapping matrix linking the forecast ensemble and the measurements. The EnKF scheme calculates this equation when a new observation becomes available. The size of the parameter space (Γ_p) is computed at the end of each step, to ensure that catastrophic divergence has not occurred (Evensen, 2003, 2009a; Gregg and Pettijohn, 2016).

Two critical updates are developed from the method introduced in Gregg and Pettijohn (2016). First, the EnKF scheme is adapted into 3D by expanding the matrixes to accommodate data and model outputs in the third dimension. Second, additional iterations of the EnKF analysis equation (2.12) are applied before progressing to the next time step. These iterations take advantage of the available observations in the present step and analyze the ensembles from the previous iteration.

2.2.4 Sensitivity tests and performance evaluation

Ideally, after several EnKF analysis steps, the parameter space and the solution space

should shrink significantly and reproduce the parameters assumed in the synthetic model. In reality, the observations are limited both spatially and temporally and may impact the ability of the EnKF to converge onto a solution. A series of systematic tests are developed to test the performance of the EnKF, which allows us to develop strategies to improve the application of EnKF.

The sensitivity tests (Table 2.2) include strategies not only for testing the effect of the EnKF setup, such as: (1) the number of ensembles; (2) intra-EnKF iterations between observational time steps; (3) minimum tolerance for the size of the parameter space; and (4) initial parameter values, but also for optimizing data collection and use, including: (5) the location of GPS stations; (6) the number of GPS stations; (7) the temporal continuity of the GPS data stream; and (8) the spatial coverage of InSAR.

The performance of the EnKF analysis is quantified by two values. First, the Root Mean Squared Error (RMSE) provides the fit between the model-predicted surface displacement and the synthetic observations (Gregg and Pettijohn, 2016). Second, the parameter misfit δ_p, a dimensionless value defined as

$$\delta_p(t) = \sum_{i=1}^{Npar} \left(\frac{Z_i^t - Z_i^a}{\hat{Z}} \right)^2 , \tag{2.13}$$

where Z_i^t is an assumed parameter used for producing the synthetic data, Z_i^a is the corresponding parameter from the EnKF analysis, and $\hat{Z}$ are the assumed values used to scale the equation to a dimensionless quantity (for horizontal location of the source $\hat{Z}$ = 10 km as the half length of the study area). When calculating the misfit, we combine the radius, R, and the overpressure, ΔP, expressing them by the volume change ΔV, since the radius and overpressure are hard to be determined separately in the Mogi (1958) model. In addition, the nature of overpressure is still unclear. According to the Mogi (1958) model, the term $\Delta P a^3$ in the Equation

(2.3) and (2.4) has a linear relationship with the volume change ΔV, as

$$\Delta V = \frac{\Delta P \cdot V}{K} = \frac{4\pi \Delta P a^3}{3K}, \tag{2.14}$$

where K is the bulk modulus, and the volume change, ΔV, is small compared to the total volume, V.

2.3 Testing strategies for EnKF implementation

2.3.1 Variations in the number of ensembles and intra-EnKF iterations

While the EnKF is computationally much less expensive than the tranditional Kalman Filter and Extended Kalman Filter techniques, the ensemble-based approach can be very taxing when utilized with large finite element models (e.g., Gregg and Pettijohn, 2016). As such, it is critical to efficiently set up the EnKF in a way that optimizes the computational usage with quantifiable gains in EnKF performance. The largest increase in computation time and storage during EnKF analysis occurs from increasing the number of ensembles. Since each 3D FEM may take on the order of hours to complete and require tens of gigabytes of data storage, adding 100-1000 ensembles may prove computationally prohibitive. Alternatively, intra-EnKF iterations are very swift and require no additional storage because no additional FEM calculations are needed to iterate on the EnKF analysis step (equation 2.12), which can be performed in ~10's of seconds to minutes.

The first suite of synthetic tests investigates the effects of the number of ensembles and number of intra-EnKF iterations to determine which EnKF setup results in the most optimal model convergence and provides a better EnKF prediction most efficiently. Tests of the number of ensembles consist of five EnKF analyses with prescribed $Nens$ ranging from 50 to 1000 (Table 2.2). Results indicate that, for $Nens \geq 100$, the number of ensembles has little effect on the calculated normalized RMSE of the displacement field (Fig. 2.5a) when using InSAR data.

The parameter misfits of the models with < 100 ensemble members are significantly high, (Fig. 2.5b), but EnKF runs with > 100 ensembles exhibit obvious advantages. However, the EnKF result does not significantly improve as the ensemble sizes are increased well beyond 100. As discussed below in Section 2.4.1, these findings are in agreement with previous tests that indicate ensemble numbers as low as 100 may be sufficient for model convergence (Evensen, 2003). An important caveat to this finding is that for natural data, larger ensemble sizes may be necessary to track the dynamic system. When this approach is applied to real data, it will be important to re-test the impact of ensemble number on model convergence. For the GPS data tests, the number of ensembles does not affect the EnKF performance at all when we have > 50 ensembles. Since the number of measurement at each time step for the GPS data is at least an order less than the ensemble numbers, parameter space with 50 ensembles may already be large enough for the EnKF to obtain a good parameter estimation through a few measurements.

EnKF performance is drastically improved by incorporating an iterative EnKF analysis in between available data time steps when using temporally sparse data sets. As illustrated in Fig. 2.5c and d, a sudden drop in both the normalized RMSE and parameter misfit is found when additional iterations are applied using InSAR data; However, the improvement of the EnKF's performance is appears to plateau when the number of iterations exceeds 10. On the other hand, there does not appear to be a gain in performance when applying an iterative EnKF analysis to assimilate the GPS data. The temporally dense nature of the 1000 time-step continuous GPS data stream seems to be more than adequate for the EnKF to converge, and any additional iterations do not offer significant improvements to the analysis.

2.3.2 Catastrophic filter divergence tolerance

To avoid catastrophic filter divergence, a tolerance parameter, Γ_p, is set to restrict the minimum standard deviation of the parameter distributions determined during the EnKF analysis

(Table 2.2). Both results of the synthetic tests using InSAR and GPS data show that a lower threshold of minimum parameter space make the EnKF perform better (Fig. 2.5). The similar pattern also occurs in the RMSEs, where higher tolerance means higher RMSEs and higher standard deviations of the RMSE (Fig. 2.5e).

2.3.3 Initial parameter values

When working with a natural volcanic system, investigators may have *a priori* information about the location and extent of the magma system. However, typically, initial assessment of unrest from geodetic observations is conducted without any prior knowledge about the source of deformation. Since, the EnKF analysis requires an initial guess of the parameter space to create the initial ensemble suite, it is critical to understand the impact of the initial parameter distribution on model performance. As such, we test the impact of different initial parameter suites on the EnKF by varying, first, the average value of depth of the magma reservoir, and, second, the range of the depth (Table 2.2). Our tests indicate that, for our synthetic InSAR or GPS data, the initial assumptions have little effect on the EnKF RMSEs and the parameter misfits (Fig. 2.6). All tests illustrate similar RMSEs (~2 %) and parameter misfits, regardless of the initial parameter assumptions. This finding provides reassurance for using the EnKF approach to investigate geodetic observations at systems with little or no prior information.

2.3.4 Geodetic data coverage and quality

In the previous sections, we tested the setup and workflow of the EnKF approach and found that the greatest enhancement to EnKF performance comes from conducting intra-EnKF iterations between observation time steps to improve the filter convergence on temporally sparse data sets. We also illustrated that EnKF performance is relatively insensitive to the number of ensembles and the initial parameter distributions. The previous experiments were all conducted using optimal data coverage, and as can be expected, the quality of the observational inputs

directly affects the performance of the EnKF analysis. The goal of the next series of synthetic tests is to determine which observations provide better constraints for the EnKF analysis. We conduct four tests to consider both the spatial and temporal distribution of GPS and InSAR observations and devise strategies for future data collection and assimilation efforts. In the following tests, the parameter misfits are utilized to indicate the quality of the results, since the RMSEs are heavily biased by the variations in data distribution.

InSAR coverage

InSAR is a powerful tool for observing the onset of unrest at previously dormant volcanoes (Massonnet and Feigl, 1998; Lu et al., 2000; Chaussard et al., 2013; Pinel et al., 2014; Masterlark et al., 2016b). The source estimation using InSAR data can provide important context for future data collection efforts including a signal to optimize data collection strategies. However, the lack of InSAR data coverage may adversely impact its assimilation and the performance of the EnKF. In the InSAR coverage test, we consider two potential gaps in InSAR data (1) a topographic shadow zone restricting observations in a region of a volcano due to a volcanic edifice, and (2) a circular shadow in the center of volcano deformation created by snow or ice cover.

In the topographic shadow test, the InSAR measurements are masked over a fraction of the volcano, ranging from 12.5% to 87.5%. The results indicate that the parameter misfits with more extensive InSAR data coverage are lower than models utilizing masked InSAR coverage (Fig. 2.7d). This is particularly noticeable in predictions of the horizontal location of the magma reservoir, which is not well constrained in models with extensive InSAR LOS shadows. This effect illustrates that the percentage of InSAR data coverage affects the quality of the EnKF analysis. Our numerical tests indicate that as coverage decreases < 50% EnKF performance is

adversely impacted and parameter values are not as well constrained. Similarly, restricting data coverage at the center of the volcano due to snow cover will not significantly impact EnKF performance. However less snow coverage enhances the ability of the EnKF to tracking the correct reservoir depth, which is similar to the results observed in the GPS distance tests in the next section.

Overall, InSAR data are quite robust, providing excellent observational inputs for the EnKF, even with sparse temporal observations (e.g., Gregg and Pettijohn, 2016) and spatial limitations. In the next section, limitations posed by GPS data are investigated to determine how best to optimize on-the-ground deformation observations.

GPS Station Availability

While InSAR data tend to be spatially rich, providing extensive coverage for a region surrounding a volcano, GPS data may provide rich temporal information in discrete locations. The initial "optimal" locations of the 20 GPS stations used in the previous sensitivity tests are shown in the supporting material in Zhan and Gregg (2017). However, typically, volcanoes may only be instrumented by a few stations and often times may only have data available from yearly campaigns. In our first synthetic test, we look specifically at the limitations posed by station availability and seek to address the situation where only a few instruments are available for data collection. In the model tests, at each time step four GPS stations are removed randomly, until only the four GPS stations remain. The test shows that the misfits gradually increase with the decreasing number of GPS stations, and the calculated parameters significantly deviate from the synthetic values when more than half of the GPS stations are removed (Fig. 2.7b). As illustrated in Fig. 2.7b, as the number of continuous stations is reduced to 4 or less, there is significant increase in the parameter misfit. In a real-world data collection effort, one may take this result to

indicate that having only four continuous stations may be prohibitive for efficient use of the EnKF. However, as we will show in the following section, strategies such as episodically moving instruments to occupy a larger range of locations can significantly enhance GPS data collection when station availability is limited.

GPS data continuity

In the previous section, we illustrated the impact of data scarcity on the ability of the EnKF to accurately predict parameter values. Another potential limitation of GPS is the loss of station functionality during deployment, which may result in prolonged gaps in the GPS data stream. To mimic this situation, we conduct a test in which random GPS stations (from 1 station and 16 stations concurrently) switch off (Table 2.2) to create "gaps" in our synthetic data. The misfit plot shows that data discontinuities do not significantly impact the EnKF's ability find the assumed parameters (Fig. 2.7c). Although leaving only four GPS stations working at a given time makes EnKF lost, the performance using eight active GPS stations each time step, but moving them effectively is as good as using all station. Effectively, if only a limited number of GPS instruments are available, they will provide a similar EnKF performance as having a larger number of operational instruments as long as the stations are episodically moved to occupy more sites around the region of unrest. Of course, moving permanent stations is unrealistic, so supplementing a low number of permanent stations with campaign station observations from a variety of locations may be an effective strategy for improving model performance.

GPS station locations

The previous section focused on the number of GPS station locations necessary to provide a robust data stream for the EnKF. It is also important to optimize the locations of the installed GPS stations. In particular, when establishing permanent, continuous stations near a restless

volcano, potential risks may prohibit installation at the center of deformation. In this section, a series of tests are conducted to illustrate the impact of installing GPS stations further away from the loci of unrest. In other words, the distance between the first GPS station and the center of deformation is varied from 0.5 km to 4.5 km (Table 2.2). The results show that the EnKF performs much better when the GPS stations are closer to the volcano (Fig. 2.7a), and indicate that having a deformation signal at the center of uplift can greatly improve model fit.

2.4 Discussion

2.4.1 Optimizing the EnKF setup

One of the advantages of using the Ensemble Kalman Filter (EnKF) is computational economy, which is greatly improved over other data assimilation methods, such as the traditional Kalman Filter or the Extended Kalman Filter (Evensen, 2009a; Gregg and Pettijohn, 2016). However, when a larger ensemble space is introduced, the computational cost is greatly increased since each ensemble requires an independent model solution. In this study, we use the analytical solution from Mogi (1958) to calculate the forecast ensembles, which is computationally swift. However, a finite element approach as used by Gregg and Pettijohn (2016) will take upwards of 20 hours for an EnKF analysis with 100 ensembles run for 100 days, in 2D and several days to run in 3D.

Our synthetic tests using either InSAR or GPS data indicate that the EnKF performance is considerably enhanced when using 100 ensemble over using only 50 ensembles. This suggests, at least in this simple volcano reservoir modeling with less than ten unknown parameters, a minimum value of 50 ensemble members (Evensen, 2009a) is sufficient. Utilizing fewer FEMs in the ensemble greatly reduces the computational cost, especially as more sophisticated reservoir models are applied (Simakin and Ghassemi, 2010; Gregg et al., 2012; Ronchin et al., 2013; de Silva and Gregg, 2014; Cannavò et al., 2015). However, when applying the EnKF to

natural data sets in future investigations, it will be important to establish a critical minimum value for the number of ensembles, which may vary from system to system depending on the unrest dynamics.

Compared to increasing the number of ensembles, utilizing additional iterations between data assimilation time steps when applying InSAR data is a far more economical way to improve the EnKF performance. Usually, an InSAR image contains about 1000 measurement points even after down-sampling. Therefore, the EnKF requires more iterations to converge on a solution. However, the GPS measurements are far less than InSAR, and one iteration may be enough. The iteration test in Section 2.3.1 indicates that the RMSEs and parameter misfits are greatly reduced, even if only one additional iteration is introduced (Fig. 2.5c and d). The cost of applying more iterations can be estimated by the equation (2.12), which is ~$Ndim \times Nens^2$ (Evensen, 2003). Assuming we apply 100 ensembles and have 1000 measurements at every step, the computational costs of calculating A is around the order of 10^7. If we use a linear elastic finite element model, which takes the topography into account, to calculate the forecasting ensemble and we assume the finite element mesh creates 10^5 nodes and corresponding degrees of freedom, which is 10 times more than the synthetic model in this study. The computational cost is more than 10^{10} for every ensemble per step, which is three orders of magnitude greater than applying one additional iteration. In summary, applying several more iterations between time steps is a much more efficient way to improve the EnKF analysis and is doable with far less computational cost.

2.4.2 Does a better initial guess lead to a better solution?

As opposed to other data assimilation methods such as genetic algorithms (Barth, 1992), the EnKF requires a presumption of the initial parameter distributions to produce the initial ensembles created by a Monte Carlo method (Evensen, 2009a). Parameters such as location and

geometry of a magma reservoir are not well constrained unless additional geophysical observations or *a priori* information are available. However, the precise structure beneath many restless volcanoes, for example the volcanoes in the Sunda Arc of Indonesia, are still unknown (Chaussard and Amelung, 2014). The lack of certainty for the source parameters of the observed surface deformation might be problematic for creating an initial guess of the parameters for the magma reservoir. Furthermore, some parameters such as volume changes and pressure changes in the magma reservoir cannot be directly measured.

Fortunately, synthetic tests of varying the initial parameter guesses indicate that the distribution of the initial parameters has little to no effect on the value of the updated parameters after several steps of EnKF analysis (Fig. 2.6). Therefore, although the initial guess for the modeling parameters is needed in the EnKF analysis, a better guess of the model parameters does not necessarily lead to a better EnKF performance, meaning that the stability of this scheme is parametrically unconditional.

2.4.3 Improving data assimilation with better data

How the measurements affect the predictive performance of data assimilation schemes is of great concern to geodesists, since model predictions must be optimized with spatially and temporally limited data sets. This is especially pertinent for the collection of continuous GPS data, which requires that GPS station locations to be chosen, instrumented, and maintained; this costs time, money, and the inherent risk of installing a GPS station close to an active volcano. From the GPS location synthetic test, we conclude that the closer a GPS station is to the loci of deformation, the better the EnKF performance (Fig. 2.7a). However, to determine how close a GPS station needs to be installed, multiple EnKF experiments can be run on existing data to determine the critical distance for establishing a GPS station.

Just as instrument location is critical for constraining the evolution of a magma chamber,

the number of available instruments is also key. Given the financial considerations of installing and maintaining GPS stations, optimizing station location with number of instruments can be critical for providing optimal data coverage. As one might expect, our synthetic tests indicate that having fewer GPS stations results in larger misfits in the EnKF analysis (Fig. 2.7b). Credible results are not achieved with < 8 GPS stations (Fig. 2.7b), unless the stations are occasionally relocated to different places, which is indicated by the GPS temporal continuity test (Fig. 2.7c). In Figure 2.7c, we find that even if only 8 GPS stations are working at a given time, the EnKF analysis can provide as accurate of a result as a model with 20 continuous GPS stations. Therefore, if only a limited number of campaign GPS instruments are available, shifting them between several locations to provide discontinuous data for multiple locations is a better way to provide constrains for data assimilation, than to keep them steady in one location to provide continuous data.

InSAR measurements are routinely affected by the snow, ice, and atmospheric interference, and/or topography which can limit the coverage over a study area (Massonnet and Feigl, 1998). Especially in a volcano study, a topographically high volcano edifice may result in an InSAR LOS shadow and limit InSAR data coverage on one side of a volcano (Chaussard and Amelung, 2012; Chaussard et al., 2013). Our synthetic tests of InSAR data coverage (Fig. 2.7d), indicate that EnKF performance is seldom affected by the coverage of the InSAR data. However, in this axisymmetric, synthetic study the percentage of the study area not coved by InSAR measurement is offset by information provided by InSAR coverage from other sections of the volcano, similar to what was observed in the 2D EnKF applications (Gregg and Pettijohn, 2016). On the other hand, if the data are missing from a significant region of the volcano, due to snow or atmospheric artifacts, the EnKF derived parameters will not be well constrained (Fig. 2.7d).

Compared to the InSAR data, GPS data create better predictions on the evolution of the magma volume change. However, the EnKF can find the assumed parameters in fewer steps using InSAR data than using GPS data when applying iterative analysis. The joint assimilation of GPS and InSAR data provides the best estimation of the parameters of the magma reservoir (Gregg and Pettijohn, 2016) especially when the abundant data are supplied (Fig. 2.8). Furthermore, applying data assimilation with present data also provides information for future data collection. For example, establishing GPS stations in the area where InSAR data in not available will help to constrain estimations of a magma reservoir's location (Fig. 2.8).

Ultimately, one of the advantages to the EnKF approach is that it allows investigators to test data collection schemes and optimize future efforts at active volcanoes. InSAR can be used to set the stage for on-the-ground observations, which will in turn enhance future InSAR data collection efforts. While this particular investigation focuses on ground deformation and geodesy, the results provided by InSAR and GPS data assimilation will also inform additional geophysical data collection efforts such as gravity, tomography, and magnetotellurics.

2.4.4 The issue of non-uniqueness

The EnKF analysis sometimes results in poor performance due to the issue of non-uniqueness when a complicated system is being described by an over simplified model (Evensen, 2009a; Baehr et al., 2010; Jafarpour and Tarrahi, 2011). For the case of a deforming volcano, magma reservoir evolution is a highly non-unique problem and the same surface displacement may be generated by multiple combinations of reservoir location, geometry, and overpressure according to equations (2.3) and (2.4) (Gregg and Pettijohn, 2016). This issue is particularly pronounced when using the elegant, but simple Mogi elastic model. Enlarging the size of the parameter space is a way to produce more parametric combinations and give the EnKF more options for optimization (Fig. 2.5e and f); however, this will not solve the problem of

distinguishing which combination is the true solution.

An alternative approach is to combine two or more parameters in the Mogi (1958) model into one, as we did in this study, replacing reservoir radius and overpressure with volume change. During the tests, the predicted volume change, ΔV, is more consistent with the exact value in the synthetic model, while the radius or overpressure are not as close to the assumed value as the volume change (Fig. 2.8), since there are numerous non-unique combination of overpressure and radius that satisfy a certain volume change.

In future efforts, more types of measurements and more sophisticated models should be introduced to provide additional constrains on the overpressure or geometrical properties of the source of unrest. Additional geophysical observations such as tomography (Burnett et al., 1989; Day et al., 2001; Lees, 2007; Stankiewicz et al., 2010) may provide important constraints on magma chamber radius. In other words, assimilating geophysical observations that constrain the geometry of the magmatic system will allow future EnKF investigations to infer the magma storage evolution.

2.5 Conclusions

Developing data assimilation strategies to incorporate the vast array of volcano monitoring data sets into increasingly more sophisticated geodynamics models is critical for future efforts to assess volcanic unrest. Fields such as climate science, hydrology, and physical oceanography have long used statistical data assimilation approaches to provide forecasts and model updates from large disparate datasets (e.g. Julier et al., 2000; Bertino et al., 2003; Julier et al., 2004; Evensen, 2003, 2009a, 2009b; Dumedah et al., 2011; Dumedah, 2012). In an effort to build a data assimilation framework for volcano applications, we have developed the widely used Ensemble Kalman Filter (EnKF) sequential data assimilation method in 3D and conducted a

series of sensitivity tests using synthetic observations of surface deformation. The sensitivity tests give us insights into how to improve the EnKF performance for volcano applications and optimize both the data assimilation strategy and future data collection efforts.

The results of our sensitivity tests reveal that one may greatly improve the data assimilation efficiency with little computational expense by utilizing additional EnKF analysis iterations between observations time steps. Alternatively, we find that increasing the number of ensemble members to more than 100, the computational costs of which is at least 1000 times more than using an intra-EnKF iteration strategy, does not provide a significant gain in model convergence. Another great advantage of the EnKF method is that the stability of the EnKF method does not depend on the initial parameter guess. Specifically, tests of the impact of the initial parameter guess indicate that the parameter assumption is unconditional and that the accuracy of the initial guess has no impact on the EnKF performance.

Tests of data collection strategies provide guidance for future data collection efforts. In particular, tests for where the most proximal GPS station must be placed to provide sufficient data coverage encourage geodesists to establish the GPS station closer to the volcano uplift center. Furthermore, if the availability of GPS equipment is limited, shifting instruments between several locations to record discontinuous data provides a better data stream for data assimilation than installing a small number of stations at fixed locations. Finally, InSAR data gaps due to atmospheric noise, snow cover, or topography shadows may not significantly impact its effectiveness, unless major portions of the volcano are masked.

2.6 Figures and Tables

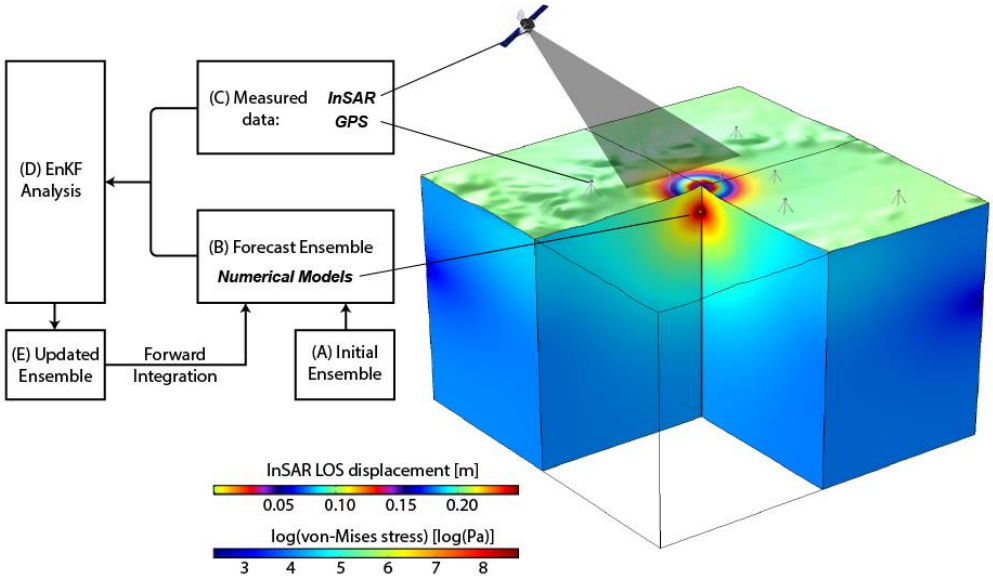

Figure 2.1 Illustration of the data assimilation strategy for magma reservoir modeling. The example model shows the predicted surface deformation (top surface) and von Mises stress (at depth) due to a magma chamber volume change of 0.003 km^3. The Ensemble Kalman Filter (EnKF) approach is modified from Gregg and Pettijohn (2016). (A) The initial ensemble of models is produced, including model uncertainties. The forecast ensemble (B) is sequentially derived from forward integration of the initial suite of models. (C) Data utilized in this implementation include InSAR and/or GPS, but could also include additional such as gravity, seismicity, and tomography. (D) When new data are available, an EnKF analysis is conducted to update the model parameters (E) and change the trajectory of the model. The updated model parameters are then used to create a new forecast ensemble.

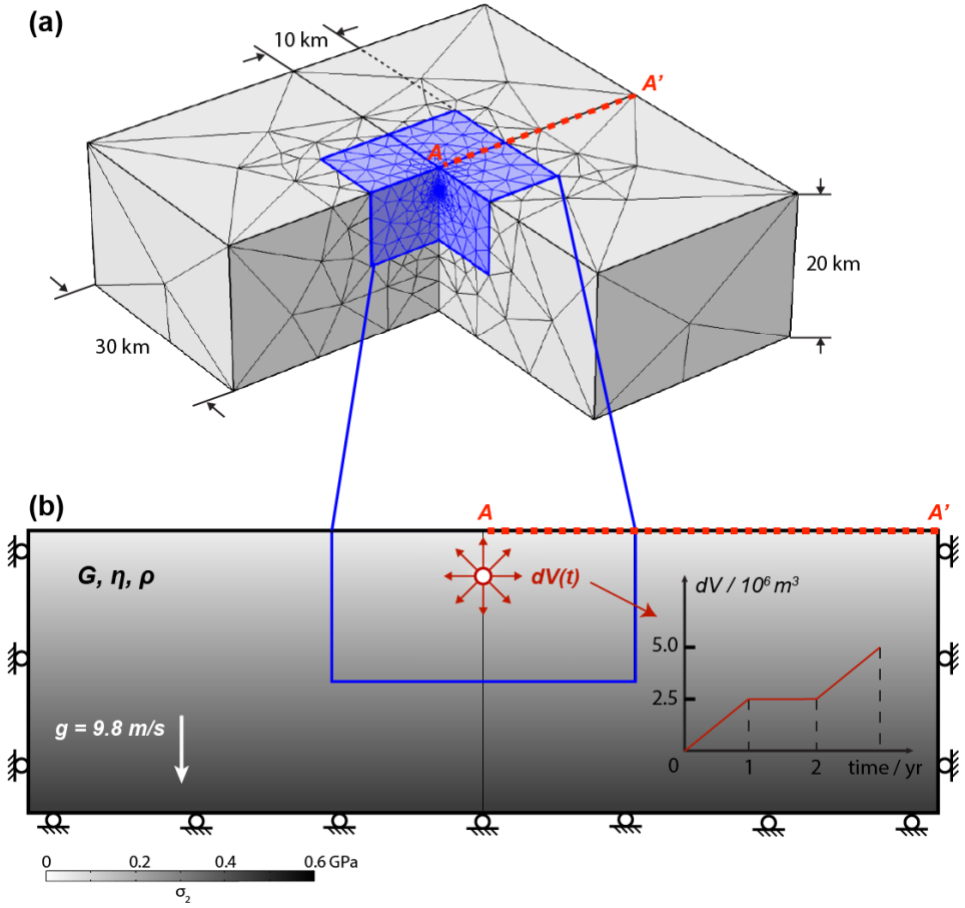

Figure 2.2 Finite Element Model (FEM) setup used to produce the synthetic InSAR and GPS data sets. (a) The 3D model is finely meshed near the magma reservoir and coarsens at distance away from the center of the expanding magma chamber. (b) The boundary conditions of the model follow Gregg et al. (2012) and are adapted for the 3D implementation. Roller, zero normal displacement, conditions are applied on the sides and bottom of the model, a free surface is assumed at the top of the model, and a pressure boundary condition is applied along the magma chamber to produce the volume change shown in the inset. The grey scale illustrates the magnitude of the isostatic stress due to gravitational loading. The line AA' is used for the displacements benchmark provided in Figure 2.3.

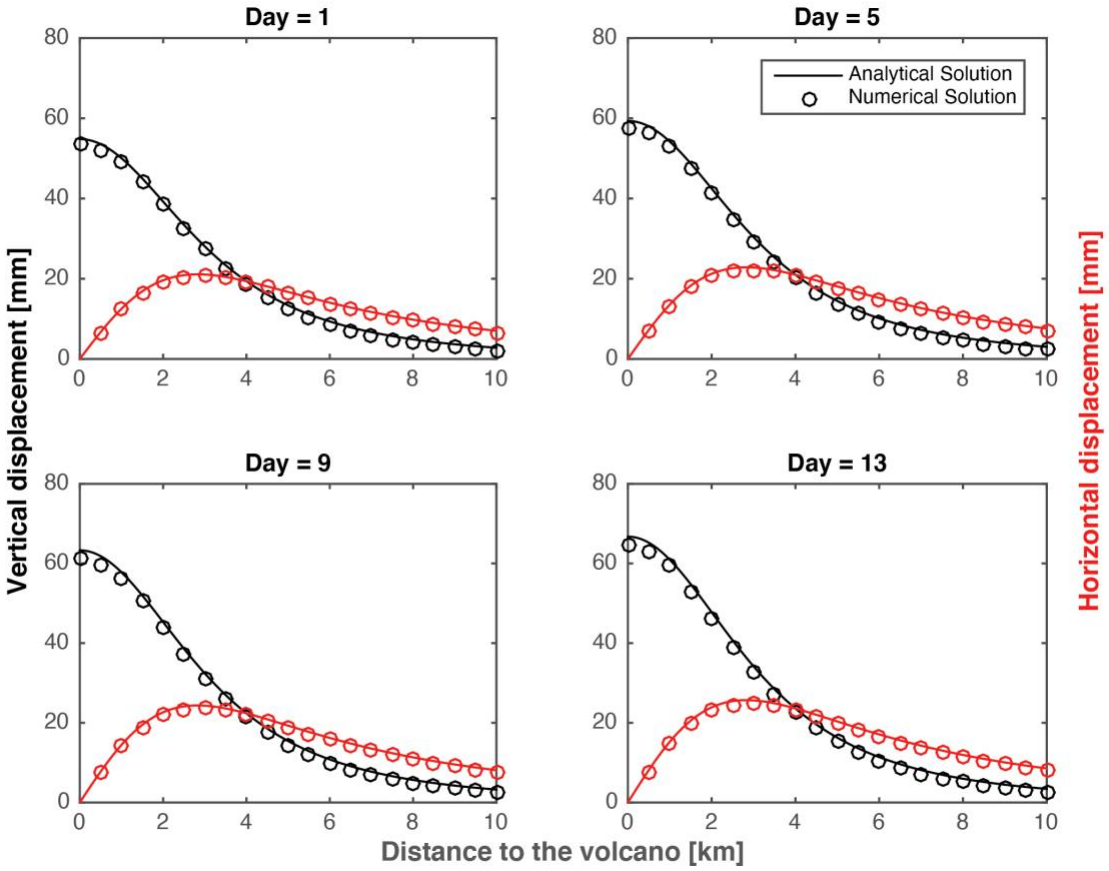

Figure 2.3 Benchmarks for surface displacement predicted by the 3D model. Vertical motion in shown in black and horizontal motion in red. We compare the 3D viscoelastic numerical solution provided by COMSOL, solid lines, with the viscoelastic analytical solution, circles (equation [1] in Gregg et al., 2012).

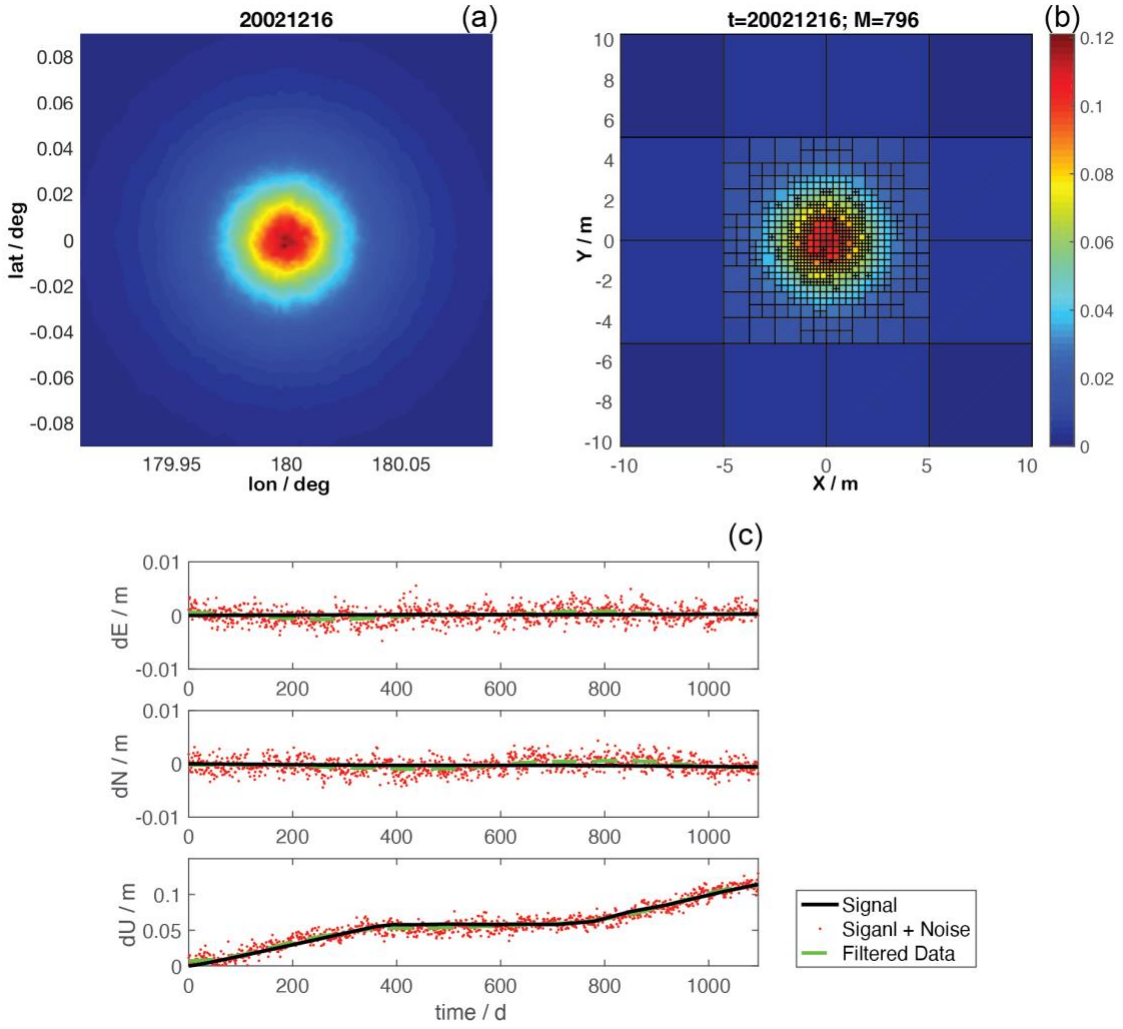

Figure 2.4 Synthetic datasets produced by the FEM setup illustrated in Figure 2.2. (a) Synthetic InSAR observations of vertical displacement with a distance-correlated noise. (b) Quadtree partition of InSAR data based on root mean square algorithm (Jónsson et al., 2002). (c) Time series of three displacement components for the GPS station at (0, 0). The solid black lines represent the signal of surface deformation from the FEM model. The red dots are the GPS signal which has been perturbed by white and flicker noise. The green dashed lines show the filtered data used in the EnKF analysis.

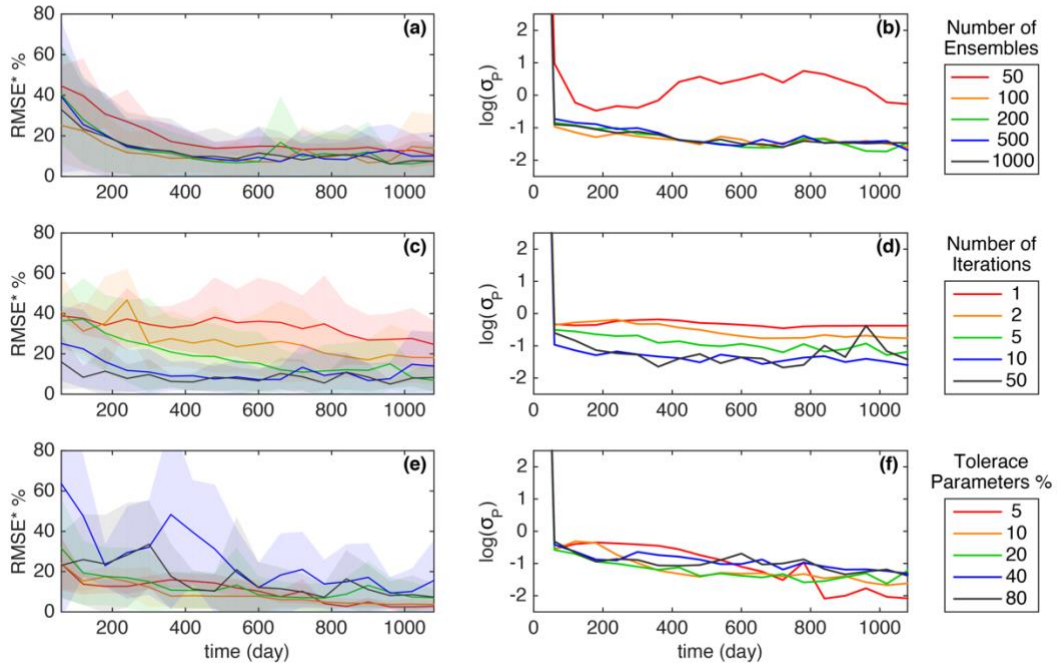

Figure 2.5 Sensitivity tests to investigate the effect of the EnKF setup using synthetic InSAR data. (a) and (b) the number of ensembles is varied from 50 to 1000. (a) The calculated normalized RMSE indicates that variations in $Nens$ has very little impact on the ability of the EnKF to match the observed surface discplacement. (b) The parameter misfit (in log) illustrates a slightly better fit at higher numbers of ensembles. (c) and (d) the number of intra-EnKF iterations are tested. The calculated normalized RMSE (c) and the parameter misfit (d) both illustrate that the additional of intra-EnKF iterations can significantly improve the model fit. However, this effect is maximized at 10 intra-EnKF iterations. (e) and (f) test variations in the minimum tolerance of the EnKF parameter standard deviation used to compose the EnKF ensembles. While variations in tolerance appear to have a minimal impact in the EnKF's ability to match the surface deformation signal (e), there is a much greater impact on the predicted parameter values. The solid lines in color show the mean values of the normalized root mean square errors (RMSE*) or parameter misfits (σ_P) in log scale. The shadows are the standard deviations.

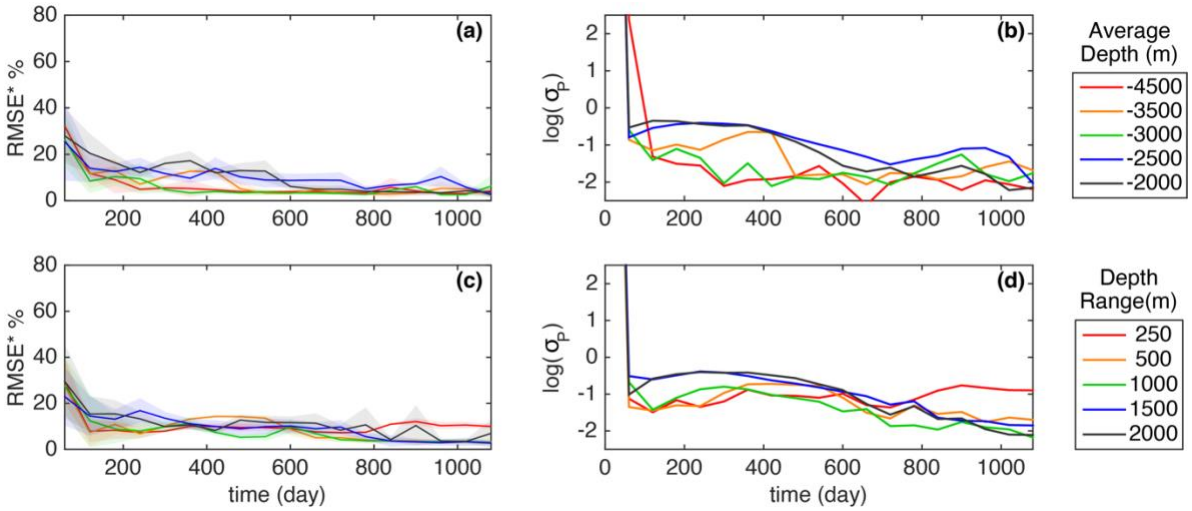

Figure 2.6 Sensitivity tests for variations in the initial distribution of magma reservoir depth using synthetic InSAR data. (a) Normalized RMSEs of the displacement field for tests considering different average values of magma reservoir depth, and (c) for tests considering different ranges of magma reservoir depth. (b) Parameter misfits for the "average value" tests, and (d) parameter misfits for "range" tests. The solid lines in color show the mean values of the normalized root mean square errors (RMSE*) or parameter misfits (σ_P) in log scale. The shadows are the standard deviations.

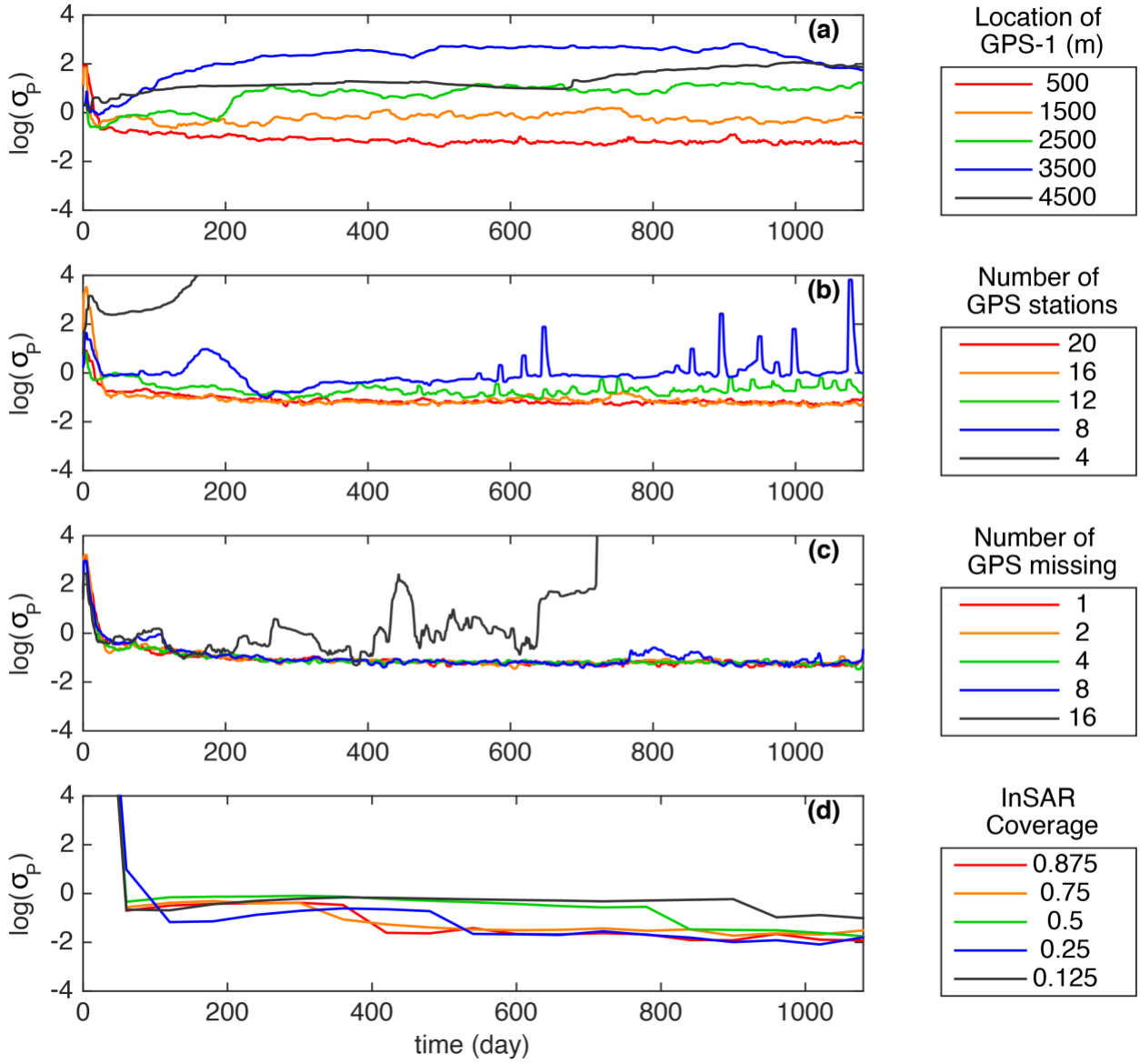

Figure 2.7 Parameter misfits for sensitivity tests investigating strategies for utilizing spotty GPS and InSAR data. (a) Variations in the distance between the nearest GPS station, GPS-1 (Fig. 2.4a), and the center of uplift. (b) Variation in the total number of available GPS stations. (c) Variations in the number of GPS stations, which do not work at each time step. (d) Fraction of the region surrounding the center of volcanic uplift where InSAR data are not available. The solid lines in color show the mean value of the parameter misfits (σ_P) in log scale(σ_P) in log scale.

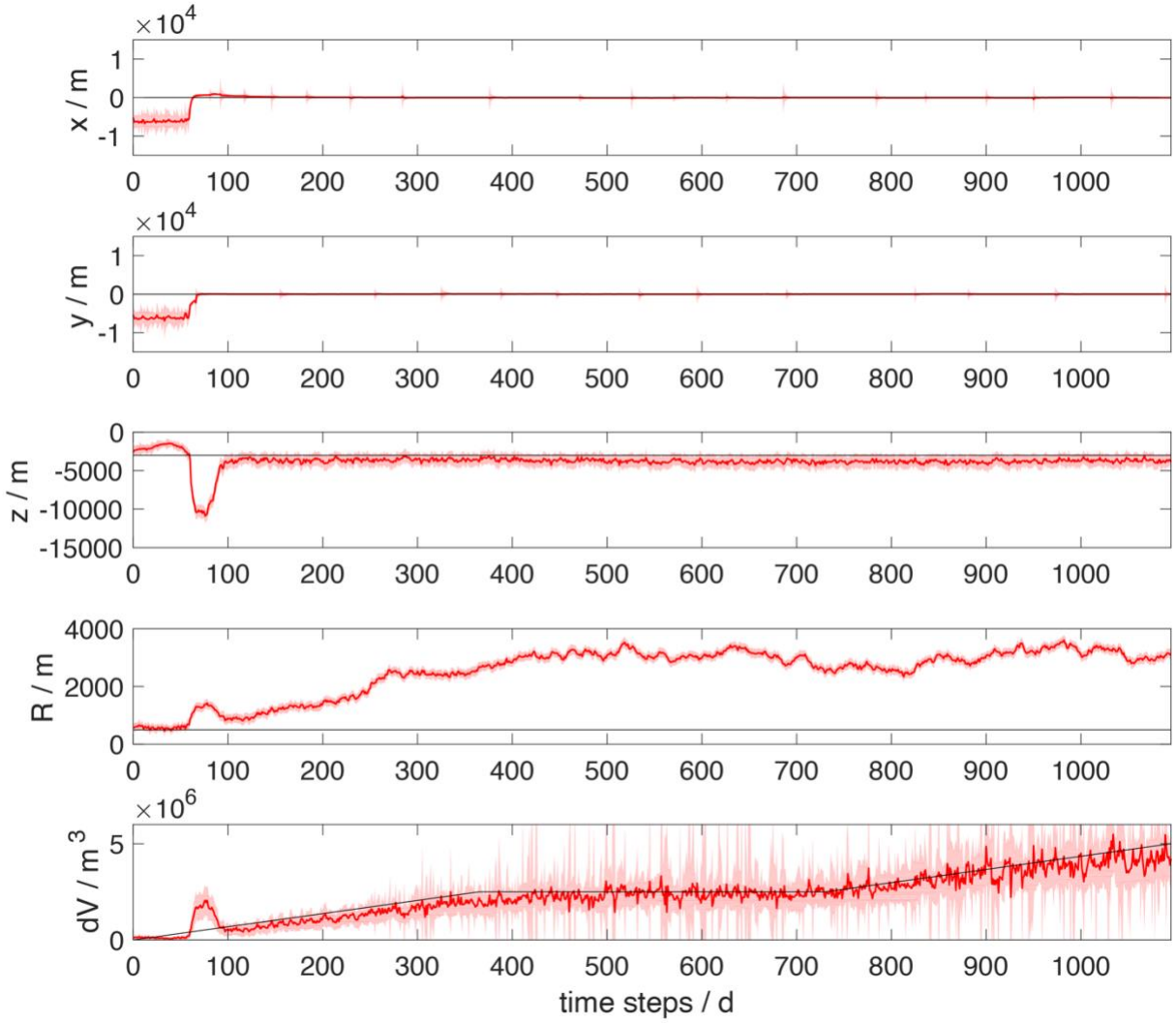

Figure 2.8 The parameter estimation of a joint InSAR and GPS data assimilation. The EnKF analysis uses 100 ensembles with 10 iterations. The minimum tolerance for parameter space is 20 %. The synthetic GPS station locations are shown at Fig. 2.4, where the distance of GPS-1 is 0.5 km. The red solid lines with shadows show the estimation of the parameters by EnKF analysis, and the black solid lines represent the parameters assumed in the synthetic model. It costs only about 100 days for the EnKF to capture the assumed values. Although, the EnKF is unable to find the real radius due to non-uniqueness, the EnKF is able to find the evolution of the volume changes within the magma reservoir.

Table 2.1 Notations.

Symbol	Description
$\boldsymbol{A}$	Forecast ensemble matrix
$\boldsymbol{A'}$	Ensemble perturbation matrix
$\boldsymbol{A}^a$	EnKF analysis matrix
$\boldsymbol{P}_e$	Covariance matrix for model perturbation
$\boldsymbol{R}_e$	Covariance matrix for measurement perturbation
$\boldsymbol{D}$	Measurement matrix
$\boldsymbol{\delta d}$	Measurement perturbation matrix
$\boldsymbol{H}$	Mapping matrix
Γ_p	Parameter space tolerance
Nens	Number of ensembles
Npar	Number of parameters
Nmes	Number of measurements
Ndim	Number of parameters adding with measurements
Z_i^t	Assumed parameter (i) for synthetic
Z_i^a	EnKF updated parameter (i)
t	Time
dP	Source overpressure
dV	Source volume change
ν	Poisson ratio
E	Young's modulus
G	Shear modulus
$\dot{\varepsilon}$	Strain rate
$\dot{\sigma}$	Stress rate
η	Viscosity
ρ	Density
σ	Stress

Table 2.2 Parameters used for the synthetic model.

Parameter	Value
Chamber location in X (m)	0
Chamber location in Y (m)	0
Chamber depth (m)	3000
Chamber Radius (m)	500
Maximum volume change (km^3)	0.005

2.7 Acknowledgements

We would like to acknowledge helpful discussions with F. Amelung, Y. Aoki, E. Chaussard, and J. Pettijohn. We would also like to thank Dr. Michael Poland and two anonymous reviewers for their comments which greatly improved our manuscript. Development of data assimilation methods for monitoring active volcanoes using InSAR is funded by NASA (13-ESI13-0034).

2.8 References

Agram, P.S., Simons, M., 2015. A noise model for InSAR time series. J. Geophys. Res. Solid Earth 120, 2752–2771. doi:10.1002/2014JB011271

Allen, J.I., Eknes, M., Evensen, G., 2003. An Ensemble Kalman Filter with a complex marine ecosystem model: hindcasting phytoplankton in the Cretan Sea. Ann Geophys 21, 399–411. doi:10.5194/angeo-21-399-2003

Alparone, S., Bonaccorso, A., Bonforte, A., Currenti, G., 2013. Long-term stress-strain analysis of volcano flank instability: The eastern sector of Etna from 1980 to 2012. J. Geophys. Res. Solid Earth 118, 5098–5108. doi:10.1002/jgrb.50364

Anderson, K., Segall, P., 2013. Bayesian inversion of data from effusive volcanic eruptions using physics-based models: Application to Mount St. Helens 2004-2008. J. Geophys. Res.-Solid Earth 118, 2017–2037. doi:10.1002/jgrb.50169

Baehr, C., Pannekoucke, O., others, 2010. Some issues and results on the EnKF and particle filters for meteorological models. Chaotic Syst. Theory Appl. 27–24.

Barth, N.H., 1992. Oceanographic experiment design II: Genetic algorithms. J. Atmospheric Ocean. Technol. 9, 434–443.

Battaglia, M., Segall, P., Murray, J., Cervelli, P., Langbein, J., 2003. The mechanics of unrest at Long Valley caldera, California: 1. Modeling the geometry of the source using GPS,

leveling and two-color EDM data. J. Volcanol. Geotherm. Res. 127, 195–217. doi:10.1016/S0377-0273(03)00170-7

Battaglia, M., Segall, P., Roberts, C., 2003. The mechanics of unrest at Long Valley caldera, California. 2. Constraining the nature of the source using geodetic and micro-gravity data. J. Volcanol. Geotherm. Res. 127, 219–245. doi:10.1016/S0377-0273(03)00171-9

Beauducel, F., Cornet, F.H., 1999. Collection and three-dimensional modeling of GPS and tilt data at Merapi volcano, Java. J. Geophys. Res. 104, 725–736.

Bertino, L., Evensen, G., Wackernagel, H., 2003. Sequential data assimilation techniques in oceanography. Int. Stat. Rev. 71, 223–241.

Bevis, M., Foster, J., 2000. January 30, 1997 eruptive event in Kilauea Volcano, Hawaii as monitored by continuous GPS. Geophys. Res. Lett. 27, 2757–2760.

Biggs, J., Ebmeier, S.K., Aspinall, W.P., Lu, Z., Pritchard, M.E., Sparks, R.S.J., Mather, T.A., 2014. Global link between deformation and volcanic eruption quantified by satellite imagery. Nat. Commun. 5.

Bonforte, A., Puglisi, G., 2006. Dynamics of the eastern flank of Mt. Etna volcano (Italy) investigated by a dense GPS network. J. Volcanol. Geotherm. Res. 153, 357–369.

Bonforte, A., Puglisi, G., 2003. Magma uprising and flank dynamics on Mount Etna volcano, studied using GPS data (1994–1995). J. Geophys. Res. Solid Earth 108.

Brusdal, K., Brankart, J.M., Halberstadt, G., Evensen, G., Brasseur, P., van Leeuwen, P.J., Dombrowsky, E., Verron, J., 2003. A demonstration of ensemble-based assimilation methods with a layered OGCM from the perspective of operational ocean forecasting systems. J. Mar. Syst. 40, 253–289. doi:10.1016/S0924-7963(03)00021-6

Burnett, M.S., Caress, D.W., Orcutt, J.A., 1989. Tomographic image of the magma chamber at

12 50’N on the East Pacific Rise.

Cannavò, F., Camacho, A.G., González, P.J., Mattia, M., Puglisi, G., Fernández, J., 2015. Real Time Tracking of Magmatic Intrusions by means of Ground Deformation Modeling during Volcanic Crises. Sci. Rep. 5.

Carbone, D., Currenti, G., Del Negro, C., 2007. Elastic model for the gravity and elevation changes before the 2001 eruption of Etna volcano. Bull. Volcanol. 69, 553–562. doi:10.1007/s00445-006-0090-5

Chaussard, E., Amelung, F., 2014. Regional controls on magma ascent and storage in volcanic arcs. Geochem. Geophys. Geosystems 15, 1407–1418. doi:10.1002/2013GC005216

Chaussard, E., Amelung, F., 2012. Precursory inflation of shallow magma reservoirs at west Sunda volcanoes detected by InSAR: InSAR Survey of West Sunda Volcanoes. Geophys. Res. Lett. 39, n/a–n/a. doi:10.1029/2012GL053817

Chaussard, E., Amelung, F., Aoki, Y., 2013. Characterization of open and closed volcanic systems in Indonesia and Mexico using InSAR time series: InSAR Time Series in Indonesia and Mexico. J. Geophys. Res. Solid Earth 118, 3957–3969. doi:10.1002/jgrb.50288

Cianetti, S., Giunchi, C., Casarotti, E., 2012. Volcanic deformation and flank instability due to magmatic sources and frictional rheology: the case of Mount Etna. Geophys. J. Int. 191, 939–953.

Currenti, G., Del Negro, C., Ganci, G., 2007. Modelling of ground deformation and gravity fields using finite element method: an application to Etna volcano. Geophys. J. Int. 169, 775–786. doi:10.1111/j.1365-246X.2007.03380.x

Day, A.J., Peirce, C., Sinha, M.C., 2001. Three-dimensional crustal structure and magma chamber geometry at the intermediate-spreading, back-arc Valu Fa Ridge, Lau Basin—

results of a wide-angle seismic tomographic inversion. Geophys. J. Int. 146, 31–52.

Del Negro, C., Currenti, G., Scandura, D., 2009. Temperature-dependent viscoelastic modeling of ground deformation: application to Etna volcano during the 1993–1997 inflation period. Phys. Earth Planet. Inter. 172, 299–309.

de Silva, S.L., Gregg, P.M., 2014. Thermomechanical feedbacks in magmatic systems: Implications for growth, longevity, and evolution of large caldera-forming magma reservoirs and their supereruptions. J. Volcanol. Geotherm. Res. 282, 77–91. doi:10.1016/j.jvolgeores.2014.06.001

Desmarais, E.K., Segall, P., 2007. Transient deformation following the 30 January 1997 dike intrusion at Kilauea volcano, Hawai'i. Bull. Volcanol. 69, 353–363. doi:10.1007/s00445-006-0080-7

Dmitrieva, K., Segall, P., DeMets, C., 2015. Network-based estimation of time-dependent noise in GPS position time series. J. Geod. 89, 591–606. doi:10.1007/s00190-015-0801-9

Dumedah, G., 2012. Formulation of the Evolutionary-Based Data Assimilation, and its Implementation in Hydrological Forecasting. Water Resour. Manag. 26, 3853–3870. doi:10.1007/s11269-012-0107-0

Dumedah, G., Berg, A.A., Wineberg, M., 2011. An Integrated Framework for a Joint Assimilation of Brightness Temperature and Soil Moisture Using the Nondominated Sorting Genetic Algorithm II. J. Hydrometeorol. 12, 1596–1609. doi:10.1175/JHM-D-10-05029.1

Emardson, T.R., Simons, M., Webb, F.H., 2003. Neutral atmospheric delay in interferometric synthetic aperture radar applications: Statistical description and mitigation. J. Geophys. Res. Solid Earth 108, 2231. doi:10.1029/2002JB001781

Evensen, G., 2009a. Data Assimilation. Springer Berlin Heidelberg, Berlin, Heidelberg.

Evensen, G., 2009b. The ensemble Kalman filter for combined state and parameter estimation. IEEE Control Syst. Mag. 29, 83–104. doi:10.1109/MCS.2009.932223

Evensen, G., 2003. The Ensemble Kalman Filter: theoretical formulation and practical implementation. Ocean Dyn. 53, 343–367. doi:10.1007/s10236-003-0036-9

Fattahi, H., Amelung, F., 2015. InSAR bias and uncertainty due to the systematic and stochastic tropospheric delay: InSAR Uncertainty Tropospheric Delay. J. Geophys. Res. Solid Earth 120, 8758–8773. doi:10.1002/2015JB012419

Gregg, P.M., de Silva, S.L., Grosfils, E.B., 2013. Thermomechanics of shallow magma chamber pressurization: Implications for the assessment of ground deformation data at active volcanoes. Earth Planet. Sci. Lett. 384, 100–108. doi:10.1016/j.epsl.2013.09.040

Gregg, P.M., de Silva, S.L., Grosfils, E.B., Parmigiani, J.P., 2012. Catastrophic caldera-forming eruptions: Thermomechanics and implications for eruption triggering and maximum caldera dimensions on Earth. J. Volcanol. Geotherm. Res. 241-242, 1–12. doi:10.1016/j.jvolgeores.2012.06.009

Gregg, P.M., Pettijohn, C., 2015. A multi-data stream assimilation framework for the assessment of volcanic unrest.

Gregg, P.M., Pettijohn, J.C., 2016. A multi-data stream assimilation framework for the assessment of volcanic unrest. J. Volcanol. Geotherm. Res. 309, 63–77. doi:10.1016/j.jvolgeores.2015.11.008

Grosfils, E.B., 2007. Magma reservoir failure on the terrestrial planets: Assessing the importance of gravitational loading in simple elastic models. J. Volcanol. Geotherm. Res. 166, 47–75. doi:10.1016/j.jvolgeores.2007.06.007

Grosfils, E.B., McGovern, P.J., Gregg, P.M., Galgana, G.A., Hurwitz, D.M., Long, S.M.,

Chestler, S.R., 2015. Elastic models of magma reservoir mechanics: a key tool for investigating planetary volcanism, in: Platz, T., Massironi, M., Byrne, P.K., Hiesinger, H. (Eds.), Volcanism and Tectonism Across the Inner Solar System. Geological Soc Publishing House, Bath, pp. 239–267.

Hickey, J., Gottsmann, J., del Potro, R., 2013. The large-scale surface uplift in the Altiplano-Puna region of Bolivia: A parametric study of source characteristics and crustal rheology using finite element analysis. Geochem. Geophys. Geosystems 14, 540–555. doi:10.1002/ggge.20057

Hickey, J., Gottsmann, J., Mothes, P., 2015. Estimating volcanic deformation source parameters with a finite element inversion: The 2001-2002 unrest at Cotopaxi volcano, Ecuador. J. Geophys. Res. Solid Earth 120, 1473–1486. doi:10.1002/2014JB011731

Jafarpour, B., Tarrahi, M., 2011. Assessing the performance of the ensemble Kalman filter for subsurface flow data integration under variogram uncertainty. Water Resour. Res. 47. doi:10.1029/2010WR009090

Jónsson, S., Zebker, H., Segall, P., Amelung, F., 2002. Fault slip distribution of the 1999 Mw 7.1 Hector Mine, California, earthquake, estimated from satellite radar and GPS measurements. Bull. Seismol. Soc. Am. 92, 1377–1389.

Julier, S.J., Julier, S.J., Uhlmann, J.K., 2004. Unscented Filtering and Nonlinear Estimation. Proc. IEEE 92, 401–422. doi:http://dx.doi.org/10.1109/jproc.2003.823141

Julier, S., Uhlmann, J., Durrant-Whyte, H.F., 2000. A new method for the nonlinear transformation of means and covariances in filters and estimators. Ieee Trans. Autom. Control 45, 477–482. doi:10.1109/9.847726

Kalman, R.E., 1960. A new approach to linear filtering and prediction problems. J. Fluids Eng.

82, 35–45.

Lees, J.M., 2007. Seismic tomography of magmatic systems. J. Volcanol. Geotherm. Res. 167, 37–56. doi:10.1016/j.jvolgeores.2007.06.008

Le Mével, H., Feigl, K.L., Córdova, L., DeMets, C., Lundgren, P., 2015. Evolution of unrest at Laguna del Maule volcanic field (Chile) from InSAR and GPS measurements, 2003 to 2014. Geophys. Res. Lett. 42, 6590–6598.

Lisaeter, K.A., Evensen, G., Laxon, S., 2007. Assimilating synthetic CryoSat sea ice thickness in a coupled ice-ocean model. J. Geophys. Res.-Oceans 112, C07023. doi:10.1029/2006JC003786

Lohman, R.B., Simons, M., 2005. Some thoughts on the use of InSAR data to constrain models of surface deformation: Noise structure and data downsampling. Geochem. Geophys. Geosystems 6, n/a–n/a. doi:10.1029/2004GC000841

Lu, Z., Dzurisin, D., Biggs, J., Wicks, C., McNutt, S., 2010. Ground surface deformation patterns, magma supply, and magma storage at Okmok volcano, Alaska, from InSAR analysis: 1. Intereruption deformation, 1997-2008. J. Geophys. Res.-Solid Earth 115, B00B02. doi:10.1029/2009JB006969

Lu, Z., Mann, D., Freymueller, J.T., Meyer, D.J., 2000. Synthetic aperture radar interferometry of Okmok volcano, Alaska: Radar observations. J. Geophys. Res. Solid Earth 105, 10791–10806.

Mao, A., Harrison, C.G.A., Dixon, T.H., 1999. Noise in GPS coordinate time series. J. Geophys. Res. Solid Earth 104, 2797–2816. doi:10.1029/1998JB900033

Massonnet, D., Feigl, K.L., 1998. Radar interferometry and its application to changes in the Earth's surface. Rev. Geophys.-RICHMOND Va. THEN Wash.- 36, 441–500.

Masterlark, T., Donovan, T., Feigl, K.L., Haney, M., Thurber, C.H., Tung, S., 2016a. Volcano deformation source parameters estimated from InSAR: Sensitivities to uncertainties in seismic tomography. J. Geophys. Res. Solid Earth 121, 3002–3016. doi:10.1002/2015JB012656

Masterlark, T., Donovan, T., Feigl, K.L., Haney, M., Thurber, C.H., Tung, S., 2016b. Volcano deformation source parameters estimated from InSAR: Sensitivities to uncertainties in seismic tomography. J. Geophys. Res. Solid Earth 121, 3002–3016.

McTigue, D.F., 1987. Elastic stress and deformation near a finite spherical magma body: Resolution of the point source paradox. J. Geophys. Res. 92, 12931. doi:http://dx.doi.org/10.1029/jb092ib12p12931

Morales Rivera, A.M., Amelung, F., Eco, R., 2015. Volcano Deformation and Modeling on Active Volcanoes in the Philippines from ALOS InSAR Time Series, in: ESA Special Publication. p. 74.

Natvik, L.-J., Evensen, G., 2003. Assimilation of ocean colour data into a biochemical model of the North Atlantic: Part 1. Data assimilation experiments. J. Mar. Syst., The Use of Data Assimilation in Coupled Hydrodynamic, Ecological and Bio-geo-chemical Models of the Ocean. Selected papers from the 33rd International Liege Colloquium on Ocean Dynamics, held in Liege, Belgium on May 7-11th, 2001. 40–41, 127–153. doi:10.1016/S0924-7963(03)00016-2

Newman, A.V., Dixon, T.H., Gourmelen, N., 2006. A four-dimensional viscoelastic deformation model for Long Valley Caldera, California, between 1995 and 2000. J. Volcanol. Geotherm. Res. 150, 244–269. doi:10.1016/j.jvolgeores.2005.07.017

Newman, A.V., Stiros, S., Feng, L., Psimoulis, P., Moschas, F., Saltogianni, V., Jiang, Y.,

Papazachos, C., Panagiotopoulos, D., Karagianni, E., Vamvakaris, D., 2012. Recent geodetic unrest at Santorini Caldera, Greece. Geophys. Res. Lett. 39, L06309. doi:10.1029/2012GL051286

Nooner, S.L., Chadwick, W.W., 2009. Volcanic inflation measured in the caldera of Axial Seamount: Implications for magma supply and future eruptions. Geochem. Geophys. Geosystems 10, Q02002. doi:10.1029/2008GC002315

Papoutsis, I., Papanikolaou, X., Floyd, M., Ji, K.H., Kontoes, C., Paradissis, D., Zacharis, V., 2013. Mapping inflation at Santorini volcano, Greece, using GPS and InSAR. Geophys. Res. Lett. 40, 267–272.

Parks, M.M., Moore, J.D.P., Papanikolaou, X., Biggs, J., Mather, T.A., Pyle, D.M., Raptakis, C., Paradissis, D., Hooper, A., Parsons, B., Nomikou, P., 2015. From quiescence to unrest: 20years of satellite geodetic measurements at Santorini volcano, Greece. J. Geophys. Res.-Solid Earth 120, 1309–1328. doi:10.1002/2014JB011540

Pinel, V., Poland, M.P., Hooper, A., 2014. Volcanology: Lessons learned from Synthetic Aperture Radar imagery. J. Volcanol. Geotherm. Res. 289, 81–113. doi:10.1016/j.jvolgeores.2014.10.010

Rivet, D., Brenguier, F., Clarke, D., Shapiro, N.M., Peltier, A., 2014. Long-term dynamics of Piton de la Fournaise volcano from 13 years of seismic velocity change measurements and GPS observations. J. Geophys. Res. Solid Earth 119, 7654–7666. doi:10.1002/2014JB011307

Ronchin, E., Masterlark, T., Molist, J.M., Saunders, S., Tao, W., 2013. Solid modeling techniques to build 3D finite element models of volcanic systems: An example from the Rabaul Caldera system, Papua New Guinea. Comput. Geosci. 52, 325–333.

doi:10.1016/j.cageo.2012.09.025

Schmidt, S.F., 1966. Application of State-Space Methods to Navigation Problems, in: LEONDES, C.T. (Ed.), Advances in Control Systems. Elsevier, pp. 293–340.

Seiler, A., Evensen, G., Skjervheim, J.-A., Hove, J., Vabø, J.G., 2010. Using the Ensemble Kalman Filter for History Matching and Uncertainty Quantification of Complex Reservoir Models, in: Biegler, L., Biros, G., Ghattas, O., Heinkenschloss, M., Keyes, D., Mallick, B., Marzouk, Y., Tenorio, L., van Bloemen Waanders, B., Willcox, K. (Eds.), Large-Scale Inverse Problems and Quantification of Uncertainty. John Wiley & Sons, Ltd, Chichester, UK, pp. 247–271.

Sigmundsson, F., Durand, P., Massonnet, D., 1999. Opening of an eruptive fissure and seaward displacement at Piton de la Fournaise volcano measured by RADARSAT satellite radar interferometry. Geophys. Res. Lett. 26, 533–536.

Simakin, A.G., Ghassemi, A., 2010. The role of magma chamber-fault interaction in caldera forming eruptions. Bull. Volcanol. 72, 85–101. doi:10.1007/s00445-009-0306-6

Skjervheim, J.-A., Evensen, G., Aanonsen, S.I., Ruud, B.O., Johansen, T.-A., 2007. Incorporating 4D Seismic Data in Reservoir Simulation Models Using Ensemble Kalman Filter. SPE J. 12, 282–292. doi:10.2118/95789-PA

Stankiewicz, J., Ryberg, T., Haberland, C., Fauzi, Natawidjaja, D., 2010. Lake Toba volcano magma chamber imaged by ambient seismic noise tomography. Geophys. Res. Lett. 37, n/a–n/a. doi:10.1029/2010GL044211

vanLeeuwen, P.J., Evensen, G., 1996. Data assimilation and inverse methods in terms of a probabilistic formulation. Mon. Weather Rev. 124, 2898–2913. doi:10.1175/1520-0493(1996)124<2898:DAAIMI>2.0.CO;2

Williams, S.D.P., Bock, Y., Fang, P., Jamason, P., Nikolaidis, R.M., Prawirodirdjo, L., Miller, M., Johnson, D.J., 2004. Error analysis of continuous GPS position time series. J. Geophys. Res. Solid Earth 109, B03412. doi:10.1029/2003JB002741

Wilson, G., Özkan-Haller, H.T., 2012. Ensemble-Based Data Assimilation for Estimation of River Depths. J. Atmospheric Ocean. Technol. 29, 1558–1568. doi:10.1175/JTECH-D-12-00014.1

Wilson, G.W., Oezkan-Haller, H.T., Holman, R.A., 2010. Data assimilation and bathymetric inversion in a two-dimensional horizontal surf zone model. J. Geophys. Res.-Oceans 115, C12057. doi:10.1029/2010JC006286

Wilson, G.W., Özkan-Haller, H.T., Holman, R.A., Haller, M.C., Honegger, D.A., Chickadel, C.C., 2014. Surf zone bathymetry and circulation predictions via data assimilation of remote sensing observations. J. Geophys. Res. Oceans 119, 1993–2016. doi:10.1002/2013JC009213

Zhang, J., Bock, Y., Johnson, H., Fang, P., Williams, S., Genrich, J., Wdowinski, S., Behr, J., 1997. Southern California permanent GPS geodetic array: Error analysis of daily position estimates and site velocities. J. Geophys. Res. Solid Earth 102, 18035–18055. doi:10.1029/97JB01380

CHAPTER 3: SEQUENTIAL ASSIMILATION OF VOLCANIC MONITORING DATA TO QUANTIFY ERUPTION POTENTIAL: APPLICATION TO KERINCI VOLCANO, SUMATRA[2]

Abstract

Quantifying the eruption potential of a restless volcano requires the ability to model parameters such as overpressure and calculate the host rock stress state as the system evolves. A critical challenge is developing a model-data fusion framework to take advantage of observational data and provide updates of the volcanic system through time. The Ensemble Kalman Filter (EnKF) uses a Monte Carlo approach to assimilate volcanic monitoring data and update models of volcanic unrest, providing time-varying estimates of overpressure and stress. Although the EnKF has been proven effective to forecast volcanic deformation using synthetic InSAR and GPS data, until now, it has not been applied to assimilate data from an active volcanic system. In this investigation, the EnKF is used to provide a "hindcast" of the 2009 explosive eruption of Kerinci volcano, Indonesia. A two-sources analytical model is used to simulate the surface deformation of Kerinci volcano observed by InSAR time-series data and to predict the system evolution. A deep, deflating dike-like source reproduces the subsiding signal on the flanks of the volcano, and a shallow spherical McTigue source reproduces the central uplift. EnKF predicted parameters are used in finite element models to calculate the host-rock stress state prior to the 2009 eruption. Mohr-Coulomb failure models reveal that the host rock around the shallow magma reservoir is trending towards tensile failure prior to 2009, which may

[2] Published as: Zhan Y., Gregg P. M., Chaussard E. and Aoki Y. (2017) Sequential Assimilation of Volcanic Monitoring Data to Quantify Eruption Potential: Application to Kerinci Volcano, Sumatra. Front. Earth Sci. 5.

be the catalyst for the 2009 eruption. Our results illustrate that the EnKF shows significant promise for future applications to forecasting the eruption potential of restless volcanoes and hind-cast the triggering mechanisms of observed eruptions.

3.1 Introduction

Volcanic unrest observations including surface deformation, seismicity, gas emissions or fumarole activity may or may not indicate that a system is trending towards eruption (Biggs et al., 2014). Understanding the dynamics of the underlying magma reservoirs is crucial for volcanologists to link volcanic unrest signals to eruption potential. A key challenge is to take full advantage of monitoring data to update and optimize dynamic models of the magma storage systems (Mogi, 1958; McTigue, 1987; Yang et al., 1988; Battaglia et al., 2003; Currenti et al., 2007; Nooner and Chadwick, 2009; Cianetti et al., 2012; Gregg et al., 2012; Newman et al., 2012; Gregg et al., 2013; Ronchin et al., 2013; Cannavò et al., 2015; Parks et al., 2015). Model-data fusion techniques are necessary to provide statistically robust estimations of volcano evolution during periods of unrest. Classically, volcanic activity has been evaluated using static inversions (Battaglia et al., 2003; Newman et al., 2012; Parks et al., 2015), finite element model optimizations (Hickey et al., 2015), model-data comparison (Le Mével et al., 2016). Most inversion techniques provide an important snap shot into the state of volcanic unrest, but are limited in their forecasting ability. Fewer studies use time-evolving inversions from the InSAR data, which successfully provide a quantitative model to explain the dynamics of the magma storage system (e.g. Pagli et al., 2012). However, this approach is limited to regions where SAR data is widely available and consistent and continuous acquisitions are guaranteed. Furthermore, this method requires separated steps to determine the chamber geometry and the time-dependent loading, which requires that the storage geometry is relatively stable. More recently, Kalman

filter statistical data assimilation approaches such as the Extended Kalman Filter (EKF) (Schmidt, 1966; Julier et al., 2000) and unscented Kalman filter (UKF) (Fournier et al., 2009) have been used to provide temporal models of volcanic evolution. However, EKF and UKF are computationally expensive and intractable for use with finite element models.

The Monte Carlo based Ensemble Kalman Filter (EnKF) successfully circumvents linearization issues and computational costs inherent to other Kalman filter approaches (Evensen, 1994). The EnKF has been widely applied and has proven effective for multi-data stream data assimilation in hydrology, physical oceanography, and climatology (vanLeeuwen and Evensen, 1996; Allen et al., 2003; Bertino et al., 2003; Evensen, 2003; Lisaeter et al., 2007; Skjervheim et al., 2007; Wilson et al., 2010). Gregg and Pettijohn (2016) first applied the EnKF in volcanology by conducting a series of 2D elliptical magma chamber tests to assimilate synthetic InSAR (Interferometric Synthetic Aperture Radar) and/or GPS data into a thermomechanical finite element model (FEM). Zhan and Gregg (2017) further establishes a 3D EnKF workflow to update a Mogi source (Mogi, 1958) using synthetic data and illustrates that the EnKF is a robust method even where data are limited. Bato et al. (2017) provides an additional synthetic test of the EnKF to track the migration of magma between two sources based on synthetic InSAR and/or GNSS data. Although these three synthetic tests indicate great potential, until now the EnKF has not been utilized to analyze volcano deformation from a natural system.

In this study, the EnKF is used to assimilate InSAR time series data (Chaussard et al., 2013; Chaussard and Amelung, 2012) from Kerinci volcano in Indonesia to investigate the surface deformation associated with the evolution of an upper crustal magma storage system leading up to its 2009 eruption. Kerinci volcano, located in Central Sumatra along the Sunda (Indonesia) Arc (Fig. 3.1), has had 32 confirmed eruptions (VEI = 1~2) since 1838, and three

recent eruptions, including the 2009/04/01 - 2009/06/19 eruption, the 2016/03/31 - 2016/08/09 eruption, and the 2016/11/15 - 2016/11/21 eruption (Global Volcanism Program, 2009), but also has more than 50,000 people living within 20 km distance around it. Previously analyzed 2007-2011 InSAR time series data from the ALOS-1 satellite (Chaussard and Amelung, 2012; Chaussard et al., 2013) provide an excellent opportunity to test the application of the EnKF in tracking the dynamics of a shallow magma storage system before and after an eruption. We apply a two-step EnKF analysis with a two-source magma storage system which models a deflating, dike-like spheroid feeding an inflating shallow, spherical magma chamber. InSAR data are assimilated as they would have become available if distributed in semi-real time following acquisition and provide model parameter updates. Finally, best-fit model parameters are used to calculate the predicted stress state of the system leading up to the 2009 eruption.

3.2 Methods

3.2.1 InSAR data

SAR data were acquired between 2008/1 to 2011/11 by the Japanese Space Exploration Agency ALOS-1 satellite (Chaussard et al., 2013; Chaussard and Amelung, 2012). The displacement time series with 14 epochs is calculated using the small baseline subset (SBAS) from the InSAR data (Chaussard et al., 2013; Chaussard and Amelung, 2012) (Fig. 3.1). To reduce the random atmospheric noise (Hanssen, 2001; Li et al., 2005), we filter the time series data spatially with a low pass median filter. The InSAR time-series dataset with a 15-m resolution contains more than 150,000 pixels for each time slice when we set the study area as a 6 km by 6 km square centered on the volcano. It is therefore computationally prohibitive to assimilate data from the entire InSAR database. A QuadTree algorithm based on root-mean-square-error of the displacement values is applied to reduce the number of samples for each

epoch of InSAR data from ~150,000 to ~800 (Jónsson et al., 2002; Lohman and Simons, 2005; Simons et al., 2002; Zhan and Gregg, 2017) (Fig. 3.2a), further reducing the short wavelength random atmospheric noise.

We use the Ensemble Kalman Filter (EnKF) data assimilation method to find the best-fit storage model for the Kerinci volcano. The EnKF uses a Markov chain of Monte Carlo (MCMC) approach to estimate the covariance matrix in the Kalman filter. The EnKF overcomes the limitations of the Kalman Filter and Extended Kalman Filter methods, such as computational expense, storage issues, and poor performance with highly nonlinear problems (Evensen, 2009). We follow the EnKF analysis scheme described by Zhan and Gregg (2017) to obtain the magma storage models. The initial ensemble of models is constructed according to the initial guess of the parameters (Table 3.1), based on which the forecast ensemble is obtained. At time t_k when new data (InSAR time series data) is available, an EnKF analysis is conducted to update the model parameters and change the trajectory of the model. The updated model parameters are then used to create a new forecast ensemble, which will be assimilated at t_{k+1} when another epoch of InSAR time series data is available. Effectively, the EnKF provides a temporal inversion that captures the system's dynamics through time. The final output of the EnKF can be used to investigate the system state at the time of the last observation, and can be propagated forward in time to provide a system forecast. The EnKF dynamic inversion strategy has proved robust, even when the InSAR data have a topographic shadow masking the flank of the volcano edifice (Zhan and Gregg, 2017). The ensemble parameters in this implementation of the EnKF analysis is chosen based on previous synthetic tests (Zhan and Gregg, 2017) (Table 3.1).

3.2.2 Magma storage model

The InSAR time series reveals uplift entered at the summit of the volcano and two

subsiding areas located on the NE and SW flanks. To simulate both the uplift and subsidence signals, we combine an inflating spherical source with a deflating dike-like source located at an angle beneath the chamber to form an upper crustal magma storage system (Gudmundsson, 2006; Chaussard et al., 2013) beneath Kerinci (Fig. 3.1) and calculate the elastic response of the country rock (Table 3.2). The deformation pattern can also be created by other sources. For example, the two-peak pattern of the subsiding signal can be approximated using two deflating sills beneath the NE and SW side of the volcano edifice. However, it is unlikely that three magma sources would develop so close to each other while remaining separate and stable thermally. On the contrast, the single deflating dike-like source at depth feeding a shallow magma reservoir is more reasonable.

We use McTigue's analytical approach (McTigue, 1987) to produce the displacement at the center due to a shallow inflating sphere. We reproduce the two-peak subsidence with a deflating near vertical oblate spheroid (Yang et al., 1988; Dzurisin, 2006), with a high ratio of its long and short axes (~10), acting as a dike-like source. The center of the Kerinci volcano is located on the dilatational Siulak segment of the Great Sumatra Fault (Bellier and Sébrier, 1994; Sieh and Natawidjaja, 2000). Therefore, we assume a near vertical, NW-SE striking dike-like source guided by the preexisting stress field of the Great Sumatra Fault (Pasquare and Tibaldi, 2003; Gudmundsson, 2006; Tibaldi, 2015).

3.2.3 Two-step data assimilation

Tracking both the upper spherical and lower dike-like source introduces too many parameters for the EnKF to obtain unique solutions. Thus, a two-step EnKF analysis is used to track the two sources separately. First, the EnKF estimates the subsidence generated by a deflating dike using the Yang et al.'s model (Yang et al., 1988) (Fig. 3.2b). During this step, the

uplift signal is masked from the InSAR data, and is treated as missing data. The Yang et al.'s model (Yang et al., 1988) requires eight independent parameters beside the Young's Modulus and Poisson's ratio, including the x, y and z coordinates, long and short axis, plunging direction and dipping angle, the overpressure of the spheroid. As many parameters may cause strong non-uniqueness during the EnKF analysis (Zhan and Gregg, 2017), we assume that the location of the center of the dike is 5 km beneath the summit of the volcano, and it is striking NW-SE aligned with the Great Sumatran Fault system (Table 3.1). The residual displacement is calculated by subtracting the predicted subsidence from the corresponding InSAR data time step (Fig. 3.2d). At the second step, the EnKF analysis (initial parameters listed in Table 3.1) tracks the inflating spherical source using the McTigue's model (Fig. 3.2e) to reproduce the uplift signal in the residual displacement obtained from Step 1. A combination of both the deeper deflating dike-like spheroid model and the shallower inflating spherical model produces a modeled displacement, which closely matches the observed pattern of central uplift and flank subsidence (Fig. 3.2c). Finally, the two models are combined to produce the total displacement. The misfit is the difference between the modeled displacement from the combined model and the measured displacement from the InSAR time series (Fig. 3.2f).

3.2.4 Stress and Coulomb failure calculation

To calculate the stress field of the country rock around the magma storage, we follow the benchmarked strategy of Zhan and Gregg (2017). Elastic finite element models are established with the parameters estimated by the two-step EnKF analysis and then solved for by COMSOL5.2. The maximum and minimum principle stresses at the top of the chamber are calculated for failure determination. The application of the Coulomb failure criterion follows the same strategy as previous studies (Gregg et al., 2012; Grosfils, 2007) (Table 3.2).

3.3 Results

3.3.1 Volcanic deformation

Down-sampled InSAR time series data (Fig. 3.3a and d) reveal two deformation signals at Kerinci Volcano, an uplifting signal centered on the summit and a subsiding signal on the NE and SW flanks. Both signals are consistent in temporal and spatial domains, suggesting they are not associated with atmospheric delay and should be treated as deformation (Fig. 3.3 and Fig. 3.4). Prior to the April 2009 eruption, the volcano experienced a continuous uplift at a maximum rate of ~4 cm/yr (Fig. 3.4a), while the NE and SW flanks subsided at a much lower rate of <1 cm/yr (Fig. 3.4b and c). At the time of the eruption, the center and flanks of the volcano went through a rapid subsidence (Fig. 3.3a and d and Fig. 3.4), reflecting withdrawal of magma from the storage system. After the eruption, central uplift recommenced while deformation of the NE and SW flanks ceased (Fig. 3.4). The deformation centered on the summit has a short wavelength, indicating a shallow source, while a deep source is more likely to create a long wavelength subsidence deformation signal. The symmetrical shape of the central uplift strongly suggests an inflating spherical source, while the two-peak pattern of the subsidence suggests a deflating dike-liked source.

A two-step data assimilation approach (Fig. 3.2) is implemented to track the surface deformation created by a shallow, inflating spherical source (McTigue, 1987) and a deeper, deflating dike-like (oblate spheroid) source (Yang et al., 1988). The two-sources model reproduces both the observed central uplift signal and the subsidence signal on the flank (Fig. 3.3e). Model errors are < 1 cm in most regions and are < 0.5 cm at the center of the volcano (Fig. 3.3c and f). A comparison of the deformation time-series and the model predictions confirms that the two-step model is able to track the observed deformation within uncertainty (Fig. 3.4). We further calculate the L_2 norm of the displacement to illustrate the total misfit between the forecast

models and the data. The L_2 norm error estimation is the sum of the square of the differences between the model values and the measurement values, which also considers the size of the quad created during QuadTree down-sampling. Normalized L_2 norms of both the spherical source and tilted dike-like source decrease through time as more InSAR data are assimilated (Fig. 3.5). The L_2 norm of the spherical source is overall significantly lower than for the tilted dike-like source, indicating that the spherical chamber model reproduces more accurately the uplift at the center of the volcano compared to the flank subsidence. The L_2 norms of the spherical source decreases rapidly after several InSAR assimilations and become static until the eruption (Fig. 3.5b). The low displacement errors (Fig. 3.3 and Fig. 3.4) and observed convergence in the L_2 norms (Fig. 3.5) suggest that the two-sources combination of a shallower inflating chamber and a deeper deflating dike-like source is a good representation of the storage system at Kerinci and their volume changes due to the magma transport explains the deformation associated with the 2009 eruption.

3.3.2 Magma source parameters

The EnKF provides evolving estimates of the model parameters for the dike-like spheroid and shallow spherical chamber as new SAR observations are assimilated (Fig. 3.6; the detailed values of the parameter estimation are listed in the supplementary table 1 and 2). We focus on EnKF's predictions of the evolution of over-pressurization and volume of the shallow chamber to investigate eruption precursors. The negative overpressure of the dike-like source is consistent with deflation of this deep source, but its rapid change is suspicious (Fig. 3.6e). It is difficult to constrain the depth of the center of the dike-like spheroid with the InSAR subsiding signal alone. To constrain the depth of the dike, we conduct a series of tests to model the deflating signal. Results indicate that a dike deeper than 7 km cannot produce the deformation signal revealed by

the InSAR data. Alternatively, a dike shallower than 3 km may overlap with the inflating magma chamber. As such, the depth to the center of the dike should be in a range of 3 to 7 km. Therefore, we assume the dike center is at a depth of 5 km. Furthermore, a 2-km uncertainty in the depth will not affect the result significantly for a near vertical dike. Due to the uncertainty in the deeper deflating source, this study instead focuses on the host rock stress evolution surrounding the shallow inflation source.

The second step of the data assimilation estimates the evolution of the shallow inflating source. The model converges after two to three time steps (05/2008-07/2008), when the standard deviation of the parameters and the L_2 norms of the model significantly decrease (Fig. 3.6 and Fig. 3.5b). After the model parameters stabilize at July 2008, the EnKF estimates that the shallow inflating source shoaled from 4.43 (±0.19) km to 3.99 (±0.05) km (depth-to-center) beneath the summit prior to the eruption, and after the eruption the shallow source migrated northward 0.46 (±0.2) km and shoaled to ~1.12 (±0.1) km depth (Fig. 3.6a, b, and c). While this outcome provides a robust estimation of the migration of the pressure source, the variation through the time likely indicates magma migration in the magma storage system (through dikes or conduits), rather than the movement of a void chamber. However, the spherical chamber model provides a first-order approximation of the deformation source location through time. The EnKF predicts that the radius of the shallow chamber is 2.27 (±0.01) km (Fig. 3.6d), which is likely too large given its shallow depth (See Supplemental Tables). However, trade-offs exists between overpressure and radius due to the non-uniqueness of the analytical model (Zhan and Gregg, 2017). To account for the non-uniqueness of the model, overpressure and radius are combined to calculate the volume evolution (Fig. 3.6f). The volume of the shallow chamber increases at a rate of 5.33 (±0.10) $\times 10^5$ (±0.04) m^3/yr (Table 3.3) throughout the pre-eruptive

time period, reaching its maximum just prior to the eruption. The volume of the dike-like source decreases (1.22 (±0.04) $\times 10^5$ m^3/yr) during the same time period (Fig. 3.6f). During the eruption period, both sources experience substantial deflation resulting in a strong subsiding signal observed in the InSAR data (Fig. 3.1). After the eruption, the deeper source returns to a steady state, while the shallower chamber continues to inflate at a much smaller rate (0.57 (±0.15) $\times 10^5$ m^3/yr) than prior to the eruption. Given that the shape of the post-eruption inflation curve does not mimic a typical viscoelastic roll-off, it likely indicates a slow recharge stage of the next eruption cycle which culminated in the 2016 eruption.

3.4 Discussion

3.4.1 Magmatic system evolution at Kerinci

Based on the converged parameter estimation and the displacement agreement between the EnKF predictions and InSAR observations, we propose that the upper crustal magma transport-storage system of Kerinci is comprised of a shallow, spherical chamber at a depth of ~4 km connected by a dike system below to a possible lower crustal reservoir (Fig. 3.1 and Fig. 3.7a and b). The dike-like source may have developed aligned with the Great Sumatran Fault (Pasquare and Tibaldi, 2003; Gudmundsson, 2006; Tibaldi, 2015). Alternatively, other source combinations can also create the displacement pattern shown by the InSAR, such as inflating and deflating sills, and connected chambers. However, to model the two-peak pattern of the subsiding signal without an inclined feeder dike, at least two deflating chambers or sills would need to flank either side of the central inflating source, which is unlikely. Additionally, the preexisting faults beneath the volcano may provide an ideal path for magma transport (Tibaldi, 2015).

The coincident volume changes of the dike-like source and the chamber imply magma

migration between these sources. Prior to the 2009 eruption, the volume of the shallow chamber continuously increased indicating possible magma injection (Lister and Kerr, 1991; Mogi, 1958) and/or differentiation (Tait et al., 1989). In the meantime, the volume of the dike-like spheroid decreased (Fig. 3.6f), indicating that the dike-like source may only act as a pathway for magma to ascent from a lower reservoir (e.g. MASH zone; Hildreth and Moorbath, 1988), as suggested by seismic tomography (Collings et al., 2012; Koulakov et al., 2007). Following the eruption, the volumes of both the dike-like spheroid and the chamber decrease drastically, but because of the lack of data in the first months after the eruption, we cannot determine how fast this subsidence occurred. The volume loss is most likely related to the erupting steam-, ash-, and cinder-bearing plumes recorded in April 2009 (Global Volcanism Program, 2009). The total volume loss of the two-sources system is ~1.6×10^6 m^3, which is consistent with volume estimates for the April 2009 eruption (VEI = 1) (Global Volcanism Program, 2009).

Although the misfits between the surface displacement model and the InSAR data are small (Fig. 3.3), some locations show higher misfits (up to 1.5 cm), especially in the subsiding areas to the SW. The minimal misfit at the volcano center confirms that the model accurately captures the parameters of the shallower spherical chamber. On the other hand, the misfit in the subsiding areas suggests a bias that could be due to lithospheric heterogenesis (Zhan et al., 2016) or could be associated with atmospheric noise in the data. We focus our discussion on the dynamics of the shallower chamber, as it is better constrained and the eruption is largely controlled by overpressure and failure of the rock surrounding it.

3.4.2 Overpressure and stress evolution prior to the 2009 eruption

A central paradigm in volcanology is that eruption is triggered when the overpressure within an expanding magma chamber exceeds the strength of the surrounding rock.

Unfortunately, analytical models such as Mogi (1958) and McTigue (1987) are limited in their ability to provide reliable overpressure predictions, because the calculations are inherently non-unique. As previously discussed, this non-uniqueness makes it difficult for the EnKF to reconcile estimations of radius and overpressure. The magma system parameters estimated by the EnKF are used in combination with a series of finite element models with different combinations of radius and overpressure to predict the stress field of the country rock prior to and directly following the 2009 eruption. Calculations of stress evolution are focused at the top of the magma chamber where confining pressures are lowest and tensile failure is most likely (Grosfils, 2007). Additionally, the 2009 eruption fed from a central vent further indicating failure at the top of the magma reservoir.

We utilize the benchmarked COMSOL Finite Element Model (FEM) approach for a pressurized sphere in 3D (Del Negro et al., 2009; Gregg et al., 2012; Zhan and Gregg, 2017) to perform a series of tests for magma chamber radius values of 100 m to 2,500 m and their corresponding overpressures (Fig. 3.7). Of particular interest is whether the magma chamber is in a stable configuration or in a state of tensile failure, potentially indicating imminent eruption.

Figure 3.7 illustrates the tradeoff between overpressure and radius required to produce the same surface deformation given the optimal EnKF magma chamber depth-to-center estimation. Model configurations that result in either tensile failure or Mohr-Coulomb failure are shown. The most striking outcome of these tests is the clear correlation between chamber radius and failure. As the radius increases, the minimum principal stresses also increase, while the maximum shear stresses are significantly reduced due to decreasing overpressure (Fig. 3.7 and Fig. 3.8c and d). This indicates that systems with smaller magma chamber radii are more likely to fail, given the same volume change. This finding has been previously indicated by other

researchers (Grosfils, 2007; Gregg et al., 2012) and further indicates the need for an independent assessment of magma reservoir size.

The predicted overpressure prior to the eruption is at least two times higher than during and after the eruption (Fig. 3.7) due to the depressurization of the system during the eruption. The models predict that a magma chamber with a radius of 500 m will experience tensile failure (Fig. 3.8c), potentially leading to an eruption. The model also predicts no tensile failure after the eruption if the chamber size is not greatly reduced (Fig. 3.8d); the total estimated volume loss of the chamber is less than 1%. Similarly, Mohr-Coulomb failure calculated in the host rock prior to eruption is more extensive than after the eruption (Fig. 3.7 and Fig. 3.8); however, while failure is predicted in both instances, the orientation and mode of failure may not be optimal for catalyzing eruption (Grosfils, 2007). Due to the non-uniqueness issue, radius estimates may be unreasonably large (Fig.6) and an analysis of the system's stress state assuming a variety of radii-overpressure combinations is necessary to investigate the possibility of an eruption. Future work using data assimilation with displacement and seismicity data may provide stronger constraints on the stress evolution, helping to decipher the dynamics of the magma storage system.

The L_2 norm evolution provides additional insights to aid eruption prediction. Since the EnKF analysis updates the model based on the previous time steps, a sudden increase of the L_2 norm (Fig. 3.5b) means that the pre-eruption model is no longer able to reproduce the observed deformation, suggesting a sudden change of the magma storage system. Volume change due to magma withdrawal, opening of fractures and dikes (Lister and Kerr, 1991), and alterations of country rock's rheology due to temperature evolution (Annen and Sparks, 2002) could explain this change. Some of these transitions may occur just prior to eruptions and are captured by

InSAR and/or GPS. Therefore, the L_2 norms provides useful information for characterization of unrest.

3.4.3 Near real-time data assimilation with InSAR data

The advantage of SAR observations is that they offer a high spatial resolution, which provides a broad view of the region surrounding the magma system. The EnKF analysis is able to efficiently track surface deformation from the down-sampled InSAR time series of Kerinci (Fig. 3.3). Prior to the 2009 eruption, the InSAR-ALOS time-series repeat interval is 46 days, providing observations of continuous uplift. The models become unconstrained just prior to and immediately following the eruption (gray shaded area in Fig. 3.5) due to the gap in acquisitions. As EnKF is able to update deformation models in near real-time, getting access to SAR data in near-real time could lead to usage of these data to provide early warning of eruption. Additionally, higher temporal repeatability of the SAR systems could lead to improved constraints of the magmatic systems worldwide and of their temporal evolution.

In this EnKF study, 200 models are used in the forecasting ensembles adding up to more than 1000 iterations. However, the computational expense is less than 3 minutes to finish the calculation on a workstation (3.2 GHz Intel Core i5). Although the EnKF is slightly longer than other inversion techniques (e.g. Pagli et al., 2012), it provides huge flexibility for incorporating a wide range of observations from deformation to seismicity, and from heat flow to geochemistry. The primary limitation of this study is the analytical models used. The analytical approach is ideal for decreasing the computational expense of calculating a large population of ensembles; however the models are oversimplified. In the future, more realistic physics-based models and finite element models will take the place of the analytical models to allow researchers to explore more realistic deformation based on other geophysical observations from tomography, gravity,

and/or magnetotellurics. Coupling solid mechanics with the fluid dynamics (Le Mével et al., 2016), the evolution of the magma storage systems will be closely related to the magma flux inferred from geological records, instead of the enigmatic and oversimplified overpressure. In the case of a finite element approach, the computational expense is far more significant and a supercomputer is necessary to conduct the Monte Carlo suites for the data assimilation. Future efforts are necessary to optimize the EnKF approach for the use of more sophisticated and computationally expensive models (Gregg and Pettijohn, 2016).

3.5 Conclusions

A two-step EnKF data assimilation provides a shallow chamber connect to a deep dike-like source as the most likely model to explain the surface displacement around the 2009 eruption of the Kerinci volcano revealed by the InSAR data. The Yang et al. (1989) model is used to mimic a deep, deflating dike-like source, which can explain the subsiding signal on the flanks of the volcano. At the meantime, a shallow spherical source (McTigue, 1988) is built to reproduce the central uplift. The parameters with highest likelihood are applied to reconstruct the stresses around the magma chamber utilizing a benchmarked finite element model. The stress model suggests that the shallow magma reservoir is most likely to fail prior to 2009, which may explain the eruption. Our results illustrate the great potential of the EnKF data assimilation as a technique to explore the dynamic evolution of the magma storage system, giving insight into the eruption forecasting of restless volcanoes.

3.6 Figures and Tables

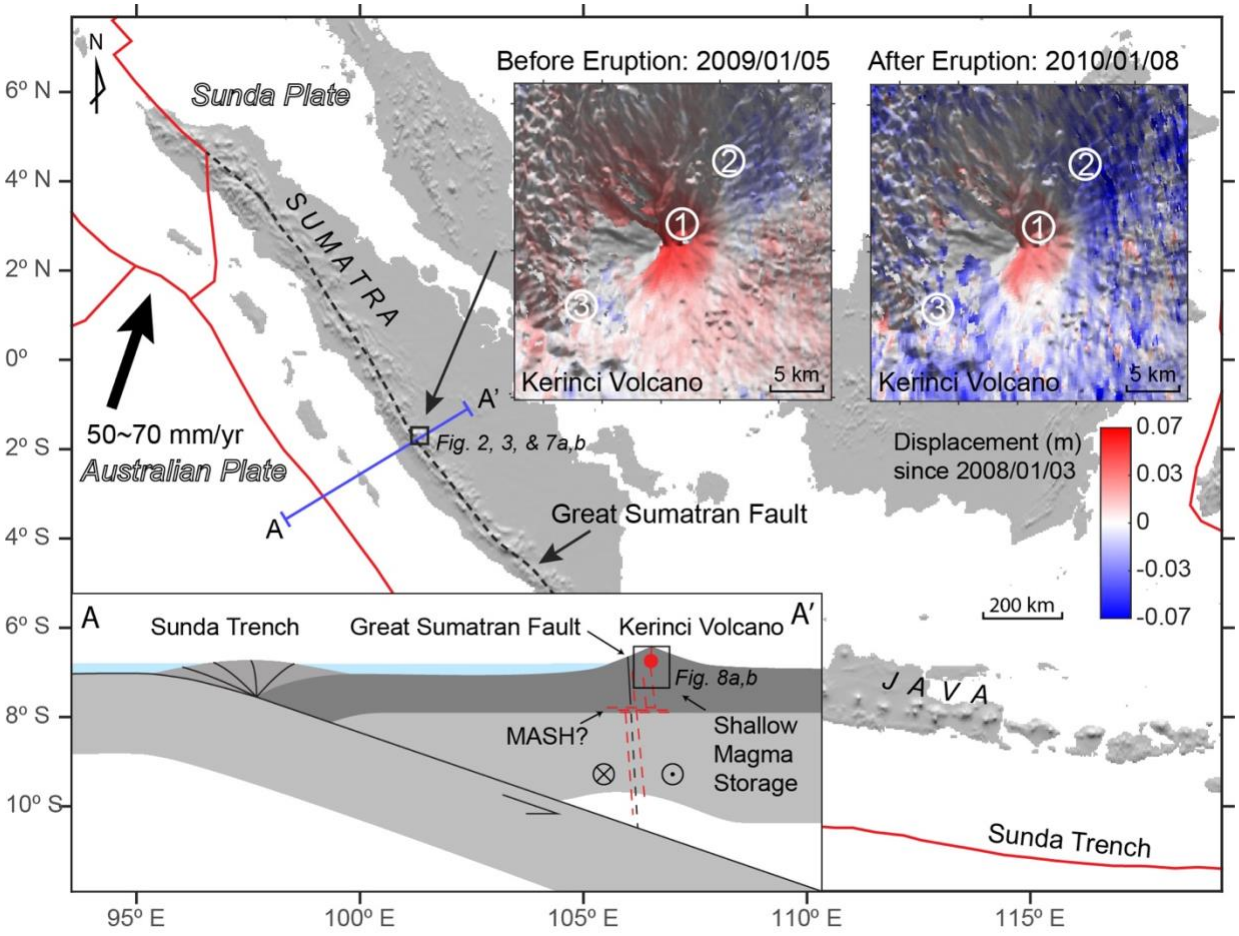

Figure 3.1 Location and tectonic setting of Kerinci volcano. More than 10% of active volcanoes on the Earth are distributed along the Sunda arc (McCaffrey, 2009), due to subduction of the Australian Plate beneath the Sunda Plate. The oblique subduction results in the right lateral Great Sumatran Fault, which is the northeastern boundary of the forearc plate (McCaffrey, 2009). Blue-red color maps show the InSAR time series data at 2009/1/5 and 2010/1/8. The numbers in the circles indicate locations used in Fig. 3.4. The left bottom insert is a sketch section (not to scale) showing the tectonic setting of the Kerinci volcano and the box highlights that the shallow magma chamber may be fed by dikes associated with the Great Sumatran Fault as magma may take the advantage of the pre-existing fractures to ascend from depth (Chaussard and Amelung, 2012; Muksin et al., 2013). The geometry of the magmatic system illustrates the dike and reservoir model used to explain the InSAR data.

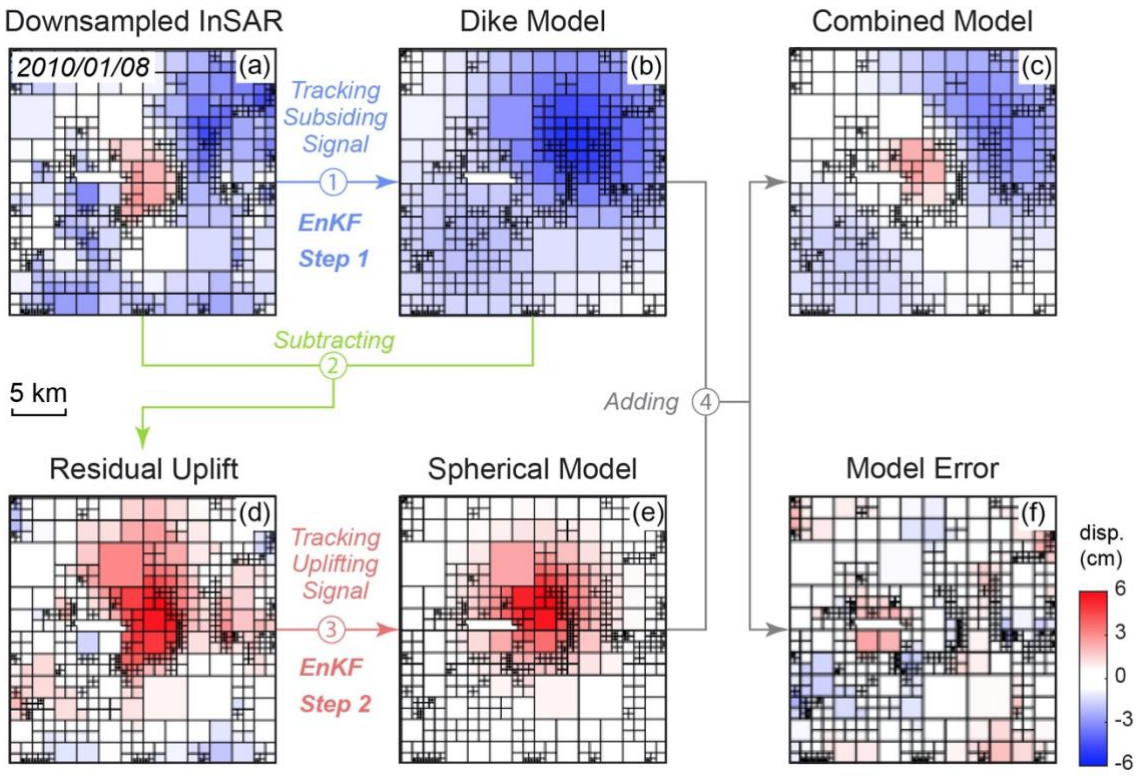

Figure 3.2 Workflow of the two-step data assimilation with the downsampled InSAR data.

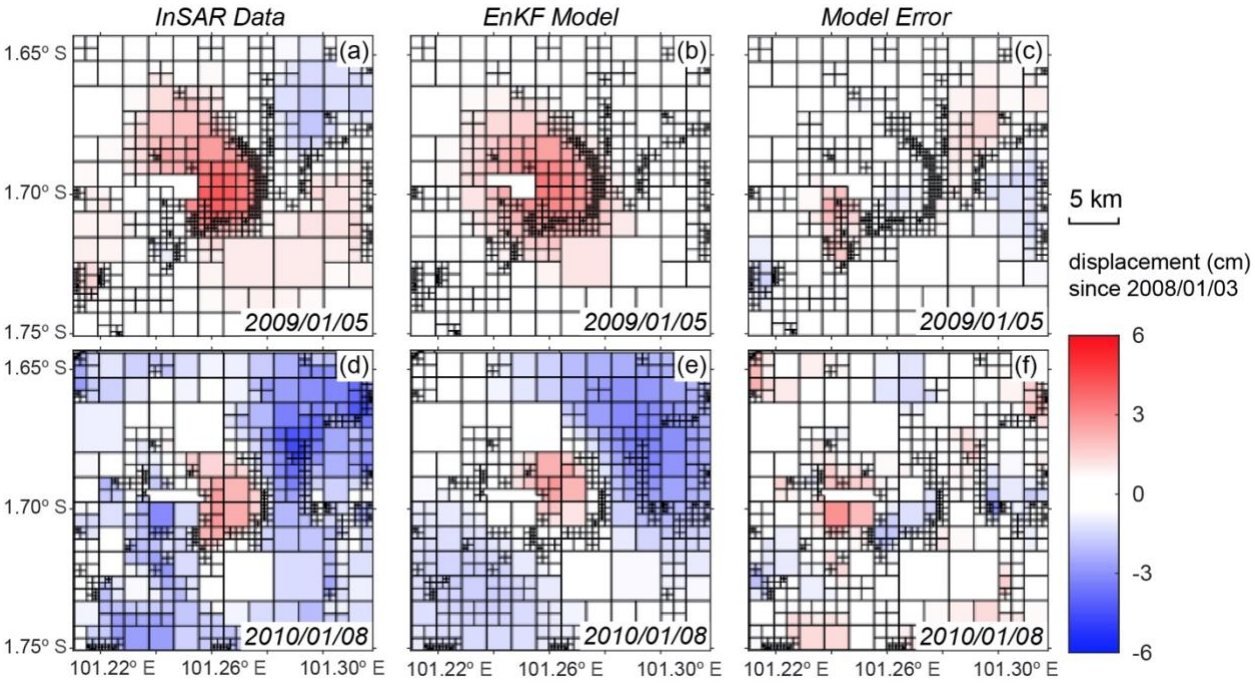

Figure 3.3 Comparison between the QuadTree down-sampled InSAR time series (a and d) and the EnKF data assimilation results (b and e), before (top row) and after (bottom row) the 2009 eruption. (b) and (e) show the best fit two-sources model obtained from the EnKF data assimilation and (c) and (f) show the misfit between the EnKF prediction and the InSAR data.

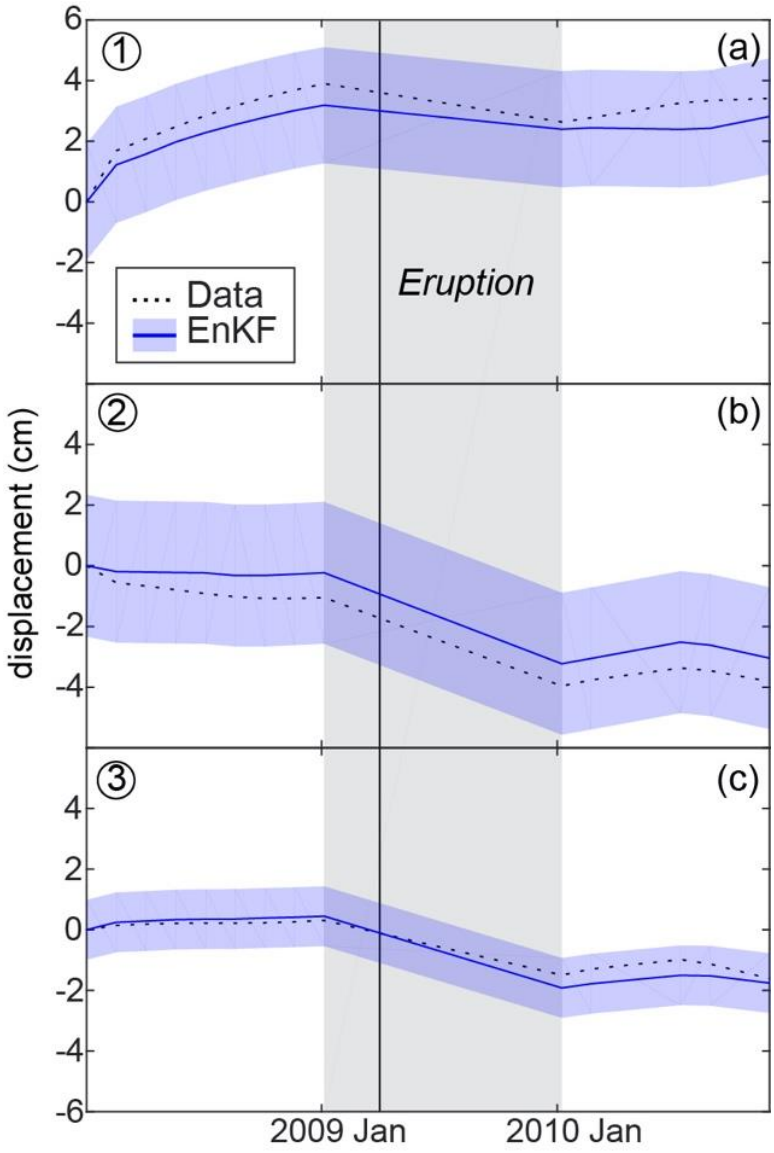

Figure 3.4 2008- 2011 displacement measured by the InSAR time series (dash line) compared to the displacement produced by the best fit combined EnKF model (full line and filled blue area). The numbers at the left-top corners correspond to the sampling locations shown on Figure 3.1. The blue shaded regions show the standard deviations of the ensembles. The black solid line indicates the time of the 2009/1/11 eruption of Kerinci, and the gray shaded region highlights the gap in SAR acquisitions.

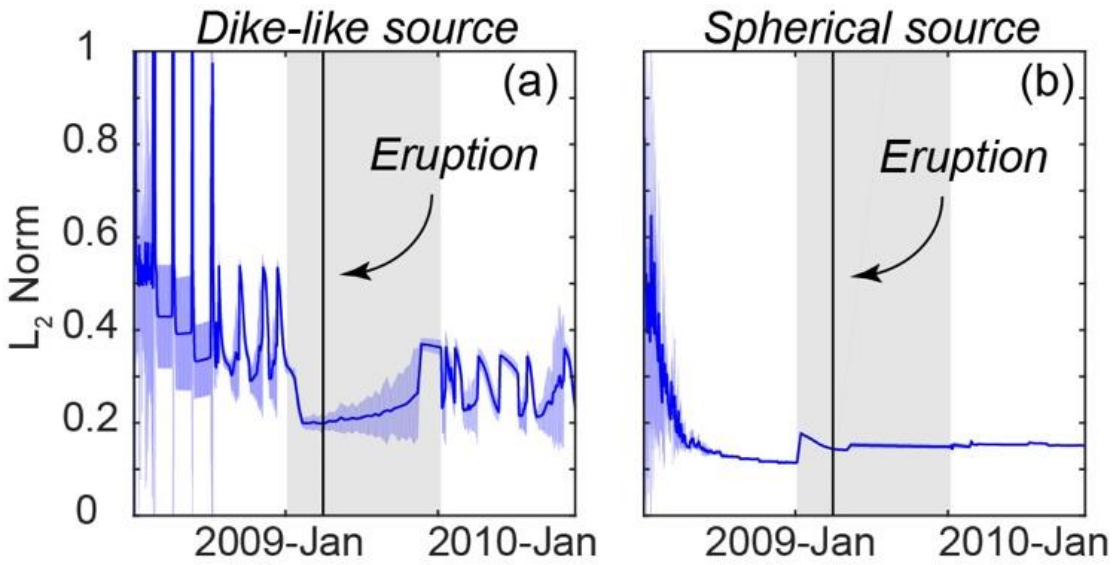

Figure 3.5 Normalized L2 norm comparing the misfit between the EnKF data assimilation results and the InSAR data. (a) L2 norm for the first step EnKF, which uses a dike-like source to track the subsiding signal. (b) L2 norm for the second step of the EnKF, which uses McTigue's model (McTigue, 1987) of an inflating spherical source to track the uplifting signal. The blue solid lines and the blue shaded regions are the mean and standard deviations respectively of the L2 norms of the 200 models in the ensembles.

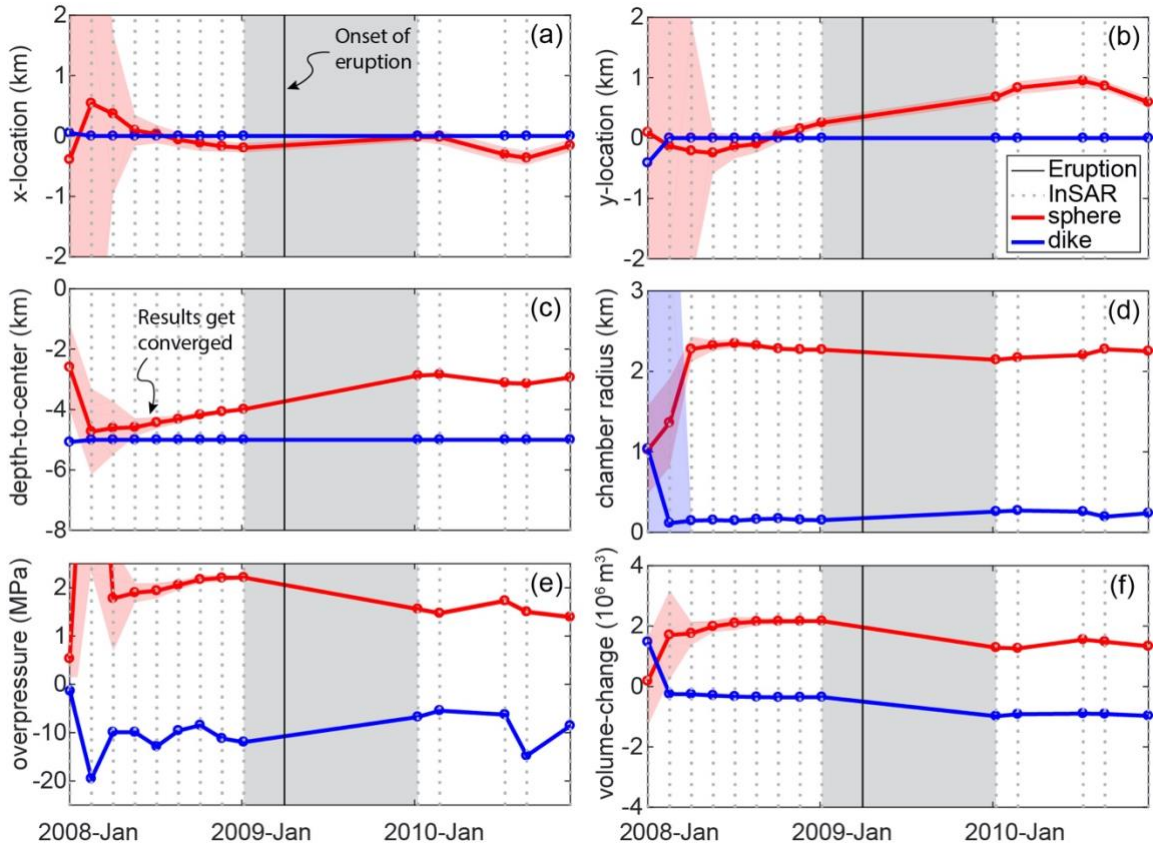

Figure 3.6 EnKF parameter estimations for the spherical (red lines) and dike-shaped (blue lines) sources. The EnKF predictions start to converge after three epochs of InSAR time series data are assimilated. The x- and y-location in (a) and (b) are the horizontal distances between the deformation sources and the center of the volcano. The colored solid lines and shaded areas indicate the ensemble means and standard deviations respectively. The colored circle symbols indicate the estimated parameters of the best-fit model from each ensemble at each time step. The black dashed lines indicate time steps when InSAR data were assimilated. Notice the upper and lower part of (e) have different scales of the Y-axis.

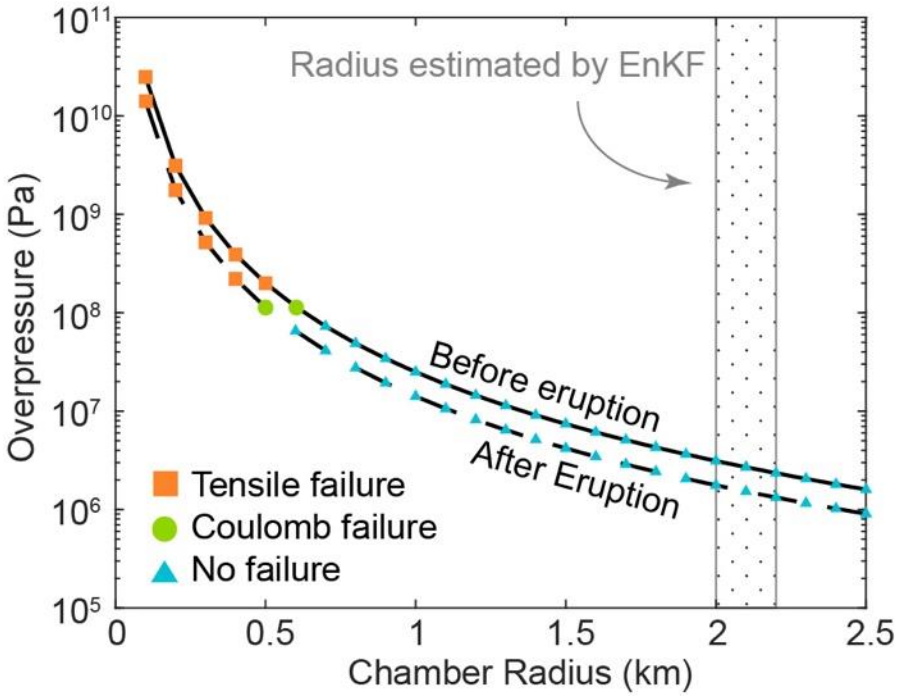

Figure 3.7 The relationship between the assumed overpressure of the chamber and its corresponding radius before (solid line) and after (dashed line) the 2009 eruption of Kerinci Volcano. The overpressure and the radius cannot be uniquely determined due to the nature of the deformation source. Colored symbols indicate that the type of the failure predicted at the top of the magma chamber is controlled by the combination of the overpressure and the radius. Blue triangles indicate a stress state where no failure is calculated. Green circles indicate a situation where only Coulomb failure is predicted. The orange squares indicate a stress state in which tensile failure is predicted. Figure 3.8 provides an illustration of this approach.

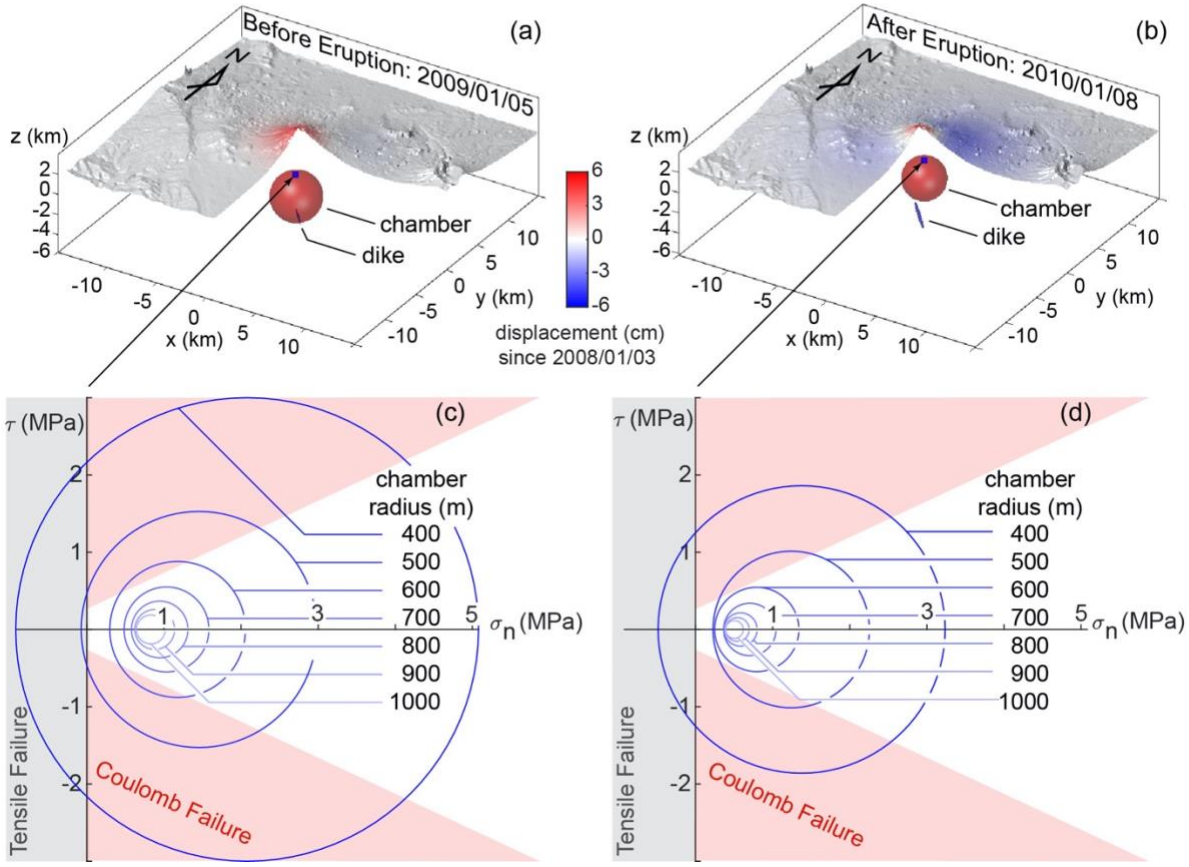

Figure 3.8 3D illustrations of the best fit models estimated by EnKF before (a) and after (b) the 2009 eruption. (c) and (d) show the estimated Mohr's circle for the country rock (Grosfils, 2007; Gregg et al., 2012) directly above the top of the spherical chamber. The predicted stress is sensitive to the radius size, which tradeoffs with the depth of the top of the chamber. Red shaded regions in (c) and (d) shows the Coulomb-failure envelop (Table. A1. C = 25 MPa, φ = 25° (Grosfils, 2007)). The gray shaded region ($\sigma_n < 0$) indicates when the system is in tension. Tensile failure may indicate dike initiation away from the magma chamber and immanent eruption.

Table 3.1 Parameters of the Ensemble Kalman Filter.

Name	Value
Number of ensembles*	200
Iterations*	40
Parameter space tolerance*	30%
Initial parameters for dike-like source:	
X-location*	0 km
Y-location*	0 km
Depth*	5 km
Short axis	0.1 ~ 2 km
Long axis / Short axis ratio*	10
Overpressure	-10 ~ 10 MPa
Short axial plunge direction*	45°
Short axial dip angle	0 ~ 90°
Initial parameters for spherical source:	
X-location	-10 ~ 10 km
Y-location	-10 ~ 10 km
Depth	0.1 ~ 5 km
Radius	0.1 ~ 2 km
Overpressure	-10 ~ 10 MPa

Note: Parameters with * are constant during the EnKF analysis.

Table 3.2 Physical properties for calculating the analytical models and the Coulomb failure.

Name	Symbol	Value	Reference
Young's modulus	E	75 GPa	(Gregg and Pettijohn, 2016)
Poisson's ratio	ν	0.25	(Gregg and Pettijohn, 2016)
Friction angle	φ	25°	(Grosfils, 2007)
Cohesion	C	25 MPa	(Grosfils, 2007)

Table 3.3 Flux rates ($\times 10^5$ m^3/yr) of the sources from the EnKF data assimilation.

Source	Prior to 2009/01/05	2009/01/05 to 2010/01/08	After 2010/01/08
Dike-like source	-1.22 (±0.04)	-6.22 (±0.04)	0.12 (±0.07)
Spherical source	5.33 (±0.10)	-8.83 (±0.11)	0.57 (±0.13)

3.7 Acknowledgements

We would like to acknowledge helpful discussions with Dr. F. Amelung, J. Albright, Dr. J.C. Pettijohn, Dr. J. Freymeuller, Dr. Z. Lu, Dr. L. Liu, Dr. J. Biggs, Dr. G. Hou and the UIUC Dynamics Group. We would also like to thank Dr. V. Acocella, Dr. Z. Lu, Dr. A. Tibaldi, and Dr. C. Pagli for their comments which greatly improved our manuscript. Development of Ensemble Kalman Filter approach for modeling active volcanic unrests using InSAR data is funded by NASA (13-ESI13-0034).

3.8 References

Allen, J. I., Eknes, M., and Evensen, G. (2003). An Ensemble Kalman Filter with a complex marine ecosystem model: hindcasting phytoplankton in the Cretan Sea. *Ann Geophys* 21, 399–411. doi:10.5194/angeo-21-399-2003.

Annen, C., and Sparks, R. S. J. (2002). Effects of repetitive emplacement of basaltic intrusions on thermal evolution and melt generation in the crust. *Earth Planet. Sci. Lett.* 203, 937–955. doi:10.1016/S0012-821X(02)00929-9.

Bato, M. G., Pinel, V., and Yan, Y. (2017). Assimilation of Deformation Data for Eruption Forecasting: Potentiality Assessment Based on Synthetic Cases. *Front. Earth Sci.* 5. doi:10.3389/feart.2017.00048.

Battaglia, M., Segall, P., Murray, J., Cervelli, P., and Langbein, J. (2003). The mechanics of unrest at Long Valley caldera, California: 1. Modeling the geometry of the source using GPS, leveling and two-color EDM data. *J. Volcanol. Geotherm. Res.* 127, 195–217. doi:10.1016/S0377-0273(03)00170-7.

Bellier, O., and Sébrier, M. (1994). Relationship between tectonism and volcanism along the Great Sumatran fault zone deduced by SPOT image analyses. *Tectonophysics* 233, 215–231.

Bertino, L., Evensen, G., and Wackernagel, H. (2003). Sequential data assimilation techniques in

oceanography. *Int. Stat. Rev.* 71, 223–241.

Biggs, J., Ebmeier, S. K., Aspinall, W. P., Lu, Z., Pritchard, M. E., Sparks, R. S. J., et al. (2014). Global link between deformation and volcanic eruption quantified by satellite imagery. *Nat. Commun.* 5. Available at: http://www.nature.com/ncomms/2014/140403/ncomms4471/full/ncomms4471.html?message-global=remove.

Cannavò, F., Camacho, A. G., González, P. J., Mattia, M., Puglisi, G., and Fernández, J. (2015). Real Time Tracking of Magmatic Intrusions by means of Ground Deformation Modeling during Volcanic Crises. *Sci. Rep.* 5. Available at: http://www.nature.com/srep/2015/150609/srep10970/full/srep10970.html?WT.ec_id=SREP-704-20150616.

Chaussard, E., and Amelung, F. (2012). Precursory inflation of shallow magma reservoirs at west Sunda volcanoes detected by InSAR. *Geophys. Res. Lett.* 39, n/a-n/a. doi:10.1029/2012GL053817.

Chaussard, E., Amelung, F., and Aoki, Y. (2013). Characterization of open and closed volcanic systems in Indonesia and Mexico using InSAR time series. *J. Geophys. Res. Solid Earth* 118, 3957–3969. doi:10.1002/jgrb.50288.

Cianetti, S., Giunchi, C., and Casarotti, E. (2012). Volcanic deformation and flank instability due to magmatic sources and frictional rheology: the case of Mount Etna. *Geophys. J. Int.* 191, 939–953.

Collings, R., Lange, D., Rietbrock, A., Tilmann, F., Natawidjaja, D., Suwargadi, B., et al. (2012). Structure and seismogenic properties of the Mentawai segment of the Sumatra subduction zone revealed by local earthquake traveltime tomography. *J. Geophys. Res. Solid Earth* 117,

B01312. doi:10.1029/2011JB008469.

Currenti, G., Del Negro, C., and Ganci, G. (2007). Modelling of ground deformation and gravity fields using finite element method: an application to Etna volcano. *Geophys. J. Int.* 169, 775–786. doi:10.1111/j.1365-246X.2007.03380.x.

Del Negro, C., Currenti, G., and Scandura, D. (2009). Temperature-dependent viscoelastic modeling of ground deformation: application to Etna volcano during the 1993–1997 inflation period. *Phys. Earth Planet. Inter.* 172, 299–309.

Dzurisin, D. (2006). *Volcano Deformation*. Berlin, Heidelberg: Springer Berlin Heidelberg Available at: http://link.springer.com/10.1007/978-3-540-49302-0.

Evensen, G. (1994). Sequential data assimilation with a nonlinear quasi-geostrophic model using Monte Carlo methods to forecast error statistics. *J. Geophys. Res. Oceans* 99, 10143–10162. doi:10.1029/94JC00572.

Evensen, G. (2003). The Ensemble Kalman Filter: theoretical formulation and practical implementation. *Ocean Dyn.* 53, 343–367. doi:10.1007/s10236-003-0036-9.

Evensen, G. (2009). *Data Assimilation*. Berlin, Heidelberg: Springer Berlin Heidelberg Available at: http://link.springer.com/10.1007/978-3-642-03711-5.

Fournier, T., Freymueller, J., and Cervelli, P. (2009). Tracking magma volume recovery at Okmok volcano using GPS and an unscented Kalman filter. *J. Geophys. Res. Solid Earth* 114, B02405. doi:10.1029/2008JB005837.

Global Volcanism Program (2009). Report on Kerinci (Indonesia). In: Wunderman, R (ed.), Bulletin of the Global Volcanism Network. Smithsonian Institution Available at: http://dx.doi.org/10.5479/si.GVP.BGVN200912-261170.

Gregg, P. M., de Silva, S. L., and Grosfils, E. B. (2013). Thermomechanics of shallow magma

chamber pressurization: Implications for the assessment of ground deformation data at active volcanoes. *Earth Planet. Sci. Lett.* 384, 100–108. doi:10.1016/j.epsl.2013.09.040.

Gregg, P. M., de Silva, S. L., Grosfils, E. B., and Parmigiani, J. P. (2012). Catastrophic caldera-forming eruptions: Thermomechanics and implications for eruption triggering and maximum caldera dimensions on Earth. *J. Volcanol. Geotherm. Res.* 241–242, 1–12. doi:10.1016/j.jvolgeores.2012.06.009.

Gregg, P. M., and Pettijohn, J. C. (2016). A multi-data stream assimilation framework for the assessment of volcanic unrest. *J. Volcanol. Geotherm. Res.* 309, 63–77. doi:10.1016/j.jvolgeores.2015.11.008.

Grosfils, E. B. (2007). Magma reservoir failure on the terrestrial planets: Assessing the importance of gravitational loading in simple elastic models. *J. Volcanol. Geotherm. Res.* 166, 47–75. doi:10.1016/j.jvolgeores.2007.06.007.

Gudmundsson, A. (2006). How local stresses control magma-chamber ruptures, dyke injections, and eruptions in composite volcanoes. *Earth-Sci. Rev.* 79, 1–31. doi:10.1016/j.earscirev.2006.06.006.

Hanssen, R. F. (2001). *Radar Interferometry: Data Interpretation and Error Analysis*. Springer Science & Business Media.

Hickey, J., Gottsmann, J., and Mothes, P. (2015). Estimating volcanic deformation source parameters with a finite element inversion: The 2001-2002 unrest at Cotopaxi volcano, Ecuador. *J. Geophys. Res. Solid Earth* 120, 1473–1486. doi:10.1002/2014JB011731.

Hildreth, W., and Moorbath, S. (1988). Crustal contributions to arc magmatism in the Andes of Central Chile. *Contrib. Mineral. Petrol.* 98, 455–489. doi:10.1007/BF00372365.

Jónsson, S., Zebker, H., Segall, P., and Amelung, F. (2002). Fault slip distribution of the 1999

Mw 7.1 Hector Mine, California, earthquake, estimated from satellite radar and GPS measurements. *Bull. Seismol. Soc. Am.* 92, 1377–1389.

Julier, S., Uhlmann, J., and Durrant-Whyte, H. F. (2000). A new method for the nonlinear transformation of means and covariances in filters and estimators. *Ieee Trans. Autom. Control* 45, 477–482. doi:10.1109/9.847726.

Koulakov, I., Bohm, M., Asch, G., Lühr, B.-G., Manzanares, A., Brotopuspito, K. S., et al. (2007). P and S velocity structure of the crust and the upper mantle beneath central Java from local tomography inversion. *J. Geophys. Res.* 112. doi:10.1029/2006JB004712.

Le Mével, H., Gregg, P. M., and Feigl, K. L. (2016). Magma injection into a long-lived reservoir to explain geodetically measured uplift: Application to the 2007–2014 unrest episode at Laguna del Maule volcanic field, Chile. *J. Geophys. Res. Solid Earth* 121, 2016JB013066. doi:10.1002/2016JB013066.

Li, Z., Muller, J.-P., Cross, P., and Fielding, E. J. (2005). Interferometric synthetic aperture radar (InSAR) atmospheric correction: GPS, Moderate Resolution Imaging Spectroradiometer (MODIS), and InSAR integration. *J. Geophys. Res. Solid Earth* 110, B03410. doi:10.1029/2004JB003446.

Lisaeter, K. A., Evensen, G., and Laxon, S. (2007). Assimilating synthetic CryoSat sea ice thickness in a coupled ice-ocean model. *J. Geophys. Res.-Oceans* 112, C07023. doi:10.1029/2006JC003786.

Lister, J. R., and Kerr, R. C. (1991). Fluid-mechanical models of crack propagation and their application to magma transport in dykes. *J. Geophys. Res. Solid Earth* 96, 10049–10077. doi:10.1029/91JB00600.

Lohman, R. B., and Simons, M. (2005). Some thoughts on the use of InSAR data to constrain

models of surface deformation: Noise structure and data downsampling. *Geochem. Geophys. Geosystems* 6, n/a-n/a. doi:10.1029/2004GC000841.

McCaffrey, R. (2009). The Tectonic Framework of the Sumatran Subduction Zone. *Annu. Rev. Earth Planet. Sci.* 37, 345–366. doi:10.1146/annurev.earth.031208.100212.

McTigue, D. F. (1987). Elastic stress and deformation near a finite spherical magma body: Resolution of the point source paradox. *J. Geophys. Res.* 92, 12931. doi:http://dx.doi.org/10.1029/jb092ib12p12931.

Mogi, K. (1958). Relations between the eruptions of various volcanoes and the deformations of the ground surfaces around them. *Bull Earthq Res Inst Univ. Tokyo* 36, 99–134.

Muksin, U., Bauer, K., and Haberland, C. (2013). Seismic Vp and Vp/Vs structure of the geothermal area around Tarutung (North Sumatra, Indonesia) derived from local earthquake tomography. *J. Volcanol. Geotherm. Res.* 260, 27–42. doi:10.1016/j.jvolgeores.2013.04.012.

Newman, A. V., Stiros, S., Feng, L., Psimoulis, P., Moschas, F., Saltogianni, V., et al. (2012). Recent geodetic unrest at Santorini Caldera, Greece. *Geophys. Res. Lett.* 39, L06309. doi:10.1029/2012GL051286.

Nooner, S. L., and Chadwick, W. W. (2009). Volcanic inflation measured in the caldera of Axial Seamount: Implications for magma supply and future eruptions. *Geochem. Geophys. Geosystems* 10, Q02002. doi:10.1029/2008GC002315.

Pagli, C., Wright, T. J., Ebinger, C. J., Yun, S.-H., Cann, J. R., Barnie, T., et al. (2012). Shallow axial magma chamber at the slow-spreading Erta Ale Ridge. *Nat. Geosci.* 5, 284–288. doi:10.1038/ngeo1414.

Parks, M. M., Moore, J. D. P., Papanikolaou, X., Biggs, J., Mather, T. A., Pyle, D. M., et al. (2015). From quiescence to unrest: 20years of satellite geodetic measurements at Santorini

volcano, Greece. *J. Geophys. Res.-Solid Earth* 120, 1309–1328. doi:10.1002/2014JB011540.

Pasquare, F. A., and Tibaldi, A. (2003). Do transcurrent faults guide volcano growth? The case of NW Bicol Volcanic Arc, Luzon, Philippines. *Terra Nova* 15, 204–212. doi:10.1046/j.1365-3121.2003.00484.x.

Ronchin, E., Masterlark, T., Molist, J. M., Saunders, S., and Tao, W. (2013). Solid modeling techniques to build 3D finite element models of volcanic systems: An example from the Rabaul Caldera system, Papua New Guinea. *Comput. Geosci.* 52, 325–333. doi:10.1016/j.cageo.2012.09.025.

Schmidt, S. F. (1966). "Application of State-Space Methods to Navigation Problems," in *Advances in Control Systems*, ed. C. T. LEONDES (Elsevier), 293–340. Available at: http://www.sciencedirect.com/science/article/pii/B9781483167169500114.

Sieh, K., and Natawidjaja, D. (2000). Neotectonics of the Sumatran fault, Indonesia. *J. Geophys. Res. Solid Earth* 105, 28295–28326. doi:10.1029/2000JB900120.

Simons, M., Fialko, Y., and Rivera, L. (2002). Coseismic Deformation from the 1999 Mw 7.1 Hector Mine, California, Earthquake as Inferred from InSAR and GPS Observations. *Bull. Seismol. Soc. Am.* 92, 1390–1402. doi:10.1785/0120000933.

Skjervheim, J.-A., Evensen, G., Aanonsen, S. I., Ruud, B. O., and Johansen, T.-A. (2007). Incorporating 4D Seismic Data in Reservoir Simulation Models Using Ensemble Kalman Filter. *SPE J.* 12, 282–292. doi:10.2118/95789-PA.

Tait, S., Jaupart, C., and Vergniolle, S. (1989). Pressure, gas content and eruption periodicity of a shallow, crystallising magma chamber. *Earth Planet. Sci. Lett.* 92, 107–123. doi:10.1016/0012-821X(89)90025-3.

Tibaldi, A. (2015). Structure of volcano plumbing systems: A review of multi-parametric effects.

J. Volcanol. Geotherm. Res. 298, 85–135. doi:10.1016/j.jvolgeores.2015.03.023.

vanLeeuwen, P. J., and Evensen, G. (1996). Data assimilation and inverse methods in terms of a probabilistic formulation. *Mon. Weather Rev.* 124, 2898–2913. doi:10.1175/1520-0493(1996)124<2898:DAAIMI>2.0.CO;2.

Wilson, G. W., Oezkan-Haller, H. T., and Holman, R. A. (2010). Data assimilation and bathymetric inversion in a two-dimensional horizontal surf zone model. *J. Geophys. Res.-Oceans* 115, C12057. doi:10.1029/2010JC006286.

Yang, X.-M., Davis, P. M., and Dieterich, J. H. (1988). Deformation from inflation of a dipping finite prolate spheroid in an elastic half-space as a model for volcanic stressing. *J. Geophys. Res. Solid Earth* 93, 4249–4257.

Zhan, Y., and Gregg, P. M. (2017). Data assimilation strategies for volcano geodesy. *J. Volcanol. Geotherm. Res.* doi:10.1016/j.jvolgeores.2017.02.015.

Zhan, Y., Hou, G., Kusky, T., and Gregg, P. M. (2016). Stress development in heterogenetic lithosphere: Insights into earthquake processes in the New Madrid Seismic Zone. *Tectonophysics* 671, 56–62. doi:10.1016/j.tecto.2016.01.016.

CHAPTER 4: HOW ACCURATELY CAN WE MODEL MAGMA RESERVOIR FAILURE WITH UNCERTAINTIES IN HOST-ROCK RHEOLOGY?[3]

Abstract

Forecasting the onset of a volcanic eruption from a closed system requires understanding its stress state and failure potential, which can be investigated through numerical modeling. However, the lack of constraints on model parameters, especially rheology, may substantially impair the accuracy of failure forecasts. Therefore, it is essential to know whether large variations and uncertainties in rock properties will preclude the ability of models to predict reservoir failure. A series of 2-dimensional, axisymmetric models are used to investigate sensitivities of brittle failure initiation to assumed rock properties. The numerical experiments indicate that the deformation and overpressure at failure onset simulated by elastic models will be much lower than the viscoelastic models, when the timescale of pressurization exceeds the viscoelastic relaxation time of the host-rock. Poisson's ratio and internal friction angle have much less effect on failure forecasts than Young's modulus. Variations in Young's modulus significantly affect the prediction of surface deformation before failure onset when Young's modulus is <40 GPa. Longer precursory volcano-tectonic events may occur in weak host-rock (E <40 GPa) due to well-developed Coulomb failure prior to dike propagation. Thus, combining surface deformation with seismicity may enhance the accuracy of eruption forecast in these situations. Compared to large and oblate magma systems, small and prolate systems create far less surface-uplift prior to failure initiation, suggesting frequent measurements are necessary.

[3] Published as: Zhan Y. and Gregg P. M. (2019) How Accurately Can We Model Magma Reservoir Failure with Uncertainties in Host Rock Rheology? Journal of Geophysical Research: Solid Earth 124, 8030–8042.

4.1 Introduction

Ground deformation is one of the most widely used methods to evaluate and forecast volcanic unrest (Sparks, 2003). Geodetic monitoring methods, including Global Navigation Satellite System (GNSS) and Interferometric Synthetic Aperture Radar (InSAR) provide temporal surface deformation observations of active volcanoes and a glimpse into the evolution of the underlying magmatic system. Geodetic data alone cannot uniquely constrain some important parameters of magma reservoirs, like size or overpressure (e.g., Segall, 2019). The architecture and evolution of a magma reservoir may be better interpreted by combining multiple geophysical observations, such as seismology, gravity, and magnetotellurics. However, a good knowledge of reservoir geometry and deformation history does not ensure an accurate eruption forecast. Substantial surface inflation may not indicate the propensity of volcano eruption (e.g., Biggs et al., 2014; Biggs & Pritchard, 2017).

Numerical volcano models provide important evaluations of ground deformation signals using stress calculations and failure predictions, which are essential to give insight into the dynamic evolution of magma systems (e.g., Grosfils, 2007; Albino et al., 2010; Gerbault et al., 2012, 2018; Gregg et al., 2012, 2013; Hickey & Gottsmann, 2014; Hickey et al., 2015). Furthermore, the recent development of sequential data assimilation approaches provides near real-time estimates of overpressure and stress state of magmatic systems, which is a promising step towards forecasting volcanic unrest with advanced observations (e.g., Gregg & Pettijohn, 2016; Bato et al., 2017, 2018; Zhan & Gregg, 2017; Zhan et al., 2017; Gregg et al., 2018; Albright et al., 2019). However, before an accurate forecast can be conducted, we need to understand the sensitivity of model results to different model parameters in a magmatic system, such as geometry, initial stress state, and rock properties. Among them, the effect of chamber geometry has been systematically studied by previous investigations (e.g., Mogi, 1958; Yang et

al., 1988; Segall, 2019), and the initial stress is controlled by many factors such as the deformation history and tectonics, which is beyond the scope of this paper. We focus our current effort on evaluating the impact of rock rheology, which is an important factor in magma system models, and is not well constrained.

Rock properties for different volcanoes can be distinct. For example, the Young's modulus inferred by static loading is no more than 1 GPa for Merapi volcano (Beauducel et al., 2000), while the Young's modulus is greater than 40 GPa for volcanoes in Iceland (Grapenthin et al., 2006). Even for one volcano, rock properties inferred by different approaches may not be consistent. Dynamic Young's modulus calculated using seismic methods can be significantly higher than static Young's modulus determined by laboratory rock tests and geodetic modeling. For example, dynamic Young's modulus of the crust in Mt. Etna inferred by P-wave velocity can reach 100 GPa (e.g., Currenti et al., 2007), while laboratory rock tests show that Young's modulus of a basaltic samples from Mt. Etna is < 30 GPa (Heap et al., 2010). Additionally, Young's modulus and Poisson's ratio can be modified by ~30% during repeating loading and unloading (Heap et al., 2010). Similarly, the viscosity of the crust varies from 10_{15} to 10_{21} $Pa \cdot s$ depending on the composition and temperature (e.g., Newman et al., 2001). Considering that a systematic discussion on the effects of rock property on modeling is still absent, this study aims to test the effect of varying rock properties on modeling brittle failure around a magma reservoir.

In this paper, we conduct a series of sensitivity tests using 2-dimensional, axisymmetric models to evaluate the impact of the uncertainties in assumed rheological parameters. First, we use viscoelastic models to evaluate the sensitivities of Critical Maximum Surface Uplift (CMSU) and overpressure before brittle failure onset to a variety of rheological parameters, such as viscosity, Young's modulus, and loading rate. Then, a series of elastic models are used to test the

effects of Young's modulus, Poisson's ratio, internal friction angle, and tensile strength on the CMSU and critical overpressure. The effects of these parameters are evaluated under different geometrical conditions including depth, size, and shape of the magma body. Of particular interest in this investigation is whether large variations and uncertainties preclude the ability of models to predict failure of a magma reservoir. Here we only consider the homogenous rock property to quantify the uncertainties from the varying values of rock properties. Heterogeneity in those properties is also important (e.g., De Natale & Pingue, 1996; Masterlark, 2007) and should be studied systematically in the future.

4.2 Methods

4.2.1 Model setup

We use 2-dimensional, axisymmetric models (Fig. 4.1a) solved by finite element code COMSOL Multiphysics 5.3 to simulate the surface deformation and failure of the host-rock due to an inflating magma body with an applied overpressure (OP; e.g., Gregg at al., 2012, 2013). Overpressure is assumed along the boundary of the magma body as a force in excesses of the lithostatic stress. Roller boundary conditions are defined at the side and bottom of the model. Gravity is loaded as a body force, which is balanced by an initial hydrostatic stress (i.e., $\sigma_1 = \sigma_2 = \sigma_3 = \rho g z$) prior to the addition of overpressure along the boundary of the spheroid (Fig. 4.1a).

4.2.2 Rupture of the magma chamber

We use the Coulomb failure criterion (Eq. 4.1) and the tensile failure criterion (Eq. 4.2) to calculate failure in the host rocks due to overpressure loading. Coulomb failure or tensile failure is triggered, when:

$$\frac{\sigma_1-\sigma_3}{2}\cos\phi - \frac{\sigma_1+\sigma_3}{2}\tan\phi - C_0 > 0 \quad (4.1)$$

or

$$-\sigma_3 - T_0 > 0, \tag{4.2}$$

where ϕ is the internal friction angle, C_0 and T_0 are the rock's cohesion and tensile strength, and σ_1 and σ_3 are maximum and minimum principal stresses (Table 4.1).

Previous rock experiments have shown a uniform, linear relationship between uniaxial compressive strength (UCS) and Young's modulus for worldwide andesites, basalt, tuff, and sandstone (e.g., $UCS = 2.28 + 4.11\ E$ by Bradford et al., 1998; $UCS = 1.65 + 5.88\ E$ by Dinçer et al., 2004). The uniaxial compressive strength is further defined by Hoek (1990) as:

$$UCS = \frac{2C_0 \cos\phi}{(1-\sin\phi)}. \tag{4.3}$$

Therefore, the cohesion of the rock is a linear function of Young's modulus at any given internal friction angle. The internal friction angle of the rock ranges from 15° to 35° (Byerlee, 1978). Combining the empirical equation of UCS (Braford et al., 1998; Dinçer et al., 2004) and Equation (3), we can express the cohesion of rock as a function of Young's modulus (Fig. A.1a). The relationship between cohesion and Young's modulus using different empirical equations and friction is in the same order (Fig. A.1a). We use the empirical equation by Bradford et al. (1998) and the friction angle as 35° assuming rock cohesion:

$$C_0 = E \times 10^{-3}. \tag{4.4}$$

The tensile strength of the rock is usually 1/10 of its UCS (e.g., Jaeger et al., 2007). Therefore, we assume the tensile strength is approximately given by (Fig. A.1b)

$$T_0 = E \times 0.4 \times 10^{-3}, \tag{4.5}$$

where E is the Young's modulus applied in the model. When a magma chamber is inflating, failure tends to initiate at (1) the vertex of an oblate spheroid, and (2) near the surface of the model space above the magma chamber (Fig. A.2). Then, the failure region expands and

connects to form through-going failure (Fig. A.2). This stage is highly path-dependent, which means the distribution of previous failure and weakness will impact generation of new fractures. Additionally, the propagation of fractures may accommodate the transport of magma if the stresses are properly oriented (i.e., dike propagation coinciding with mode-I failure). The predicted overpressure at which the through-going failure has formed (Fig. A.2) may be greatly overestimated, if the accumulated damage in host-rocks is not taken into consideration. In this study, we focus on failure initiated along the magma chamber, representing chamber rupture (Fig. 4.1b). We calculate the overpressure and the maximum surface uplift (i.e., the maximum vertical surface displacement directly above the source center) of a volcano at its initial rupture as a function of the Critical Maximum Surface Uplift (CMSU). Brittle failure of rock is generally thought to trigger high-frequency or "volcano- tectonic" (VT) earthquakes (e.g., Roman and Cashman, 2006). In practice, CMSU can infer how much precursory deformation can be observed before the onset of VT earthquakes.

4.2.3 Calculation of CMSU and critical overpressure

The viscous effect is tested by a series of viscoelastic models which employ a standard linear solid rheology (after Del Negro et al., 2009). In the viscoelastic tests, viscosity varies from 10_{15} to 10_{21} $Pa \cdot s$ (Newman et al., 2001) and different overpressure loading rates are assumed from 50 MPa per day to 50 MPa per 100,000 days representing unrest episodes from single-day-scale to hundred-year-scale (Table 4.1). Each viscous model is loaded by a constant overpressure rate from an equilibrium stress state. The loading process has been evenly divided into 50 steps until the overpressure reaches 50 MPa. We choose 50 MPa as a terminal overpressure to ensure the failure occurrence. Using Eq. 4.1 and 4.2, we can determine at which step failure has been initiated along the chamber wall. Therefore, the overpressure and CMSU at that step are the critical overpressure and CMSU. The viscous tests aim to show whether and when host rock

viscosity will impact failure initiation.

In the elastic tests, the Young's modulus varies from 5 GPa to 80 GPa, covering the range in uncertainty for upper crustal rocks (e.g., Aggistalis et al., 1996; Dinçer et al., 2004). Although a significantly low Young's modulus (E<1 GPa) has been observed at Merapi volcano (e.g., Beauducel et al., 2000), it may present the effect of an unconsolidated edifice material, which is too low to represent the average upper crust. We also test three Poisson's ratios from 0.15 to 0.35 (Christensen, 1996; Gercek, 2007) and three internal friction angles from 15° to 35° (Byerlee, 1978). The parameters and variables used in the models are shown in Table 4.1. For elastic tests, we use an approach method to calculate the CMSU and critical overpressure. First, we model the stress field with an initial overpressure (i.e., 50 MPa, but not important). Then, we calculate residual strengths along the chamber wall, which are defined by the left-hand sides (LHS) of Eq. 4.1 and 4.2. In the next iteration, we either increase or decrease the overpressure to reduce the residual. We iterate this process until absolute residual strength of any point along the chamber wall is < 5% of the rock cohesion or tensile strength. It usually takes less than 10 iterations to approach the critical overpressure and CMSU at failure onset. In all tests, the critical overpressure and CMSU for both tensile and Coulomb failure are calculated to determine which type failure occurs first.

All models are assumed to be homogeneous and isotropic to simplify the calculation. More sophisticated models with temperature dependent rheology and pre-existing features will be tested in future investigations. However, this simple approach is capable of providing a meaningful evaluation of when uncertainties in elastic moduli overwhelm a model's ability to predict the failure of a magmatic system.

4.3 Results

4.3.1 The viscous effect

We calculate the Critical Maximum Surface Uplift (CMSU) prior to the presence of the initial tensile or Coulomb failure for the models with different viscosities and Young's moduli (Fig. A.3 and A4). Since the loading rate is important in viscoelastic models, we test rates from 50 MPa / day to 50 MPa / 100,000 day to mimic a wide range of replenishment rates for magma chambers. In general, when the loading rate is low enough, the CMSUs calculated by the viscoelastic models start to deviate from the elastic models. Higher CMSUs are expected in viscous models compared to elastic models, if the characteristic time of loading (i.e., the time-span for the chamber to be pressurized to 50 MPa) is larger than the viscoelastic relaxation time (Fig. A.3). Models with higher viscosity ($\eta > 10^{19}\ Pa \cdot s$) tend to behave elastically creating the same CMSU as the elastic model even if the loading rate is as low as 50 MPa per 10 years (Fig. A.3). We argue that the viscous effect can be neglected if the CMSU prior to failure calculated by a viscoelastic model equals the elastic model with the same elastic moduli (Fig. A.3). The deviation of the CMSU by a viscoelastic model from an elastic model is controlled by the relaxation time of host-rock and the characteristic time of loading (Fig. 4.2). When the characteristic time is significantly longer than the relaxation time of the model, the viscous effect cannot be neglected (Fig. 4.2). A rock with lower Young's modulus or higher viscosity has a longer relaxation time, which is more likely to behave elastically under the same loading rate. Both viscoelastic and elastic models predict the same critical overpressure prior to failure onset at a given Young's modulus, indicating that the overpressure is independent of the viscosity and loading rate (Fig. A.4). The critical overpressure is only controlled by the Young's modulus and rock strength.

4.3.2 Elastic properties

According to the viscoelastic tests, a linear elastic model is appropriate in cases when the loading time span from zero overpressure to reservoir failure is shorter than the relaxation time (i.e., high loading rate, > 50 MPa / 10 year). Therefore, in these conditions, the elastic moduli and brittle failure parameters become critical for forecasting failure onset. To further examine the effects of other rock properties, we conduct a series of elastic tests on Young's modulus, rock strength which is determined by Young's modulus, Poisson's ratio, and internal friction angle. In particular, the depth, radius, and aspect ratio of the chamber are varied to provide a broad view of the failure predictions (Table 4.2; Fig. A.5).

Geodetic data recording the pattern of surface deformation can constrain depth and aspect ratio of the magma chamber. For example, a deeper chamber exhibits a longer wavelength signal (Fig. A.5a) as illustrated elegantly by the Mogi (1958) model. The horizontal displacement is more sensitive to the aspect ratio (e.g., Dieterich and Decker, 1975; Yang et al., 1988; Fig. A.5d), the vertical displacement patterns of the models with different aspect ratios are similar. Parameters like radius or total volume of the chamber cannot be constrained by the deformation patterns alone (Fig. A.5b).

Given the same size and shape of a chamber (Elastic Test 1), deeper magma bodies generate lower CMSU before failure onset than shallower magma bodies (Fig. 4.3a). Although a deeper chamber requires a higher overpressure to fail due to the more substantial confining pressure (Fig. 4.3b), the higher overpressure generates less detectable surface deformation. Deeper chambers also have a smaller range of CMSU for different Young's moduli. The range of CMSU for a chamber below 7 km is less than 0.3 m, even if Young's modulus of crust varies from 20 GPa to 80 GPa, indicating that variation in Young's modulus has a less of an effect on the accuracy of the failure forecast. Similar to the depth-dependent results, weaker host-rock

generates a greater CMSU prior to failure onset. At a given depth, the variability in predicted CMSU and critical overpressure significantly decreases when Young's modulus is greater than 40 GPa, suggesting that host-rock deformation is no longer sensitive to Young's modulus once the host-rock is strong enough (Fig. 4.3). The models with different Poisson's ratio from 0.15 to 0.35 have similar CMSUs and critical overpressures before failure onset (Fig. 4.3). Therefore, the brittle failure of the magma chamber is much more sensitive to Young's modulus than to Poisson's ratio. Like Poisson's ratio, the internal friction angle has less effect on the CMSU before brittle failure for stiffer host-rocks (Fig. 4.4), especially when the chamber is deep. However, for the soft host-rock (E = 5 GPa), the variation in CMSU or overpressure due to the internal friction angle is still large even for a deep chamber, indicating an accurate estimation in rock properties for weak host-rock is crucial to failure prediction (Fig. 4.4).

For the chambers located at the same depth (Elastic Test 2), smaller chambers fail with lower CMSUs due to the higher overpressures needed to generate surface deformation (Fig. 4.5a). The size of the chamber also magnifies the range of the CMSU caused by the Young's modulus, suggesting that the behavior of large magmatic systems is strongly dependent on rock properties whereas smaller chambers (R_1 < 1 km) may be less sensitive (Fig. 4.5a). The overarching control on failure onset appears to be overpressure. Regardless of the assumed chamber geometry, the overpressure magnitude is similar at the moment of failure onset for a given Young's modulus (Fig. 4.5b). All of the models in Elastic Test 2 have the same magma chamber aspect ratio (R_1/R_2), which leads to the same pattern of near-field stress concentration regardless of the scales of the model. Like Elastic Test 1, the Poisson's ratio (Fig. 4.5) and internal friction angle (Fig. A.6a and b) has little impact on the brittle failure.

In Elastic Test 1, larger overpressures are necessary for deeper chambers to create the same

amount of surface uplift, while the overpressure and size of the chamber is not distinguishable in Elastic Test 2. A deep magma chamber can also generate the same magnitude of surface uplift as the shallower chambers by enlarging the chamber instead of accumulating overpressure, but the wavelength will vary (Fig. A.7; Elastic Test 3). Unlike Elastic Test 1, a deep and large chamber creates larger CMSU than a shallow and small chamber (Fig. A.7c). The range of the CMSU also increases with increasing depth and size. A greater overpressure is needed to initiate failure in models with deeper and larger chambers, simply due to higher confining pressure (Fig. A.7d).

The aspect ratio of an oblate spheroidal chamber with the same volume has less impact on the CMSU than the depth and radius (Elastic Test 4; Fig. 4.6a). A prolate (conduit-like) chamber has lower CMSU at failure, and its aspect ratio has far less effects on the CMSU compared to an oblate chamber. When the magma body is sill-like, the CMSU decrease slightly with growing aspect ratio. The CMSU is much less sensitive to aspect ratios than to depth (Fig. 4.3 and 4.4) and radius (Fig. 4.5) at least for oblate chambers. However, the variability of the overpressures required to initiate failure is quite large (Fig. 4.6b). A highly-oblate chamber ($R_1/R_2 = 5$) requires less than 25 MPa to initiate failure, while this value rises to 150 MPa for a spherical chamber whose aspect ratio is one (Fig. 4.6b). The critical overpressure falls back to 40 MPa when the chamber becomes prolate. Notably, the extremely high overpressure for the spherical chamber does not create a significant uplift, suggesting the stability of the whole system is sensitive to aspect ratio. Although a perfectly spherical chamber has the greatest stability, it is unlikely to exist in natural settings.

In all elastic tests (Figs. 3-6), Young's modulus shows the most significant effect on the development of brittle failure. The stiffer (Young's modulus > 40 GPa) and stronger (C_0 > 40 MPa and T_0 > 16 MPa) the host-rock (e.g., intact granite, diorite, and metamorphic rocks; Perras

& Diederichs, 2014) is assumed to be, the more likely that tensile failure will initiate around the chamber boundary first, while models with a weak host rock favor Coulomb failure at the chamber wall. Because a higher cohesion is expected in stronger rocks, making their Coulomb failure envelope more difficult to reach (Fig. 4.7). Additionally, deeper chambers prefer Coulomb failure as the first failure onset, since tensile failure is harder to initiate due to the high confining pressure at depth.

Although laboratory rock tests indicate that tensile strength of rocks ranges from ~1 to ~20 MPa, in natural conditions, the host-rock may be fractured, causing its tensile strength greatly decreased. We compare the CMSU and critical overpressure of the models assuming $T_0 = E/2500$ to the models with $T_0 = 0$ (Fig. A.8). The results show that using zero tensile strength makes slightly lower CMSU at tensile failure onset, indicating CMSU is not sensitive to tensile strength (Fig. A.8). The critical overpressure of the models with $T_0 = 0$ is constant for each model with the same geometry but different Young's modulus, indicating that the critical overpressure for tensile failure is independent of Young's modulus.

4.4 Discussion

4.4.1 Uncertainty derived from rock properties

The results of the viscoelastic tests indicate that the overpressure at failure onset is independent of the viscosity of the host-rock (Fig. A.4) and is only determined by its elastic moduli. A higher overpressure is needed to trigger failure in a stiffer and stronger system (Fig. A.4 and Fig. 4.3-4.6). Whether or not the viscosity of the host-rock will impact the brittle failure forecast is determined by viscoelastic relaxation time of the crust (Fig. 4.2). The CMSU at failure onset for a particular elastic model will be lower than the viscous model with the same elastic moduli, only if the time scale of the pressurization episode is longer than the viscous relaxation time. Therefore, knowing the relaxation time of the system as well as the over-pressurizing rate

is useful to determine if the model needs to take viscosity into consideration. Models with higher viscosities and lower Young's moduli have longer relaxation times. For a cold crust with a viscosity larger than 10^{20} $Pa \cdot s$, an elastic model is sufficient to simulate the deformation and failure if the replenishment prior to the failure is < 100 years. For a quartz-bearing crust at 350°C (Newman et al., 2001), the crust will still behave elastically if the replenishment episode lasts no more than several years. For a rhyolite close to the solidus, the viscous effect cannot be neglected if it takes more than one day to build overpressure to fail the host-rock (Fig. 4.2). The overpressures required for all viscoelastic models to initiate failure along the chamber wall are the same as the elastic models with the same elastic moduli (Fig. A.4), since the brittle failure of the rocks is only controlled by its strength and current stress state.

Among Young's modulus, Poisson's ratio, internal friction angle and tensile strength, Young's modulus plays the most important role in the displacement at brittle failure onset. All tests conducted indicate that a lower Young's modulus results in greater surface deformation (i.e., CMSU) before the host-rock starts to fail, even if the host-rock has lower compressive and tensile strengths (Fig. 4.3-4.6). The difference in CMSU between the stiffest and weakest rocks is largely dependent on the location and geometry of the magma body. This difference can be as great as several meters if the magma body is large and shallow (Fig. 4.3a and 4.5a). The accuracy of the failure forecast for a system with a low Young's modulus is tenuous without constraining the elastic properties. However, the sensitivity of the CMSU to Young's modulus decreases with increasing Young's modulus, especially when assuming a proportional rock strength (Aggistalis et al., 1996; Dinçer et al., 2004). The elastic properties of the host-rock are determined by the composition and depth. Generally, the Young's modulus of the upper crust increases with depth from ~10 GPa at the surface to ~50 GPa around 2~3 km, and up to ~100

GPa below 5~6 km (e.g., Gudmundsson, 1988). The uncertainty of Poisson's ratio does not significantly impact the CMSU (Fig. 4.3, 4.5, and 4.6). Poisson's ratio of the upper crust is more well constrained than Young's modulus (Christensen, 1996). A poor constraint on internal friction angle will introduce large uncertainties when the Young's modulus is < 5 GPa (Fig. 4.4). Therefore, if the magma body is near the surface or in the volcanic edifice, where the Young's modulus is low, the uncertainty in its material properties will be problematic for forecasting failure initiation. This limitation may be overcome by conducting rock tests on samples from the volcano, since the near surface samples may represent the host-rock for a shallow magma body. But laboratory test results can only be scaled up to represent in-situ/outcrop scale host-rocks, if the host-rock is not strongly fractured. On the other hand, for a deep magma body, the uncertainty introduced by elastic moduli is negligible compared to the uncertainties derived from other factors such as depth (Fig. 4.3) and radius (Fig. 4.4).

4.4.2 Geometrical considerations for geodetic observations

The magnitude of the surface deformation before the onset of host-rock failure (CMSU) is strongly affected by the depth (Fig. 4.3 and 4.4), size (Fig. 4.5), and shape (Fig. 4.6) of the magma body. Under the same overpressure, a deep, small, or prolate magma chamber is limited in the magnitude of vertical surface displacement it can promote before its failure. For example, the conduit inflation of Colima volcano created only ~4 cm uplift no earlier than 11 days prior to the 2013 explosive eruption (Salzer et al., 2014). While, an oblate source under Sierra Negra volcano, Galápagos created ~5 m vertical displacement from 1992 until its 2005 eruption (Chadwick et al., 2006). Beside the absolute magnitude of vertical displacement, the rate of displacement is also important. For volcanoes with small CMSUs, slow deformation rates can ensure their precursory deformation being captured by weekly or monthly geodetic measurement such as InSAR (e.g., Lohman & Simons, 2005; Pinel et al., 2014).

Among all of the geometric uncertainties, the error introduced by the inaccurate estimation of a magma system's size has the greatest effect on producing a failure forecast. Unlike depth and aspect ratio, size and overpressure of a magma body can hardly be distinguished from one another by geodetic observations alone (e.g., Mogi, 1958). Therefore, additional constraints on the dimensions of the magma plumbing system are necessary, such as seismic tomography, gravity, and/or magnetotellurics.

4.4.3 Failure and VT-earthquakes

Volcano-Tectonic (VT) earthquakes can be triggered by the brittle failure of the host-rock. A combination of seismicity and geodesy gives insight into both stress field and deformation field which increases the accuracy of forecasting volcanic unrest (e.g., Lengliné et al., 2008, Carrier et al., 2015). Our models show that, when the overpressure of the magma chamber increases gradually, stronger host-rock favors the initiation tensile failure (Fig. 4.8), while weaker host-rock favors Coulomb failure and the generation of shear fractures first. In the weak host rock case, more overpressure is needed to open tensional cracks for dikes, even though the occurrence of the shear fractures will greatly reduce the tensile strength of the rock (Fig. 4.7a). Therefore, during the period between Coulomb failure onset and tensile failure onset, the earthquake swarms are only generated by shear fractures, indicating that seismicity should be dominated by high-frequency (VT) events. Once tensile failure is initiated, it is very likely followed by dike propagation and possible eruption (White & McCausland, 2016). During dike propagation, earthquakes can be triggered by both brittle failure of host-rocks (Roman & Cashman, 2006), and magma/volatile movement in the dike, indicating low-frequency earthquakes may be observed (McNutt, 2005). Since Coulomb failure does not open a pathway for magma to move to the surface, volcanoes triggering Coulomb failure first may experience a longer period of seismic unrest until tensile failure is initiated. The numerical results show that

shallow magma chambers surrounded by stronger host-rock favor tensile failure as their initial failure type, indicating those systems are likely to erupt without triggering a lot of VT earthquakes, if the speed of dike propagation is fast enough. For example, the 2008 Okmok eruption was preceded by less than 5 hours of seismicity (Larsen et al., 2009), which may be related with dike propagation after tensile failure initiated.

4.4.4 Limitations

Forecasting eruptions by modeling failure as an instantaneous response to the host rock stress state has three main limitations. First, the relationship between failure and eruptions is unclear. Through-going failure which connects the magma chamber to the surface has been indicated as a potential catalyst of caldera formation eruptions (e.g., Gregg et al., 2012, 2013; Cabaniss et al., 2018). However, large caldera eruption cycles may be much longer than thousands of years, far outside of the time scales in this investigation. When forecasting eruptions of a system with much shorter eruption cycles, the effect of diking events cannot be neglected. Dikes may be solidified and trapped depending on their temperature and viscosity (e.g., Delaney & Pollard, 1982; Rubin, 1995; Maccaferri et al., 2011), laying huge uncertainties between failure initiations and the ability of magma to propagate to the surface and erupt. The second shortcoming in the current models is the lack of changes in the rock properties due to failure accumulation. In this study, we focus on the initiation of the failure controlled by the pre-failure stress state, which is more predictable than the stress state evolution during failure propagation. Failure introduces localization of weakness in the host-rock and is usually anisotropic (e.g., Heap et al., 2010). The first two limitations may be overcome by applying dynamic failure propagation models, which are widely used in hydrofracturing studies (e.g., Camacho & Ortiz, 1996; Fu et al., 2013). However, numerical models of dike propagation may be more complicated than hydrofracturing due to the multiphase nature of propagating magma.

Another limitation is the use of homogeneous rock properties, since rock properties vary with depth and temperature, and are also affected by pre-existing structures. A final limitation of these models, which is also fundamental to most volcano modeling approaches, is the lack of knowledge of the initial state. In the presented approach, it is assumed that there is no stress accumulation prior to the observed inflation of the magma chamber. The assumption of an intact host-rock in equilibrium before precursory deformation may greatly impact model forecasts in many systems. Studying multiple volcanic eruption cycles may help to eliminate the effect of the unknown initial state. Furthermore, healing of the host-rock is another important factor, especially under the conditions such as high temperature, confining pressure, and repeated loading (e.g., Batzle et al., 1980; Fredrich & Wong, 1986; Smith et al., 2009). Future efforts should focus particular care to evaluate the impact of the pre-deformation stress condition on forecasts of system unrest and eruption potential.

4.5 Conclusion

A suite of numerical experiments was implemented to answer what is the effect of variations in rock properties on modeled overpressure and critical maximum surface uplift (CMSU) at failure onset along the wall of magma chambers. Model results indicate that, in most of cases, the predicted overpressure and CMSU at failure onset is sensitive to rock properties, which means without knowing rock properties can impair the accuracy of failure modeling.

The overpressure of the magma chamber at failure onset is affected by the elastic properties and strength of the host-rock. Neglecting the viscous effect results in lower CMSU predictions than the calculated CMSU if the time scale of pressurization is longer than the relaxation time of the crust. The CMSU before failure onset is much more sensitive to Young's modulus than to Poisson's ratio or internal friction angle, especially when the Young's modulus of the host-rock

is < 20 GPa. The accuracy of host-rock stability estimates for a deep (> 5 km), small (half-width < 1 km) or prolate magma chamber are less likely to be impaired by the uncertainty from rock properties than by other uncertainties such as geometry. To forecast the unrest of small and/or prolate magma systems, frequent observations are necessary to record the subtle, and often rapid, precursory deformation prior to eruption. However, for shallow, large, or sill-like magma bodies, significant surface deformation may be observed prior to host rock failure initiation. Magma chambers surrounded by a weak host-rock (Young's modulus < 20 GPa) will continue to inflate after triggering Coulomb failure until tensile failure is initiated and dike propagation can be catalyzed. Therefore, prolonged earthquake swarms associated with Coulomb failure may be observed, providing extra information for eruption forecast.

4.6 Figures and Tables

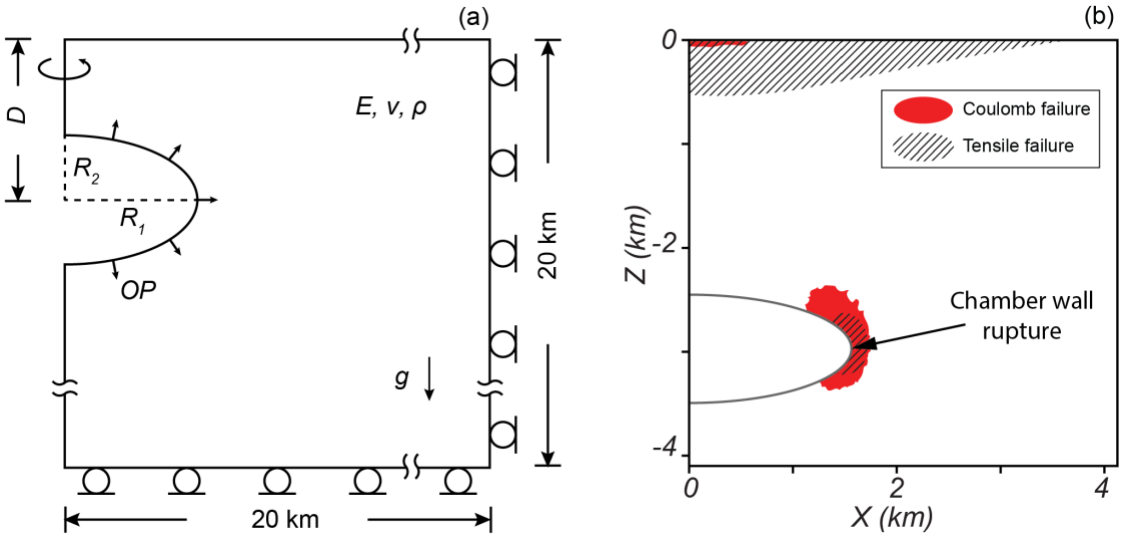

Figure 4.1 Model setup and failure onset. (a) The 2-dimensional axial symmetric model (20 x 20 km). The left boundary is the axis of symmetry. The right and bottom boundaries are defined as roller-type boundary condition. The magma body is represented by an elliptical void along which an overpressure (OP = pressure in excess of the lithostatic pressure) boundary condition is applied. The mesh size of the model ranges from ~100 m around the chamber to ~1000 m near the right and bottom edges. (b) The failure distribution for a model with a Young's modulus of 50 GPa when the surface uplift is 3 m. The Critical Maximum Surface Uplift (CMSU) is the calucated uplift when the chamber wall rupture is initiated, and is much lower than 3 m. The shaded red area indicates Coulomb failure, while the hatched region indicates tensile failure.

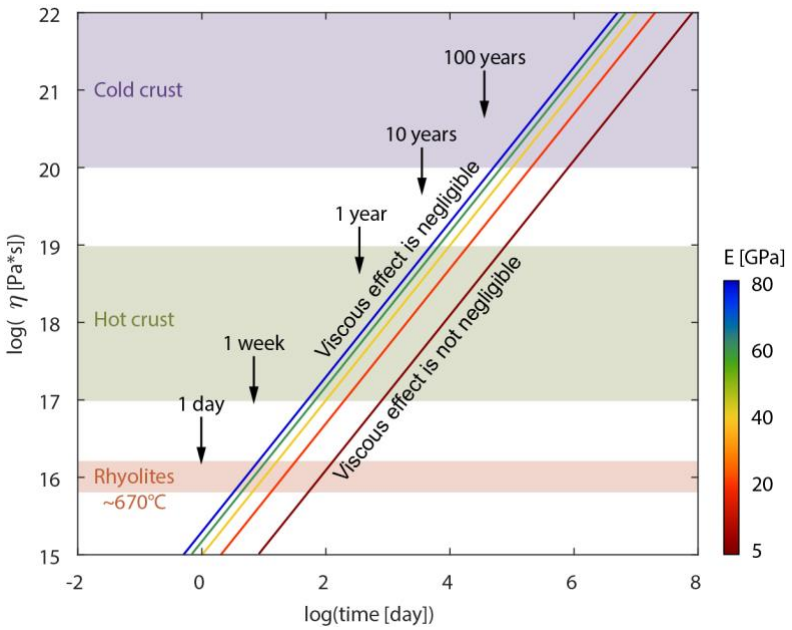

Figure 4.2 The relaxation times for the viscoelastic models. If the time span of pressurization prior to rupture of the magma chamber's wall is shorter than the relaxation time, the viscous effect can be neglected. The Critical Maximum Surface Deformation (CMSU; Fig. A.3) calculated by a viscoelastic model is larger than the CMSU calculated by an elastic model with the same Young's modulus. The viscosity of the crust at different conditions are taken from Newman et al. (2001).

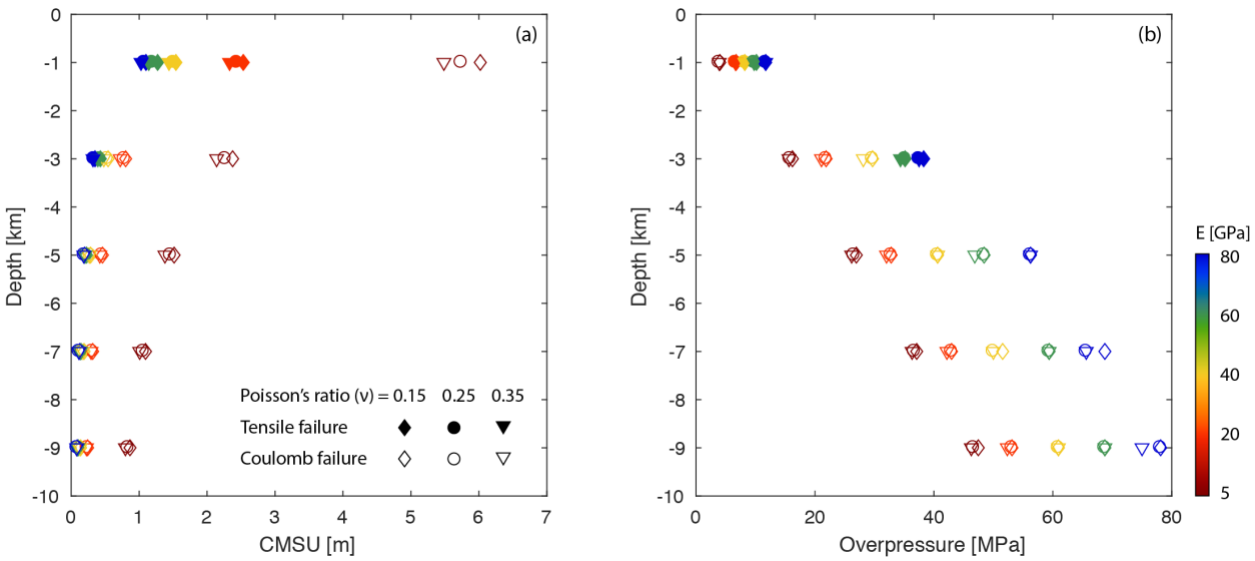

Figure 4.3 The effects of Young's modulus and Poisson's ratio on brittle failure with variations in the source depth to center (Elastic Test 1). A constant internal friction angle ($\varphi = 25°$) is assumed. (a) The Critical Maximum Surface Uplift (CMSU) for models with different magma chamber depths. The CMSU is the maximum value of the surface uplift that can be observed before any failure is initiated around the magma chamber. (b) The corresponding overpressures of the magma chamber when failure occurs. The shape of the marker indicates the Poisson's ratio of the model. The filled or open marker shows the case that the initial failure is tensile or Coulomb, respectively, same as Figs 4-6. The color represents the assumed Young's Modulus of the host, rock same as Figs 4-6.

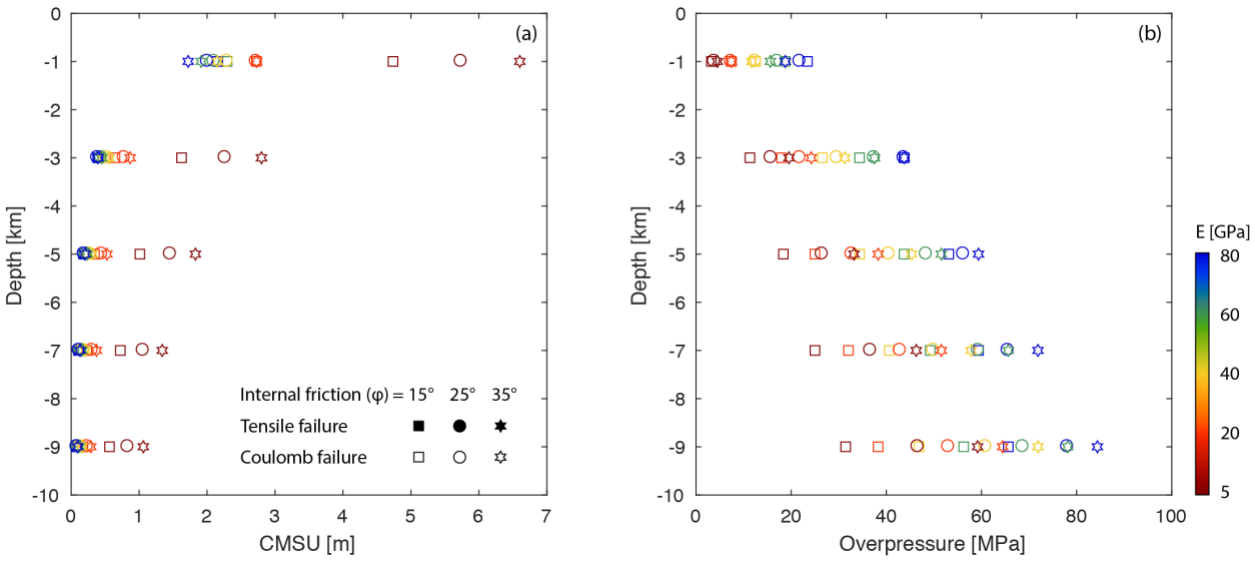

Figure 4.4 The effects of Young's modulus and internal friction angle on Coulomb failure with variations in the source depth to center (Elastic Test 1). A constant Poisson's ratio (ν = 0.25) is assumed. (a) The Critical Maximum Surface Uplift (CMSU) for models with different sizes of magma chamber. (b) The corresponding overpressures of the magma chamber when failure occurs. The shape of the marker indicates the internal friction angle of the model.

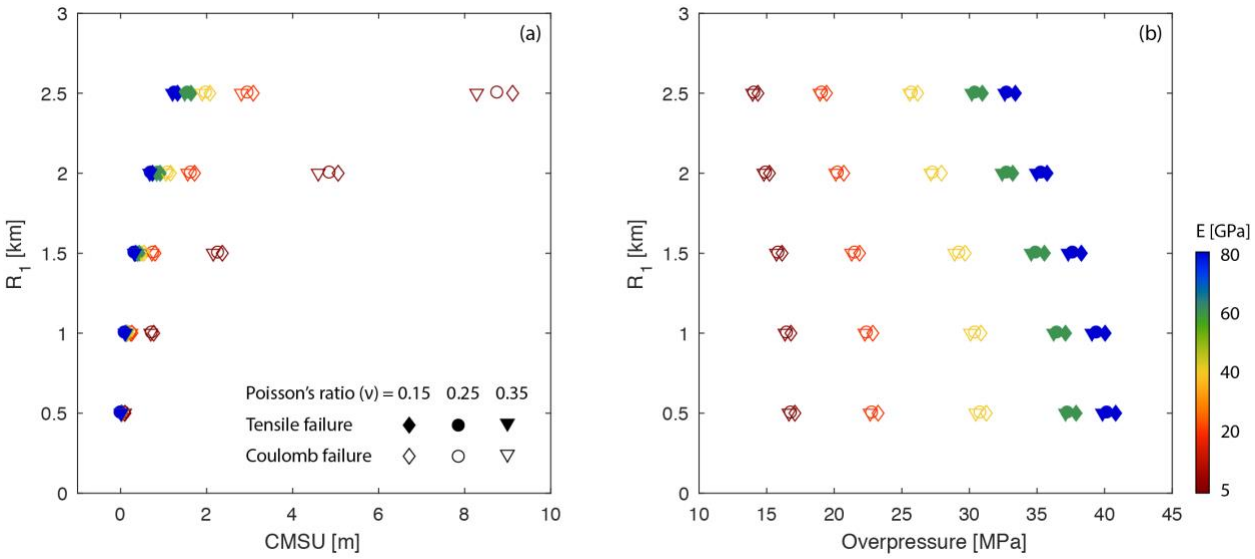

Figure 4.5 The effects of Young's modulus and Poisson's ratio on brittle failure with variations in the chamber size as described by the half-width (Elastic Test 2). A constant internal friction angle ($\varphi = 25°$) is assumed. (a) The Critical Maximum Surface Uplift (CMSU) for models with different size of magma chamber. R_1 is the length of the long axis of the magma chamber, which is three times longer than the short axis. (b) The corresponding overpressures of the magma chamber when failure occurs. The shape of the marker indicates the Poisson's ratio of the model.

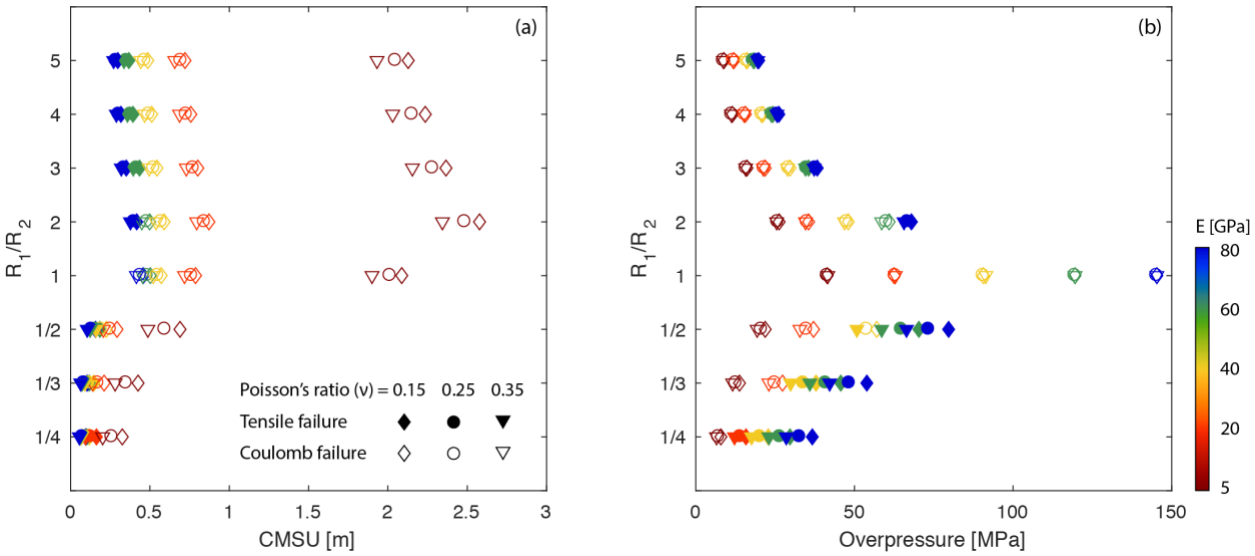

Figure 4.6 The effects of Young's modulus and Poisson's ratio on brittle failure with variations in the chamber aspect ratio (Elastic Test 4). A constant internal friction angle ($\varphi = 25°$) is assumed. (a) The Critical Maximum Surface Uplift (CMSU) for models with different shapes of the magma chamber. The sensitivity of the CMSU to the aspect ratio is noticeably decreased when the magma body is conduit-like ($R_1/R_2 < 1$). (b) The corresponding overpressures of the magma chamber when failure occurs. The shape of the marker indicates the Poisson's ratio of the model.

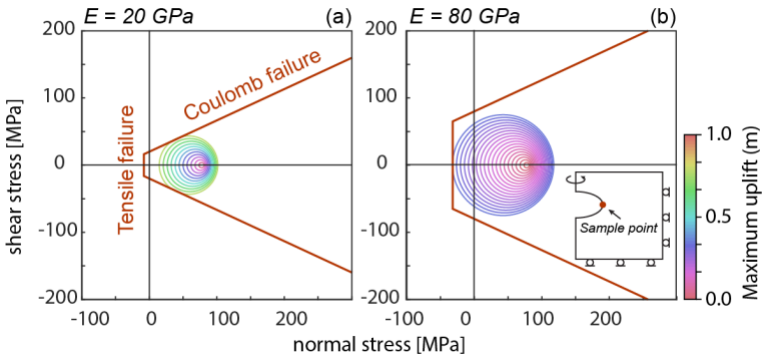

Figure 4.7 Mohr circle diagrams illustrating that the initial failure type is controlled by host-rock stiffness and strength. The Mohr circles represent of the stress state at the tip of the chamber in Model Dp2 (Table 4.2; Depth = 3 km, R_1 = 1.5 km, and R_2 = 0.5 km) as shown in the inserted plot. (a) For the host-rock with relatively low Young's Modulus (E = 20 GPa) and cohesion (20 MPa), the Mohr circle increases and touches the Coulomb failure envelop first. (b) The high cohesion (80 MPa) of the stronger rock (E = 80 GPa) allows the Mohr circle to reach tensile failure first.

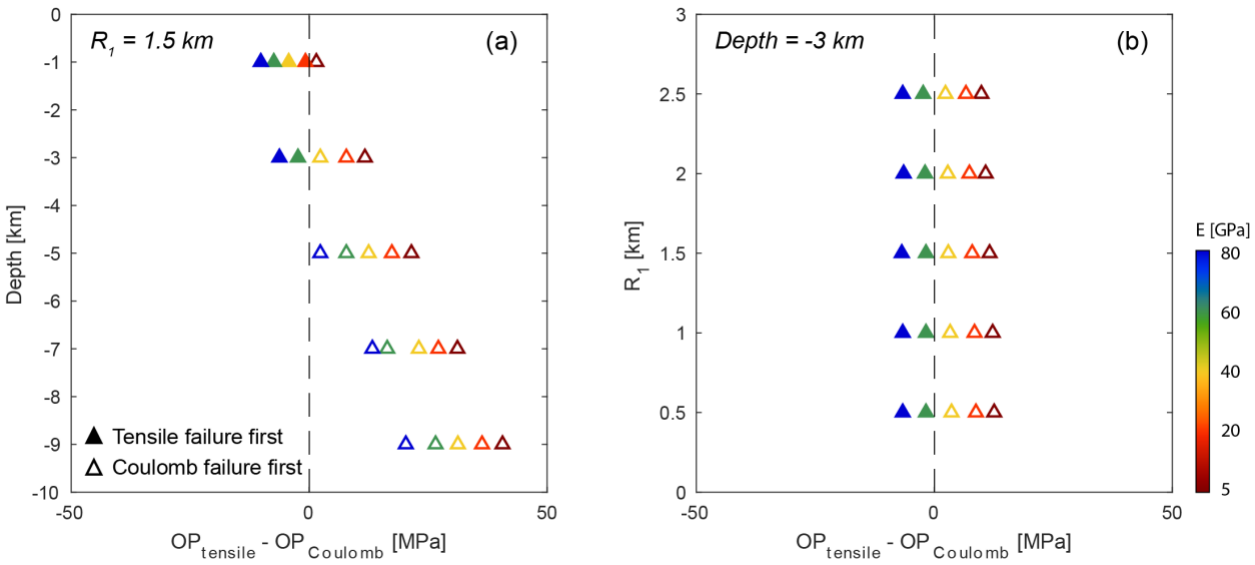

Figure 4.8 The overpressure required to initiate tensile failure compared to the overpressure required to initiate Coulomb failure ($OP_{Tensile} - OP_{Coulomb}$) for models with different chamber depths (a) and half-widths (b). (a) and (b) show the results from models with internal friction = 25° and Poisson's ration = 0.25 in Elastic Test 1 and Elastic Test 2. If the difference in overpressure for the two types of failure is positive, tensile failure will occur after Coulomb failure is triggered. In this case, it is expected that shear fractures will develop generating earthquake swarms during a relatively long period prior to the onset of tensile failure and magma propagation. On the other hand, if the difference in overpressure is negative, Coulomb failure will not be triggered prior to dike propagation.

Table 4.1 Model variables and parameters

Name	Description
D	Depth to the center of the magma chamber (-1, -3, -5, -9 km)
R_1	Half-width of the chamber (variable; km)
R_2	Half-height of the chamber (variable; km)
OP	Overpressure - pressure excess the lithostatic pressure (variable; MPa)
$d(OP)/dt$	Overpressure loading rate for viscous tests $(5 \times 10^1, 5 \times 10^0, 5 \times 10^{-1}, 5 \times 10^{-2}, 5 \times 10^{-3}, 5 \times 10^{-4}\ MPa/day)$
η	Viscosity ($2\times 10^{15}, 2 \times 10^{17}, 2 \times 10^{19}, 2 \times 10^{21}\ Pa \cdot s$)
E	Young's Modulus (5, 20, 40, 60, 80 GPa)
v	Poisson's ratio (0.15, 0.25, 0.35)
ρ	Density of the host-rock (2700 kg/m$_3$)
g	Gravitational acceleration (9.8 m/s$_2$)
C_0	Cohesion of the host-rock (E / 1000; MPa)
T_0	Tensile strength of the host-rock (C_0 / 2.5; MPa)
φ	Internal friction angle of the host-rock (15° ~ 35°)
σ_1	Maximum principal stress (variable; MPa)
σ_3	Minimum principal stress (variable; MPa)
$CMSU$	Critical maximum surface uplift (variable; m)

Table 4.2 Geometric parameters and model notation

Model No.	***Depth-to-center D (km)***	***Half-width R_1 (km)***	***Aspect ratio R_1/R_2***
Viscous Test	-3	1.5	3
Elastic Elastic Test 1 (Depth)			
Dp1	-1	1.5	3
Dp2	-3	1.5	3
Dp3	-5	1.5	3
Dp4	-7	1.5	3
Dp5	-9	1.5	3
Elastic Elastic Test 2 (Size)			
Rd1	-3	0.5	3
Rd2	-3	1.0	3
Rd3	-3	1.5	3
Rd4	-3	2.0	3
Rd5	-3	2.5	3
Elastic Elastic Test 3 (Depth + Size)			
DR1	-1	0.74	3
DR2	-2	1.15	3
DR3	-3	1.50	3
DR4	-4	1.81	3
DR5	-5	2.09	3
Elastic Elastic Test 4 (Aspect Ratio)			
L1	-3	1.04	1
L2	-3	1.31	2
L3	-3	1.50	3
L4	-3	1.65	4
L5	-3	1.78	5
H2	-3	0.83	1/2
H3	-3	0.72	1/3
H4	-3	0.66	1/4

4.7 Acknowledgement

We are grateful for helpful discussions with D. Roman, H. Le Mével, Z. Lu, M. Poland, R. Bendick, M. Coombs, J. Freymueller, J. Albright, H. Cabaniss, R. Goldman, V. Romano, and the UIUC Geodynamics Group. We would also like to thank J. Hickey, Y. Aoki, and two anonymous reviewers for their comments which greatly improved our manuscript. Research reported in this publication is supported by grants from NASA (19-EARTH19R-0104 – Zhan, 18-ESI18-0002 – Gregg) and the National Science Foundation (OCE 1834843, EAR 1752477 – Gregg). Model implementations presented here are available at GitHub (https://github.com/geoyanzhan3/JGR2019_RockProperty).

4.8 References

Aggistalis, G., Alivizatos, A., Stamoulis, D., & Stournaras, G. (1996). Correlating uniaxial compressive strength with schmidt hardness, point load index, Young's modulus, and mineralogy of gabbros and basalts (northern Greece). Bulletin of the International Association of Engineering Geology - Bulletin de l'Association Internationale de Géologie de l'Ingénieur, 54(1), 3–11. https://doi.org/10.1007/BF02600693

Albino, F., Pinel, V., & Sigmundsson, F. (2010). Influence of surface load variations on eruption likelihood: application to two Icelandic subglacial volcanoes, Grímsvötn and Katla. Geophysical Journal International, 181(3), 1510–1524. https://doi.org/10.1111/j.1365-246X.2010.04603.x

Albright, J. A., P. M. Gregg, Z. Lu, and J. Freymueller (2019), Hindcasting magma reservoir stability preceding the 2008 eruption of Okmok, Alaska, Geophysical Research Letters, https://doi.org/10.1029/2019GL083395.

Bato, M. G., Pinel, V., & Yan, Y. (2017). Assimilation of Deformation Data for Eruption Forecasting: Potentiality Assessment Based on Synthetic Cases. Frontiers in Earth Science,

5. https://doi.org/10.3389/feart.2017.00048

Bato, M. G., Pinel, V., Yan, Y., Jouanne, F., & Vandemeulebrouck, J. (2018). Possible deep connection between volcanic systems evidenced by sequential assimilation of geodetic data. Scientific Reports, 8(1), 11702. https://doi.org/10.1038/s41598-018-29811-x

Batzle, M. L., Simmons, G., & Siegfried, R. W. (1980). Microcrack closure in rocks under stress: Direct observation. Journal of Geophysical Research, 85(B12), 7072. https://doi.org/10.1029/JB085iB12p07072

Beauducel, F., Cornet, F.-H., Suhanto, E., Duquesnoy, T., & Kasser, M. (2000). Constraints on magma flux from displacements data at Merapi volcano, Java, Indonesia. Journal of Geophysical Research: Solid Earth, 105(B4), 8193–8203. https://doi.org/10.1029/1999JB900368

Biggs, J., Ebmeier, S. K., Aspinall, W. P., Lu, Z., Pritchard, M. E., Sparks, R. S. J., & Mather, T. A. (2014). Global link between deformation and volcanic eruption quantified by satellite imagery. Nature Communications, 5. http://www.nature.com/ncomms/2014/140403/ncomms4471/full/ncomms4471.html?message-global=remove

Biggs, Juliet, & Pritchard, M. E. (2017). Global Volcano Monitoring: What Does It Mean When Volcanoes Deform? Elements, 13(1), 17–22. https://doi.org/10.2113/gselements.13.1.17

Bradford, I. D. R., Fuller, J., Thompson, P. J., & Walsgrove, T. R. (1998). Benefits of assessing the solids production risk in a North Sea reservoir using elastoplastic modelling. In SPE/ISRM Rock Mechanics in Petroleum Engineering. Society of Petroleum Engineers.

Byerlee, J. D. (1978). Rock Friction and Earthquake Prediction, 414.

Cabaniss, H. E., Gregg, P. M., & Grosfils, E. B. (2018). The Role of Tectonic Stress in

Triggering Large Silicic Caldera Eruptions. Geophysical Research Letters, 45(9), 3889–3895. https://doi.org/10.1029/2018GL077393

Camacho, G. T., & Ortiz, M. (1996). Computational modelling of impact damage in brittle materials. International Journal of Solids and Structures, 33(20–22), 2899–2938. https://doi.org/10.1016/0020-7683(95)00255-3

Carrier, A., Got, J.-L., Peltier, A., Ferrazzini, V., Staudacher, T., Kowalski, P., & Boissier, P. (2015). A damage model for volcanic edifices: Implications for edifice strength, magma pressure, and eruptive processes. Journal of Geophysical Research: Solid Earth, 120(1), 567–583. https://doi.org/10.1002/2014JB011485

Chadwick, W. W., Geist, D. J., Jónsson, S., Poland, M., Johnson, D. J., & Meertens, C. M. (2006). A volcano bursting at the seams: Inflation, faulting, and eruption at Sierra Negra volcano, Galápagos. Geology, 34(12), 1025–1028. https://doi.org/10.1130/G22826A.1

Chang, C., Zoback, M. D., & Khaksar, A. (2006). Empirical relations between rock strength and physical properties in sedimentary rocks. Journal of Petroleum Science and Engineering, 51(3), 223–237. https://doi.org/10.1016/j.petrol.2006.01.003

Cheng, C. H., & Johnston, D. H. (1981). Dynamic and static moduli. Geophysical Research Letters, 8(1), 39–42. https://doi.org/10.1029/GL008i001p00039

Christensen, N. I. (1996). Poisson's ratio and crustal seismology. Journal of Geophysical Research: Solid Earth, 101(B2), 3139–3156. https://doi.org/10.1029/95JB03446

Currenti, G., Del Negro, C., & Ganci, G. (2007). Modelling of ground deformation and gravity fields using finite element method: an application to Etna volcano. Geophysical Journal International, 169(2), 775–786. https://doi.org/10.1111/j.1365-246X.2007.03380.x

De Natale, G., & Pingue, F. (1996). Ground Deformation Modeling in Volcanic Areas. In R.

Scarpa & R. I. Tilling (Eds.), Monitoring and Mitigation of Volcano Hazards (pp. 365–388). Berlin, Heidelberg: Springer Berlin Heidelberg. https://doi.org/10.1007/978-3-642-80087-0_11

Del Negro, C., Currenti, G., & Scandura, D. (2009). Temperature-dependent viscoelastic modeling of ground deformation: application to Etna volcano during the 1993–1997 inflation period. Physics of the Earth and Planetary Interiors, 172(3), 299–309.

Delaney, P. T., & Pollard, D. D. (1982). Solidification of basaltic magma during flow in a dike. American Journal of Science, 282(6), 856–885. https://doi.org/10.2475/ajs.282.6.856

Dinçer, I., Acar, A., Çobanoğlu, I., & Uras, Y. (2004). Correlation between Schmidt hardness, uniaxial compressive strength and Young's modulus for andesites, basalts and tuffs. Bulletin of Engineering Geology and the Environment, 63(2), 141–148. https://doi.org/10.1007/s10064-004-0230-0

Fredrich, J. T., & Wong, T. (1986). Micromechanics of thermally induced cracking in three crustal rocks. Journal of Geophysical Research: Solid Earth, 91(B12), 12743–12764. https://doi.org/10.1029/JB091iB12p12743

Fu, P., Johnson, S. M., & Carrigan, C. R. (2013). An explicitly coupled hydro-geomechanical model for simulating hydraulic fracturing in arbitrary discrete fracture networks. International Journal for Numerical and Analytical Methods in Geomechanics, 37(14), 2278–2300. https://doi.org/10.1002/nag.2135

Gerbault, M., Cappa, F., & Hassani, R. (2012). Elasto-plastic and hydromechanical models of failure around an infinitely long magma chamber. Geochemistry, Geophysics, Geosystems, 13(3). https://doi.org/10.1029/2011GC003917

Gerbault, M., Hassani, R., Lizama, C. N., & Souche, A. (2018). Three-Dimensional Failure

Patterns Around an Inflating Magmatic Chamber. Geochemistry, Geophysics, Geosystems, 19(3), 749–771. https://doi.org/10.1002/2017GC007174

Gercek, H. (2007). Poisson's ratio values for rocks. International Journal of Rock Mechanics and Mining Sciences, 44(1), 1–13. https://doi.org/10.1016/j.ijrmms.2006.04.011

Grapenthin, R., Sigmundsson, F., Geirsson, H., Árnadóttir, T., & Pinel, V. (2006). Icelandic rhythmics: Annual modulation of land elevation and plate spreading by snow load. Geophysical Research Letters, 33(24). https://doi.org/10.1029/2006GL028081

Gregg, P. M., Mével, H. L., Zhan, Y., Dufek, J., Geist, D., & Chadwick, W. W. (2018). Stress triggering of the 2005 eruption of Sierra Negra volcano, Galápagos. Geophysical Research Letters. https://doi.org/10.1029/2018GL080393

Gregg, Patricia M., & Pettijohn, J. C. (2016). A multi-data stream assimilation framework for the assessment of volcanic unrest. Journal of Volcanology and Geothermal Research, 309, 63–77. https://doi.org/10.1016/j.jvolgeores.2015.11.008

Gregg, P.M., de Silva, S. L., Grosfils, E. B., & Parmigiani, J. P. (2012). Catastrophic caldera-forming eruptions: Thermomechanics and implications for eruption triggering and maximum caldera dimensions on Earth. Journal of Volcanology and Geothermal Research, 241–242, 1–12. https://doi.org/10.1016/j.jvolgeores.2012.06.009

Gregg, P.M., de Silva, S. L., & Grosfils, E. B. (2013). Thermomechanics of shallow magma chamber pressurization: Implications for the assessment of ground deformation data at active volcanoes. Earth and Planetary Science Letters, 384, 100–108. https://doi.org/10.1016/j.epsl.2013.09.040

Grosfils, E. B., McGovern, P. J., Gregg, P. M., Galgana, G. A., Hurwitz, D. M., Long, S. M., & Chestler, S. R. (2015). Elastic models of magma reservoir mechanics: a key tool for

investigating planetary volcanism. In T. Platz, M. Massironi, P. K. Byrne, & H. Hiesinger (Eds.), Volcanism and Tectonism Across the Inner Solar System (Vol. 401, pp. 239–267). Bath: Geological Soc Publishing House.

Gudmundsson, A. (1988). Effect of tensile stress concentration around magma chambers on intrusion and extrusion frequencies. Journal of Volcanology and Geothermal Research, 35(3), 179–194. https://doi.org/10.1016/0377-0273(88)90015-7

Heap, M. J., Faulkner, D. R., Meredith, P. G., & Vinciguerra, S. (2010). Elastic moduli evolution and accompanying stress changes with increasing crack damage: implications for stress changes around fault zones and volcanoes during deformation: Elastic moduli evolution and stress changes. Geophysical Journal International, 183(1), 225–236. https://doi.org/10.1111/j.1365-246X.2010.04726.x

Hickey, J., & Gottsmann, J. (2014). Benchmarking and developing numerical Finite Element models of volcanic deformation. Journal of Volcanology and Geothermal Research, 280, 126–130. https://doi.org/10.1016/j.jvolgeores.2014.05.011

Hickey, J., Gottsmann, J., & Mothes, P. (2015). Estimating volcanic deformation source parameters with a finite element inversion: The 2001-2002 unrest at Cotopaxi volcano, Ecuador. Journal of Geophysical Research: Solid Earth, 120(3), 1473–1486. https://doi.org/10.1002/2014JB011731

Jaeger, J. C., Cook, N. G. W., & Zimmerman, R. W. (2007). Fundamentals of rock mechanics (4th ed). Malden, MA: Blackwell Pub.

Larsen, J., Neal, C., Webley, P., Freymueller, J., Haney, M., McNutt, S., et al. (2009). Eruption of Alaska Volcano Breaks Historic Pattern. Eos, Transactions American Geophysical Union, 90(20), 173. https://doi.org/10.1029/2009EO200001

Lengliné, O., Marsan, D., Got, J.-L., Pinel, V., Ferrazzini, V., & Okubo, P. G. (2008). Seismicity and deformation induced by magma accumulation at three basaltic volcanoes. Journal of Geophysical Research: Solid Earth, 113(B12). https://doi.org/10.1029/2008JB005937

Lohman, R. B., & Simons, M. (2005). Some thoughts on the use of InSAR data to constrain models of surface deformation: Noise structure and data downsampling. Geochemistry, Geophysics, Geosystems, 6(1), n/a-n/a. https://doi.org/10.1029/2004GC000841

Maccaferri, F., Bonafede, M., & Rivalta, E. (2011). A quantitative study of the mechanisms governing dike propagation, dike arrest and sill formation. Journal of Volcanology and Geothermal Research, 208(1–2), 39–50. https://doi.org/10.1016/j.jvolgeores.2011.09.001

Masterlark, T. (2007). Magma intrusion and deformation predictions: Sensitivities to the Mogi assumptions. Journal of Geophysical Research, 112(B6). https://doi.org/10.1029/2006JB004860

McNutt, S. R. (2005). Volcanic Seismology. Annual Review of Earth and Planetary Sciences, 33, 461–491. https://doi.org/10.1146/annurev.earth.33.092203.122459

Mogi, K. (1958). Relations between the eruptions of various volcanoes and the deformations of the ground surfaces around them. Bull. Earthq. Res. Inst., University of Tokyo, 36, 99–134.

Newman, A. V., Dixon, T. H., Ofoegbu, G. I., & Dixon, J. E. (2001). Geodetic and seismic constraints on recent activity at Long Valley Caldera, California: evidence for viscoelastic rheology. Journal of Volcanology and Geothermal Research, 105(3), 183–206.

Perras, M. A., & Diederichs, M. S. (2014). A Review of the Tensile Strength of Rock: Concepts and Testing. Geotechnical and Geological Engineering, 32(2), 525–546. https://doi.org/10.1007/s10706-014-9732-0

Pinel, V., Poland, M. P., & Hooper, A. (2014). Volcanology: Lessons learned from Synthetic

Aperture Radar imagery. Journal of Volcanology and Geothermal Research, 289, 81–113. https://doi.org/10.1016/j.jvolgeores.2014.10.010

Roman, D. C., & Cashman, K. V. (2006). The origin of volcano-tectonic earthquake swarms. Geology, 34(6), 457. https://doi.org/10.1130/G22269.1

Rubin, A. M. (1995). Propagation of Magma-Filled Cracks. Annual Review of Earth and Planetary Sciences, 23(1), 287–336. https://doi.org/10.1146/annurev.ea.23.050195.001443

Salzer, J. T., Nikkhoo, M., Walter, T. R., Sudhaus, H., Reyes-DÃ¡vila, G., BretÃ³n, M., & ArÃ¡mbula, R. (2014). Satellite radar data reveal short-term pre-explosive displacements and a complex conduit system at VolcÃ¡n de Colima, Mexico. Frontiers in Earth Science, 2. https://doi.org/10.3389/feart.2014.00012

Segall, P. (2019). Magma chambers: what we can, and cannot, learn from volcano geodesy. Philosophical Transactions of the Royal Society A: Mathematical, Physical and Engineering Sciences, 377(2139), 20180158. https://doi.org/10.1098/rsta.2018.0158

Smith, R., Sammonds, P. R., & Kilburn, C. R. J. (2009). Fracturing of volcanic systems: Experimental insights into pre-eruptive conditions. Earth and Planetary Science Letters, 280(1–4), 211–219. https://doi.org/10.1016/j.epsl.2009.01.032

Sparks, R. S. J. (2003). Forecasting volcanic eruptions. Earth and Planetary Science Letters, 210(1–2), 1–15. https://doi.org/10.1016/S0012-821X(03)00124-9

White, R., & McCausland, W. (2016). Volcano-tectonic earthquakes: A new tool for estimating intrusive volumes and forecasting eruptions. Journal of Volcanology and Geothermal Research, 309, 139–155. https://doi.org/10.1016/j.jvolgeores.2015.10.020

Yang, X.-M., Davis, P. M., & Dieterich, J. H. (1988). Deformation from inflation of a dipping finite prolate spheroid in an elastic half-space as a model for volcanic stressing. Journal of

Geophysical Research: Solid Earth, 93(B5), 4249–4257.

Zhan, Y., & Gregg, P. M. (2017). Data assimilation strategies for volcano geodesy. Journal of Volcanology and Geothermal Research, 344(Supplement C), 13–25. https://doi.org/10.1016/j.jvolgeores.2017.02.015

Zhan, Y., Gregg, P. M., Chaussard, E., & Aoki, Y. (2017). Sequential Assimilation of Volcanic Monitoring Data to Quantify Eruption Potential: Application to Kerinci Volcano, Sumatra. Frontiers in Earth Science, 5. https://doi.org/10.3389/feart.2017.00108

CHAPTER 5: INTEGRATING RESERVOIR DYNAMICS, CRUSTAL STRESS, AND GEOPHYSICAL OBSERVATIONS OF THE LAGUNA DEL MAULE MAGMATIC SYSTEM BY FEM MODELS AND DATA ASSIMILATION[4]

Abstract

The Laguna del Maule (LdM) volcanic field is a large rhyolitic magmatic system in the Chilean Andes, which has exhibited frequent eruptions during the past 20 ka. Rapid surface uplift (>20 cm/yr) has been observed since 2007 accompanied by localized earthquake swarms and micro-gravity changes, indicating the inflating magma reservoir may interact with a pre-existing weak zone (i.e., Troncoso fault). In this investigation, we model the magma reservoir by data assimilation with InSAR data. The reservoir geometry is comparable to the magma body inferred by seismic tomography, magnetotelluric, and gravity studies. The models also suggest that a weak zone, which has little effect on surface displacement, is important as a fluid transport channel to promote earthquakes and microgravity changes. In particular, concentrated dilatancy within the weak zone facilitates the microfracture formation during reservoir inflation. High-pressure fluid can inject into the weak zone from the magma reservoir to trigger earthquakes, and further migrate upwards to create positive gravity changes by occupying unsaturated storages. The pore pressure will then decrease, halting the seismicity swarm until the next cycle. This "hydrofracturing" process may release some accumulated stress along the magma reservoir delaying an eventual eruption in turn. Besides, the resultant models are propagated forward in time to evaluate potential stress trajectories for future unrest.

[4] Published as Zhan Y., Gregg P. M., Mével H. L., Miller C. A. and Cardona C. (2019) Integrating Reservoir Dynamics, Crustal Stress, and Geophysical Observations of the Laguna del Maule Magmatic System by FEM Models and Data Assimilation. Journal of Geophysical Research: Solid Earth 124, 13547–13562.

5.1 Introduction

Large silicic volcanoes can play host to devastating explosive eruptions that pose significant regional and global hazards (Rymer et al., 2005; Self & Blake, 2008). The unrest phase of large silicic systems can often be prolonged and highly variable from system to system (Hill, 1984; Newhall & Dzurisin, 1989; Lowenstern et al., 2006; Sparks et al., 2012). During an unrest episode, multiple physical and chemical processes are involved reflecting complicated interactions between magma reservoir, hydrothermal system, and even regional tectonics (Bacon, 1985; Newhall & Dzurisin, 1989; Hutchison et al., 2016). However, not all unrest episodes are followed by eruptions (Tilling, 2008; Moran et al., 2011; Trasatti et al., 2011; Sparks et al., 2012). Understanding the mechanism and evolution of volcanic unrest is one of the great challenges in volcanology, and it is critical for deciphering the behavior of an active volcano and forecasting the onset of devastating eruptions (Acocella, 2014).

The Laguna del Maule (LdM) volcanic field in the Southern Volcanic Zone of the Andes, is a large rhyolitic magmatic system formed at least 1.5 Ma ago with numerous rhyolitic eruptions during the past 20 ka (Fig. 5.1a; Hildreth et al., 2010; Singer et al., 2014, 2018; Andersen et al., 2017, 2018). A significant uplift rate (> 20 cm/yr), attributed to an inflating magma reservoir has been observed since 2007 revealed by Interferometric Synthetic Aperture Radar (InSAR) and Global Navigation Satellite System (GNSS) data (Fig. 5.1b; Fournier et al., 2010; Feigl et al., 2014; Le Mével et al., 2015). A variety of geophysical methods have been applied to evaluate the location and architecture of the LdM magma system (Fig. 5.1b), including gravity (Miller et al., 2017a), magnetotellurics (MT; Cordell et al., 2018), and seismic tomography (Wespestad et al., 2019). Additionally, recent microgravity (Miller et al., 2017b) and seismicity (Cardona et al., 2018) investigations suggest that fluid migration coinciding with the Troncoso fault zone may be interacting with the magma reservoir during the recent unrest

episode. However, the potential hydrothermal system is not visible through any hydrothermal surface activities (Andersen et al., 2018) or ground deformation (Le Mével et al., 2015). A unifying model that links the unrest observations of rapid surface deformation, seismicity, and microgravity change is needed to evaluate the evolution of the magma system and its potential for eruption. Therefore, the Laguna del Maule volcanic field provides an excellent location to test numerical models for synthesizing a variety of observations to investigate the unrest of a large silicic magmatic system.

Numerical modeling techniques such as finite element method (FEM) and discrete element method are commonly used to study the volcanic deformation and crustal dynamics. Previous efforts and model development provide a framework for evaluating additional complexities in (1) magma system geometry (e.g. Trasatti et al., 2003; Fukushima et al., 2005; Ronchin et al., 2013; Hickey et al., 2015), (2) rheological heterogeneities (e.g. Currenti et al., 2007; Masterlark, 2007; Long & Grosfils, 2009; Manconi et al., 2010; Gregg et al., 2012, 2013; Charco & Galán del Sastre, 2014; Masterlark et al., 2016), (3) inelastic behavior (e.g. Jellinek & DePaolo, 2003; Del Negro et al., 2009; Gregg et al., 2012, 2013; Segall, 2016), (4) gravitational loading (e.g. Grosfils, 2007; van Wyk de Vries & Matela, 1998), (5) failure propagation (e.g. Gerbault et al., 2012, 2018), (6) thermal and hydrothermal effects (e.g.Fournier & Chardot, 2012; Gregg et al., 2012, 2013; Hickey et al., 2015), and (7) interaction with recharging magma (e.g. Le Mével et al., 2016; Gregg et al., 2018; Segall Paul, 2019). The recently collected datasets (geodesy, seismology, gravity, and MT) at LdM allow us to constrain an advanced model. Therefore, we focus on the use of numerical models to consider the interplay between modeled thermal structure, gravitational loading, rheological heterogeneity, and rock failure to link the

variety of observations and better understand the complicated magmatic system of the LdM volcanic field.

In this study, a series of 3D FEM models are applied to simulate the volcanic deformation of the LdM volcanic field inferred by geodetic data. Further, calculations based on the FEM models are applied to interpret other geophysical data such as gravity and seismicity. First, a best-fit magma reservoir geometry is determined using statistical data assimilation to evaluate the InSAR observations. The best-fit geometry inferred by the geodetic data is then compared with seismic tomography, gravity, and magnetotelluric data. Second, the overpressure of the magma reservoir is calculated based on the best-fit geometry and the observed deformation trajectory derived from InSAR and GNSS (Le Mével et al., 2015). Third, the effects of a pre-exiting weak zone (i.e., the Troncoso fault) on the volcanic deformation is tested. Fourth, failure development in the host-rock is calculated to illustrate that an increase in pore fluid is necessary to explain the observed seismicity and gravity change. Fifth, the modeled stress and strain state is evaluated to investigate a hydrofracturing process with fluid migration to further explain the seismicity and microgravity change. Finally, by developing a comprehensive understanding of the magmatic-hydrothermal system, the current and future unrest trajectory of the LdM volcanic field is evaluated.

5.2 Magma body architecture

5.2.1 InSAR data

InSAR data are used to constrain the geometry of the magma reservoir pressure source. Five InSAR tracks are analyzed by GMTSAR (Sandwell et al., 2011), including two ALOS tracks (112 and 113) and three Terrasar-X tracks (111, 119, and 28), covering different time intervals between 2007 and 2016. The LOS displacement time series of each track is calculated following a small-baseline subset technique (Berardino et al., 2002) as implemented in the

Generic InSAR Analysis Toolbox (GIAnT; Agram et al., 2012). The stratified tropospheric artefacts are estimated using the PyAPS (Jolivet et al., 2011, Agram et al., 2012) module implementing interferometric phase delay corrections from the ERA-interim weather model (available from European Center for Medium-Range Weather Forecast). Other potential sources of uncertainties in the InSAR signal include orbital errors and ionospheric delays which are not accounted for in this study but cannot be responsible for the observed fringe pattern (Feigl et al., 2014).

The location and geometry of the large silicic magma reservoir in LdM have not changed significantly during the past decade according to the InSAR data spanning 2007 to 2016. We, therefore, normalize all five InSAR velocity maps to their maximum values keeping the information of deformation patterns only. Since these five normalized maps are in different InSAR looking angles, the geometry of the magma reservoir can be well constrained. The normalized velocity maps are further down-sampled to 500±50 sampling points by the quadtree algorithm (Zhan & Gregg, 2017) to feed the data assimilation (Section 5.2.3).

5.2.2 Physical models of the Laguna del Maule magmatic system

The physical models of the LdM magmatic system are built and calculated using COMSOL Multiphysics 5.3. The ellipsoid magma reservoir model has been well benchmarked with analytical solutions (e.g., Gregg et al., 2012; Zhan and Gregg, 2017). We model the crust of the study area using a 100x100x30 km box (Fig. 5.2a) centered at the Laguna del Maule lake (36.058°S, 70.492°W). No InSAR evidence supports the existence of multiple deformation centers. The magma chamber is treated as one pressurized spheroid described by location (X, Y, and Z), size (R1 and R2), dip direction (φ), and dip angle (θ), whose set up is similar to Yang et al (1988)'s ellipsoid analytical model. A data assimilation framework, described in Section 5.2.3, is used to determine the geometric parameters of the magma body. A roller-type boundary

condition is defined at the bottom and lateral edges of the box. Gravity is included as a prescribed body force, and the system is assumed to be in lithostatic equilibrium. An overpressure (OP) in excess of the lithostatic pressure is defined along the boundary of the spheroid to create the inflation. The overpressure is estimated from observed surface uplift at GPS-MAU2 using the best-fit geometry of the magma chamber in Section 5.3.

The rheology of the model is governed by the linear elastic equation. The Young's modulus (E_{Td}) is temperature and depth dependent. We assume the Young's modulus decreases by more than 50% near the magma chamber due to the rising temperature (Smith et al., 2009). An exponential smoothing function is used to estimate the Young's modulus (E_{Td}) such that:

$$\boldsymbol{E_{Td} = E_d * \left[1 - \frac{1}{2} * \exp\left(\frac{T}{T_c} - \frac{z}{T_c} * \frac{dT}{dz} - 1\right)\right]}. \quad (5.1)$$

The temperature (T) is calculated considering the heat conduction of an 850 °C (T_c) magma body (Singer et al., 2014) in the crust with a high geothermal gradient (Currie & Hyndman, 2006, dT/dz = 30 °C/km; Fig. 5.2b). The thermal conductivity ($\boldsymbol{K_c}$) and specific heat capacity ($\boldsymbol{C_p}$) are assumed constants for simplification, which are not important as we assume the model reaches thermal equilibrium. The far-field Young's modulus without a hot magma reservoir is assumed to vary as a function of depth inferred by the seismic velocity models in this region (Bohm et al., 2002; Ciccotti, & Mulargia, 2004; Cardona et al., 2018; Fig. B.1), which is defined as:

$$\boldsymbol{E_d = D_1 * z^2 + D_2 * z + D_3} \quad (5.2)$$

The constants and variables in Equation (5.1) and (5.2) are listed in the Table B.1 and B.2. Although the Young's modulus is varied, the first stage of the modeling approach does not consider pre-existing weak zones. The strategy of modeling a weak zone is discussed in Section 5.4.

5.2.3 Magma body geometry estimation by data assimilation

We use the Ensemble Kalman Filter (EnKF) data assimilation method to determine the magma body geometry and pressurization. The EnKF solves the Bayesian update problem using a Monte Carlo method (Evensen, 2003). We follow the same strategy developed in previous studies using the EnKF method to model volcanic deformation (Fig. 5.3; Gregg & Pettijohn, 2015; Zhan & Gregg, 2017; Zhan et al., 2017; Bato et al., 2017, 2018; Albright et al., 2019). The EnKF analysis updates the physical model ($\boldsymbol{A^a}$) by:

$$\boldsymbol{A^a = A + P_e H^T (H P_e H^T + R_e)^{-1} (D - HA)}, \tag{5.3}$$

where A is a matrix containing the parameters and states of all ensemble models whose covariance matrix is P_e. In this study, the parameters in A matrix are the geometry parameters describing the magma body (Fig. 5.2a), and the number of the ensemble models is 256. The model states are the calculated surface deformation. D is a matrix of perturbed measurements whose covariance matrix is R_e, and H is the mapping matrix (Evensen, 2003). The observation in the D matrix is the down-sampled InSAR data. At each iteration, four ensemble models are assigned to run on one physical CPU on the Bluewater Supercomputer and total of 64 CPUs are used (Fig. B.2). The results start to converge after 20 iterations, and the overall calculation takes ~8 hours to complete all 100 iterations.

The geometry of the magma body is determined by the EnKF using the normalized InSAR velocity maps as input data (Fig. 5.3a). An ellipsoid pressure source reproduces the deformation patterns revealed by InSAR (Fig. 5.3b). The overall misfits between data and models are less than 10% and are even less where the ground has uplifted significantly in the central part of the LdM volcano field (Fig. 5.3c). Negative misfit values show residuals in the area of uplift to the SW of the basin (Fig. 5.3c) and could be attributed to localized deformation

(subsidence) and/or orbital artefacts not taken into account by the simple pressurized ellipsoid model.

The ellipsoid pressure source parameters from the 256 EnKF ensembles exhibit a Gaussian distribution (Fig. B.3). The final iteration shows that the pressure source is an oblate ellipsoid slightly dipping to the West (268±6°) by 16±3°. The center of the ellipsoid is located 4.78±0.08 km below the surface near GPS station MAU2 (X = -3.23±0.16 km and Y = -0.84±0.16 km). The half-height of the ellipsoid is 1.46±0.03 km and the half-width is 5.43±0.14 km. The mean parameter values are used to build the best-fit model of the pressure source (Fig. 5.4). Since in the first stage, the numerical modeling does not incorporate a fault zone. The best-fit model is named as Model-NF (No Fault).

5.2.4 Comparison with other observations

The magma reservoir model provides a geometry comparable to previous sill models (Fig. 5.1b) inferred by the InSAR and GNSS data (Feigl et al., 2014; Le Mével et al., 2015). Both the sill model determined by previous inversions and our best-fit model which is a highly oblate ellipsoid create a similar deformation pattern. The center of our ellipsoid model offsets the center of the previously determined sill model by < 1 km (Fig. 5.1b), and the dipping direction of the ellipsoid is also similar (i.e., dipping SW by a low angle <20°). The ellipsoid chamber is larger than the previous determined sill source, since to create similar deformation pattern spherical sources usually need to be larger than a rectangular source (e.g., Okada, 1985; Yang et al., 1988).

The location of our best-fit model agrees with the region of low shear wave velocity (low-Vs) (Wespestad et al., 2019) and also overlaps with the low-density zone inferred by gravity data analyses (Miller et al., 2017a). The low-Vs body is roughly a NE-SW elongated ellipsoid dipping to the West (Wespestad et al., 2019), overlapping the west part of our pressure

source (Fig. 5.4). The center of the low-density body and the low-Vs body are offset by 3-4 kilometers. The lower part of the low-density body is overlapping with the central part of our model (Fig. 5.4). The magnetotelluric (MT) data shows no obvious electric conductors at the location of the pressure source, low-Vs zone, or low-density zone (Cordell et al., 2018; Fig. B.4). A large conductor C3 (Fig. B.4) is present at depth beneath our modeled pressure source, which may represent a deeper recharging process (Anderson et al., 2018). To the south of the conductor C3, a weak conductor along the trace of the Troncoso fault is recognizable from 1.2 km to 5 km, indicating the fault may contain low resistivity fluids.

The inconsistency in the magma reservoir geometries from the different geophysical methods likely results from the complexity of the magma reservoir itself. Petrological and geochemical evidence suggests that the magma reservoir at LdM is a heterogenous crystal-mush that is predominantly a crystal-rich magma with some portions of high melt fraction (Hildreth et al., 2010; Singer et al., 2014; Andersen et al., 2017, 2018). Due to the heterogeneity of the magma reservoir, the physical properties can vary significantly spatially. Each geophysical method is sensitive to one or several physical properties and may only image a part of the crystal-mush. For example, about 9% melt fraction is needed to create 15% shear wave anomaly (Flinders & Shen, 2017), while very little melt fraction (~2%) is needed to wet grain boundaries and provide connectivity for a crystal-mush to share the same pressure (Zhu et al., 2011). As such, calculated pressure sources derived from geodetic data may be larger than the extent of low-Vs bodies. Similarly, a small fraction of melt (~2%), which significantly increases electric resistivity if connected, will not necessarily result in a lower density or lower seismic velocity. Future studies are necessary to explore geophysical observations of magma reservoirs from a heterogenous, crystal-mush perspective.

5.3 Overpressure evolution and extrapolation

The normalized InSAR data constrains the geometry of the magma pressure source where overpressure is defined as the pressure above lithostatic along the assumed magma chamber boundary. InSAR data are assimilated to calculate a best-fit magma reservoir model (Model-NF; Fig. 5.4). The overpressure history of the magma body is then determined to reproduce the modeled displacement at GPS-MAU2 (Fig. 5.5; Le Mével et al., 2015; Singer et al., 2018). To further forecast the possible behavior of the LdM magmatic system in the next decade, the overpressure evolution is extrapolated using both a linear and cubic trend (Fig. 5.5). The linear and cubic trajectories represent two end-member conditions, which are (a) a constant or gradually decreasing mass flux into the magma reservoir, and (b) an increasing mass flux (Gregg et al., 2018). Actually, the cubic trend is an extreme case which can hardly happen in a real magmatic system.

Based on the best-fit model (Model-NF), the overpressure is calculated to create the same amount of uplift at GPS-MAU2 as the results in the previous studies (Le Mével et al., 2015; Singer et al., 2018). The uplift at MAU2 from 2007 to 2016 is about 2.1 m. The overpressure required to create the surface uplift is about 6.3 MPa according to the best-fit geometry. To test the stability of the magma body in the future, we extrapolate the overpressure after 2016 by both linear trend and cubic trend (Fig. 5.5). The failure of host-rock will be discussed in the Section 5.5.

5.4 Effect of the Troncoso fault on surface deformation

5.4.1 Adding weak zone to the best-fit model

Although there is no observable surface displacement associated with regional faulting (Fournier et al., 2010; Feigl et al., 2014; Le Mével et al., 2015), previous research indicates a pre-existing weak zone associated with the Troncoso fault may play a role in triggering

seismicity and gravity changes (Cardona et al., 2018; Miller et al., 2017b). To further discuss the effect of the Troncoso fault on the pressurization of the magmatic system, the fault is incorporated into the model as a vertical thin slat embedded in the host-rock (Fig. 5.2a). The magma reservoir and the overpressure serve as the initial model stress state for the fault models. The trace of the fault follows the strike of the canyon to the SW of lake and is also inferred by the observed seismicity (Fig. 5.1a). The strike of the fault in the model coordinate system is defined as

$$\boldsymbol{Y = \frac{20}{17}(X - 18) + 20 \ \ \left(if - 30 < X < -D_f\right) \ (km)}, \tag{5.4}$$

where $\boldsymbol{D_f}$ is the distance between the NE end of the fault and the center of model, whose value is tested in the models. Combinations of the different fault parameters are varied to investigate their effects on the surface deformation pattern (Fig. 5.6). The Young's modulus within the fault zone is assumed to be proportional to its surrounding host rock. The ratio of Young's modulus between the fault and the host-rock is defined as $(\frac{\boldsymbol{E_f}}{\boldsymbol{E_r}})$ and is varied to test the sensitivity of the model results to the chosen ratio. In addition, the thickness ($\boldsymbol{W_f}$) and depth ($\boldsymbol{H_f}$) of the fault zone are tested (Fig. 5.2a).

5.4.2 Fault parameter constraints derived from synthetic tests

A series of synthetic models are run with the varying fault setups to create a predicted deformation signal for an interferogram of ALOS data (unit vector = [-0.6242, -0.1851, 0.7590]) spanning three years from 2007 to 2010. Since the observed satellite data (Fig. 5.6c) show line-of-sight fringe offset associated with the fault zone is less than 500 m, any model which creates significant fringe offsets larger than 500 m due to the addition of a mechanically weak zone can be ruled out.

The perturbation of the surface displacement shows different sensitivities to different

fault parameters. The assumed Young's moduli and fault zone widths have the greatest impact on the predicted surface deformation. When Young's modulus of the fault is 20% lower than that of the surrounding host-rock, the fringes of synthetic interferograms are significantly offset (Fig. 5.6a). Therefore, Young's modulus of the fault should be 20-100% of the surrounding rock. A similar decoupling effect can be also observed when the width of the fault zone is increased (Fig. 5.6a), suggesting the fault zone must be < 200 meters. However, the synthetic interferograms are not sensitive to the assumed depths and distance-to-center of the fault (Fig. 5.6b). For Young's modulus and fault zone width, the parameters of Model-E5W1 ($\frac{E_f}{E_r}$ = 1/5, W_f = 100 m) are chosen in the further tests of stress, failure, and pore fluid. This model represents an end member in which the weak zone can have the maximum effect on stress field but still fit the surface deformation observations. Since the InSAR data cannot constrain depth and distance-to-center of the fault, we assume Hf is 7 km and D is 0 km (Model-H7D0; same as Model-E5W1), according to the distribution of earthquakes (Fig. 5.7).

5.5 Failure of the host-rock without pore fluid

5.5.1 Failure criterion

Similar to Zhan and Gregg (2019), host-rock failure initiates as the overpressure of the magma reservoir is increased. The occurrence of Coulomb failure or tensile failure can be predicted by

$$\tau > C_0 \cos\phi_i + \sigma_n \sin\phi_i, \tag{5.5}$$

or

$$-\sigma_3 > T_0, \tag{5.6}$$

where σ_n and τ are the normal and maximum shear stresses. The internal friction angle is assumed to be a constant (ϕ_i = 25°; Grosfils, 2007) and its variation does not have a large effect

on forecasts of failure compared to geometry, Young's modulus, and rock strength (Zhan and Gregg, 2019). C_0 and T_0 are the rock's cohesion and tensile strength which are proportional to its Young's modulus (Aggistalis et al., 1996; Dinçer et al., 2004), such that the cohesion is defined as:

$$C_0 = E \times 5 \times 10^{-4} \text{ and } T_0 = E \times 10^{-4}. \quad (5.7)$$

5.5.2 Failure prediction

Failure is calculated in four tests, including: (1) a model without a weak fault zone (Model-NF, described above) with a linear overpressure (OP) trajectory (Fig. 5.7a); (2) a model with a fault zone (Model-E5W1) with a linear OP trajectory (Fig. 5.7b); (3) a model without a fault zone with a cubic OP trajectory (Fig. 5.7c); and (4) a model with a fault zone with a cubic OP trajectory (Fig. 5.7d). For all of the models, both the Coulomb failure and tensile failure are more likely to initiate at the surface above the magma reservoir due to a lower confining pressure at the shallow depth. Using a linear overpressure buildup, the magma reservoir is not predicted to fail in the next 20 years for both the models with and without a fault zone (Fig. 5.7a and b). When a cubic overpressure buildup is assumed, the magma reservoir experiences tensile failures around 2025 when the overpressure exceeds 21 MPa, regardless of the presence of a weak fault zone (Fig. 5.7c and d). The initial point of tensile failure always happens at the NE edge of the magma reservoir, since it is closer to the surface and under lower confining pressure (Fig. B.5). In 2030, through-going Mohr-Coulomb failure is predicted to connect the chamber edge and the surface of the model when the overpressure excesses 50 MPa (Fig. 5.7d). Failure can initiate earlier if the stress derived from previous eruption cycles is not totally released. However, we suggest that the initial stress prior to 2007 is not significant, although 62-m uplift has been accumulated over 9,400 years (Singer et al., 2018). If the total deformation is composed of

similar rapid-uplift events as observed during the 2007-present unrest, more than 15 rapid-uplift episodes are needed to create the total deformation signal. The recurrence interval would be more than 600 years (Singer et al., 2018), which is long enough for the stress associated with the uplift event to relax since the maximum relaxation time for a warm crust (~350°C) is about 100 years (Zhan and Gregg, 2019).

Besides, the structure of Young's modulus used in the models will also affect the failure forecasts. If we underestimate the Young's modulus, the real overpressure to create the same surface deformation will be higher than the model prediction (Zhan and Gregg, 2019). Our model predicts higher Vp and Vs than the regional velocity models above 5 km (Fig. B.1), which rules out the possibility of a significant underestimation of the Young's modulus. If we overestimate the Young's modulus, the real overpressure will be lower than the model, which means the failure will be even less likely to occur. The assumption of Poisson's ratio may also introduce bias in the model. However, Poisson's ratio has a much smaller effect on forecasting failure than Young's modulus (Zhan and Gregg, 2019).

5.5.3 Effect of the Troncoso fault on failure development

The pre-existing weak zone generates two opposing effects on failure accumulation. On one hand, the low Young's modulus of the weak zone leads to low shear stress concentration (Fig. B.6), prohibiting failure development. On the other hand, the weak zone exhibits a low rock strength, facilitating failure development. At a shallow depth (< ~2 km), the effect of rock strength is dominant. More failure is generated inside the weak zone (Fig. 5.7b). At deeper levels (> 2 km), the low stress concentration of the weak zone keeps rocks from failing (Fig. 5.7d). However, the existence of the pre-existing weak zone does not motivate failure near the SW edge of the magma reservoir, but instead makes failure harder to generate. Therefore, under dry rock

conditions modeled here, the weak zone created by the Troncoso fault does not appear to be the reason for the observed seismicity.

5.6 Effects of the pore fluid on predicted seismicity and gravity

5.6.1 A pore pressure catalyst for seismicity

From previous discussion, we find failure difficult to generate near the SW edge of the magma reservoir where earthquake swarms were frequently observed during 2011-2015 (Cardona et al., 2018; Fig. 5.7a). Miller et al. (2017b) suggest a possible hydrofracturing event inferred by microgravity change may explain the earthquake swarms. MT data also indicate that the Troncoso fault zone is one of the weak conductors, indicating fluids may be present in the fault zone (Fig. B.3; Cordell et al., 2018). To investigate this mechanism, we calculate the pore pressure required to trigger the rock failure to investigate whether the pore fluid can trigger the earthquakes in this region.

The minimum pore pressure required to initiate Coulomb failure (P_w^C) and tensile failure (P_w^T) is calculated by Terzaghi (1951) equations:

$$P_w^C = \sigma_n - (\tau - C_0^f \cos\phi_i)/\sin\phi_i, \tag{5.8}$$

$$P_w^T = T_0^f + \sigma_3, \tag{5.9}$$

where C_0^f and T_0^f are cohesion and tensile strength of the fault zone, whose values are much lower than the surrounding host-rocks. Two models with different cohesion and tensile strength are tested. The first model is a "crack sliding" model with zero cohesion. The cracks within the fault start to slide when the pore pressure is high enough (Fig. 5.8a). In this model, only crack sliding can happen, which is similar to Coulomb failure. The second model is the "weak cohesion" model, where the cohesion (C_0^f) is ~ 1 MPa and the tensile strength (T_0^f) is ~ 0.2 MPa (Fig. 5.8b) assuming Young's modulus and rock strengths of the fault zone follow the

relationship described by equation (7). In this model, tensile failure and Coulomb failure can happen in different parts of the model depending on the stress states.

For both the "crack sliding" model and "weak cohesion" model, the pore pressure required to initiate failures increases with depth from near 0 MPa at the surface to about 200 MPa at a depth of 7 km (Fig 8a and b). The pore pressure is about 160 MPa at the average depth of the earthquake swarms. The pore pressure is mainly controlled by the normal stresses (Fig. B.5) which is consistent with the lithostatic stress and much higher than the maximum shear stresses ($\boldsymbol{\tau}$) (Fig. B.6). In the "crack sliding" model, the increasing pore pressure triggers a Coulomb type failure (Fig. 5.8a). While, in the "weak cohesion" model, the Coulomb failure is triggered around the chamber edge and near the surface (Fig. 5.8b), where the maximum shear stresses are roughly larger than the cohesion of the fault zone. For the most part of the "weak cohesion" model, only tensile failure can be triggered with an increasing pore pressure. The observed failure along the surface of the model ("Already failed" zone in Fig. 5.8a & b) can be generated with zero pore pressure due to inflation of the magma reservoir and a low least compressional stress. However, this subsurface failure zone is not associated with earthquakes, likely because the models neglect the effect of topography. Laguna del Maule lake has a low elevation compared to the surrounding area. The flat surface assumption in our models can lead to an underestimation of the least compressional stress (McTigue and Mei, 1981), which drives the Mohr circle closer to the failure envelope (Fig. 5.8).

5.6.2 "Hydrofracturing" process

From the pore pressure calculation, we know that the pore pressure must be > ~160 MPa to trigger the earthquakes near the SW edge of the magma reservoir. This "hydrofracturing" process can only occur when two requirements are fulfilled at the same time. First, the pore fluid must be injected into the region where the seismicity is observed. Second, the pore pressure must reach

160 MPa to trigger earthquakes. We argue that the pore fluid may be directly generated by the differentiation of the magma in the reservoir or transported from a deeper source (e.g., electric conductor C4 in Fig. B.3; Cordell et al., 2018). Therefore, the pore fluid may experience the pressure from the magma reservoir, which can be equal to or larger than the minimum pore pressure required, even if the pressure is diffused. However, why does the pore fluid inject laterally to trigger the seismicity next to the SW edge of the magma chamber?

To explain the diffusion pattern of the pore fluid, we calculate the volumetric strain of the fault zone (Fig. 5.8c). The predicted volumetric strains due to a pressurized magma chamber are favored to accumulated within the fault zone (Fig. B.7) since the fault zone is more deformable. The fractured rock near the surface above the chamber exhibits the highest volumetric strain increment (Fig. 5.8c). The SW edge of magma chamber also concentrates positive volumetric strain, while the roof of the magma chamber is dominated by negative volumetric strain. In this study, we are using linear elasticity but with lower Young's moduli and higher Poisson's ratio to simulate the behavior of the fault zone. In reality, the fault zone should behave inelastically. The volumetric strain increment may approximately represent the opening or connection of microfractures, which will cause a permeability increase. However, the roof of the magma reservoir is experiencing a decrease in volumetric strain indicating the closure of microfractures and a reduction in permeability. Therefore, the fluid is more likely to inject laterally into the fractured rock with higher permeability to the SW edge of the reservoir.

The pore pressure at the SW edge of the reservoir should be equal to the pressure of the magma which is the sum of lithostatic pressure and magma overpressure. Since the pore pressure required to initiate the crack sliding model is lower than the lithostatic pressure, seismicity can be triggered near the SW edge of the chamber. The pore pressure of the fault decreases away

from the magma reservoir due to diffusion (e.g. Talwani & Acree, 1985; Scholz, 2019) and/or the drop of the permeability where the fault zone is no longer dilatant (Mitchell & Faulkner, 2008; Zhang et al., 2008). Therefore, earthquakes at a distance from the magma reservoir cannot be triggered. However shallower earthquakes are also observed (Cardona et al., 2018), which indicates the fluid may also inject upward. This observation agrees with the volumetric strain calculation, since more "dilatancy" occurs at the shallow depth with the fault zone (Fig. 5.8c), which is also consistent with a shallow high electric-conductivity area (C2 in Fig. B.4; Cordell et al., 2018). Although the pore pressure will decrease at distance from the reservoir, the pore pressure required to trigger earthquakes is also much lower at shallow depth. Therefore, shallower earthquakes can still be triggered during the upward injection of the fluid.

In addition, we calculate the principal stress directions of the fault zone (Fig. 5.8d) to predict the focal mechanism of the earthquakes. North-South trending extension is dominant at the lower part of the fault southwest to the magma reservoir (Fig. 5.8d), which is consistent with both direction and location of the focal mechanism observations for well-located VT events (Figure 9 in Cardona et al., 2018).

5.6.3 Microgravity changes due to fluid migration

From the discussion above, we suggest that pore fluid migration triggered the observed earthquake swarms. We further suggest that the pore fluid originates from the magma reservoir where it is first injected laterally into the dilatant part of the fault zone at the SW edge of the magma chamber, and then diffuses upward to a shallow dilatant zone. The movement of the fluid is mainly caused by the increasing connectivity of cracks and pores during magma reservoir induced deformation. Therefore, filling newly connected unsaturated cracks and pores with fluid will affect the density of the rock generating an observable gravity change at surface.

Positive microgravity changes (up to 0.1 mGal) have been observed at the NE end of Troncoso fault between 2014 and 2015, which has been previously explained by fluid injection into pre-existing pores at a shallow storage (Miller et al., 2017b). To test this idea, we assume the density of the fault which experiences volumetric strain increment will increase due to fluid injection. The gravity change is generated based on the modeled density increment, which is compared to the microgravity observation (Miller et al., 2017b). The density structure of the model is discretized into a grid of finite prisms (50x50x100 m) to calculate the overall gravitational potential and therefore the gravity change (Blakely, 1995).

We assume that the fluid is water-dominated with a density of 1 g/cm3. We have modeled four density distributions as different functions of the volumetric strain. The first model assumes that the hydrothermal brine fills 10% of the pore space where the volumetric strains are positive (Fig. 5.9e). This model creates a significant gravity anomaly (Fig. 5.9a), which is much greater than the observation (Miller et al., 2017b), suggesting that this model overestimate the density increment due to fluid injection. In addition, the location of the largest gravity change is offset southwest compared to the observation. The second model assumes a threshold volumetric strain (0.01% in this study) is required to connect the unsaturated pores. Therefore, only the fault zone exhibiting the volumetric strain greater than this value will have a uniform density increment of 0.1 g/cm3, which also represents a 10% porosity occupation same as the first model (Fig. 5.9f). This model also shows a gravity change focused along the fault (Fig. 5.9b). The first two models assume that fluid can inject into the unoccupied pores even near the surface. This shallow gravity source makes the wavelength of the gravity anomaly too small. Considering the shallow pores may already be saturated with fluid or some impermeable layers may prevent the new injection, a third model based on the second model is investigated assuming the density does not increase in

the shallow model space above -1 km (Fig. 5.9g). This model predicts a gravity anomaly that is less than 0.1 mGal along the Troncoso fault and its distribution is similar to the observations (Miller et al., 2017b). A fourth model is run assuming a ramp function between density increment and volumetric strain ($\boldsymbol{d\rho = 500\ \varepsilon_V\ \left[\frac{g}{cm^3}\right],\ if\ \varepsilon_V < 0.02\%;\ d\rho = 0.1\ \left[\frac{g}{cm^3}\right],\ if\ \varepsilon_V \geq 0.02\%}$), and no fluid injection above -1 km (Fig. 5.9h). The gravity anomaly calculated by this model is similar to the third model (Fig. 5.9d), consistent with the positive gravity change on the southwest side of the Laguna del Maule lake. All models have limitations in reproducing any gravity changes on the north or east side of the lake where gravity variations may indicate other hydrological processes.

In summary, the inflating magma body promotes dilatancy in some part of the pre-existing weak zone (Fig. 5.8c) by increasing the connectivity of the pre-existing pores or cracks or generating new micro-fractures (Fig. 5.10a). A high-pressure fluid from the magma reservoir injects into the dilatant fault zone triggering seismicity (Fig. 5.10b). The unsaturated rock in the fault zone is filled with the fluid (e.g., hydrothermal brine) to generate a positive micro-gravity change (Fig. 5.10c). In this study, we think the fluid is generated from the magma reservoir, which migrates laterally into the dilatant zone (Fig. 5.10a), and then moved upward along the dilatant zone to shallower depths (Fig. 5.10c). However, we cannot rule out that the fluid present in the shallower dilatant zone may come from other sources (e.g., groundwater). We suggest that crack opening or connection in the pre-existing weak zone due to the inflation of the magma body is the key to trigger fluid migration, earthquake swarms, and gravity change.

5.6.4 Pore fluid: lubricant to eruption or not?

From the failure calculation with zero pore pressure, we know that the magma reservoir is likely to remain stable until the overpressure exceeds 20 MPa. Even if the magma reservoir is

recharged at an increasing mass flux causing the overpressure to increase cubically, the magma chamber will not rupture until 2025 (Fig. 5.5 and 5.7), although we don't think the overpressure will follow the cubic trajectory, since the surface uplift has started to decelerate since 2016 according to the InSAR data (Singer et al., 2018). In addition, stress is more difficult to accumulate in a weak zone, which hinders the occurrence of host-rock failure, the effect of which is to make the magma reservoir more stable. On the other hand, the pre-existing fault can act as a channel for the pore fluid to trigger failure and, therefore, earthquake swarms. Thus, whether the pre-existing weak zone makes the system stable or unstable is not intuitive.

According to our model, the triggering effect of the seismicity and gravity increment is the injection of pore fluid, which is motivated by the dilatancy of the fault zone. The dilatancy is derived from the inflation of the magma reservoir. Therefore, higher inflation rate of the magma reservoir creates a higher surface deformation rate, and, at the same time, more earthquakes and a greater microgravity increment. However, we have not found any correlation among the rate of surface uplift (Le Mével et al., 2015), the accumulative energy of the VT earthquake swarms (Cardona et al., 2018), and microgravity change (Miller et al., 2017), which suggests that the interaction between the magma reservoir and the hydrology of fractured rocks is complicated. Currently, there is no evidence to indicate that the VT earthquake and fluid migration have a significant feedback on the magma reservoir. Actually, the release of stresses during the earthquake swarms may delay the rupture of the SW edge of the magma reservoir. Extended model forecasts indicate that eruption may occur at the NE edge of the chamber, when a through-going failure is triggered (Fig. 7d).

5.7 Conclusions

The best-fit magma reservoir to explain the prolonged surface deformation from 5 InSAR tracks from 2007 to 2016 is an oblate ellipsoid centered at a depth of ~5 km beneath the west LdM lake, which is dipping west at a low angle. The ellipsoid reservoir derived from the pressure source overlaps with tomography and gravity data but is larger than other models, indicating the overpressure may be shared throughout the crystal-mush zone making up the LdM magma system, even where the melt fraction is low. The overpressure of the magma reservoir calculated by InSAR and GNSS data assimilation has increased by 6.3 MPa from 2007 to 2016. Our models indicate that the host rock surrounding the magma reservoir will not fail under this overpressure even if a pre-existing weak zone is introduced. The parameters of the pre-existing weak zone such as stiffness, thickness, depth, and length are tested to recreate the observations. A weak zone with a stiffness 20% lower than the surrounding rock, or a weak zone wider than 200 meters will not reproduce the InSAR deformation observations. By maximizing the effects of the weak zone on the stresses and strains within the constraints of the observations, we investigate the possibility that the Troncoso fault is a facilitator for pore fluid injection, seismicity, and gravity change. Calculated stress and strain along the fault illustrate that the dilatant regions of the fault enable high-pressure fluid to inject triggering earthquake swarms. Furthermore, fluid injection into the porous media due to the dilatancy creates gravity change in line with observations. Fortunately, this “hydrofracturing” process may release some accumulated stress along the magma reservoir delaying eruption.

5.8 Figures

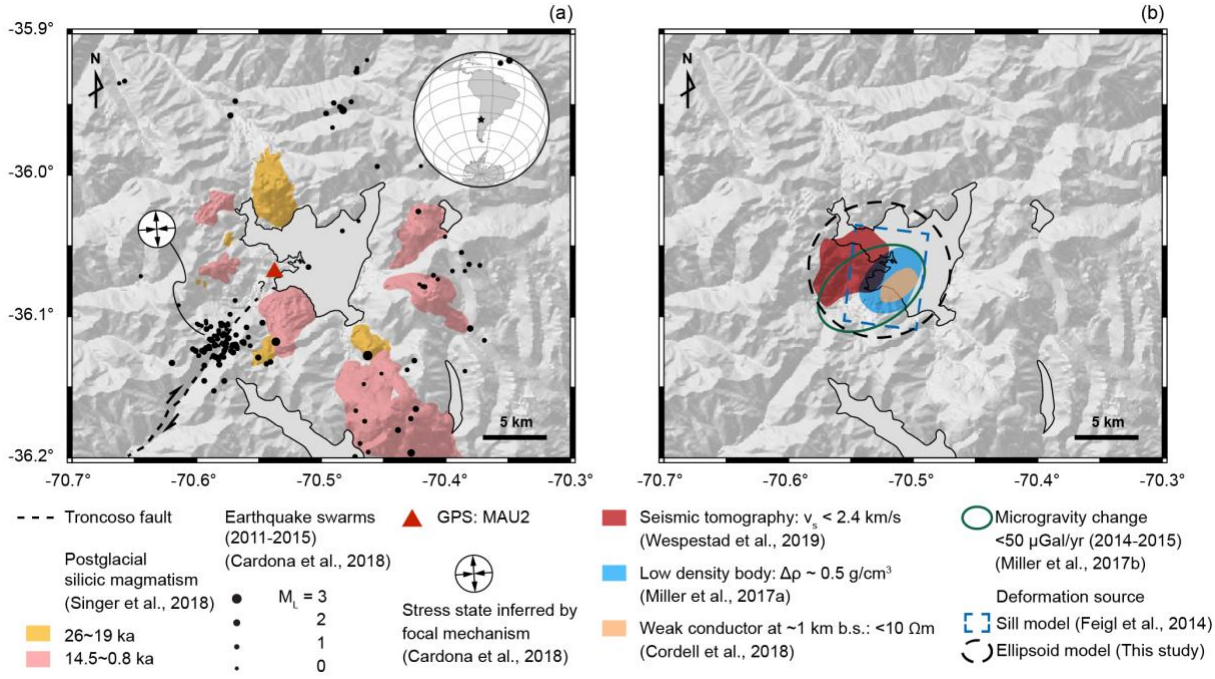

Figure 5.1 (a) Location of Laguna del Maule volcanic field. The shaded colors show the distribution of two episodes of postglacial silicic magmatism (Singer et al., 2018). The star indicates the 2011-2015 VT earthquake swarms located along the Troncoso fault; the dominant focal mechanism of the earthquakes is N-S trending extension (Cardona et al., 2018). (b) Results from previous geophysical investigations. The red and blue shaded regions outline the low S-wave velocity body (Wespestad et al., 2019) and the low-density body (Miller et al., 2017a) shallower than 7 km below surface. The green ellipse outlines the area where gravity changes <0.1 mGal during 2014 (Miller et al., 2017b) are recorded. The surface uplift revealed by InSAR data has been modeled by a sill (Feigl et al., 2014) and an ellipsoid (this study) indicated by the dashed rectangle and circle respectively.

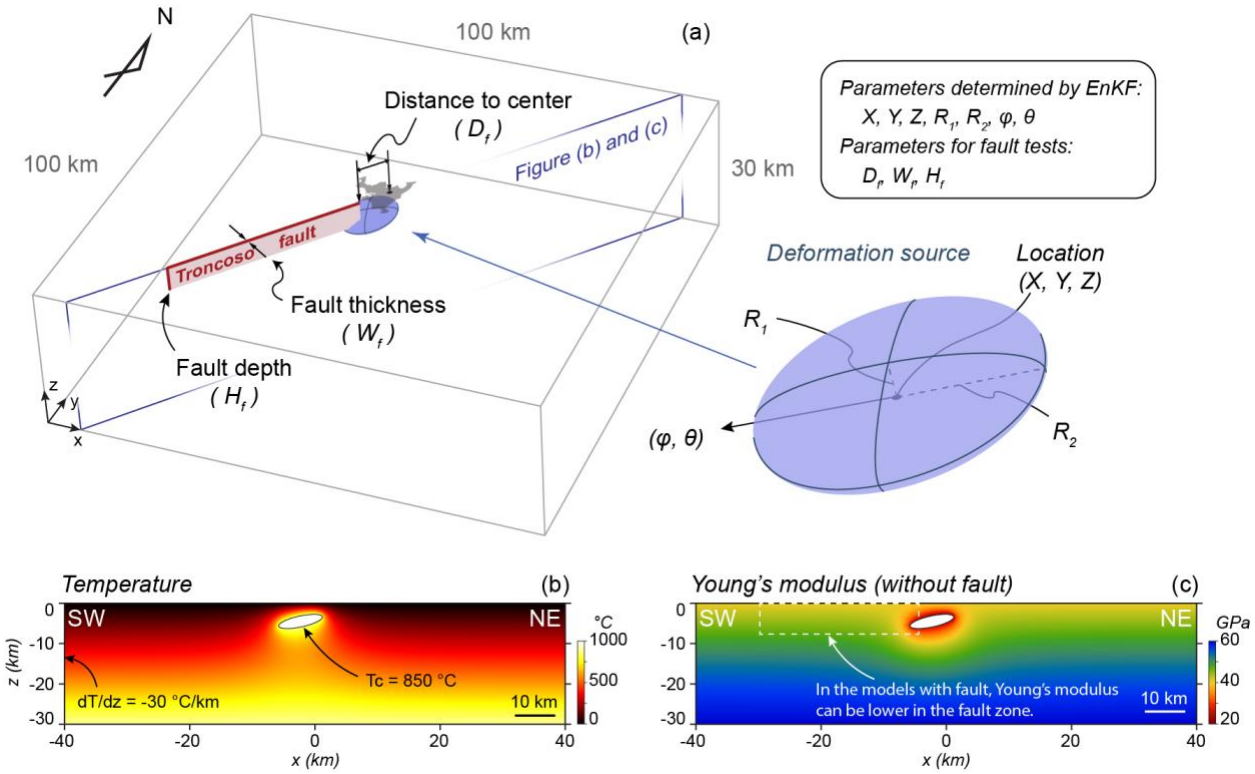

Figure 5.2 FEM model setup. (a) The host-rock of the Laguna del Maule magmatic system is modeled using an elastic solid domain. The magma body is a pressurized, oblate ellipsoid. The Troncoso fault is modeled using a thin vertical slat. The trend of the fault follows the morphological trace of the valley in Figure 5.1a. (b) and (c) are cross-sections of temperature and Young's modulus. In the second stage of modeling (described in Section 5.4) the Young's modulus is further reduced along the Troncoso fault to approximate a weak zone.

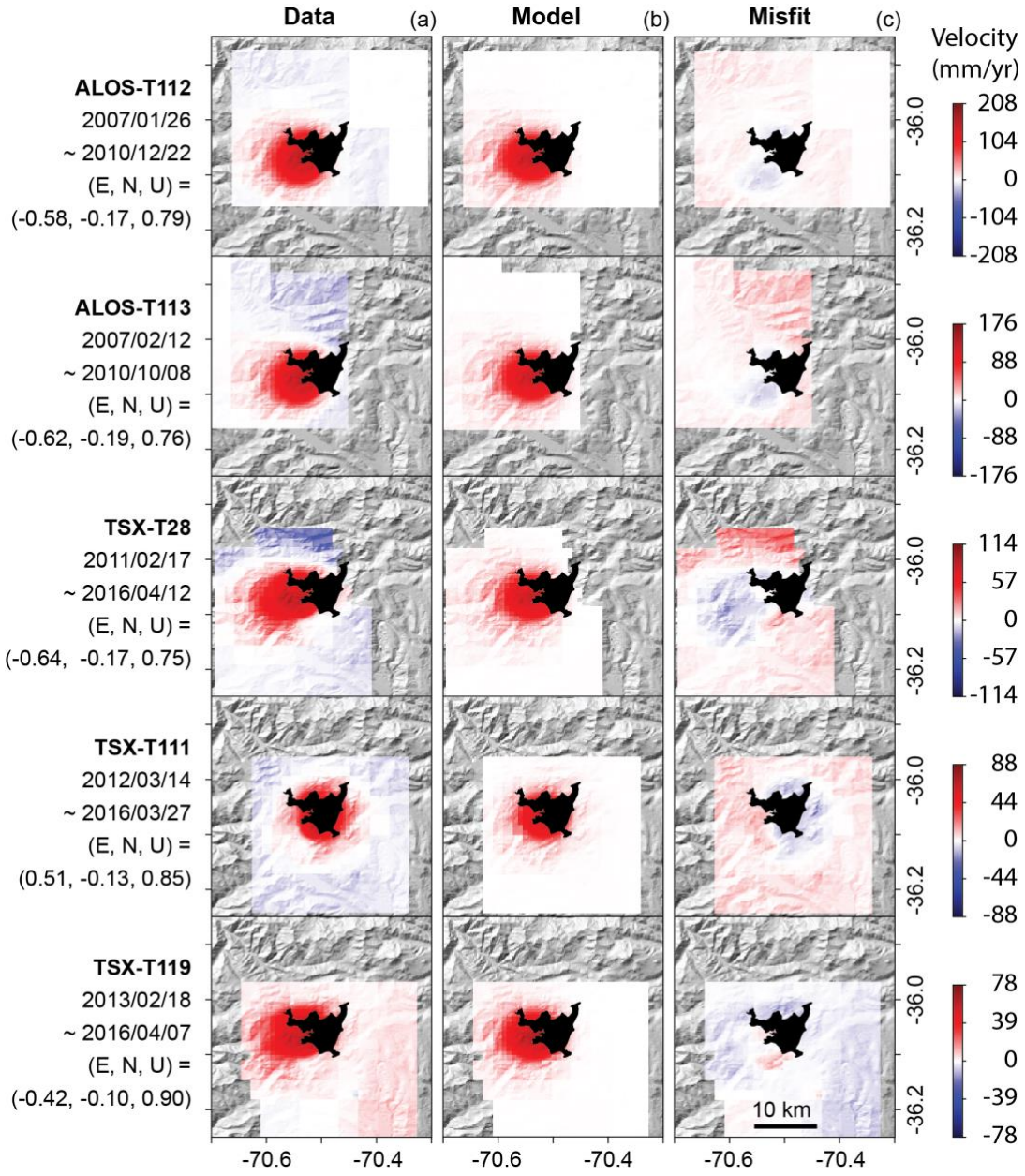

Figure 5.3 Comparison between InSAR data and modeled deformation. Averaged InSAR LOS velocity maps during the time spans are down-sampled using a quadtree algorithm and normalized by their maximum values. The second column shows the best-fit LOS velocity calculated by the EnKF. The third column shows the misfits between modeling results and the data. Each row shows a different InSAR track labeled with its time period and LOS direction as (E, N, U).

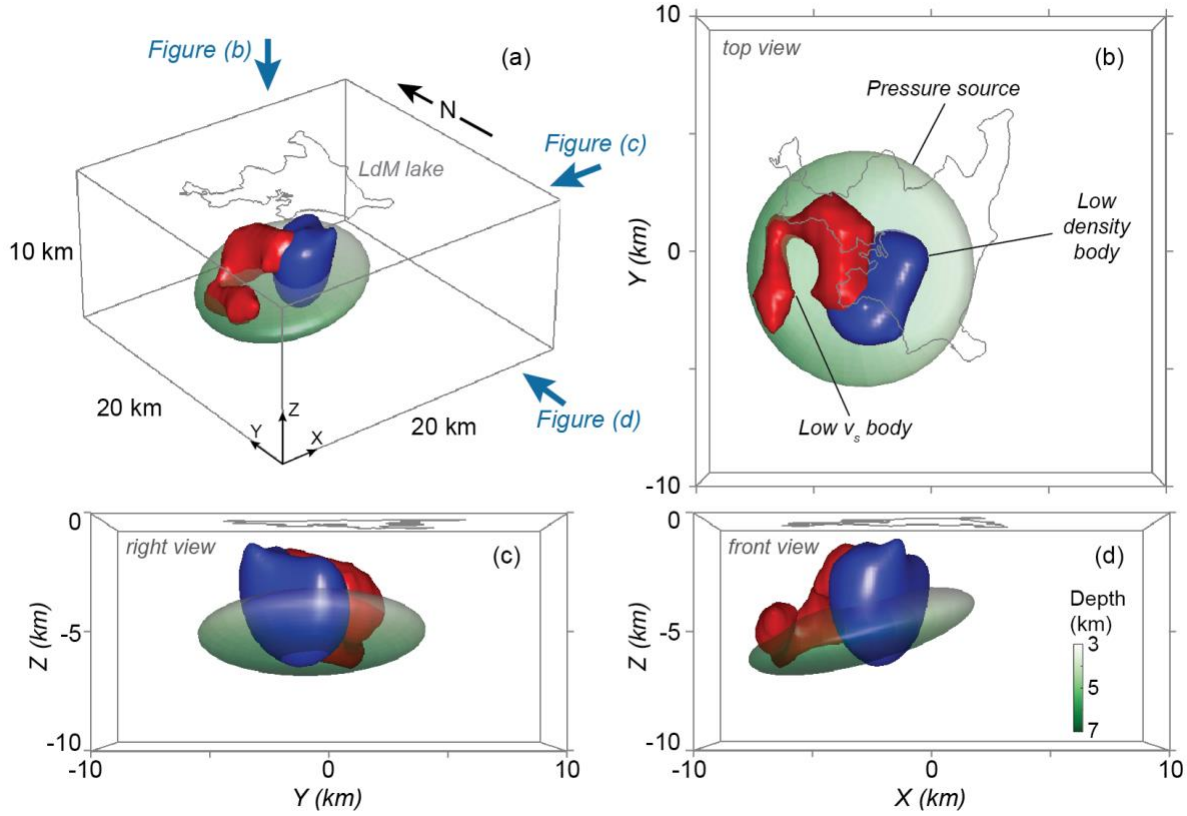

Figure 5.4 3D view of the calculated pressure source (green region) in comparison with the low S-wave velocity body (red region) and low-density body (blue region).

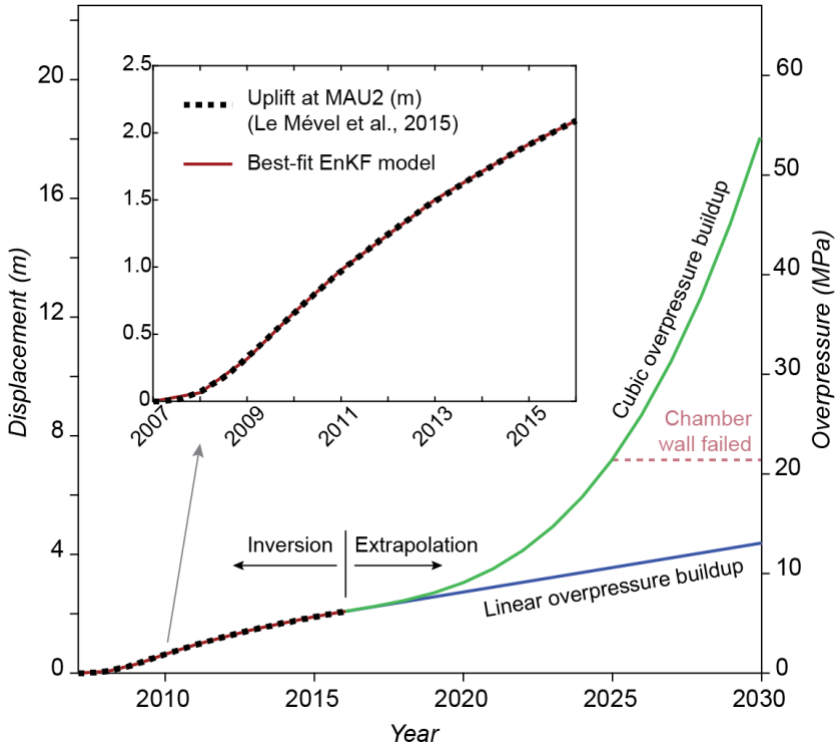

Figure 5.5 Surface uplift and overpressure as a function of time. The magma body geometry is from the best-fit model by data assimilation. The overpressure is recovered by reproducing the calculated uplift (2007~2017) at the GPS station MAU2 modeled by Le Mével et al. (2015) and Singer et al. (2018). The forecasted overpressure trajectory is generated by extending the data-constrained overpressure either linearly or cubically. The host-rock surrounding the magma chamber is going to fail when the overpressure is about 22 MPa.

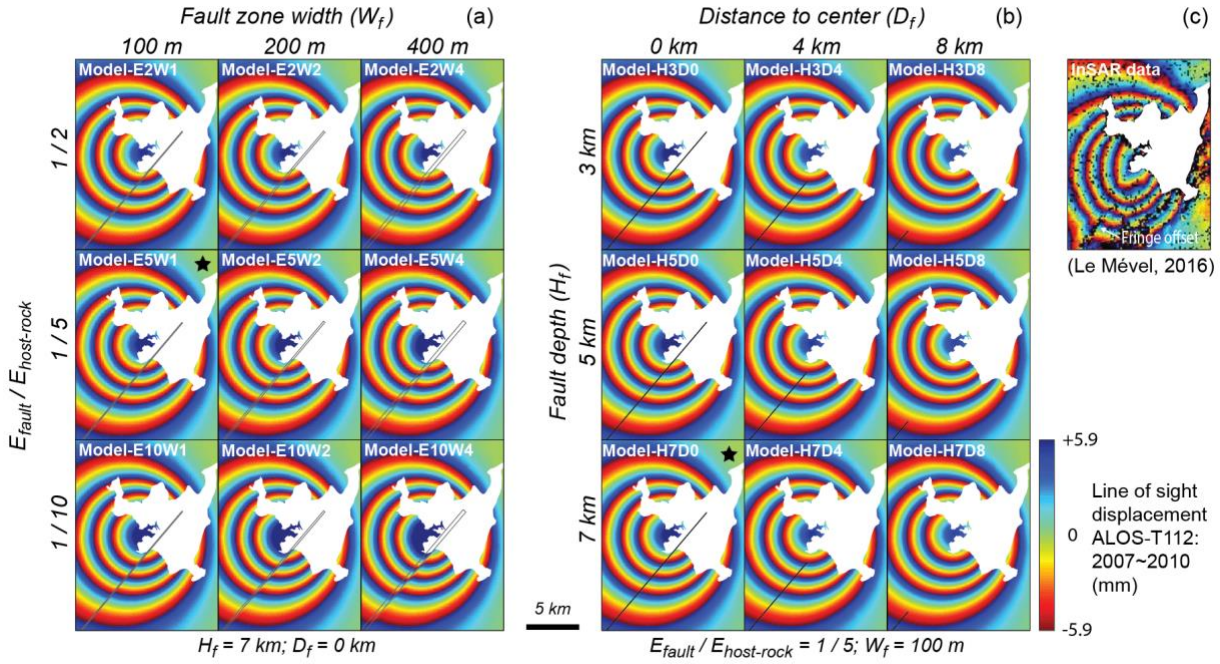

Figure 5.6 The predicted LOS displacements (ALOS-T112) from 2007 to 2010 are calculated by the interaction of the best-fit pressure source and a pre-existing weak zone as the Troncoso fault. The effect of the Troncoso fault on the surface displacement can be explored. (a) The model with a wide (W_f > 200 m) and weak (E_{fault} < 1/5 $E_{host\text{-}rock}$) fault zone creates a significant offset (> 500 m) of LOS fringes crossing the fault. (b) The magnitude of fringe offsets from the models with different depths and extensions of fault has a much narrower range than the models with different widths and Young's moduli of fault. (c) The InSAR data from Le Mével (2016) shows no significant fringe offset (> 500 m) crossing the fault. Black stars highlight the models used to calculate the failure in the Section 5.5.

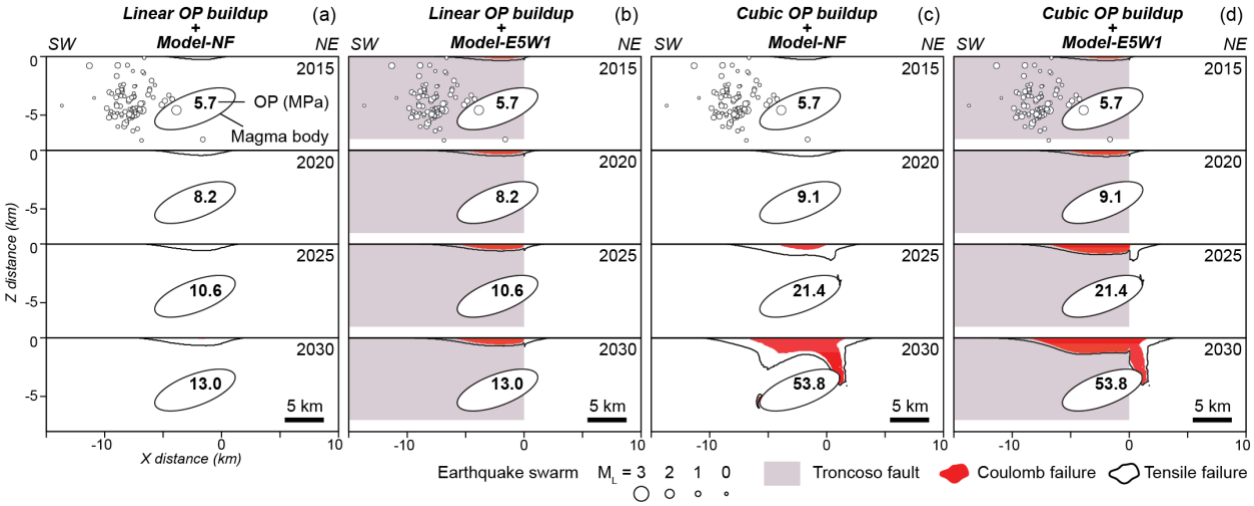

Figure 5.7 Predicted failure evolution under different model settings. (a) and (b) show the failure in the model with a linear overpressure buildup without or with the effect of the pre-existing weak zone. (c) and (d) are results from the model under a cubic overpressure buildup without or with the weak zone. For the fault model, the width, depth and distance-to-center of the fault zone is 100 m, 7 km, and 0 km. The fault zone has 1/5 of the surrounding Young's modulus (Model-E5W1). The location of the cross-sections is shown in Fig. 5.2.

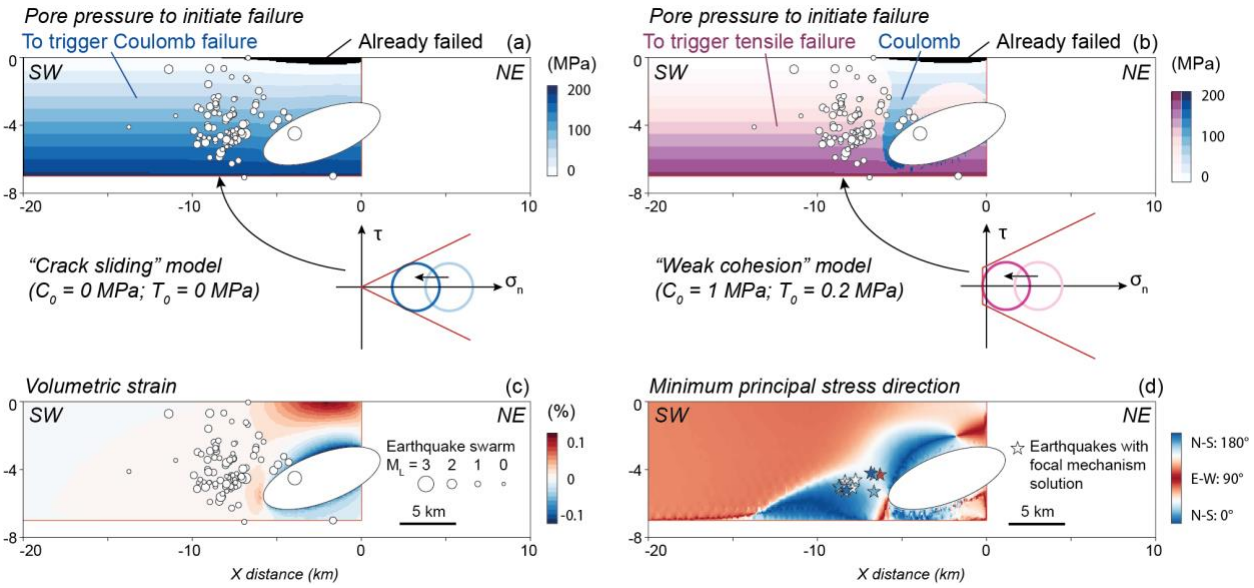

Figure 5.8 The stresses and strains in the fault zone of the Model-E5W1. (a) The minimum pore pressure required to trigger failures by a "crack sliding" model. (b) The minimum pore pressure required to trigger failures by a "weak cohesion" model. In (a) and (b), the area for Coulomb failure is shown as blue contours. Tensile failure is shown as purples. The black areas are failed area under dry condition. (c) The volumetric strain. (d) The direction of the minimum principle stress. The colored stars show the stress direction from the focal mechanism of the well-located VT events (Cardona et al., 2018). The location of the cross-sections is shown in Fig. 5.2.

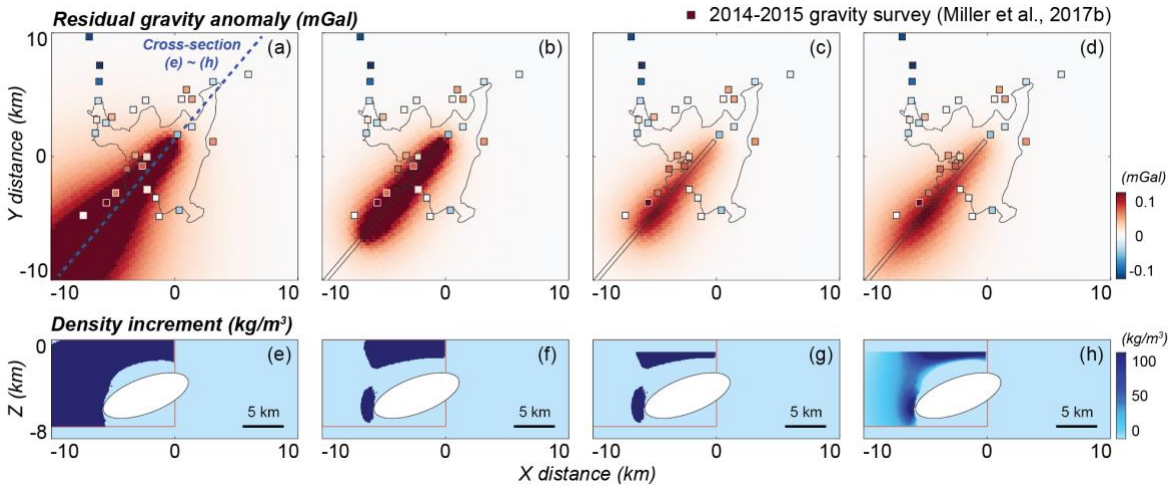

Figure 5.9 Modeled gravity change (a-d) created by corresponding density structures (e-f). The density changes are derived from fluid injection assumed based on the volumetric strains (ε_v). (a, e) Density increased by 100 g/cm3 uniformly where $\varepsilon_v > 0$. (b, f) Density increased by 100 g/cm3 uniformly where $\varepsilon_v > 0.01\%$. (c, g) Density increased by 100 g/cm3 uniformly where $\varepsilon_v > 0.01\%$ but $Z < -1$ km. (d, h) Density increased by at most 100 g/cm3 where $\varepsilon_v \geq 0.02\%$ but also proportion to the ε_v. The squares show the observed gravity changes during 2014-2015 (Miller et al., 2017b).

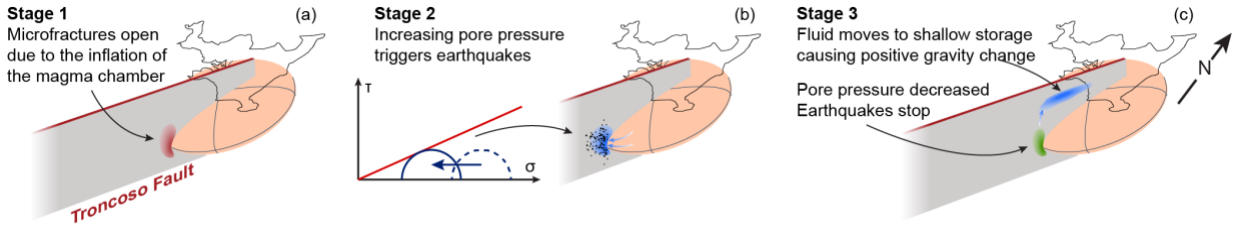

Figure 5.10 A 3D cartoon illustrating the interaction between the magma reservoir and hydrothermal system. (a) Microfractures open or get connected due to the inflation of the magma chamber. (b) A high-pressure fluid from the magma reservoir then injects into the dilatant fault zone triggering seismicity. (c) The fluid moves to unsaturated shallow storages to create a positive gravity anomaly, and the pore pressure will decrease after that to stop the seismic swarm until the next cycle.

5.9 Acknowledgements

We are grateful for helpful discussions with C. Thurber, K. Feigl, J. Dufek, B. Singer, N. Andersen, M. Poland, J. Albright, H. Cabaniss, R. Goldman, V. Romano, and the UIUC Geodynamics Group. We would also like to thank M. Pritchard, P. MacQueen, A. Hooper, S. Parman, and an anonymous reviewer for their comments which greatly improved our manuscript. The development of a high-performance computing data assimilation framework for forecasting volcanic unrest is supported by grants from NASA (19-EARTH19R-0104 – Zhan, 18-ESI18-0002 – Gregg) and the National Science Foundation (OCE 1834843, EAR 1752477 – Gregg). We acknowledge SAR data from DLR (TerraSAR-X) and JAXA (ALOS) space agencies. All data and modeling results are available at "Figshare" (https://doi.org/10.6084/m9.figshare.11369940.v1).

5.10 References

Acocella, V. (2014). Great challenges in volcanology: how does the volcano factory work? *Frontiers in Earth Science*, *2*, 4. https://doi.org/10.3389/feart.2014.00004

Aggistalis, G., Alivizatos, A., Stamoulis, D., & Stournaras, G. (1996). Correlating uniaxial compressive strength with schmidt hardness, point load index, Young's modulus, and mineralogy of gabbros and basalts (northern Greece). *Bulletin of the International Association of Engineering Geology - Bulletin de l'Association Internationale de Géologie de l'Ingénieur*, *54*(1), 3–11. https://doi.org/10.1007/BF02600693

Agram, P., Jolivet, R., & Simons, M. (2012). Generic InSAR Analysis Toolbox (GIAnT). User Guide, Ed.

Albright, J. A., P. M. Gregg, Z. Lu, and J. Freymueller (2019), Hindcasting magma reservoir stability preceding the 2008 eruption of Okmok, Alaska, *Geophysical Research Letters*, DOI:10.1029/2019GL083395.

Andersen, N. L., Singer, B. S., Jicha, B. R., Beard, B. L., Johnson, C. M., & Licciardi, J. M. (2017). Pleistocene to Holocene Growth of a Large Upper Crustal Rhyolitic Magma Reservoir beneath the Active Laguna del Maule Volcanic Field, Central Chile. *Journal of Petrology*, *58*(1), 85–114. https://doi.org/10.1093/petrology/egx006

Andersen, N. L., Singer, B. S., Costa, F., Fournelle, J., Herrin, J. S., & Fabbro, G. N. (2018). Petrochronologic perspective on rhyolite volcano unrest at Laguna del Maule, Chile. *Earth and Planetary Science Letters*, *493*, 57–70. https://doi.org/10.1016/j.epsl.2018.03.043

Bacon, C. R. (1985). Implications of silicic vent patterns for the presence of large crustal magma chambers. *Journal of Geophysical Research: Solid Earth*, *90*(B13), 11243–11252. https://doi.org/10.1029/JB090iB13p11243

Bato, M. G., Pinel, V., & Yan, Y. (2017). Assimilation of Deformation Data for Eruption Forecasting: Potentiality Assessment Based on Synthetic Cases. *Frontiers in Earth Science*, *5*. https://doi.org/10.3389/feart.2017.00048

Bato, M. G., Pinel, V., Yan, Y., Jouanne, F., & Vandemeulebrouck, J. (2018). Possible deep connection between volcanic systems evidenced by sequential assimilation of geodetic data. *Scientific Reports*, *8*(1), 11702. https://doi.org/10.1038/s41598-018-29811-x.

Berardino, P., Fornaro, G., Lanari, R., & Sansosti, E. (2002). A new algorithm for surface deformation monitoring based on small baseline differential SAR interferograms. IEEE Transactions on Geoscience and Remote Sensing, 40(11), 2375–2383. https://doi.org/10.1109/TGRS.2002.803792

Blakely, R. J. (1995). *Potential Theory in Gravity and Magnetic Applications*. Cambridge: Cambridge University Press. https://doi.org/10.1017/CBO9780511549816

Bohm, M., Lüth, S., Echtler, H., Asch, G., Bataille, K., Bruhn, C., et al. (2002). The Southern

Andes between 36° and 40°S latitude: seismicity and average seismic velocities. Tectonophysics, 356(4), 275–289. https://doi.org/10.1016/S0040-1951(02)00399-2

Cardona, C., Tassara, A., Gil-Cruz, F., Lara, L., Morales, S., Kohler, P., & Franco, L. (2018). Crustal seismicity associated to rpid surface uplift at Laguna del Maule Volcanic Complex, Southern Volcanic Zone of the Andes. *Journal of Volcanology and Geothermal Research*, *353*, 83–94. https://doi.org/10.1016/j.jvolgeores.2018.01.009

Charco, M., & Galán del Sastre, P. (2014). Efficient inversion of three-dimensional finite element models of volcano deformation. *Geophysical Journal International*, *196*(3), 1441–1454. https://doi.org/10.1093/gji/ggt490

Ciccotti, M., & Mulargia, F. (2004). Differences between static and dynamic elastic moduli of a typical seismogenic rock. Geophysical Journal International, 157(1), 474–477. https://doi.org/10.1111/j.1365-246X.2004.02213.x

Cordell, D., Unsworth, M. J., & Díaz, D. (2018). Imaging the Laguna del Maule Volcanic Field, central Chile using magnetotellurics: Evidence for crustal melt regions laterally-offset from surface vents and lava flows. *Earth and Planetary Science Letters*, *488*, 168–180. https://doi.org/10.1016/j.epsl.2018.01.007

Currenti, G., Del Negro, C., & Ganci, G. (2007). Modelling of ground deformation and gravity fields using finite element method: an application to Etna volcano. *Geophysical Journal International*, *169*(2), 775–786. https://doi.org/10.1111/j.1365-246X.2007.03380.x

Currie, C. A., & Hyndman, R. D. (2006). The thermal structure of subduction zone back arcs. Journal of Geophysical Research: Solid Earth, 111(B8). https://doi.org/10.1029/2005JB004024

Del Negro, C., Currenti, G., & Scandura, D. (2009). Temperature-dependent viscoelastic

modeling of ground deformation: application to Etna volcano during the 1993–1997 inflation period. *Physics of the Earth and Planetary Interiors*, *172*(3), 299–309.

Dinçer, I., Acar, A., Çobanoğlu, I., & Uras, Y. (2004). Correlation between Schmidt hardness, uniaxial compressive strength and Young's modulus for andesites, basalts and tuffs. *Bulletin of Engineering Geology and the Environment*, *63*(2), 141–148. https://doi.org/10.1007/s10064-004-0230-0

Evensen, G. (2003). The Ensemble Kalman Filter: theoretical formulation and practical implementation. *Ocean Dynamics*, *53*(4), 343–367. https://doi.org/10.1007/s10236-003-0036-9

Feigl, K. L., Le Mével, H., Tabrez Ali, S., Córdova, L., Andersen, N. L., DeMets, C., & Singer, B. S. (2014). Rapid uplift in Laguna del Maule volcanic field of the Andean Southern Volcanic zone (Chile) 2007–2012. *Geophysical Journal International*, *196*(2), 885–901. https://doi.org/10.1093/gji/ggt438.

Flinders, A. F., & Shen, Y. (2017). Seismic evidence for a possible deep crustal hot zone beneath Southwest Washington. Scientific Reports, 7(1), 1–10. https://doi.org/10.1038/s41598-017-07123-w

Fournier, N., & Chardot, L. (2012). Understanding volcano hydrothermal unrest from geodetic observations: Insights from numerical modeling and application to White Island volcano, New Zealand. *Journal of Geophysical Research: Solid Earth*, *117*(B11). https://doi.org/10.1029/2012JB009469

Fournier, T. J., Pritchard, M. E., & Riddick, S. N. (2010). Duration, magnitude, and frequency of subaerial volcano deformation events: New results from Latin America using InSAR and a global synthesis. *Geochemistry, Geophysics, Geosystems*, *11*(1), Q01003.

https://doi.org/10.1029/2009GC002558

Fukushima, Y., Cayol, V., & Durand, P. (2005). Finding realistic dike models from interferometric synthetic aperture radar data: The February 2000 eruption at Piton de la Fournaise. *Journal of Geophysical Research: Solid Earth*, *110*(B3), B03206. https://doi.org/10.1029/2004JB003268

Gerbault, M., Cappa, F., & Hassani, R. (2012). Elasto-plastic and hydromechanical models of failure around an infinitely long magma chamber. *Geochemistry, Geophysics, Geosystems*, *13*(3). https://doi.org/10.1029/2011GC003917

Gerbault, M., Hassani, R., Lizama, C. N., & Souche, A. (2018). Three-Dimensional Failure Patterns Around an Inflating Magmatic Chamber. *Geochemistry, Geophysics, Geosystems*, *19*(3), 749–771. https://doi.org/10.1002/2017GC007174

Gregg, P. M., & Pettijohn, C. (2015). *A multi-data stream assimilation framework for the assessment of volcanic unrest*.

Gregg, P. M., de Silva, S. L., Grosfils, E. B., & Parmigiani, J. P. (2012). Catastrophic caldera-forming eruptions: Thermomechanics and implications for eruption triggering and maximum caldera dimensions on Earth. *Journal of Volcanology and Geothermal Research*, *241–242*, 1–12. https://doi.org/10.1016/j.jvolgeores.2012.06.009

Gregg, P. M., de Silva, S. L., & Grosfils, E. B. (2013). Thermomechanics of shallow magma chamber pressurization: Implications for the assessment of ground deformation data at active volcanoes. *Earth and Planetary Science Letters*, *384*, 100–108. https://doi.org/10.1016/j.epsl.2013.09.040

Gregg, P. M., Mével, H. L., Zhan, Y., Dufek, J., Geist, D., & Chadwick, W. W. (2018). Stress triggering of the 2005 eruption of Sierra Negra volcano, Galápagos. *Geophysical Research*

Letters. https://doi.org/10.1029/2018GL080393

Grosfils, E. B. (2007). Magma reservoir failure on the terrestrial planets: Assessing the importance of gravitational loading in simple elastic models. *Journal of Volcanology and Geothermal Research*, *166*(2), 47–75. https://doi.org/10.1016/j.jvolgeores.2007.06.007

Hickey, J., Gottsmann, J., & Mothes, P. (2015). Estimating volcanic deformation source parameters with a finite element inversion: The 2001-2002 unrest at Cotopaxi volcano, Ecuador. *Journal of Geophysical Research: Solid Earth*, *120*(3), 1473–1486. https://doi.org/10.1002/2014JB011731

Hildreth, W., Godoy, E., Fierstein, J., & Singer, B. (2010). Laguna del Maule Volcanic Field: Eruptive history of a Quaternary basalt-rhyolite distributed vent volcanic field on the Andean rangecrest in central Chile. *Servicio Nacional de Geología y Minería, Boletin*, *63*, 145.

Hill, D. P. (1984). Monitoring unrest in a large silicic caldera, the long Valley-inyo craters volcanic complex in east-central California. *Bulletin Volcanologique*, *47*(2), 371–395. https://doi.org/10.1007/BF01961568

Hutchison, W., Biggs, J., Mather, T. A., Pyle, D. M., Lewi, E., Yirgu, G., et al. (2016). Causes of unrest at silicic calderas in the East African Rift: New constraints from InSAR and soil-gas chemistry at Aluto volcano, Ethiopia. *Geochemistry, Geophysics, Geosystems*, *17*(8), 3008–3030. https://doi.org/10.1002/2016GC006395

Jellinek, A. M., & DePaolo, D. J. (2003). A model for the origin of large silicic magma chambers: precursors of caldera-forming eruptions. *Bulletin of Volcanology*, *65*(5), 363–381. https://doi.org/10.1007/s00445-003-0277-y

Jolivet, R., Agram, P. S., Lin, N. Y., Simons, M., Doin, M.-P., Peltzer, G., & Li, Z. (2014).

Improving InSAR geodesy using Global Atmospheric Models. Journal of Geophysical Research: Solid Earth, 119(3), 2324–2341. https://doi.org/10.1002/2013JB010588

Le Mével, H., Feigl, K. L., Córdova, L., DeMets, C., & Lundgren, P. (2015). Evolution of unrest at Laguna del Maule volcanic field (Chile) from InSAR and GPS measurements, 2003 to 2014. *Geophysical Research Letters*, *42*(16), 6590–6598.

Le Mével, H., Gregg, P. M., & Feigl, K. L. (2016). Magma injection into a long-lived reservoir to explain geodetically measured uplift: Application to the 2007–2014 unrest episode at Laguna del Maule volcanic field, Chile. *Journal of Geophysical Research: Solid Earth*, *121*(8), 2016JB013066. https://doi.org/10.1002/2016JB013066

Long, S. M., & Grosfils, E. B. (2009). Modeling the effect of layered volcanic material on magma reservoir failure and associated deformation, with application to Long Valley caldera, California. *Journal of Volcanology and Geothermal Research*, *186*(3–4), 349–360. https://doi.org/10.1016/j.jvolgeores.2009.05.021

Lowenstern Jacob B, Smith Robert B, & Hill David P. (2006). Monitoring super-volcanoes: geophysical and geochemical signals at Yellowstone and other large caldera systems. *Philosophical Transactions of the Royal Society A: Mathematical, Physical and Engineering Sciences*, *364*(1845), 2055–2072. https://doi.org/10.1098/rsta.2006.1813

Manconi, A., Walter, T. R., Manzo, M., Zeni, G., Tizzani, P., Sansosti, E., & Lanari, R. (2010). On the effects of 3-D mechanical heterogeneities at Campi Flegrei caldera, southern Italy. *Journal of Geophysical Research: Solid Earth*, *115*(B8), B08405. https://doi.org/10.1029/2009JB007099

Masterlark, T. (2007). Magma intrusion and deformation predictions: Sensitivities to the Mogi assumptions. *Journal of Geophysical Research*, *112*(B6).

https://doi.org/10.1029/2006JB004860

Masterlark, T., Donovan, T., Feigl, K. L., Haney, M., Thurber, C. H., & Tung, S. (2016). Volcano deformation source parameters estimated from InSAR: Sensitivities to uncertainties in seismic tomography. *Journal of Geophysical Research: Solid Earth*, *121*(4), 3002–3016.

McTigue, D. F., & Mei, C. C. (1981). Gravity-induced stresses near topography of small slope. Journal of Geophysical Research: Solid Earth, 86(B10), 9268–9278. https://doi.org/10.1029/JB086iB10p09268

Miller, C. A., Williams-Jones, G., Fournier, D., & Witter, J. (2017a). 3D gravity inversion and thermodynamic modelling reveal properties of shallow silicic magma reservoir beneath Laguna del Maule, Chile. *Earth and Planetary Science Letters*, *459*, 14–27. https://doi.org/10.1016/j.epsl.2016.11.007

Miller, C. A., Le Mével, H., Currenti, G., Williams-Jones, G., & Tikoff, B. (2017b). Microgravity changes at the Laguna del Maule volcanic field: Magma-induced stress changes facilitate mass addition. *Journal of Geophysical Research: Solid Earth*, *122*(4), 2017JB014048. https://doi.org/10.1002/2017JB014048

Mitchell, T. M., & Faulkner, D. R. (2008). Experimental measurements of permeability evolution during triaxial compression of initially intact crystalline rocks and implications for fluid flow in fault zones. *Journal of Geophysical Research: Solid Earth*, *113*(B11). https://doi.org/10.1029/2008JB005588

Moran, S. C., Newhall, C., & Roman, D. C. (2011). Failed magmatic eruptions: late-stage cessation of magma ascent. *Bulletin of Volcanology, 73*(2), 115–122. https://doi.org/10.1007/s00445-010-0444-x

Newhall, C. A., & Dzurisin, D. (1989). Historical unrest at large calderas of the world. *Journal*

of Geology; (USA), 97:5. Retrieved from https://www.osti.gov/biblio/6852453

Okada, Y. (1985). Surface deformation due to shear and tensile faults in a half-space. Bulletin of the Seismological Society of America, 75(4), 1135–1154.

Ronchin, E., Masterlark, T., Molist, J. M., Saunders, S., & Tao, W. (2013). Solid modeling techniques to build 3D finite element models of volcanic systems: An example from the Rabaul Caldera system, Papua New Guinea. *Computers & Geosciences*, *52*, 325–333. https://doi.org/10.1016/j.cageo.2012.09.025

Rymer, H., Sparks, S., Self, S., Grattan, J., Oppenheimer, C., & Pyle, D. (2005). Super-eruptions: Global effects and future threats. Retrieved from https://pure.aber.ac.uk/portal/en/publications/supereruptions(62f0a6be-d0c6-43ec-8dcd-68752b4b7c7c)/export.html

Scholz, C. H. (2019). *The mechanics of earthquakes and faulting*. Cambridge university press.

Segall, P. (2016). Repressurization following eruption from a magma chamber with a viscoelastic aureole. *Journal of Geophysical Research: Solid Earth*, *121*(12), 8501–8522. https://doi.org/10.1002/2016JB013597

Segall Paul. (2019). Magma chambers: what we can, and cannot, learn from volcano geodesy. *Philosophical Transactions of the Royal Society A: Mathematical, Physical and Engineering Sciences*, *377*(2139), 20180158. https://doi.org/10.1098/rsta.2018.0158

Self, S., & Blake, S. (2008). Consequences of Explosive Supereruptions. *Elements*, *4*(1), 41–46. https://doi.org/10.2113/GSELEMENTS.4.1.41

Singer, B. S., Andersen, N. L., Le Mével, H., Feigl, K. L., DeMets, C., Tikoff, B., et al. (2014). Dynamics of a large, restless, rhyolitic magma system at Laguna del Maule, southern Andes, Chile. *GSA Today*, 4–10. https://doi.org/10.1130/GSATG216A.1

Singer, B. S., Mével, H. L., Licciardi, J. M., Córdova, L., Tikoff, B., Garibaldi, N., et al. (2018). Geomorphic expression of rapid Holocene silicic magma reservoir growth beneath Laguna del Maule, Chile. *Science Advances*, 18.

Smith, R., Sammonds, P. R., & Kilburn, C. R. J. (2009). Fracturing of volcanic systems: Experimental insights into pre-eruptive conditions. *Earth and Planetary Science Letters*, *280*(1–4), 211–219. https://doi.org/10.1016/j.epsl.2009.01.032

Sparks, R. S. J., Biggs, J., & Neuberg, J. W. (2012). Monitoring Volcanoes. *Science*, *335*(6074), 1310–1311. https://doi.org/10.1126/science.1219485

Talwani, P., & Acree, S. (1985). Pore Pressure Diffusion and the Mechanism of Reservoir-Induced Seismicity. In K. Shimazaki & W. Stuart (Eds.), *Earthquake Prediction* (pp. 947–965). Basel: Birkhäuser Basel. https://doi.org/10.1007/978-3-0348-6245-5_14

Terzaghi, K. (1951). *Theoretical soil mechanics*. Chapman and Hall, Limited.; London.

Tilling, R. I. (2008). The critical role of volcano monitoring in risk reduction. Advances in Geosciences, 14, 3–11.

Trasatti, E., Giunchi, C., & Bonafede, M. (2003). Effects of topography and rheological layering on ground deformation in volcanic regions. *Journal of Volcanology and Geothermal Research*, *122*(1), 89–110. https://doi.org/10.1016/S0377-0273(02)00473-0

Trasatti, E., Bonafede, M., Ferrari, C., Giunchi, C., & Berrino, G. (2011). On deformation sources in volcanic areas: Modeling the Campi Flegrei (Italy) 1982–84 unrest. *Earth and Planetary Science Letters*, *306*(3), 175–185. https://doi.org/10.1016/j.epsl.2011.03.033

Wespestad, C. E., Thurber, C. H., Andersen, N. L., Singer, B. S., Cardona, C., Zeng, X., et al. (2019). Magma Reservoir Below Laguna del Maule Volcanic Field, Chile Imaged with Surface-Wave Tomography. *Journal of Geophysical Research: Solid Earth*, *0*(ja).

https://doi.org/10.1029/2018JB016485

van Wyk de Vries, B., & Matela, R. (1998). Styles of volcano-induced deformation: numerical models of substratum flexure, spreading and extrusion. *Journal of Volcanology and Geothermal Research*, *81*(1), 1–18. https://doi.org/10.1016/S0377-0273(97)00076-0

Yang, X.-M., Davis, P. M., & Dieterich, J. H. (1988). Deformation from inflation of a dipping finite prolate spheroid in an elastic half-space as a model for volcanic stressing. *Journal of Geophysical Research: Solid Earth*, *93*(B5), 4249–4257.

Zhan, Y., & Gregg, P. M. (2017). Data assimilation strategies for volcano geodesy. *Journal of Volcanology and Geothermal Research*, *344*(Supplement C), 13–25. https://doi.org/10.1016/j.jvolgeores.2017.02.015

Zhan, Y., Gregg, P. M., Chaussard, E., & Aoki, Y. (2017). Sequential Assimilation of Volcanic Monitoring Data to Quantify Eruption Potential: Application to Kerinci Volcano, Sumatra. *Frontiers in Earth Science*, *5*. https://doi.org/10.3389/feart.2017.00108.

Zhan, Y., & Gregg, P. M. (2019). How Accurately Can We Model Magma Reservoir Failure With Uncertainties in Host Rock Rheology? Journal of Geophysical Research: Solid Earth, 124(8), 8030–8042. https://doi.org/10.1029/2019JB018178

Zhang, Y., Schaubs, P. M., Zhao, C., Ord, A., Hobbs, B. E., & Barnicoat, A. C. (2008). Fault-related dilation, permeability enhancement, fluid flow and mineral precipitation patterns: numerical models. *Geological Society, London, Special Publications*, *299*(1), 239–255. https://doi.org/10.1144/SP299.15

Zhu, W., Gaetani, G. A., Fusseis, F., Montesi, L. G. J., & De Carlo, F. (2011). Microtomography of Partially Molten Rocks: Three-Dimensional Melt Distribution in Mantle Peridotite. Science, 332(6025), 88–91. https://doi.org/10.1126/science.1202221

CHAPTER 6: MODELING MAGMA SYSTEM EVOLUTION DURING 2006-2007 VOLCANIC UNREST OF ATKA VOLCANIC CENTER, ALASKA[5]

Abstract

Surface deformation and seismicity coupled with advanced physics-based models, provide critical information to better understand the dynamics of volcanic unrest. During 2006-2007, > 80 mm/yr uplift was observed at the central Atka volcanic center, Alaska, by InSAR, coinciding with an increasing seismicity rate. At 2006/11/25, a phreatic eruption was observed at the Korovin volcano, 5-km north to the central Atka after drainage of its crater lake a month before the eruption. We use 3-D finite element models with data assimilation by the InSAR data to investigate (1) pressure source of the surface displacement, (2) mechanism of the volcano-tectonic (VT) earthquakes, and (3) triggering of the phreatic eruption. The Ensemble Kalman Filter tests show that a NE-tilted, oblate, ellipsoidal pressure source may migrate and rotate upward during 2006/6-2006/11 to create the surface deformation. A pre-existing weak zone, the Amlia-Amukta fault, may serve as a channel for pore fluid to inject into and to trigger the seismicity. Both spatial and temporal evolutions of the VT earthquakes are correlated to the fault dilatancy, leading to fracture-dominated increase of permeability and pore fluid injection. The drop in the water table at Atka is likely due to the generation of a large sink (~10^5 m3) for water within the pre-existing weak zone, causing lake drainage at the crater of Korovin by October 19, 2006. Consequently, the phreatic eruption of the Korovin volcano can be triggered.

[5] Submitted to JGR solid earth as: Zhan Y., Gregg P. M., and Lu Z. Modeling magma system evolution during 2006-2007 volcanic unrest of Atka volcanic center, Alaska.

6.1 Introduction

Volcanic unrest is defined when the behavior of a volcano deviates from its baseline or background (e.g., Phillipson et al., 2013; Acocella, 2014), which may lead to and provide critical warnings for potential volcanic eruptions (e.g., Sparks, 2003; Moran et al., 2011; Phillipson et al., 2013). To determine whether and when an eruption will follow unrest, we need to understand the geophysical, geodetic, and geochemical processes occurring during the volcanic unrest. Recent developments in volcanic monitoring by geodesy (e.g., InSAR, GNSS) and seismology (e.g., broadband seismometer) allow us to explore the host-rock responses to the changes of physical condition in a magmatic system (Sparks et al., 2012). While the mechanism controlling the physical processes during volcanic unrest can hardly be understood without the supports from experimental, analytical, and numerical models (e.g., Mogi, 1958; McTigue, 1987; Yang et al., 1988; Masterlark, 2007; Grosfils, 2007; Del Negro et al., 2009; Manconi et al., 2010; Gerbault, 2012; Fournier & Chardot, 2012; Gregg et al., 2013; Segall, 2013; Currenti et al., 2007; Charco & Galán del Sastre, 2014; Hickey et al., 2015; Le Mével et al., 2016; Zhan & Gregg, 2019). Besides, data assimilation techniques based on Bayesian Markov chain Monte Carlo method allow us to utilize volcanic monitoring data to obtain probabilistic estimates of model parameters, and further to forecast future behavior (e.g., Anderson & Segall, 2013; Segall, 2013; Gregg & Pettijohn, 2016; Bato et al., 2017; Zhan & Gregg, 2017; Albright et al., 2019). Combining surface deformation and seismicity data with advanced numerical models can provide us critical insights into the mechanism of the restless behavior of a volcanic system prior to its eruption. In particular, the volcano-tectonic (VT) earthquakes during volcanic unrest represent the brittle failure of the host-rock due to the changes in stress conditions, which should closely link to surface deformation (e.g., Segall et al., 2013; Zhan & Gregg, 2019). However, this linkage can be alerted due to crustal heterogeneity, hydrothermal systems, and other factors

(Zhan et al., 2019), which significantly varies from systems to systems (Roman & Cashman, 2018).

The Atka volcanic center is located at the northeast end of Atka island (Fig. 6.1a), which is the largest modern magmatic complex in the central Aleutian arc, with an estimated eruptive volume of ~200 km3 (Myers et al., 2002). The Atka complex belongs to an extended crust to the north of the Andreanof Block (Geist et al., 1987; Singer et al., 1992). Two faults, Amlia-Anukta (AA) fault, and Seguam fault, cut the Akta volcanic center. Although at Atka, the nature of the AA fault is unclear, the fault controls the distribution of the earthquakes (Power et al., 2019) (Fig. 6.1b). The youngest phase of volcanic activity in Atka began about 1-2 Ma ago (Myers et al., 2002), when the Atka volcano was once a large shield volcano, destroyed due to a caldera collapse eruption 300,000-500,000 years ago (Marsh, 1990). After that, four major volcanic cones (Korovin, Kliuchef, Sarichef and Konia) ringed around the Atka caldera, through a series of complicated magmatic processes, including melting, crystal fractionation, and magma mixing (Myers et al., 2002). The Korovin cone, the largest of the post-caldera edifices with a height of 1.5 km and basal diameter of 7 km, is reported to be active with several confirmed eruptions (i.e., 1976, 1987, 1998, 2006) and numerous fumarolic and hydrothermal activities during the past 200 years (Lu & Dzurisin, 2014).

During 2006/6-2007/1, an uplift with a rate > 80 mm/yr was observed at the center of Atka volcanic center (Fig.1a) by InSAR (Lu & Dzurisin, 2014), coinciding with an increased seismicity rate near the uplift center of deformation (Power et al., 2019) (Fig. 6.1b & Fig. 6.2). Simultaneously, increased fumarolic and hydrothermal activities occurred at the Korovin volcano, which located at 5-km north to the central uplift. The unrest in Korovin was followed by lake drainage at the crater of Korovin by October 19, 2006 (Neal et al., 2008) (Fig. 6.2). On

November 25, 2006, an eruption happened in the Korovin volcano. Although the satellite image shows there is a small amount of ash deposited near the vent of Korovin, they are very likely to be re-mobile ash during a phreatic eruption (Neal et al., 2008). Although the restless behavior of the Atka volcanic center has been recorded by the geodesy and seismology, the relationship between the surface deformation, seismicity, and eruption is still unclear. In particular, the key puzzle of the 2006-2007 volcanic unrest is whether the restless behavior occurring at the center of the Atka triggered the phreatic eruption at the Korovin volcano, which is 5-km away from the center.

In this study, a series of 3-D finite element models are established to simulate the surface deformation revealed by the multi-temporal InSAR data from 1999/7 to 2007/7. The probabilistic estimation of the pressure source evolution is obtained by the Ensemble Kalman Filter data assimilation. The stress, strain, and failure of the crust are calculated to explore the interaction between the pressurized source and two pre-existing weak zones (i.e., Amlia-Amukta fault and Seguam fault). The fracturing and hydrous processes of the fault zone are inferred by the model to explain the spatial and temporal evolution of the volcano-tectonic (VT) earthquakes during the unrest. Finally, the 2006/11/25 phreatic eruption of the Korovin volcano is linked to the restless behavior at the Atka volcanic center by combining modeling and multiple observations.

6.2 Pressure source evolution

6.2.1 InSAR data

We generated interferometric synthetic aperture radar (InSAR) images acquired by ERS-2 or Envisat between mid-June and late October during 1999-2007 to ensure the InSAR coherence. The coherence is easy to lose due to seasonal snow and ice cover but maintained during or between summers (Lu & Dzurisin, 2014). We further used the multiple InSAR small

baseline subset (MSBAS) technique (Samsonov et al., 2013) to obtain the timeseries of surface deformation in both up-down and east-west components (Fig. C.1 and C.2). Each image in the timeseries is further down-sampled to about 2,500 data points by the quadtree partitioning (e.g., Zhan et al., 2019).

6.2.2 Numerical model of the Atka volcanic system

The setup of the numerical model of the Atka volcanic system is similar to the previous study in the Laguna del Maule volcano (Zhan et al., 2019). The finite element models are built and solved using COMSOL Multiphysics 5.3a, which has been well benchmarked with analytical solutions (e.g., Gregg et al., 2012; Zhan & Gregg, 2017).

The crust of the study area is modeled as a $100 \times 100 \times 30$ km box (Fig. 6.3) centered at the Atka volcanic field (51.331°N, 174.139°W). The Global Multi-Resolution Topography Data (Ryan et al., 2009) is used to build the surface elevation of the model. A pressurized spheroid within the box is used to create the surface deformation at the center of the Atka island. The geometry of the spheroid is defined by its location (*X*, *Y*, and *Z*), half-height (*a*), half-width (*b*), angle between b axis and z-direction (θ), and azimuth of b axis (φ) (Fig. 6.3), similar to Yang et al. (1988)'s ellipsoid analytical model. The bottom and lateral edges of the crustal model are defined as a roller-type boundary condition. The model is loaded into two steps. First, the model is loaded by a gravitational body force and a surface water pressure ($\rho_w g h_w$) to calculate the initial stress. The initial stress is departing from the lithostatic stress near the surface with topography (McTigue & Mei, 1981). Second, a pressure excess to the initial pressure along the boundary of the ellipsoid is loaded, named as overpressure (*OP*). The deformation during the second step represents the response of the host-rock to the pressure source, which is used in data assimilation with the InSAR data.

The model is assumed as a linear elasticity with temperature and depth-dependent Young's modulus (E_{td}) and a constant Poisson's ratio (v), since Poisson's ratio has much less impact on the model results than Young's modulus (Zhan and Gregg, 2019). Similar to Zhan et al. (2019), Young's modulus is a function of both depth and temperature, which is defined by

$$E_{Td} = \beta_T \, E_d, \tag{6.1}$$

where E_d is far-field Young's modulus without a heated magma reservoir. β_T is a temperature-controlled coefficient defined as

$$\beta_T = 1 - \frac{1}{2} exp \, (\frac{T}{T_c} - \frac{z}{T_c}\frac{dT}{dz} - 1), \tag{6.2}$$

since an approximately 50% decrease in Young's modulus is observed at the silicic rock close to its solidus (Smith et al., 2009). The temperature of the magma reservoir, T_c, is 850°C, considering a silicic crystal mush may underlay the center of Atka (Myers et al., 2002). The geothermal gradient, *dT/dz* is 30 °C/km (Currie & Hyndman, 2006).

The far-field Young's modulus E_d is defined by

$$E_d = -0.0125 \, z^2 - 1.25 \, z + 40.25, \tag{6.3}$$

which is consistent to the seismic velocity profiles in the adjacent area (Fliedner & Klemperer, 1999), considering the relationship between dynamic and static Young's modulus (Starzec, 1999; Ciccotti & Mulargia, 2004) (Fig. C.3). The constants and variables in the equations are listed in Table S1 and Table S2.

6.2.3 Model parameter estimation by Ensemble Kalman Filter

The pressure source generating the ground deformation is determined by the Ensemble Kalman Filter (EnKF) workflow for volcanoes as the previous studies (Zhan & Gregg, 2017). The EnKF analysis updates the model states by solving the Bayesian problem using a Monte

Carlo method (Evensen, 2003). A matrix containing all the model parameters and results can be updated by:

$$\boldsymbol{A_{i+1}} = \boldsymbol{A_i} + \boldsymbol{X_i H^T}(\boldsymbol{H X_i H^T} + \boldsymbol{R_i})^{-1}(\boldsymbol{M_i} - \boldsymbol{H A_i}), \quad (6.4)$$

where $\boldsymbol{A_{i+1}}$ is updated ensemble by the EnKF analysis, $\boldsymbol{A_i}$ is a forecasting ensemble by the numerical models, $\boldsymbol{X_i}$ is the covariance matrix of $\boldsymbol{A_i}$, $\boldsymbol{M_i}$ is perturbed measurements whose covariance matrix is $\boldsymbol{R_i}$, and $\boldsymbol{H}$ is the coordinating matrix (Evensen, 2003). In this study, the results from the numerical models are East-West and Up-Down components of surface displacement (Fig. 6.4), which will be assimilated in each step when the corresponding InSAR timeseries data is available. The parameters solved by the EnKF analysis (Fig. 6.5) are the geometric parameters of the pressure source (X, Y, Z, a, b, θ, φ), and the overpressure (OP). The numbers of ensemble members (i.e., numerical models) and intra-step iterations are set as 100 and 5 to reach maximum efficiency.

In this study, three EnKF tests are conducted with different model settings or data usages. In Model I, the pressure source is an ellipsoid with a fixed, upright "a" axis ($\theta = 90°$ in Fig. 6.3). In Model II, the ellipsoid is allowed to rotate freely. In Model III, the ellipsoid is allowed to rotate freely, but the model is constrained by a masked InSAR data, where the displacement around Korovin volcano is not used in the data assimilation (Fig. C.4).

6.2.4 Volcanic deformation and pressure source

The InSAR data shows the surface deformation at the Atka center accelerated from ~5 mm/yr to ~80 mm/yr in June 2006 when the volcanic unrest started (Fig. 6.2a and c). Then, the rate of uplift at the center dropped to ~10 mm/yr in September 2006 until the 2006/11/25 eruption (Fig. 6.2c). There was an uplift of ~40 mm occurring at the Atka center within six months after the eruption (Fig. 6.2c). After that, the rate of uplift was back to the background

level (<5 mm/yr). However, we have no information on surface deformation from 2006/11/14 to 2007/6/12 due to the lack of coherent InSAR acquisition.

The center of the uplift locates ~3-km west of Kliuchef near the central Atka volcanic center (Fig. 6.4 and Fig. C.4). An uplift of ~40 mm was observed during both the 6-month time interval before and after the eruption (Fig. 6.4d). However, the East-West component of the surface deformation is inconsistent with the Up-down component (Fig. 6.4c). During the 6-month interval before the eruption (2006/7/8-2006/11/14), the East-West deformation was negligible (Fig. 6.4c), indicating minor lateral inflation. During the 6-month interval after the eruption (2006/11/14-2007/7/28), a 40-mm west-warding and a 20-mm east-warding displacement were observed respectively at the west and east Atka island (Fig. 6.4c).

Our numerical models reproduce the surface deformation revealed by the InSAR timeseries (Fig. 6.2a and c, Fig. 6.4c and d) using the EnKF data assimilation. The mean values and standard deviations of the parameter estimations from three tests (i.e., Model I, II, and III) are calculated (Fig. 6.5). The parameter estimations from Model II and III are almost identical (Fig. 6.5), indicating the local deformation near the Korovin volcano does not affect the pressure source determination. At the beginning of the unrest (2006/6), the pressure source by Model I is sill-like ellipsoid located 4-km west of Kliuchef (Fig. 6.6a), and at a depth of 7 km (b.s.l.). While Models II and III suggest a dike-like source centered at 6-km west of Kliuchef (Fig. 6.6a) with a depth of ~6 km (b.s.l.). At 2006/11/14, prior to the eruption, the pressure source from Model I has moved ~1-km upward and ~1-km eastward since the beginning of the unrest (Fig. 6.6b). Meanwhile, Model II and III (Fig. 6.6b) show the pressure source, an oblate ellipsoid, was rotating to be more horizontal with an angle of ~50° during the unrest (2006/6-2006/11). Prior to the eruption, the center of the pressure source from Model II or III was located 4-km west of

Kliuchef with a depth of 5 km (b.s.l.) (Fig. 6.5b), which is shallower than the beginning of the unrest. At 2007/7/28, eight months after the eruption, all models indicate the pressure source is a sill-like ellipsoid located 3-km west of Kliuchef with a depth of 5.5 km (b.s.l.) (Fig. 6.6c).

The overpressure of Model I mimicked the evolution of the surface uplift, exhibiting a rapid increasing (from ~3 MPa to ~10 MPa) during the unrest (2006/6-2006/11) (Fig. 6.5e). The overpressure of Model II or III has increased slightly (from ~6.5 MPa to ~8 MPa) during the unrest. The surface uplift is mainly due to the migration of the pressure source.

We favor Model II and III, since they can better explain the pattern of surface deformation, especially the East-West component (Fig. 6.4 and Fig. C.4). The East-West component deformation during the volcanic unrest (2006/6-2006/11) exhibits strongly asymmetric where the east-ward motion is larger than the west-ward motion by at least two times (Fig. 6.4c). The models with ellipsoids which can rotate freely (i.e., Model II and III) are able to reproduce this asymmetric deformation pattern by tilting the pressure source (Fig. 6.6a and b). Model I with an upright "a" axis can only create symmetric deformation pattern (Fig. 6.6), leading larger misfits of the surface deformation (Fig. 6.4 and Fig. C.4), and, therefore, larger L2 norm error (Zhan & Gregg, 2017) compared to Model II and III (Fig. 6.5i).

6.2.5 Implication on magma reservoir

By data assimilation with the InSAR timeseries data, we find the pressure source to create the ground deformation was moving and rotating during the volcanic unrest (Fig. 6.6). There are three possible explanations. The first hypothesis is that the migration of pressure is due to the transportation of magma or hydrothermal fluid through dike propagation (e.g., Mastin & Pollard, 1988). This hypothesis can be quickly ruled out since the moving direction of the pressure source is perpendicular to the direction of the long axis of the ellipsoid. Dikes favor propagating parallelly to the long axis of a magma body. In addition, there is no corresponding

VT earthquake associated with the diking or dike-related brittle failing process (Roman & Cashman, 2006). On the contrary, most VT events occurred along the Amlia-Amukta fault during the unrest (Fig. 6.1b and Fig. 6.6b). The fault can serve as a pre-existing weak zone to facilitate dike propagation. However, the surface deformation pattern rules out the displacement of the fault, indicating the pressure source is not controlled by the fault.

The second hypothesis is that the magma or fluid can transport through some pre-existing channels or conduits (e.g., Bonaccorso & Davis, 1999) to create a moving pressure source. However, the pressure source is moving laterally with a ~30° rotation, which can hardly be explained by magma or fluid moving along a straight channel or conduit. In addition, even if the fluid is moving through a complicated channel system, we still have difficulty in explaining why the magma does not take advantage of the pre-existing weak zone, the Amlia-Amukta fault. Besides, seismic tremors are usually triggered during fluid migration (e.g., Yamamoto et al., 2002). No evidence shows the number of tremor events is increasing during the unrest (Fig. 6.2).

We favor the third hypothesis that the pressure source migration is due to the changes in the connectivity of the magma reservoir dominated by a crystal mush. Previous studies by petrology and geochemistry indicated that the Atka volcanic field is supplied by a series of poor communicating, but adjacent magma bodies (e.g., Myers et al., 2002). The magma reservoir of Atka is likely to comprise interleaved lenses of melt, partially molten crystal mushes, or solid material (Cashman & Giordano, 2014). The pressure source of Atka, however, is not necessary a single body filled with melt. A pressure source can be an interconnected network with a small proportion of melt or fluid since ~2% of melt or fluid can provide enough connectivity for a crystal mush to share the pressure (Zhu et al., 2011). The ellipsoidal pressure source inferred by the InSAR data (Fig. 6.6) can be a smoothed image of such an interconnected network with a

small amount of melt or fluid. Therefore, the connectivity of this network can be changed during the deformation of the magma reservoir. Even with a negligible migration of magma or fluid, the distribution of pressurized magma can change dramatically to create an effect that the pressure source is moving rapidly. In this study, the ellipsoid is an approximation of the pressurized magma body. While, in nature, the pressurized part of the magma reservoir can be irregular, which cannot be constrained by surface deformation data alone.

6.3 Stress and failure development

6.3.1 Failure criteria

To explain how ground motion and seismicity can link to each other, we evaluate stress and failure development associated with the host-rock deformation due to the pressure source. We calculate the stresses of the Atka host-rock using the pressure source defined by the mean values of the estimated parameters (Fig. 6.5). We use Coulomb and tensile failure criteria to predict whether shear or tensile failure can happen in the host-rock. To quantify the likelihood of failure occurring, we calculate the "stress to failure" (e.g., Zhan and Gregg, 2019), which is defined as the distance of the Mohr circle to the Coulomb or tensile failure envelope (Fig. 6.7a and b). The stress to Coulomb failure (CF) and tensile failure (TF) are given by

$$CF = \tau - C_0 \cos \phi_i - \sigma_n \sin \phi_i \,, \tag{6.5}$$

and

$$TF = \sigma_3 + \sigma_T, \tag{6.6}$$

where τ, σ_n, and σ_3 are the maximum shear stress, normal stress, and least principal stress (positive for compression). Similar to Zhan et al. (2019), the internal friction angle (ϕ_i) is 25°, cohesion (C_0) is $E \times 5 \times 10^{-4}$, and tensile strength ($\sigma_T$) is $E \times 10^{-4}$.

6.3.2 Overpressure to generate host-rock failure

The failure calculation shows that there is no failure occurring in the host-rock by 2006/11/14 (Fig. 6.7c and d). The overpressures calculated by the EnKF are less than 10 MPa (Fig. 6.5e) to create an 80-mm surface uplift (Fig. 6.2). At least 30 MPa is needed for any model to generate Coulomb failure along the boundary of the pressure source (Fig. 6.7c). Such an overpressure will create at least 300-mm surface uplift, which is larger than the observation by at least three times.

Therefore, we argue that the host-rock failure due to a pressurized magma reservoir is hard to explain the volcano-tectonic earthquake during the volcanic unrest in this area. First, the overpressure prior to the eruption is much less than the overpressure required to initiate failure in the host-rock. Besides, the distribution of failure, if triggered, is not consistent with the earthquakes (Fig. C.5). The host-rock surrounding the pressure source can generate widespread failure, only if the overpressure is greater than 100 MPa, which is less likely in a natural system. Even if the magma reservoir can be pressurized to >100 MPa, the failure happens mainly surrounding the pressure source or near the surface above the pressure source (Fig. C.5), which has no consistency with the distribution of the VT events (Fig. 6.6).

6.4 Effects of the pre-existing weak zones

We need an alternative explanation to link the surface deformation and VT events occurring during the unrest. A previous study in Laguna del Maule shows that a pre-existing weak fault, Troncoso fault, may serve as a channel for pore fluid (i.e., water or brine) to trigger "hydrofracturing" seismicity during the volcanic deformation (Zhan et al., 2019). By borrowing this idea, we are going to test whether the local fault zones (i.e., Amlia-Amukta fault and Seguam fault) can facilitate pore fluid to trigger the VT earthquakes.

6.4.1 Modeling pre-existing weak zone

Similar to Zhan et al. (2019), we model the fault zone as a thin vertical slab (~100-1,000 m) embedded in the host-rock (Fig. C.6). Within the fault zones, Young's modulus is lower than the surrounding host-rock. The traces of the fault zones are defined after previous studies (Fig. 6.1; e.g., Geist et al., 1987; Singer et al., 1992). We assume the Amlia-Amukta (AA) fault is an at least 10-km deep, nearly-vertical fault, according to the distribution of the earthquakes (Fig. 6.6b). Since we have less constraint on the geometry of the Seguam fault at the Atka island, we assume it shares the same depth and dipping as the AA fault. In addition, the Seguam fault is > 7 km away from the deformation center. In the later discussion, we find the volcanic deformation has negligible effects on the Seguam fault compared to the AA fault.

To maximize the effects of the fault zones on the stress field, we need the fault zone to be as significant as possible, which can be achieved either by increasing the thickness of the fault or by decreasing Young's modulus. However, as the fault becomes wider or weaker, it can strongly affect the surface deformation pattern. Similar to Zhan et al. (2019), we conduct a series of sensitivity tests to determine the relationships between the significance (i.e., thickness and weakness) of the fault zone and its perturbation to the pattern of surface deformation. We find that the faults with either a thickness greater than 500 m, or Young's modulus lower than 50% of the surrounding host-rock will create a >10% perturbation of surface deformation, which can be observable in the InSAR data (Fig. C.7). This result is very similar to the study in Laguna del Maule (Zhan et al., 2019), where the magma reservoir is also next to the fault zone. Since there is no evidence showing the pattern of surface deformation is affected by any linear, fault-like structure, we argue that the fault zones should not be wider than 500 m and weaker than the surrounding rocks by more than 50%.

6.4.2 VT-earthquakes distribution

In Laguna del Maule, some parts of the fault zone may experience dilatancy during the volcanic deformation due to the pressure source, which helps to increase the connectivity of the pre-existing fractures within the fault zone (Zhan et al., 2019). The earthquakes can be triggered due to pore pressure increment when some isolated or poor-connected fractures or pores are connected and filled with pore fluids.

In this study, we calculate the volumetric strain evolution within the fault zones (Fig. C.8-C.11). We compare the change of volumetric strain of the Amlia-Amukta (AA) fault zone and the distribution of VT earthquakes occurring within a 2-km distance to the AA fault. We find that the VT earthquakes generally favor places with positive volumetric strain changes (Fig. C.8-C.10). This correlation cannot be found before 2006/6 since the EnKF has not obtained convincing estimation of the pressure source, as the L2 norm error is high (Fig. 6.5i).

The pattern of volumetric strain prior to and 6-month after the eruption experienced significant changes due to the migration of the pressure source (Fig. 6.8). At the same time, the distribution of the VT earthquake also shifted downward (Fig. 6.8), which is consistent with the volumetric strain changes. Among the three models, Model I, using the ellipsoid with a fixed "a" axis, only captures the downward shifting of the zone with positive strain changes (Fig. 6.8a). Model II and III with tilted ellipsoid, however, suggest that the place with volumetric increment in the fault extends deep in NE and shallow in SE, which coincides with the earthquake distribution (Fig. 6.8b and c). Compared to Model I, Model II and III have better performances not only in reproducing the surface displacement (Fig. 6.4), but also in explaining the earthquake distribution.

For exploring the effects of Seguam fault, we calculate the volumetric strain evolution within the Seguam fault. The magnitude of volumetric strain change is 1-2 orders lower than the

AA fault (Fig. C.11), which is consistent with its much fewer VT events (Fig. 6.1b). The ML3.1 earthquake in 2006/6/15 is probably associated with tectonic processes, for example, the clockwise rotation of the Andreanof Block (Fig. 6.1a). Therefore, the dilatancy of the AA fault due to volcanic deformation may create more connectivity for fluid (e.g., water) to inject into, which facilitates triggering the VT events.

Alternative to the "hydrofracturing" mode as we have discussed above, the VT earthquakes can also be triggered due to a Coulomb stress change (CF) along the fault. Since the pressurized magma reservoir can directly change the local stress field, making some parts of the fault closer to failure. If there is initial stress accumulated crossing the fault, a small amount of stress change may trigger the slippage along the fault plane. To test this idea, we calculate the Coulomb stress change along the AA fault and Seguam fault. We assume the sliding friction angle (Φi) of the fault zone is as low as 15° (Collettini et al., 2009) to maximize the Coulomb stress change. No obvious correlation between the distribution of VT earthquakes and positive Coulomb stress change can be found (Fig. C.12-C.14). Therefore, we argue that the Coulomb stress is not the reason to trigger the VT events along the fault zone, although it may facilitate the failure initiation. In addition, the Coulomb stress change along the Seguam fault is much low than the AA fault (Fig. C.15), indicating that the magma reservoir dynamics have little effect on the Seguam fault.

6.4.3 Energy released from the VT-earthquakes along the fault

In addition to the spatial correlation between seismicity and fault dilatancy, we also find there is a temporal correlation between these two processes. We calculate the total volume change (ΔV^{tot}) of the AA fault at each InSAR acquisition time,

$$\Delta V^{tot} = \iiint_0^V \epsilon_V dV, \tag{6.7}$$

where ϵ_V is volumetric strain, and V is the total volume of the fault.

We find that the total volume change of the AA fault (ΔV^{tot}), and the energy released from the VT earthquake within a 2-km-distance to the fault (E_{eq}) share a very similar evolution pattern (Fig. 6.9), if the time series of ΔV^{tot} and E_{eq} are normalized to their maximum values respectively. In particular, Model II and III have much better consistency with the observation than Model I, indicating the models with a better ability explaining the surface deformation are also good at explaining the seismicity. This phenomenon further confirms the linkage between the deformation and seismicity during the volcanic unrest. The consistencies between E_{eq} and ΔV^{tot} (Fig. 6.9) can be expressed as

$$E_{eq} \cong \gamma_1 \, \Delta V^{tot}, \tag{6.8}$$

where γ_1 is a constant which may be controlled by the structure of the system, but should be a constant. The linear relationship between E_{eq} and ΔV^{tot} may be explained by the formation of the microfractures (Jaeger et al., 2007). If we only consider the opening of cracks (Mode I in fracture mechanics), the energy release dQ due to the growth of a crack (length = $2c$, and thickness = t_c; Fig. C.16) by dc can be expressed by

$$dQ = \frac{2K_I^2 t_c}{E'} dc \tag{6.9}$$

where E' is effective Young's modulus of the fault zone. K_I is the stress intensity factor given by

$$K_I = \sigma_{tip}\sqrt{\pi c}, \tag{6.10}$$

where σ_{tip} is the stress at the tip of the crack, and c is the half length of the crack. Therefore, the energy (Q) released by the opening of a single crack with a length of c is given by

$$Q = \int_0^c \frac{2\pi\sigma_{tip}^2}{E'} t_c \, dc = \frac{\pi\sigma_{tip}^2}{E'} t_c c^2, \tag{6.11}$$

If we assume the crack is an elliptical cylinder, the volume of the crack opened during the fracturing is $\pi c^2 t_c A_c$, where A_c is the aspect ratio of the crack (Fig. C.16c). We further assume that the effective Young's modulus of the fault is a constant. Besides, we can use the tensile strength of the rock to take place the stress at the crack tip, σ_{tip}, which can also be assumed as constant. If the aspect ratio of the crack A_c is a constant during the crack growth, which means the crack growth is self-similar, the energy released by the earthquake can approximately be a linear function of the volume change due to opening of the crack.

We calculate the total volume change by integrating the volumetric strain, which is in the elastic regime, while we use fracture mechanics to explain the energy release, which represents the inelastic behavior of rock. Although these two processes are based on two different theorems, we argue that the inelastic behavior of the fault in the microscale (i.e., fracture opening and growth) can perform like the elastic deformation in a large scale, if the pre-existing weakness is homogenous within the fault. In summary, the correlation between the energy released from the VT-earthquakes and total volume change of the fault suggests that the dilatancy of the fault (Fig. 6.9a) may play an important role in the seismicity during the unrest. However, future studies are necessary to understand the details in fracturing processes during the volcanic unrest.

6.5 2006 – 2007 Atka volcanic unrest and the eruption at Korovin

By integrating the surface deformation modeling, stress and strain calculation, and seismicity observation, we suggest that the surface deformation and seismicity during the volcanic unrest are closely linked to each other. In particular, the pressure source may form due to magma/fluid injection to, or differentiation of a long-existing, complicated magma system (Myers et al., 2002) (Fig. 6.10a). The deformation of the mushy magma reservoir may change the connectivity of a pressurized magma network, causing the migration of the pressure source

(Fig. 6.6). At the same time, the pressure source may trigger the opening and growth of the fractures within the AA fault (Fig. 6.10b), leading to an increment in conductivity or permeability of the fault. The pore fluid may inject into the dilatant parts of the fault, decreasing the effective stress, and triggering the brittle failures (i.e., the VT earthquakes) (Fig. 6.10c). The pore fluid triggering the VT earthquakes is very likely to be water, considering there is an active hydrothermal system in this area (McGimsey et al., 2007, 2011; Neal et al., 2008). The dilatant fault may serve as a huge sink (in order of $10^5\ m^3$) for the underground water in Atka. The water table at Korovin may also drop due to water discharge (Fig. 6.10d), which is consistent with the observation of a lake drainage event starting between 2006/9 and 2006/10 (Neal et al., 2008). The subsidence near the Korovin vent may also associate with the drainage of the crater lake. Finally, the drop in the water table may trigger the phreatic eruption of Korovin.

According to this study and previous study at the Laguna del Maule volcanic field (Zhan et al., 2019), we argue that pre-existing weak zone and pore fluid, such as water and brine from a hydrothermal system, may play a much more important role in volcanic unrest than previously thought. The "hydrofracturing" system is sensitive to the changes in physical conditions within a magma reservoir. Understanding such a process may help us forecast the volcanic eruptions by monitoring the restless behaviors beforehand.

6.6 Conclusions

Constrained by the InSAR timeseries data, our models show that a NE-tilted, oblate, ellipsoidal pressure source may generate the rapid uplift (~80 mm/yr) during the 2006-2007 volcanic unrest at the Atka volcanic center. This pressure source migrated and rotated upward during 2006/6-2006/11 creating an asymmetric deformation pattern. The migration of the pressure source may be derived from deformation of the magma reservoir dominated by a crystal

mush, which changes the distribution of an interconnected melt network. In this scenario, only a little overpressure increment is needed to trigger the changes in melt connectivity within a crystal mush to generate remarkable surface deformation. To explain the volcano tectonic (VT) earthquakes at the Atka volcanic center, we calculate the stress and failure within the host-rock due to the source pressurization. However, no failure can be triggered according to the observed surface deformation and corresponding overpressure during the unrest. More than three time of current overpressure is needed to initiate the failure within the host-rock near the pressure source without considering the effect of pore pressure. Then, we test the hypothesis that a pre-existing weak zone, the Amulia-Amukta fault, may serve as a channel for pore fluid to inject into and to trigger the seismicity. The calculation of volume change within the fault suggests that the distribution of the seismicity is consistent to the dilatant parts of the fault. In addition, the energy released from the VT earthquakes along the fault is proportional to the volume increment of the fault during the unrest. The VT earthquakes may be triggered by pore fluid injections, which are associated with permeability increase due to opening and growth of the fractures within the fault during the volcanic deformation. We argue that the pore fluid may be water, since the Atka volcanic center exhibits frequent hydrothermal and fumarolic activities. A water discharge, in an order of 105 m3, in Atka may happen due to the injection of water into a pre-existing weak zone. The drop of water table might cause the drainage of the crater lake at Korovin by October 19, 2006, finally triggering the phreatic eruption of the Korovin volcano at November 25, 2006.

6.7 Figures

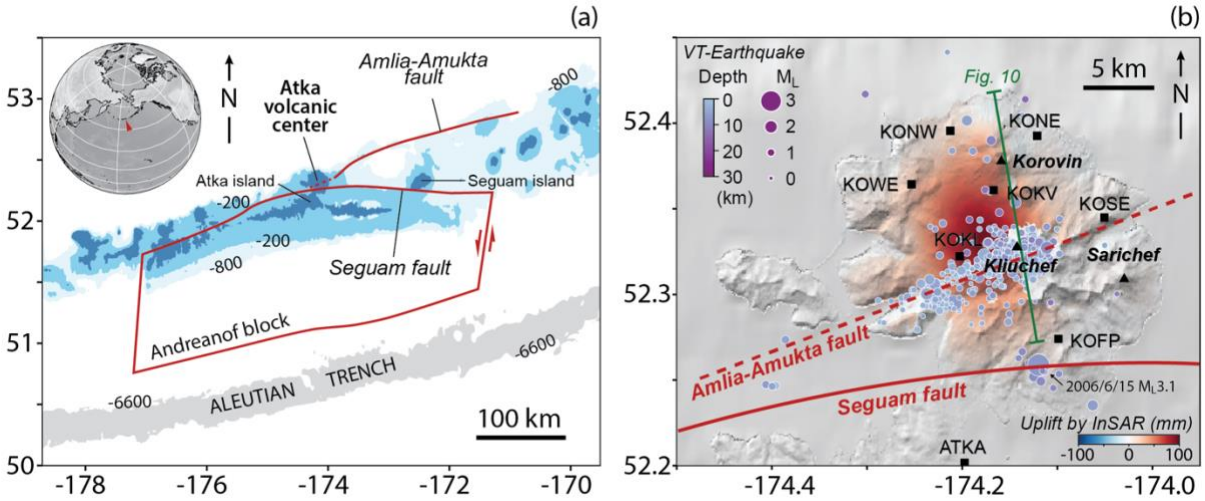

Figure 6.1 (a) The location of the Atka volcanic center (called Atka for simplification). Atka is located on an extended crust in the north of the Andreanof Block (After Geist et al., 1987; Singer et al., 1992). Atka is also at the junction of the Seguam and Amlia-Amukta faults. (b) The surface uplift from 2000/7/1 to 2006/11/14 revealed by the InSAR data. Volcano-tectonic (VT) earthquakes (Power et al., 2019) occurring between 2006/6/1 and 2007/1/1 are plotted as purple circles whose color and size represent depth and magnitude. The black squares are the location of seismometers. The black triangles show the locations of some major volcanoes at Atka. The red lines show the trace of two faults. The green line shows the location of the cross-section in Figure 6.10.

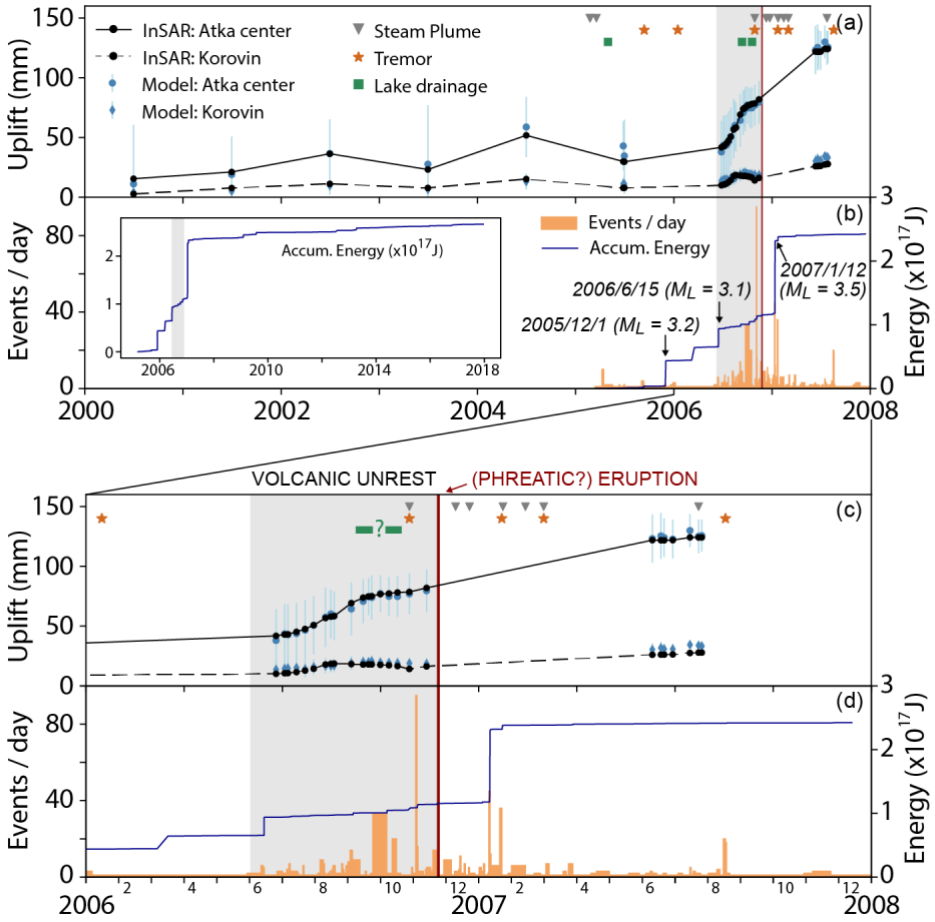

Figure 6.2 The time series of ground deformation and volcano-tectonic (VT) earthquakes from 2000 to 2008. (a) Surface uplift histories at Atka center (near Kliuchef) and Korovin (Fig. 6.1b) revealed by InSAR data are shown as solid and dashed lines in black. Each black circle represents one InSAR time slice. The blue circles and diamonds are the surface deformation calculated by the numerical models (i.e., Model II) with data assimilation. The unrest events, including steam plumes, tremors, and lake drainage, are labeled as gray triangles, orange stars, and green squares (McGimsey et at., 2007, 2011; Neal et al., 2008). (b) The numbers of VT earthquakes per day are shown as orange bars. The blue line is the accumulated energy calculated by log10(Energy) = 11.8 + 1.5 M (Gutenberg, 1956). The inserted plot shows the accumulated energy from 2005 to 2018. (c) and (d) show the ground deformation and VT earthquakes from 2006 to 2008. The grey shadows highlight the volcanic unrest. The red lines illustrate the possible phreatic eruption.

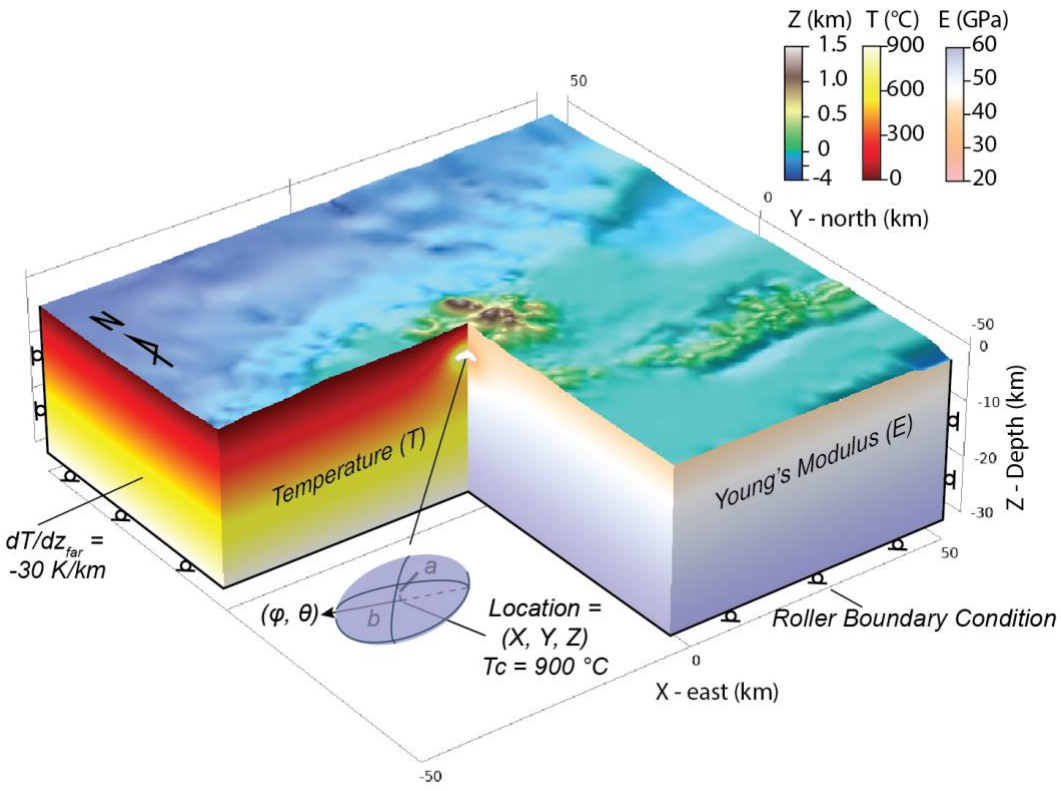

Figure 6.3 The temperature and Young's modulus of the numerical model. The pressure source for the ground deformation during the volcanic unrest is modeled by an ellipsoid. The center of the ellipsoid is at (X, Y, Z). The half-height and half-width of the ellipsoid are a and b. The dipping angle and direction of the half-width are θ and φ. The bottom and lateral edges are in the roller-type boundary condition.

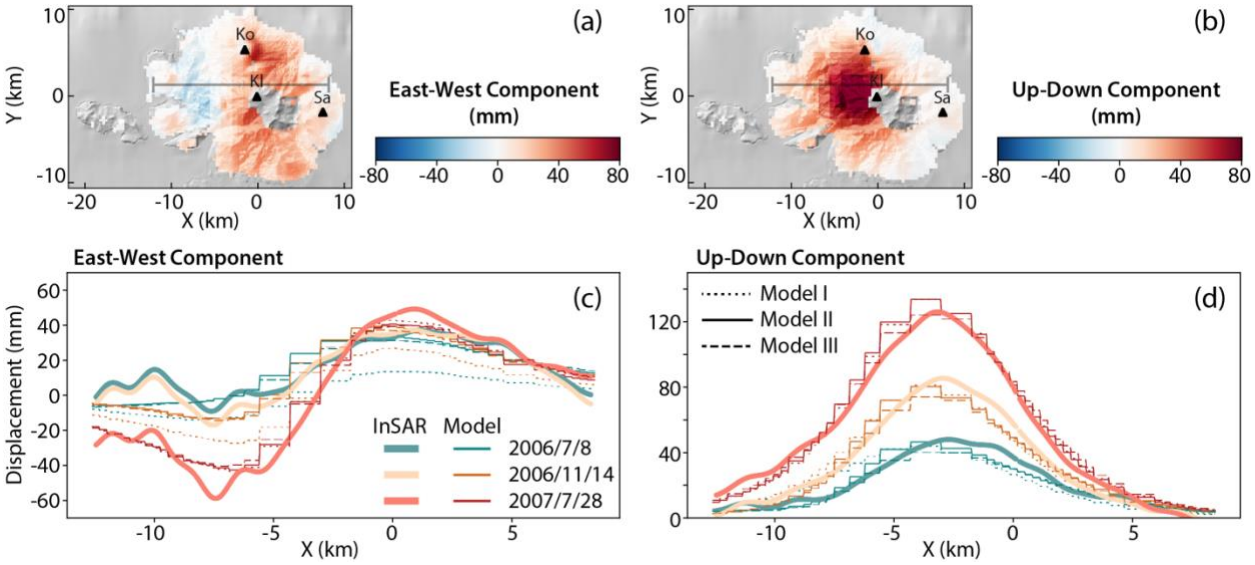

Figure 6.4 Comparison between InSAR timeseries data and modeled surface displacement. (a) and (b) show the East-West and Up-Down components of surface displacement by the down-sampled InSAR timeseries data on 2006/11/14. The black triangles represent the volcanos Korovin (Ko), Kliuchef (Kl), and Sarichef (Sa). The grey lines show the cross-sections in the figure (c) and (d). (c) and (d) are two cross-sections showing the comparison between InSAR and modeled displacement in East-West and Up-Down components. Different colors represent different InSAR time. In Model I (dotted lines), the pressure source is an ellipsoid with a fixed dipping angle ($\theta = 90°$ in Fig. 6.3). In Model II (thin solid lines), the dipping angle (θ) and direction (φ) are unfixed. Model III (dashed lines) has the same setup as Model II but is constrained by masked InSAR data (Fig. C.4). Thick solid lines are InSAR data.

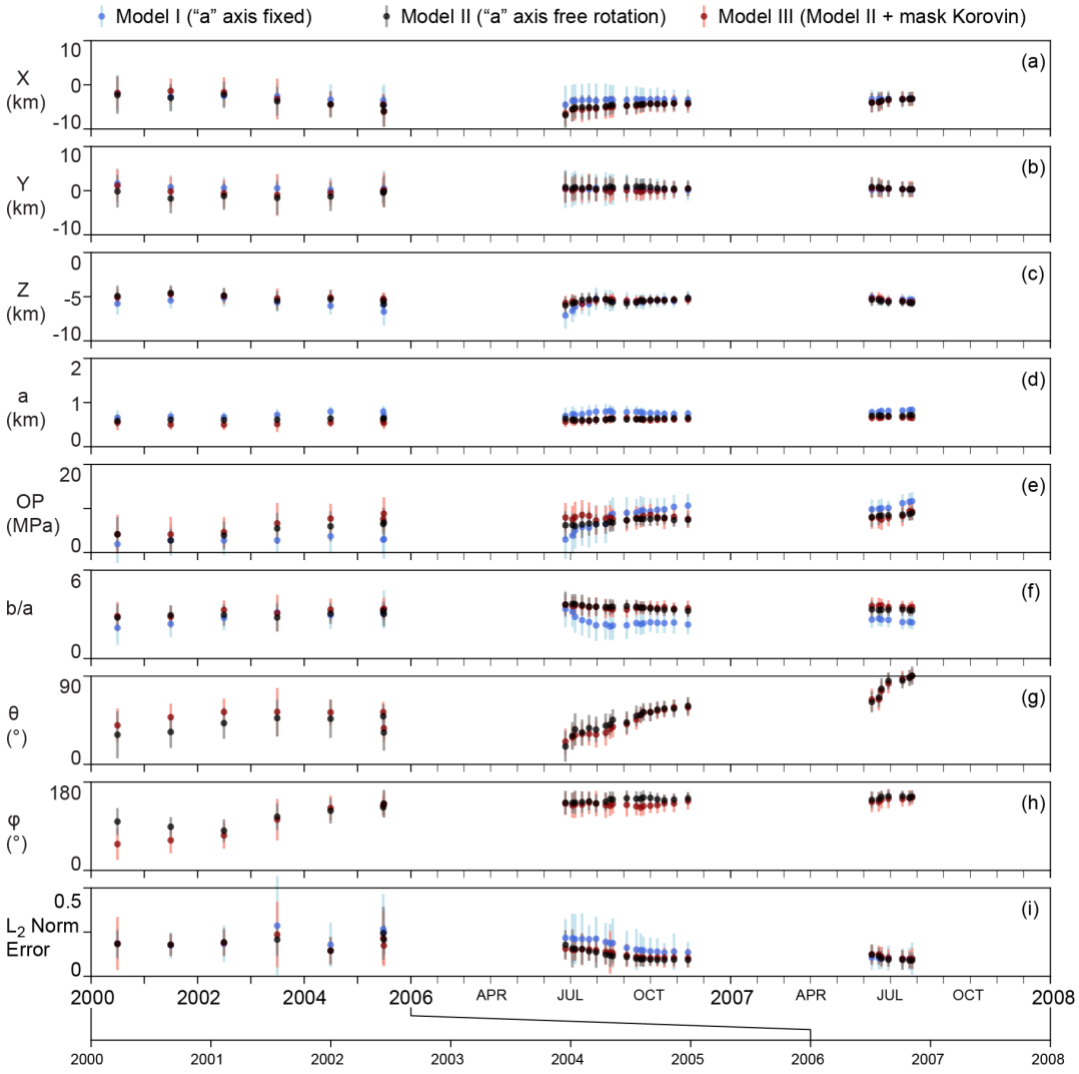

Figure 6.5 Model state evolution by the EnKF. The parameter estimation of the pressure source for each InSAR acquisition includes (a) X-location, (b) Y-location, (c) Z-location, (d) half-height, (e) overpressure, (f) ratio between half-width and half-height, (g) dipping angle of half-width axis, and (h) dipping direction of the ellipsoid. (i) The L2 norm error of surface displacement (e.g., Zhan et al., 2017) shows the overall misfit between models and data. The colored circles are the mean values of the ensemble members, and the bars are the standard deviations. Different colors represent different models. Blue shows the model (Model I) with an upright "a" axis ($\theta = 90°$ in Fig. 6.3). Black shows the model (Model II) with a freely rotating ellipsoid. Red shows the model (Model III) constrained by masked InSAR data, where the displacement around Korovin volcano is not used in the data assimilation (Fig. C.4).

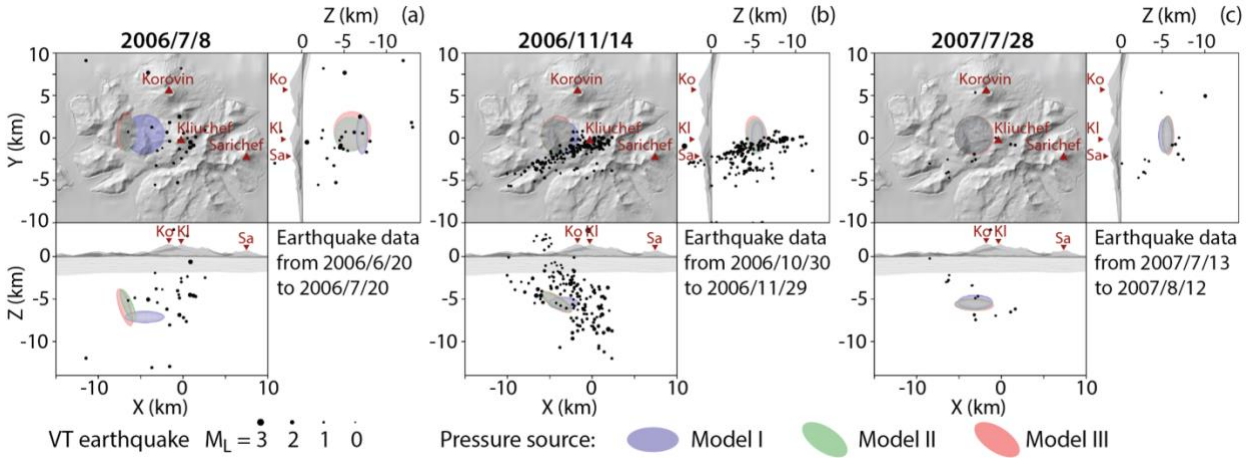

Figure 6.6 Geometry of the pressure sources at three different epochs of InSAR timeseries. (a) 2006/7/8, the beginning of the volcanic unrest. (b) 2006/11/14, prior to the eruption. (c) 2007/7/28, 7 months after the eruption. The colored ellipses are the projections of the pressure sources on the XY-, ZY-, and XZ-planes. The blue, green, and red pressure sources represent the ensemble averages of Model I, II, and III at the given times. The volcano-tectonic (VT) earthquakes within a range of 15 days before and after the InSAR epochs are plotted as black dots.

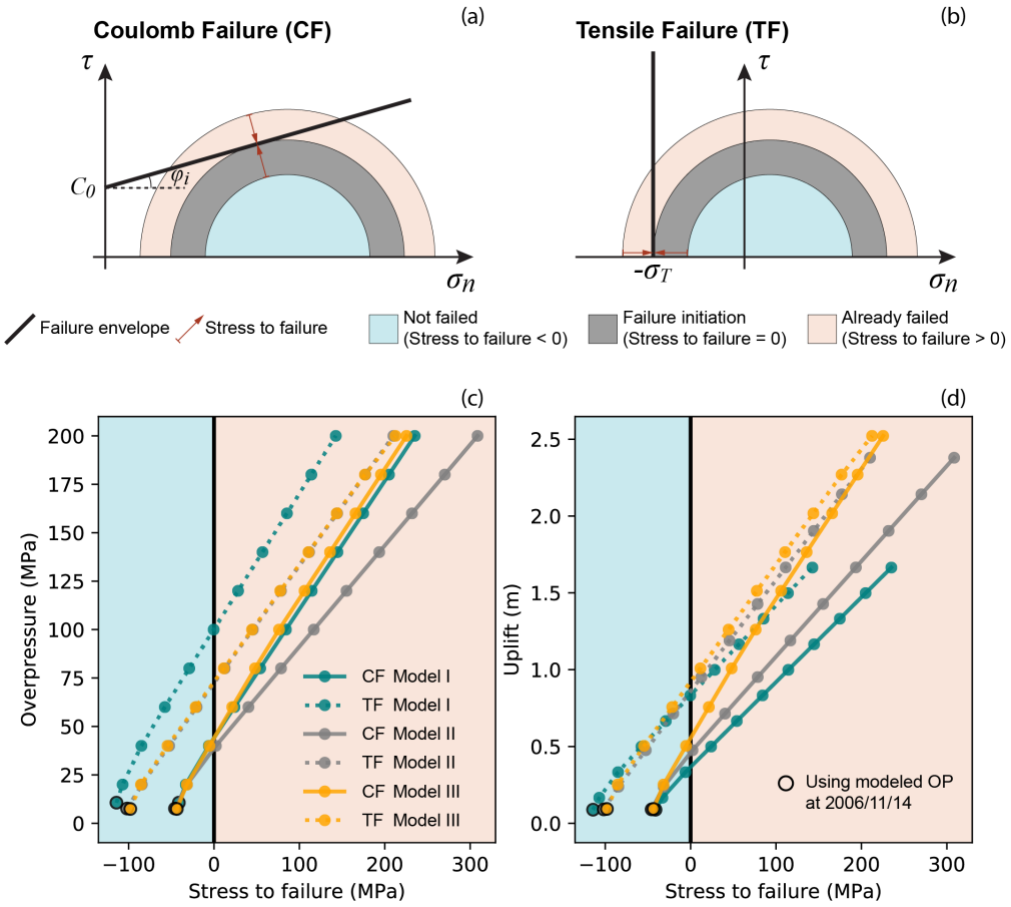

Figure 6.7 The potential of failure occurring at the boundary of the pressure source. (a) and (b) illustrate Coulomb and tensile failure criteria. The possibility of failure is expressed as "stress to failure" (CF and TF). Mohr circles defined by normal stress (σn) and shear stress (τ). Φi and $C0$ are the internal friction angle and cohesion for Coulomb failure. σT is the tensile strength. (c) The "stress to failure" varies with overpressure (c) and surface displacement (d). The colored solid or dotted lines represent the results from different models with different failure types. The black solid illustrate the initiation of failure along with the chamber. All plots are calculated by using the geometry of the best-fit pressure sources at 2006/11/14 in respect of different tests (i.e., Model I, II, and III). Different overpressures are used to test their relationship with the "stress to failure." Therefore, the values of overpressure can be unreasonably high. Only the points with black circles show the overpressure (OP) constrained by the InSAR data on 2006/11/14.

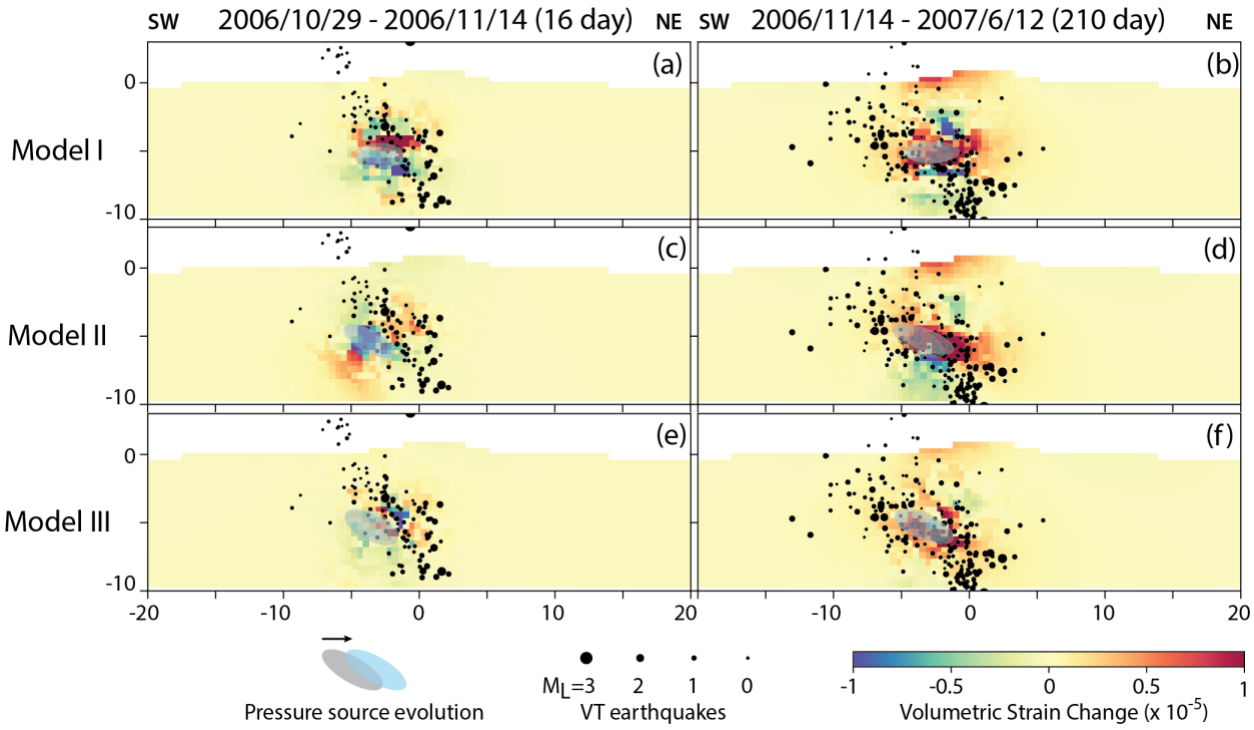

Figure 6.8 Volumetric strain changes within the Amlia-Amukta fault during a time period between different epochs of InSAR timeseries. (a), (c), and (e) show the strain changes during two InSAR epochs (2006/10/29 & 2006/11/14) prior to the eruption. (b), (d), and (f) show the strain changes between the time prior to the eruption (2006/11/14) and 6 months after the eruption (2007/6/12) due to the lack of InSAR acquisition. Different rows represent the results from different models. The grey and light blue ellipses are the projections of the pressure sources on the fault plane at the beginning and end of the time period. The VT earthquakes which occur within a 2-km-distance to the fault and during the time period are plotted as black dots.

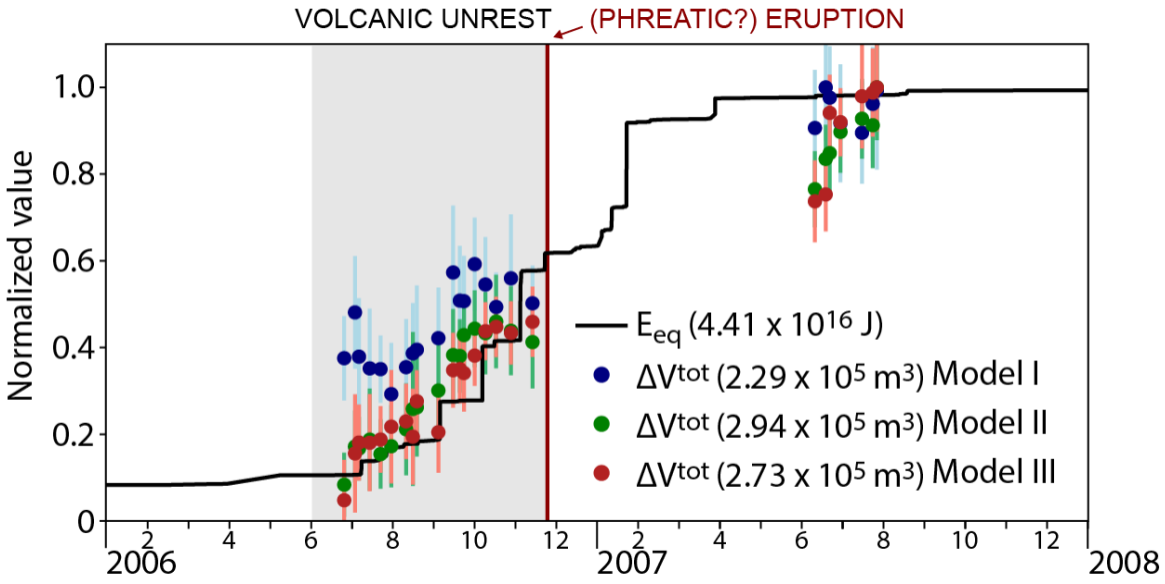

Figure 6.9 Comparison between VT earthquake energy and fault dilatancy. Time series of total volume change (ΔV^{tot}) of the Amlia-Amukta (AA) fault calculated by ensemble models are shown as colored dots with error bars. The error bar represents the uncertainty of the ensemble models according to the displacement misfit (i.e., L2 norm error). The solid black line shows the accumulated energy releasing (E_{eq}) of the VT-earthquakes occurring within a 2-km-distance to the AA fault since 2005/1. In the plots, the time series of ΔV^{tot} and E_{eq} are normalized by their maximum values respectively as shown in the parenthesis.

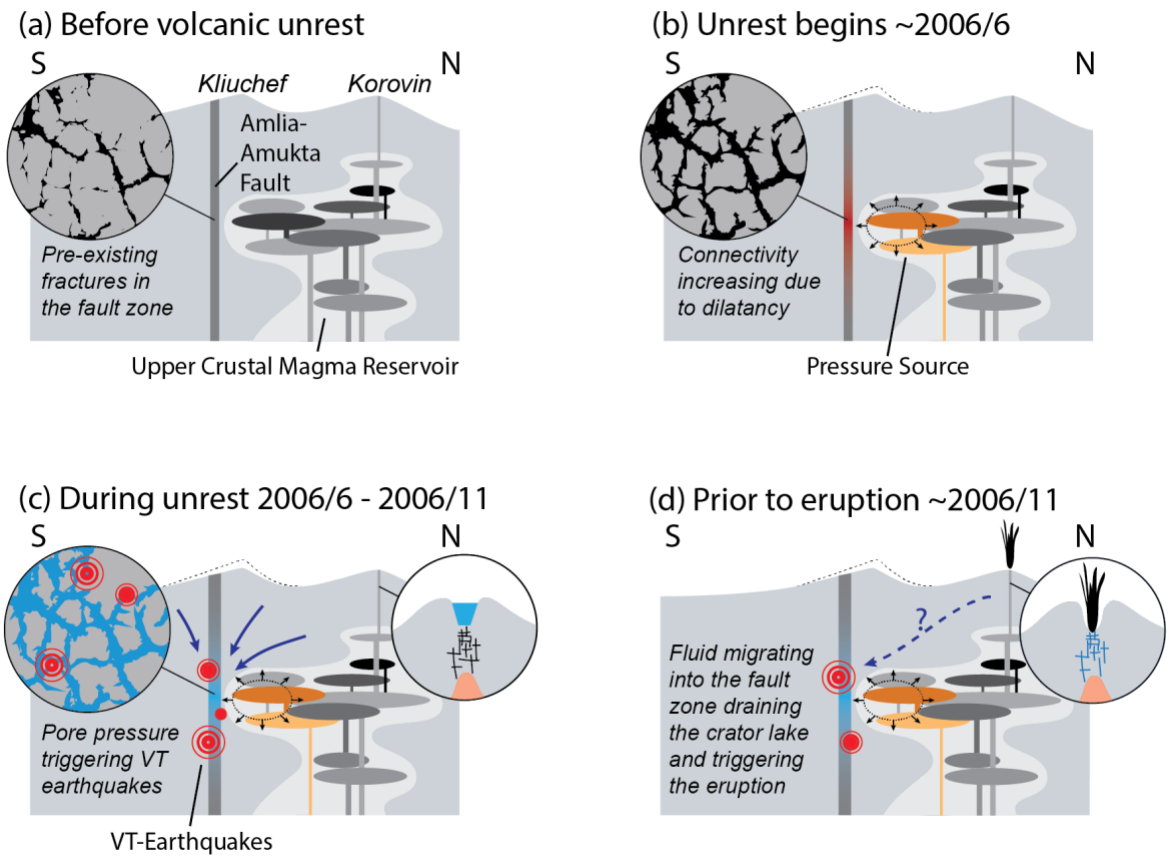

Figure 6.10 Cartoons illustrating the interaction between the magma reservoir and Amlia-Amukta fault during the volcanic unrest and its implication to the 2006/11/25 eruption. (a) Before 2005-2007 volcanic unrest, the Atka volcanic center has developed a complicated upper crustal magma reservoir generating a series of Quaternary volcanic activities (Myers et al., 2002). The magma reservoir is likely composed of a series of poor communicating magma body and crystal mush (modified after Myers et al., 2002). The Amlia-Amukta (AA) Fault is a pre-existing weak zone with fractures and pores. (b) When the volcanic unrest begins around June 2006, a pressure source due to possible melt/fluid injection or crystal fractionation generated surface deformation and the dilatancy in some parts of the AA fault, causing connectivity of the fault to increase. (c) The fluid (e.g., water or brine) can migrate into the fault zone where the permeability is increased. Pore pressure elevation can trigger the VT earthquakes around the AA fault zone. (d) Once the fluid is migrated into the fault zone, the crater lake at Korovin drained according to the report from USGS (Neal et al., 2008). A phreatic eruption may be triggered due to the drop of the water table.

6.8 Acknowledgements

We are grateful for helpful discussions with J. Power, B. Singer, C. Lundstrom, L. Liu, S. Marshak, D. Peng, J. Albright, H. Cabaniss, R. Goldman, and the UIUC Geodynamics Group. The development of a high-performance computing data assimilation framework for forecasting volcanic unrest is supported by grants from NASA (19-EARTH19R-0104 – Zhan, 18-ESI18-0002 – Gregg/Lu) and the National Science Foundation (OCE 1834843, EAR 1752477 – Gregg). All data and modeling results will be available at "Figshare".

6.9 References

Acocella, V. (2014). Structural control on magmatism along divergent and convergent plate boundaries: Overview, model, problems. *Earth-Science Reviews*, *136*(Supplement C), 226–288. https://doi.org/10.1016/j.earscirev.2014.05.006

Albright, J. A., Gregg, P. M., Lu, Z., & Freymueller, J. T. (2019). Hindcasting Magma Reservoir Stability Preceding the 2008 Eruption of Okmok, Alaska. *Geophysical Research Letters*, *46*(15), 8801–8808. https://doi.org/10.1029/2019GL083395

Anderson, K., & Segall, P. (2013). Bayesian inversion of data from effusive volcanic eruptions using physics-based models: Application to Mount St. Helens 2004-2008. *Journal of Geophysical Research-Solid Earth*, *118*(5), 2017–2037. https://doi.org/10.1002/jgrb.50169

Bato, M. G., Pinel, V., & Yan, Y. (2017). Assimilation of Deformation Data for Eruption Forecasting: Potentiality Assessment Based on Synthetic Cases. *Frontiers in Earth Science*, *5*. https://doi.org/10.3389/feart.2017.00048

Bonaccorso, A., & Davis, P. M. (1999). Models of ground deformation from vertical volcanic conduits with application to eruptions of Mount St. Helens and Mount Etna. *Journal of Geophysical Research: Solid Earth*, *104*(B5), 10531–10542. https://doi.org/10.1029/1999JB900054

Cashman, K. V., & Giordano, G. (2014). Calderas and magma reservoirs. *Journal of Volcanology and Geothermal Research*, *288*, 28–45. https://doi.org/10.1016/j.jvolgeores.2014.09.007

Charco, M., & Galán del Sastre, P. (2014). Efficient inversion of three-dimensional finite element models of volcano deformation. *Geophysical Journal International*, *196*(3), 1441–1454. https://doi.org/10.1093/gji/ggt490

Ciccotti, M., & Mulargia, F. (2004). Differences between static and dynamic elastic moduli of a typical seismogenic rock. *Geophysical Journal International*, *157*(1), 474–477. https://doi.org/10.1111/j.1365-246X.2004.02213.x

Collettini, C., Niemeijer, A., Viti, C., & Marone, C. (2009). Fault zone fabric and fault weakness. *Nature*, *462*(7275), 907–910. https://doi.org/10.1038/nature08585

Currenti, G., Del Negro, C., & Ganci, G. (2007). Modelling of ground deformation and gravity fields using finite element method: an application to Etna volcano. *Geophysical Journal International*, *169*(2), 775–786. https://doi.org/10.1111/j.1365-246X.2007.03380.x

Currie, C. A., & Hyndman, R. D. (2006). The thermal structure of subduction zone back arcs. *Journal of Geophysical Research: Solid Earth*, *111*(B8). https://doi.org/10.1029/2005JB004024

Del Negro, C., Currenti, G., & Scandura, D. (2009). Temperature-dependent viscoelastic modeling of ground deformation: application to Etna volcano during the 1993–1997 inflation period. *Physics of the Earth and Planetary Interiors*, *172*(3), 299–309.

Evensen, G. (2003). The Ensemble Kalman Filter: theoretical formulation and practical implementation. *Ocean Dynamics*, *53*(4), 343–367. https://doi.org/10.1007/s10236-003-0036-9

Fliedner, M. M., & Klemperer, S. L. (1999). Structure of an island-arc: Wide-angle seismic studies in the eastern Aleutian Islands, Alaska. *Journal of Geophysical Research: Solid Earth*, *104*(B5), 10667–10694. https://doi.org/10.1029/98JB01499

Fournier, N., & Chardot, L. (2012). Understanding volcano hydrothermal unrest from geodetic observations: Insights from numerical modeling and application to White Island volcano, New Zealand. *Journal of Geophysical Research: Solid Earth*, *117*(B11). https://doi.org/10.1029/2012JB009469

Geist, E. L., Childs, J. R., & Scholl, D. W. (1987). Evolution and petroleum geology of Amlia and Amukta intra-arc summit basins, Aleutian Ridge. *Marine and Petroleum Geology*, *4*(4), 334–352. https://doi.org/10.1016/0264-8172(87)90011-0

Gerbault, M. (2012). Pressure conditions for shear and tensile failure around a circular magma chamber; insight from elasto-plastic modelling. *Geological Society, London, Special Publications*, *367*(1), 111–130. https://doi.org/10.1144/SP367.8

Gregg, P. M., & Pettijohn, J. C. (2016). A multi-data stream assimilation framework for the assessment of volcanic unrest. *Journal of Volcanology and Geothermal Research*, *309*, 63–77. https://doi.org/10.1016/j.jvolgeores.2015.11.008

Gregg, P. M., de Silva, S. L., Grosfils, E. B., & Parmigiani, J. P. (2012). Catastrophic caldera-forming eruptions: Thermomechanics and implications for eruption triggering and maximum caldera dimensions on Earth. *Journal of Volcanology and Geothermal Research*, *241–242*, 1–12. https://doi.org/10.1016/j.jvolgeores.2012.06.009

Gregg, P. M., de Silva, S. L., & Grosfils, E. B. (2013). Thermomechanics of shallow magma chamber pressurization: Implications for the assessment of ground deformation data at active volcanoes. *Earth and Planetary Science Letters*, *384*, 100–108.

https://doi.org/10.1016/j.epsl.2013.09.040

Grosfils, E. B. (2007). Magma reservoir failure on the terrestrial planets: Assessing the importance of gravitational loading in simple elastic models. *Journal of Volcanology and Geothermal Research*, *166*(2), 47–75. https://doi.org/10.1016/j.jvolgeores.2007.06.007

Gutenberg, B. (1956). The energy of earthquakes. *Quarterly Journal of the Geological Society*, *112*(1–4), 1–14. https://doi.org/10.1144/GSL.JGS.1956.112.01-04.02

Hickey, J., Gottsmann, J., & Mothes, P. (2015). Estimating volcanic deformation source parameters with a finite element inversion: The 2001-2002 unrest at Cotopaxi volcano, Ecuador. *Journal of Geophysical Research: Solid Earth*, *120*(3), 1473–1486. https://doi.org/10.1002/2014JB011731

Jaeger, J. C., Cook, N. G. W., & Zimmerman, R. W. (2007). *Fundamentals of rock mechanics* (4th ed). Malden, MA: Blackwell Pub.

Le Mével, H., Gregg, P. M., & Feigl, K. L. (2016). Magma injection into a long-lived reservoir to explain geodetically measured uplift: Application to the 2007–2014 unrest episode at Laguna del Maule volcanic field, Chile. *Journal of Geophysical Research: Solid Earth*, *121*(8), 2016JB013066. https://doi.org/10.1002/2016JB013066

Lu, Z., & Dzurisin, D. (2014). *InSAR Imaging of Aleutian Volcanoes*. Berlin, Heidelberg: Springer Berlin Heidelberg. Retrieved from http://link.springer.com/10.1007/978-3-642-00348-6

Manconi, A., Walter, T. R., Manzo, M., Zeni, G., Tizzani, P., Sansosti, E., & Lanari, R. (2010). On the effects of 3-D mechanical heterogeneities at Campi Flegrei caldera, southern Italy. *Journal of Geophysical Research: Solid Earth*, *115*(B8), B08405. https://doi.org/10.1029/2009JB007099

Marsh, B. D. (1990). Atka, Central Aleutian Islands. *Volcanoes of North America*, 29–31.

Masterlark, T. (2007). Magma intrusion and deformation predictions: Sensitivities to the Mogi assumptions. *Journal of Geophysical Research*, *112*(B6). https://doi.org/10.1029/2006JB004860

Mastin, L. G., & Pollard, D. D. (1988). Surface Deformation and Shallow Dike Intrusion Processes at Inyo Craters, Long Valley, California. *Journal of Geophysical Research: Solid Earth*, 13221–13235. https://doi.org/10.1029/JB093iB11p13221@10.1002/(ISSN)2169-9356.LVCCAL1

McGimsey, R. G., Neal, C. A., Dixon, J. P., & Ushakov, S. (2007). *2005 Volcanic Activity in Alaska, Kamchatka, and the Kurile Islands: Summary of Events and Response of the Alaska Volcano Observatory* (No. 2007–5269). U.S. Geological Survey. Retrieved from https://pubs.usgs.gov/sir/2007/5269/

McGimsey, R. G., Neal, C. A., Dixon, J. P., Malik, N., & Chibisova, M. (2011). *2007 Volcanic Activity in Alaska, Kamchatka, and the Kurile Islands: Summary of Events and Response of the Alaska Volcano Observatory* (No. 2010–5242) (p. 110). Retrieved from https://pubs.usgs.gov/sir/2010/5242/

McTigue, D. F. (1987). Elastic stress and deformation near a finite spherical magma body: Resolution of the point source paradox. *Journal of Geophysical Research*, *92*(B12), 12931. http://dx.doi.org/10.1029/jb092ib12p12931

McTigue, D. F., & Mei, C. C. (1981). Gravity-induced stresses near topography of small slope. *Journal of Geophysical Research: Solid Earth*, *86*(B10), 9268–9278. https://doi.org/10.1029/JB086iB10p09268

Mogi, K. (1958). Relations between the eruptions of various volcanoes and the deformations of

the ground surfaces around them. *Bull. Earthq. Res. Inst., University of Tokyo*, *36*, 99–134.

Moran, S. C., Newhall, C., & Roman, D. C. (2011). Failed magmatic eruptions: late-stage cessation of magma ascent. *Bulletin of Volcanology*, *73*(2), 115–122. https://doi.org/10.1007/s00445-010-0444-x

Myers, J. D., Marsh, B. D., Frost, C. D., & Linton, J. A. (2002). Petrologic constraints on the spatial distribution of crustal magma chambers, Atka Volcanic Center, central Aleutian arc. *Contributions to Mineralogy and Petrology*, *143*(5), 567–586. https://doi.org/10.1007/s00410-002-0356-7

Neal, C. A., McGimsey, R. G., Dixon, J. P., Manevich, A., & Rybin, A. (2008). *2006 Volcanic Activity in Alaska, Kamchatka, and the Kurile Islands: Summary of Events and Response of the Alaska Volcano Observatory* (USGS Numbered Series No. 2008–5214). U.S. Geological Survey. Retrieved from http://pubs.er.usgs.gov/publication/sir20085214

Phillipson, G., Sobradelo, R., & Gottsmann, J. (2013). Global volcanic unrest in the 21st century: An analysis of the first decade. *Journal of Volcanology and Geothermal Research*, *264*, 183–196. https://doi.org/10.1016/j.jvolgeores.2013.08.004

Power, J. A., Friberg, P. A., Haney, M. M., Parker, T., Stihler, S. D., & Dixon, J. P. (2019). *A unified catalog of earthquake hypocenters and magnitudes at volcanoes in Alaska—1989 to 2018* (USGS Numbered Series No. 2019–5037) (p. 17). Reston, VA: U.S. Geological Survey. Retrieved from http://pubs.er.usgs.gov/publication/sir20195037

Roman, D. C., & Cashman, K. V. (2006). The origin of volcano-tectonic earthquake swarms. *Geology*, *34*(6), 457. https://doi.org/10.1130/G22269.1

Roman, D. C., & Cashman, K. V. (2018). Top–Down Precursory Volcanic Seismicity: Implications for 'Stealth' Magma Ascent and Long-Term Eruption Forecasting. *Frontiers in*

Earth Science, *6*. https://doi.org/10.3389/feart.2018.00124

Ryan, W. B. F., Carbotte, S. M., Coplan, J. O., O'Hara, S., Melkonian, A., Arko, R., et al. (2009). Global Multi-Resolution Topography synthesis. *Geochemistry, Geophysics, Geosystems*, *10*(3). https://doi.org/10.1029/2008GC002332

Samsonov, S., d'Oreye, N., & Smets, B. (2013). Ground deformation associated with post-mining activity at the French–German border revealed by novel InSAR time series method. *International Journal of Applied Earth Observation and Geoinformation*, *23*, 142–154. https://doi.org/10.1016/j.jag.2012.12.008

Segall, P. (2013). Volcano deformation and eruption forecasting. *Geological Society, London, Special Publications*, *380*(1), 85–106. https://doi.org/10.1144/SP380.4

Segall, P., Llenos, A. L., Yun, S.-H., Bradley, A. M., & Syracuse, E. M. (2013). Time-dependent dike propagation from joint inversion of seismicity and deformation data. *Journal of Geophysical Research: Solid Earth*, *118*(11), 5785–5804. https://doi.org/10.1002/2013JB010251

Singer, B. S., Myers, J. D., & Frost, C. D. (1992). Mid-Pleistocene lavas from the Seguam volcanic center, central Aleutian arc: closed-system fractional crystallization of a basalt to rhyodacite eruptive suite. *Contributions to Mineralogy and Petrology*, *110*(1), 87–112. https://doi.org/10.1007/BF00310884

Smith, R., Sammonds, P. R., & Kilburn, C. R. J. (2009). Fracturing of volcanic systems: Experimental insights into pre-eruptive conditions. *Earth and Planetary Science Letters*, *280*(1–4), 211–219. https://doi.org/10.1016/j.epsl.2009.01.032

Sparks, R. S. J. (2003). Forecasting volcanic eruptions. *Earth and Planetary Science Letters*, *210*(1–2), 1–15. https://doi.org/10.1016/S0012-821X(03)00124-9

Sparks, R. S. J., Biggs, J., & Neuberg, J. W. (2012). Monitoring Volcanoes. *Science*, *335*(6074), 1310–1311. https://doi.org/10.1126/science.1219485

Starzec, P. (1999). Dynamic elastic properties of crystalline rocks from south-west Sweden. *International Journal of Rock Mechanics and Mining Sciences*, *36*(2), 265–272. https://doi.org/10.1016/S0148-9062(99)00011-X

Yamamoto, M., Kawakatsu, H., Yomogida, K., & Koyama, J. (2002). Long-period (12 sec) volcanic tremor observed at Usu 2000 eruption: Seismological detection of a deep magma plumbing system. *Geophysical Research Letters*, *29*(9), 43-1-43–4. https://doi.org/10.1029/2001GL013996

Yang, X.-M., Davis, P. M., & Dieterich, J. H. (1988). Deformation from inflation of a dipping finite prolate spheroid in an elastic half-space as a model for volcanic stressing. *Journal of Geophysical Research: Solid Earth*, *93*(B5), 4249–4257.

Zhan, Y., & Gregg, P. M. (2017). Data assimilation strategies for volcano geodesy. *Journal of Volcanology and Geothermal Research*, *344*(Supplement C), 13–25. https://doi.org/10.1016/j.jvolgeores.2017.02.015

Zhan, Y., & Gregg, P. M. (2019). How Accurately Can We Model Magma Reservoir Failure With Uncertainties in Host Rock Rheology? *Journal of Geophysical Research: Solid Earth*, *124*(8), 8030–8042. https://doi.org/10.1029/2019JB018178

Zhan, Y., Gregg, P. M., Mével, H. L., Miller, C. A., & Cardona, C. (2019). Integrating Reservoir Dynamics, Crustal Stress, and Geophysical Observations of the Laguna del Maule Magmatic System by FEM Models and Data Assimilation. *Journal of Geophysical Research: Solid Earth*, *124*(12), 13547–13562. https://doi.org/10.1029/2019JB018681

Zhu, W., Gaetani, G. A., Fusseis, F., Montesi, L. G. J., & De Carlo, F. (2011). Microtomography

of Partially Molten Rocks: Three-Dimensional Melt Distribution in Mantle Peridotite. *Science*, *332*(6025), 88–91. https://doi.org/10.1126/science.1202221

CHAPTER 7: CONCLUSIONS AND FUTURE DIRECTIONS

7.1 Conclusions

This Ph.D. thesis has three main conclusions. First, a robust data assimilation framework is critical to accelerating the understanding of physical processes during volcanic unrest. With a powerful data assimilation framework, Models can be tested more effectively and efficiently, so that they can be rapidly updated and hybridized under the constraints of waves by waves of data tsunami nowadays. Second, although geodetic data provides crucial information of host-rock response to the physical condition changes during volcanic unrest, understanding the detailed mechanisms of a volcanic system cannot be accomplished without support from multi-disciplinary observations, experiments, and models. In Chapters 5 and 6, complicated interactions between magma reservoir and a heterogenous host-rock with pre-existing fault zones is explored by integrating surface deformation, seismicity, gravity, and other observations through numerical modeling. Finally, by investigating the mechanisms of volcanic unrest in the Laguna del Maule and Atka volcanic centers, I find that pre-existing structures and pore fluids may play a more critical role in trajecting volcanic unrest than previously thought. Volcanic activity due to the response of a hydrothermal system is sensitive to the physical conditions and changes occurring in a magma reservoir. Understanding the reaction of a hydrothermal system may help us to better decipher early warning signals from a volcano.

7.2 Future directions

7.2.1 Forecasting volcanic unrest precursors

Advanced physical models have shown their potential in forecasting whether, when, where, and how volcanic unrest may lead to an eruption (Zhan et al., 2017; Zhan and Gregg, 2017; Zhan et al., 2019). In particular, surface deformation (Dzurisin, 2003) and volcano-

tectonic (VT) earthquakes (Roman and Cashman, 2006) can reflect strain and stress evolution of the host-rock, which is driven by the pressure of a magma reservoir. Gas emission rates determined by magma decompression can also cause pore-pressure to change to trigger seismicity (Werner et al., 2008).

However, in general cases, the mechanism of earthquake migration prior to eruptions and its relationship with precursory deformation and gas emission is still unclear (Roman and Cashman, 2018). Advanced physical models are needed to explore (1) deformation and stress buildup due to magma reservoir dynamics, (2) failure initiation due to stress or pore-pressure accumulation, (3) failure propagation due to progressive damage, (4) gas emission associated with pressure variation, and (5) fracture healing after volcanic unrest which affects the initial state for the next unrest cycle.

7.2.2 Investigations of magma reservoir dynamics from a crystal mush perspective

When the melt is generated deep within the Earth, some magma may be stored in a reservoir during its migration through the crust. Traditionally, a magma reservoir is described by the conceptual model in which solid host rocks surround a homogenous body of liquid magma (e.g., Tait et al., 1989). However, more evidence suggests that a magma reservoir is a heterogeneous crystal mush, which is a mixture of crystals, liquid, and gas (Sparks and Cashman, 2017). The fraction of liquid melt can vary throughout the magma reservoir and gradually decrease at the transition to the host rock. Therefore, modeling a magma reservoir as a single domain controlled by one uniform constitutive law is potentially inadequate. The behavior of the magma varies depending on temperature, composition, crystallinity, bubble fraction, strain rate, and so on (Gonnermann and Manga, 2007). From a highly heterogenous and dynamic crystal mush perspective, the traditional understanding of magma reservoir dynamics based on the "magma chamber" concept needs to be reconsidered. This paradigm shift is opening new

fundamental questions, such as (1) determining overpressure within a crystal mush, (2) investigating the brittle-ductile transition in a magma reservoir, (3) predicting the geophysical observations obtained from a mushy magma reservoir model (Magee et al., 2018).

7.3 References

Dzurisin D. (2003) A comprehensive approach to monitoring volcano deformation as a window on the eruption cycle. Rev. Geophys. 41. Available at: http://doi.wiley.com/10.1029/2001RG000107.

Gonnermann H. M. and Manga M. (2007) The Fluid Mechanics Inside a Volcano. Annu. Rev. Fluid Mech. 39, 321–356.

Magee C., Stevenson C. T. E., Ebmeier S. K., Keir D., Hammond J. O. S., Gottsmann J. H., Whaler K. A., Schofield N., Jackson C. A.-L., Petronis M. S., O'Driscoll B., Morgan J., Cruden A., Vollgger S. A., Dering G., Micklethwaite S. and Jackson M. D. (2018) Magma Plumbing Systems: A Geophysical Perspective. J. Petrol. 59, 1217–1251.

Roman D. C. and Cashman K. V. (2006) The origin of volcano-tectonic earthquake swarms. Geology 34, 457.

Roman D. C. and Cashman K. V. (2018) Top–Down Precursory Volcanic Seismicity: Implications for 'Stealth' Magma Ascent and Long-Term Eruption Forecasting. Front. Earth Sci. 6. Available at: https://www.frontiersin.org/articles/10.3389/feart.2018.00124/full#B13.

Sparks R. S. J. and Cashman K. V. (2017) Dynamic Magma Systems: Implications for Forecasting Volcanic Activity. Elements 13, 35–40.

Tait S., Jaupart C. and Vergniolle S. (1989) Pressure, gas content and eruption periodicity of a shallow, crystallising magma chamber. Earth Planet. Sci. Lett. 92, 107–123.

Werner C., Hurst T., Scott B., Sherburn S., Christenson B. W., Britten K., Cole-Baker J. and Mullan B. (2008) Variability of passive gas emissions, seismicity, and deformation during crater lake growth at White Island Volcano, New Zealand, 2002–2006. J. Geophys. Res. Solid Earth 113. Available at:

https://agupubs.onlinelibrary.wiley.com/doi/abs/10.1029/2007JB005094.

Zhan Y. and Gregg P. M. (2017) Data assimilation strategies for volcano geodesy. J. Volcanol. Geotherm. Res. 344, 13–25.

Zhan Y., Gregg P. M., Chaussard E. and Aoki Y. (2017) Sequential Assimilation of Volcanic Monitoring Data to Quantify Eruption Potential: Application to Kerinci Volcano, Sumatra. Front. Earth Sci. 5. Available at: https://www.frontiersin.org/articles/10.3389/feart.2017.00108/full.

Zhan Y., Gregg P. M., Mével H. L., Miller C. A. and Cardona C. (2019) Integrating Reservoir Dynamics, Crustal Stress, and Geophysical Observations of the Laguna del Maule Magmatic System by FEM Models and Data Assimilation. J. Geophys. Res. Solid Earth 124, 13547–13562.

APPENDIX A: SUPPLEMENTARY FILE FOR CHAPTER 4

Enclosed are the Supplementary Figures A.1 to A.8 for "How accurately can we model magma reservoir failure with uncertainties in host-rock rheology?[6]"

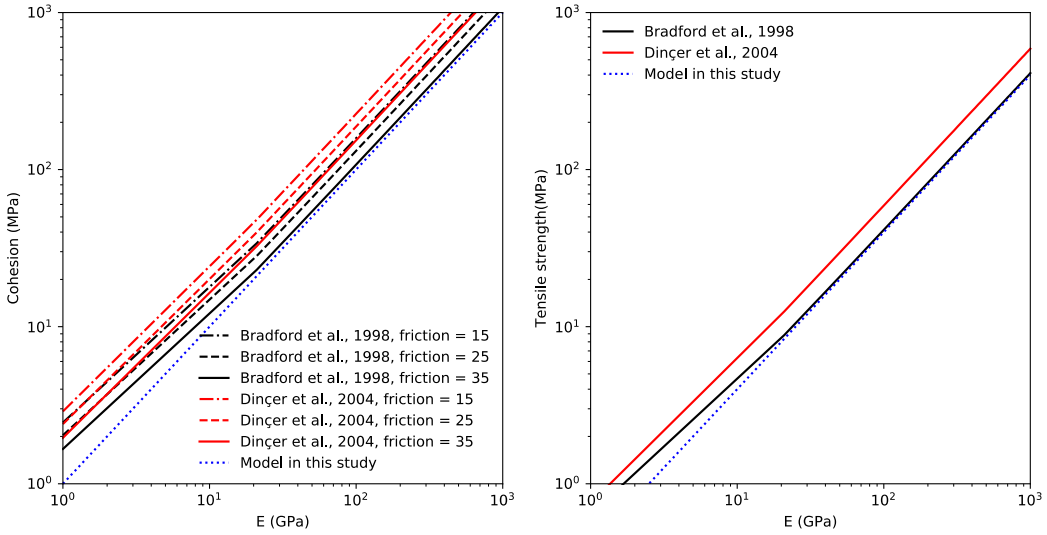

Figure A.1 Relationship between rock strength and Young's modulus. (a) Cohesion as a function of Young's modulus. Cohesion is defined as a function of uniaxial compressive strength (UCS) and internal friction angle (Eq. 3). UCS can be empirically expressed by linear functions of Young's modulus (Bradford et al., 1994; Dinçer et al., 2004). To simplify the calculation, we assume cohesion is E/1000. (b) Tensile strength as a function of Young's modulus, assuming tensile strength is UCS/10.

[6] Published as: Zhan Y. and Gregg P. M. (2019) How Accurately Can We Model Magma Reservoir Failure With Uncertainties in Host Rock Rheology? Journal of Geophysical Research: Solid Earth 124, 8030–8042.

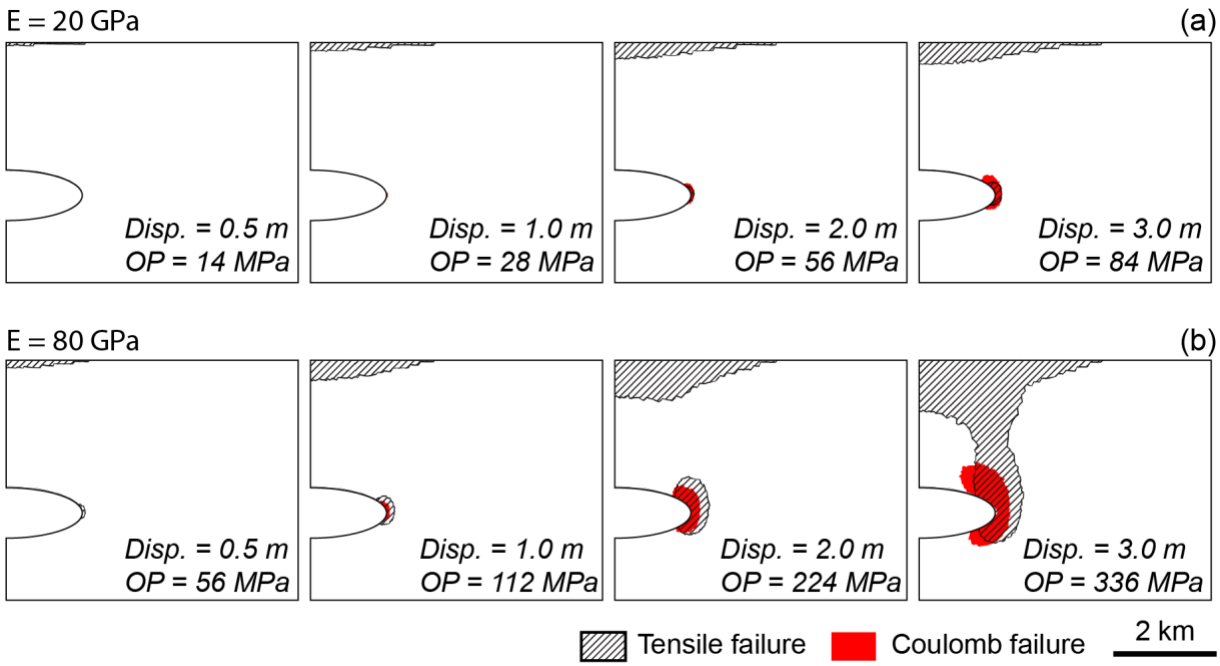

Figure A.2 Failure evolution of the host-rock with low Young's Modulus (a) and high Young's Modulus (b). The shaded red area experiences Coulomb failure, while the hatched region indicates tensile failure. The maximum surface displacement (Disp.) and overpressure (OP) are listed for each step.

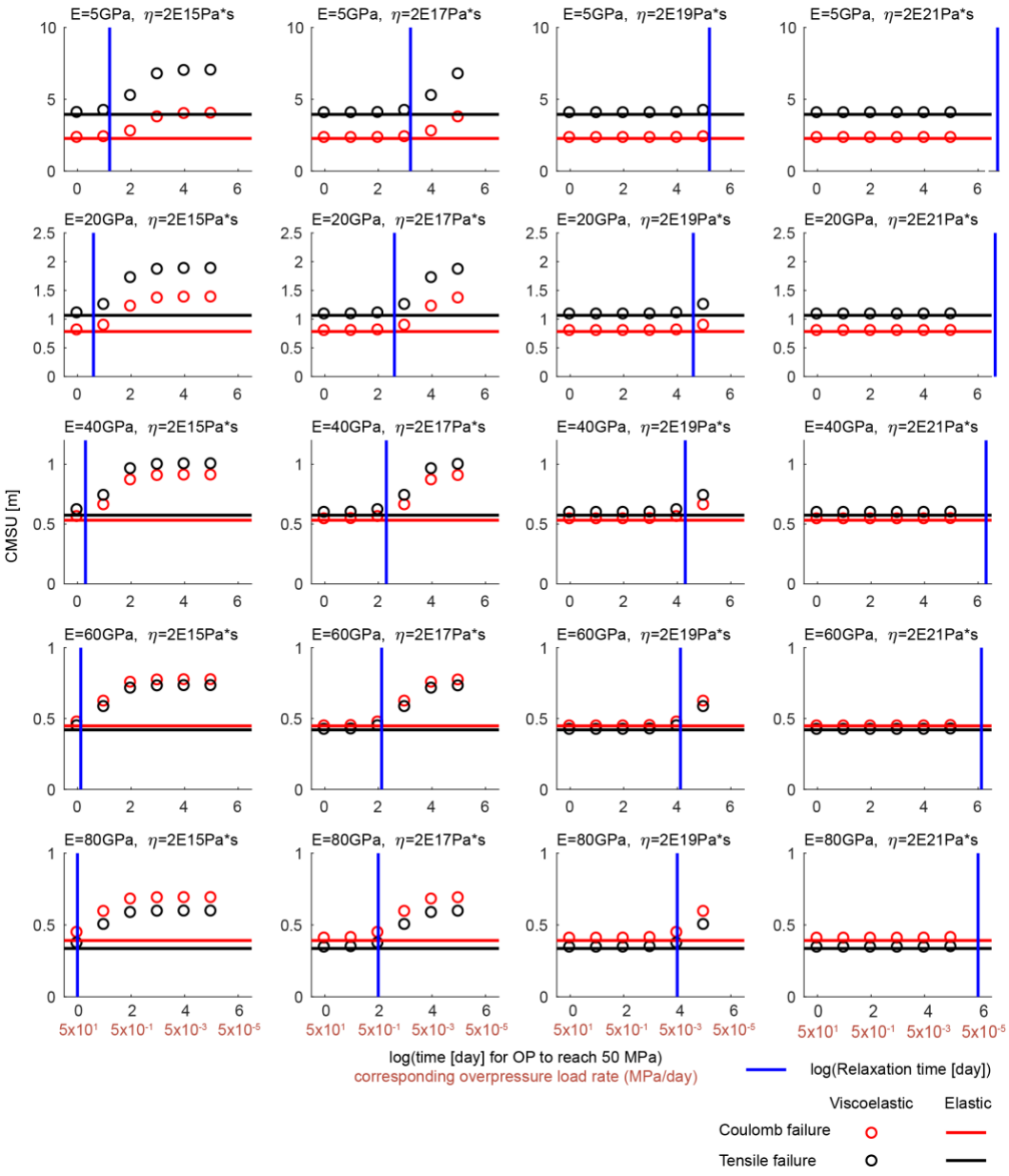

Figure A.3 Critical Maximum Surface Uplift (CMSU) vs. the time span for models with different Young's moduli and viscosities to be pressurized by 50 MPa. The magma chamber depth = 3 km, R1 = 1.5 km, and R2 = 0.5 km. The host-rock Poisson's ratio = 0.25 and internal friction = 25°. The red and black lines show the CMSU prior to Coulomb and tensile failure calculated by instantaneous elastic models. The circle symbols show the CMSU calculated by viscoelastic models. Blue lines indicate the viscoelastic relaxation times of the models. The CMSU calculated by viscoelastic models are much larger than the those resulting from the elastic models once the loading time span exceeds the relaxation times.

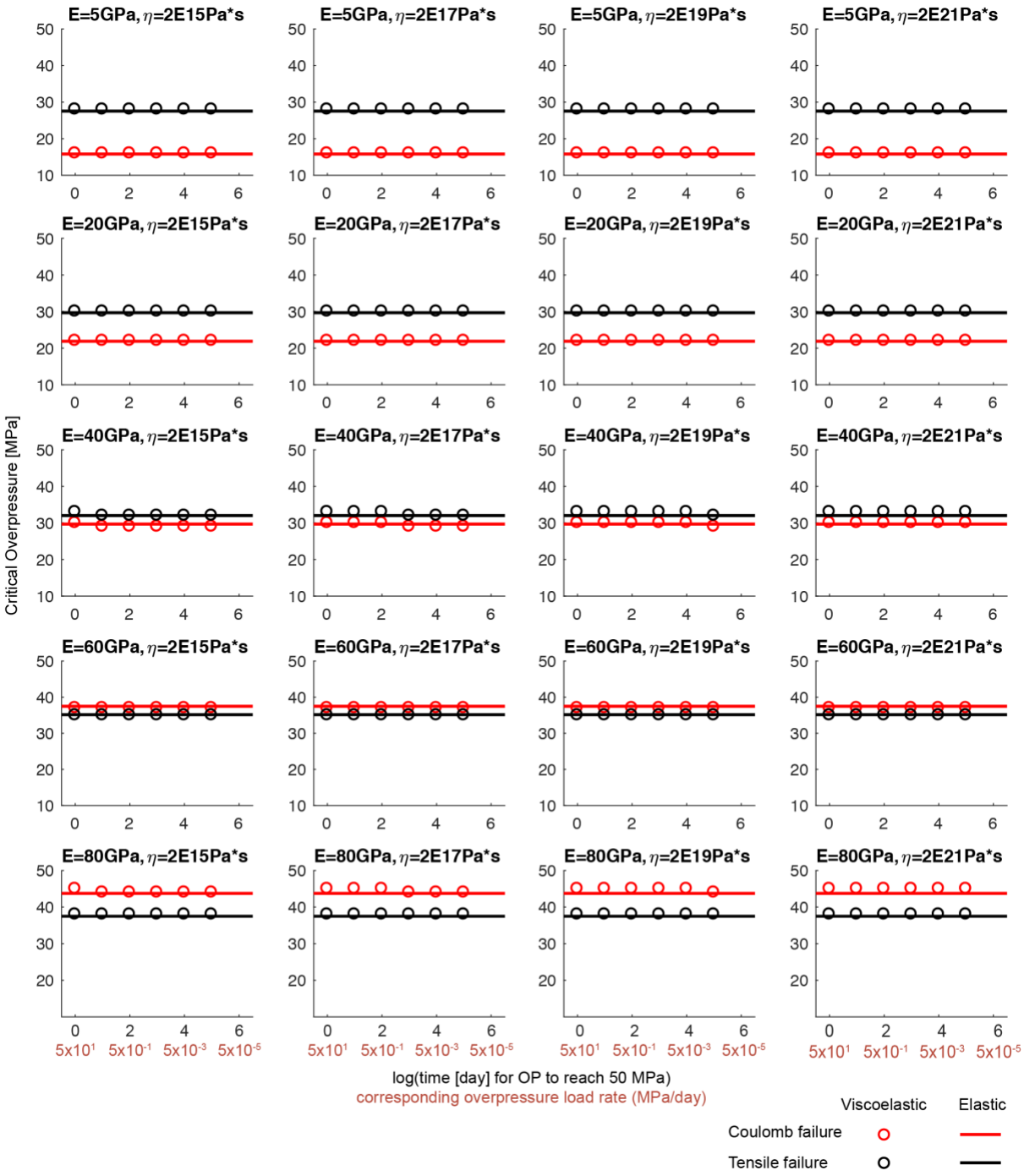

Figure A.4 Critical overpressure vs. the time span for models with different Young's moduli and viscosities to be pressurized by 50 MPa. The magma chamber depth = 3 km, R1 = 1.5 km, and R2 = 0.5 km. The host-rock Poisson's ratio = 0.25 and internal friction = 25°. The red and black lines indicate the critical overpressure prior to Coulomb and tensile failure calculated by elastic models. The circles show the critical overpressure calculated by viscoelastic models. The critical overpressures of the viscoelastic models are approximately the same as the elastic models regardless of the time span and viscosities.

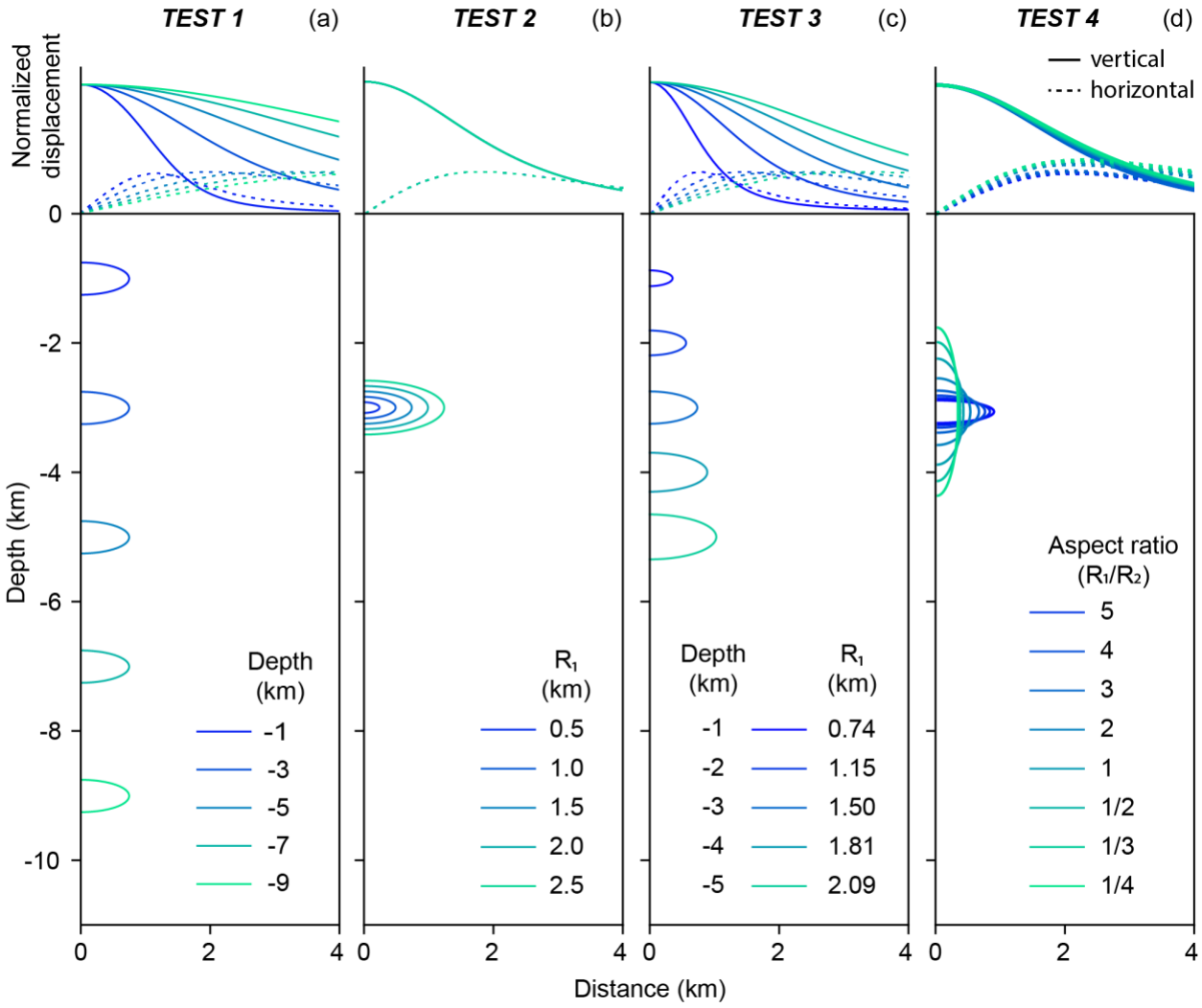

Figure A.5 The model geometries and normalized surface displacements for all tests discussed in the main text (Table 1). For the surface displacement plots, the solid lines are vertical uplift and the dashed lines are horizontal displacement. The displacement of each model is normalized by its maximum uplift to highlight the variation in wavelength.

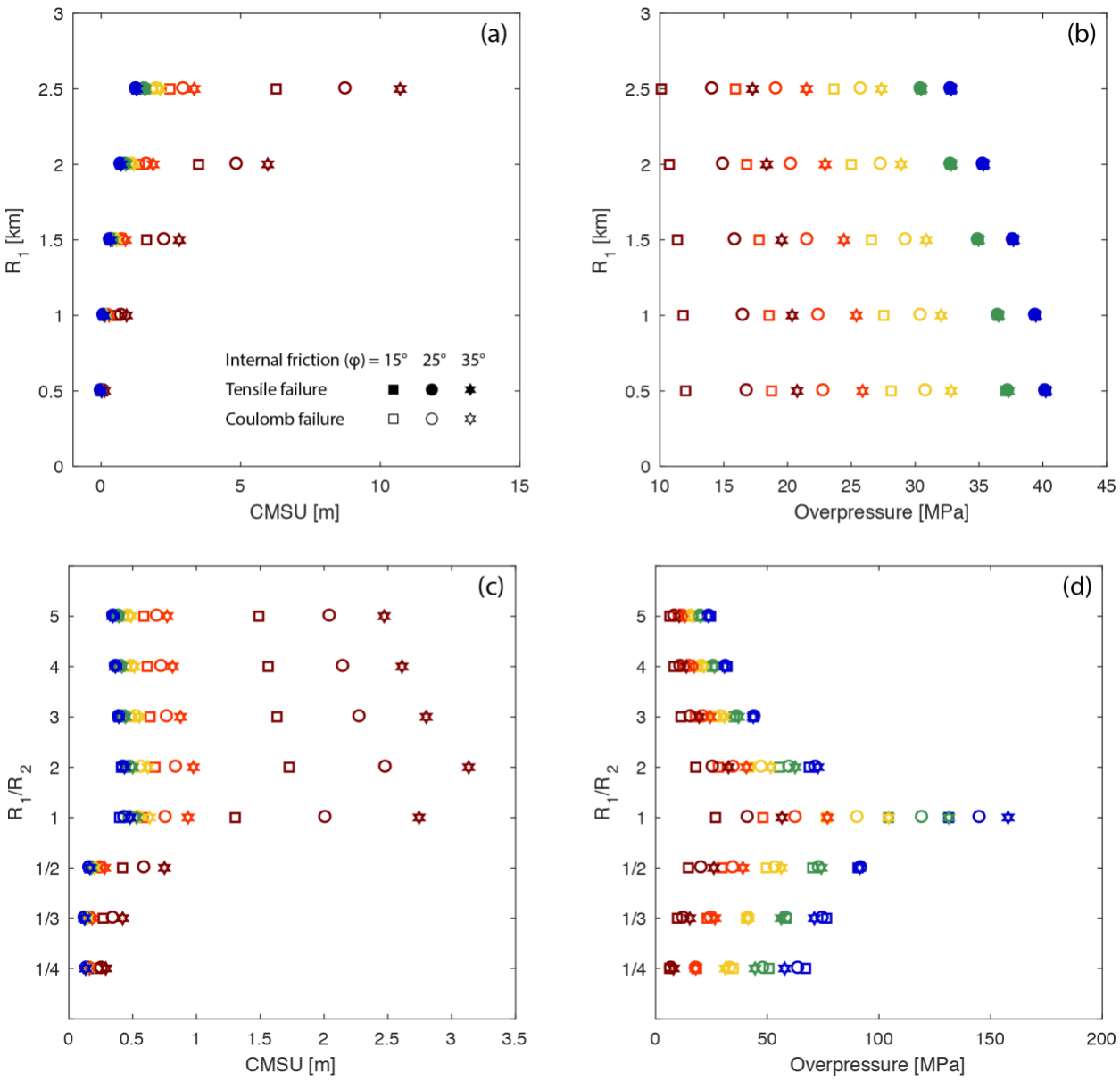

Figure A.6 The effects of Young's modulus and internal friction angle on Coulomb failure with variations in radius (Test 2) and aspect ratio (Test 4). A constant Poisson's ratio ($\nu = 0.25$) is assumed. (a) The Critical Maximum Surface Uplift (CMSU) for models with different sizes of magma chamber. (b) The corresponding overpressures of the magma chamber when failure occurs. The shape of the marker indicates the internal friction angle of the model.

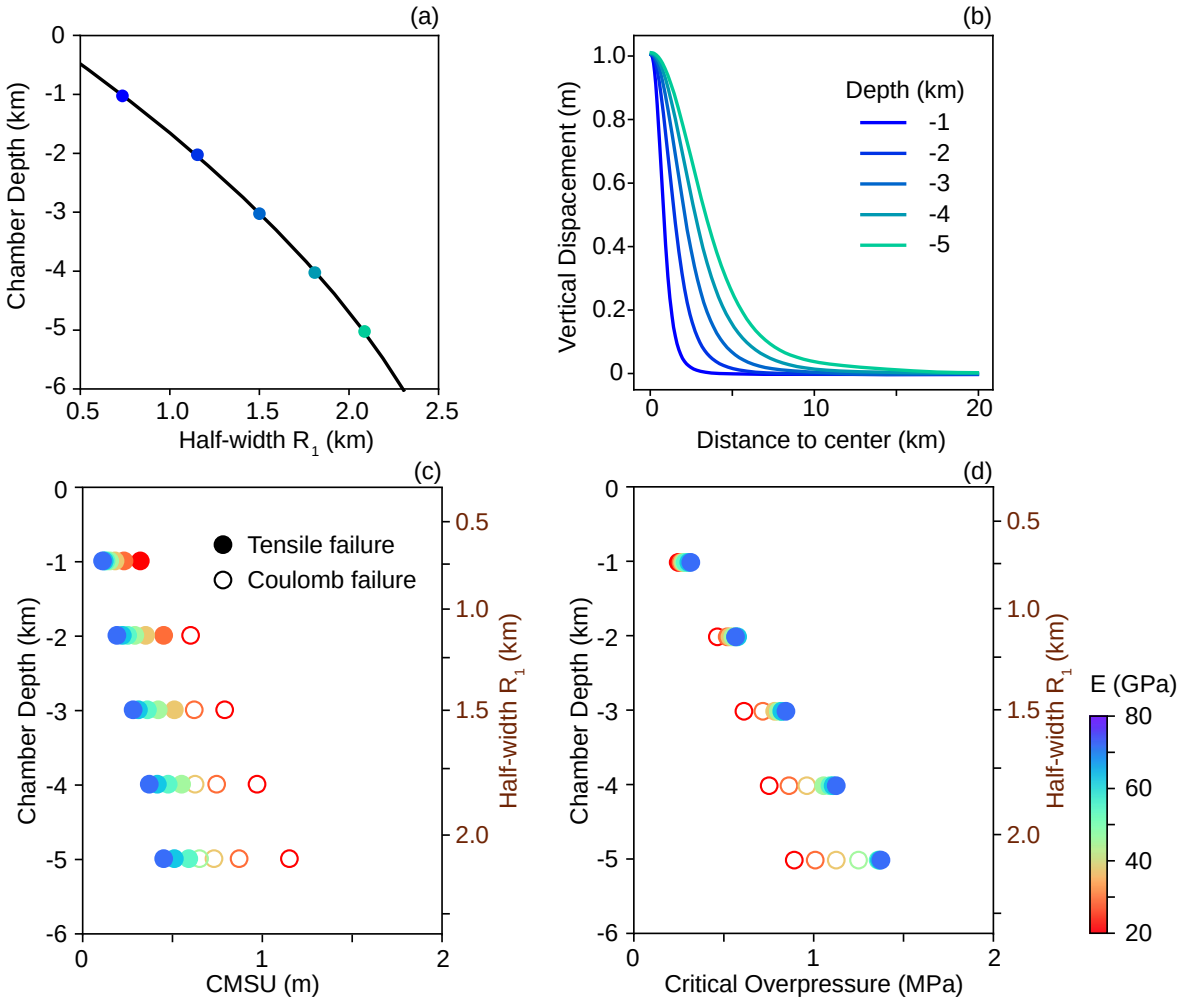

Figure A.7 Results of Test 3 (depth + size). (a) The size of the chamber increases with depth to create the same magnitude of surface uplift. (b) The wavelength of the deformation signal varies with depth, but the magnitude of vertical displacement is held constant. (c) The CMSU gradually increases with the depth and size of the chamber. (d) The corresponding critical overpressures of the magma chamber when failure occurs. The filled circle shows the case that the initial failure is tensile, while the open circle is for Coulomb failure. The color represents the Young's Modulus of the host rock.

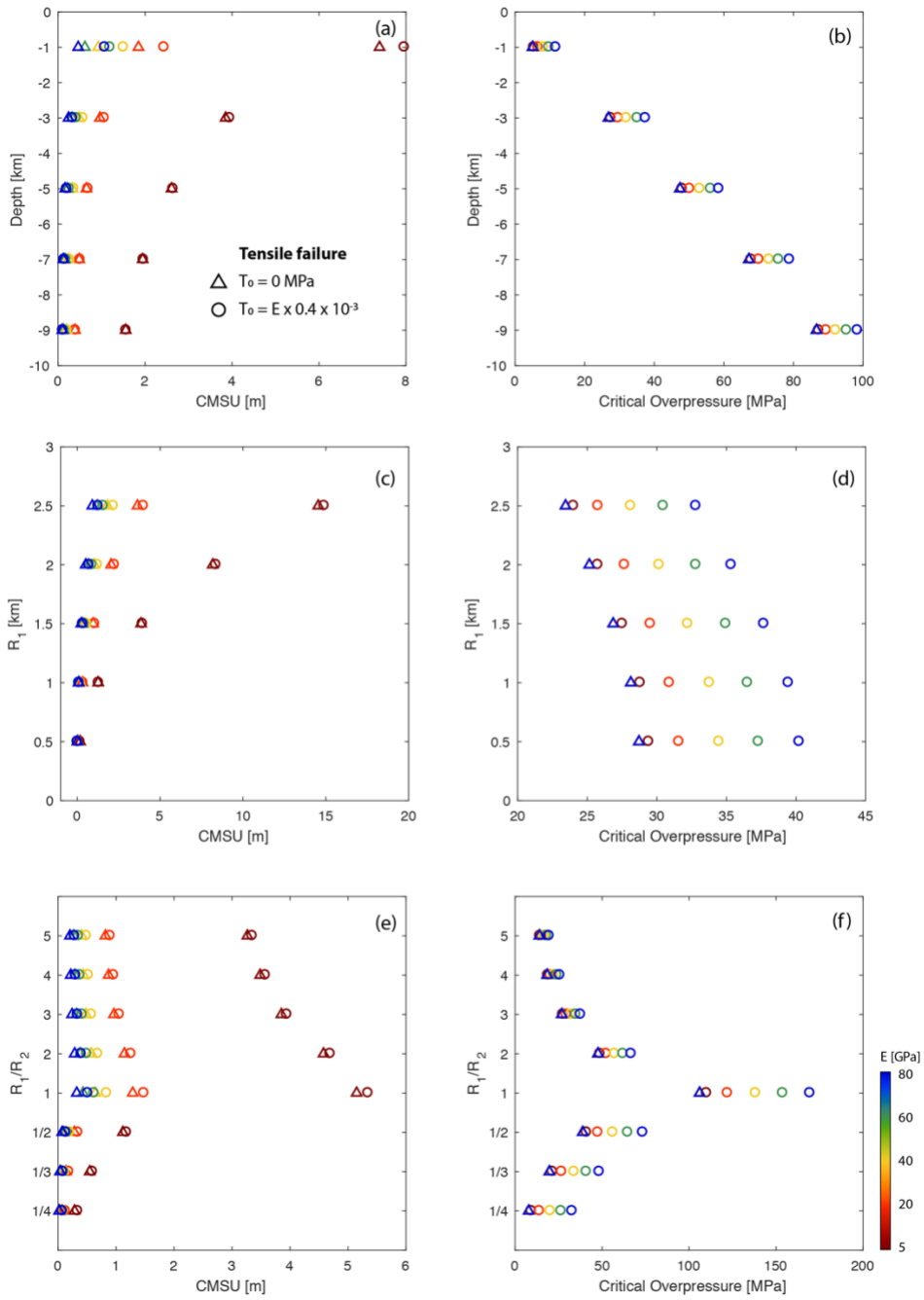

Figure A.8 The effects of tensile strength on tensile failure initiation with variations in (a & b) source depth to center (Elastic Test 1), (c & d) chamber size as described by the half-width (Elastic Test 2), and (e & f) chamber aspect ratio (Elastic Test 4). Circles represent tensile strength of the host-rock with E / 2500. Triangles represent tensile strength of 0. A constant internal friction angle ($\varphi = 25°$) and Poisson's ratio ($\nu = 0.25$) are assumed. The Critical Maximum Surface Uplift (CMSU; a, c, & e) is the maximum value of the surface uplift that is observed before tensile failure is initiated around the magma chamber. The critical overpressures at failure onset are shown in b, d, & f.

APPENDIX B: SUPPLEMENTARY FILE FOR CHAPTER 5

Enclosed are the Supplementary Figures B.1 to B.7, and Table B.1 and B.2 for "Integrating reservoir dynamics, crustal stress, and geophysical observations of the Laguna del Maule magmatic system by FEM models and data assimilation[7]".

[7] Published as: Zhan Y., Gregg P. M., Mével H. L., Miller C. A. and Cardona C. (2019) Integrating Reservoir Dynamics, Crustal Stress, and Geophysical Observations of the Laguna del Maule Magmatic System by FEM Models and Data Assimilation. Journal of Geophysical Research: Solid Earth 124, 13547–13562.

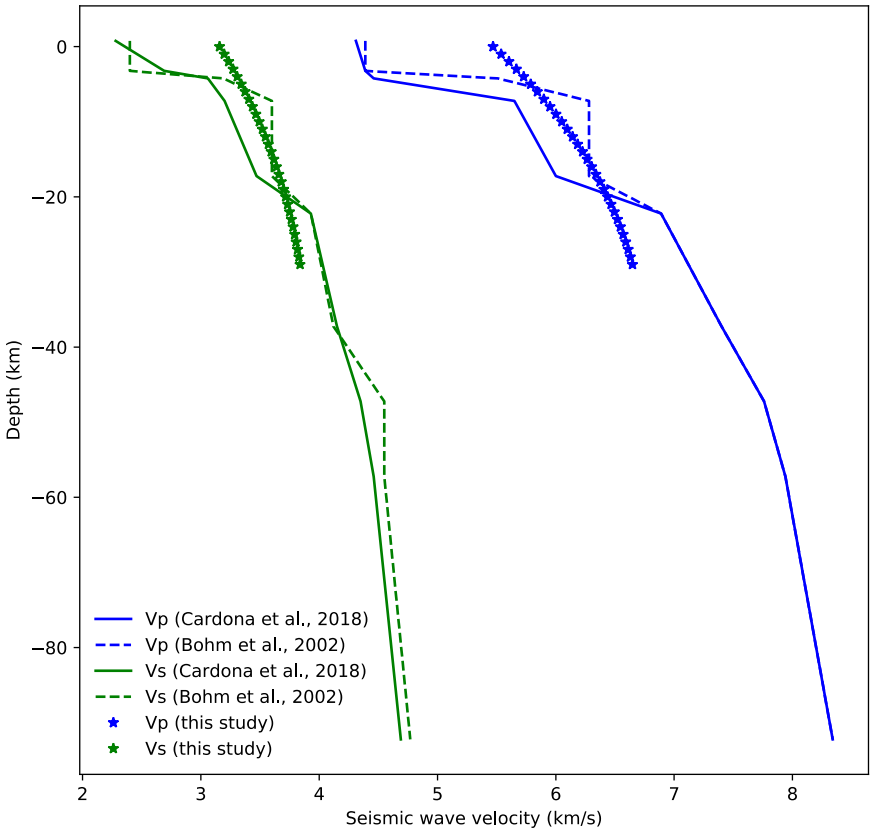

Figure B.1 Comparison of the seismic velocity model of this study and regional velocity models of Laguna del Maule (Bohm et al., 2002; Cardona et al., 2018). Vp and Vs in this model are calculated by assuming the Poisson's ratio and density are constants (Table B.1). The dynamic Young's modulus for calculating the seismic velocity is converted by the static far-field Young's modulus ($\boldsymbol{E_d}$ in Eq. 5.2). We assume the ratio between the dynamic Young's modulus and the static Young's modulus is ~1.5 (Ciccotti & Mulargia, 2004).

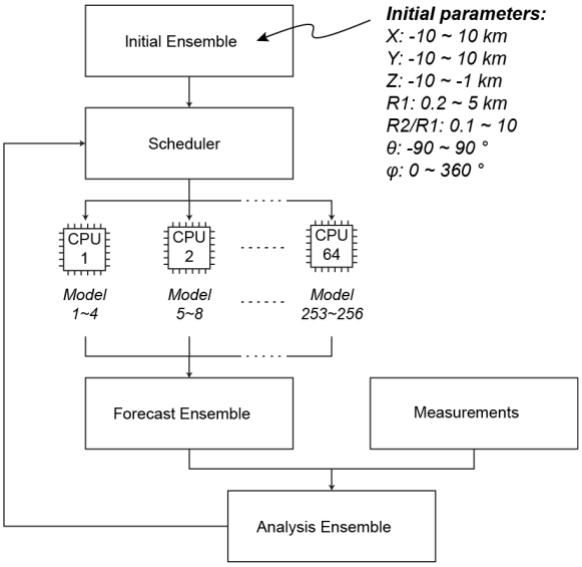

Figure B.2 Workflow of the Ensemble Kalman Filter with the High-Performance Computing.

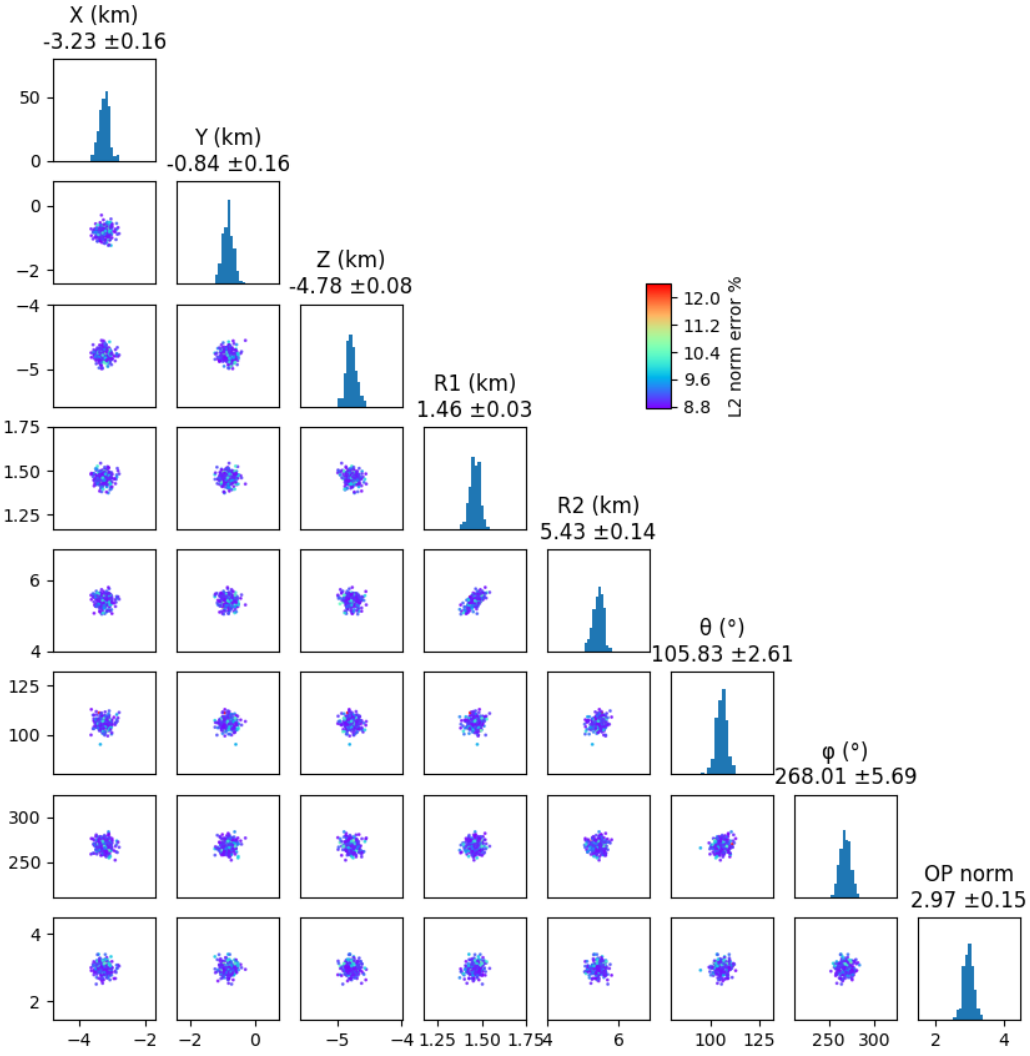

Figure B.3 Distributions and correlations of the ensemble parameters for the magma reservoir at the last iteration.

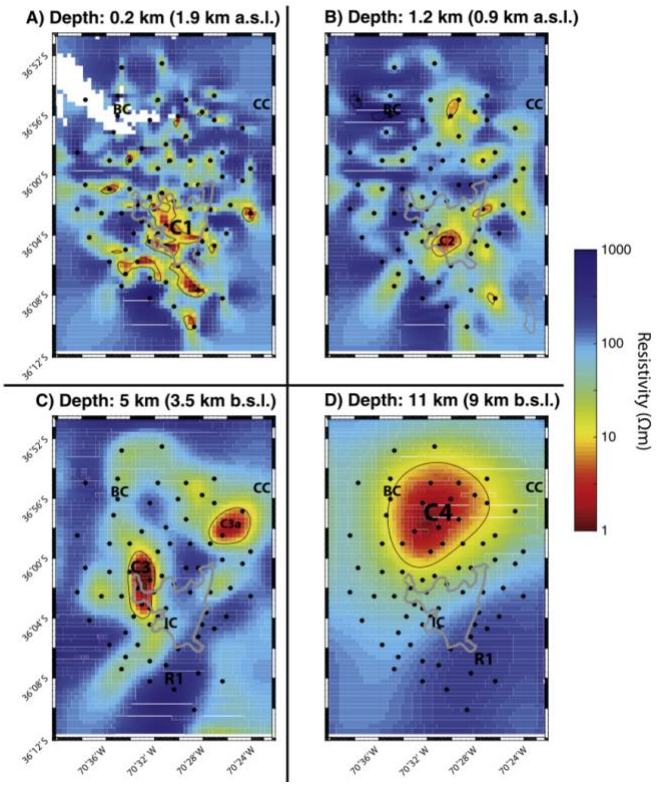

Figure B.4 Modeled resistivity maps by the magnetotelluric data (from Figure 3a-d of Cordell et al., 2018).

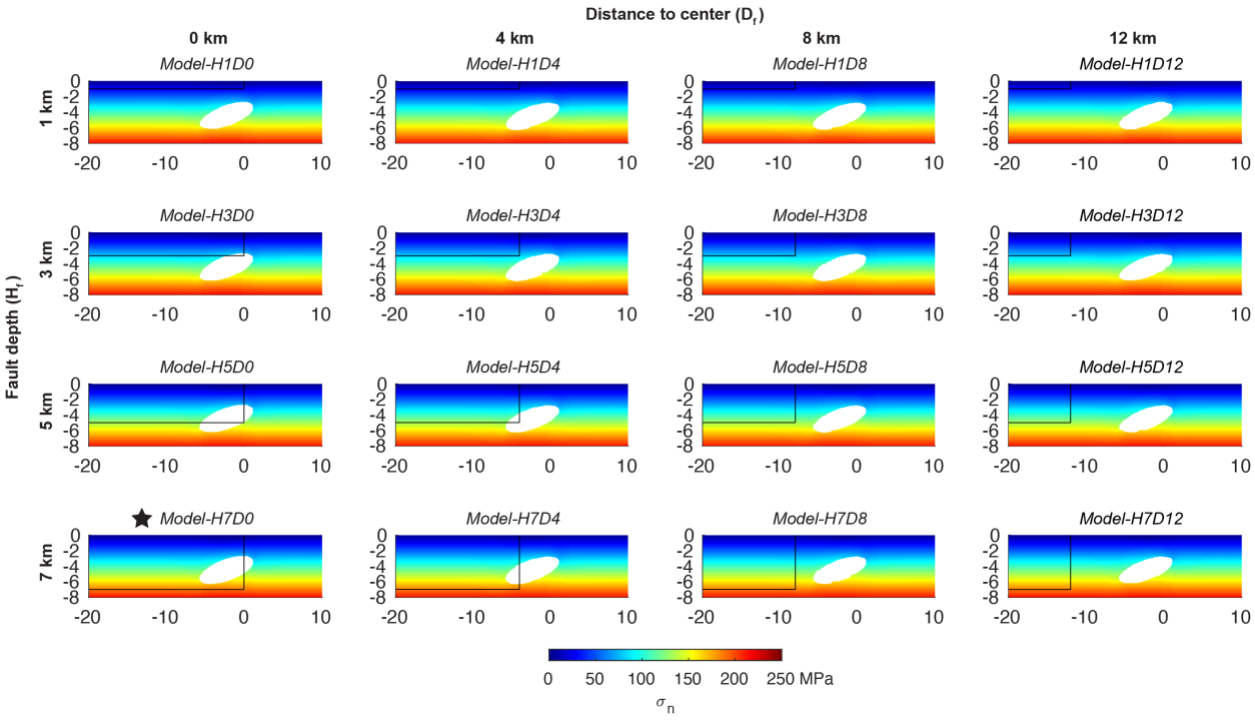

Figure B.5 Normal stresses at the end of 2016 for the models with the fault. Young's modulus of the fault is 20% of the host rock. The width of the fault is 200 m. Model-H7D0 (label with a black star) is used for later calculation.

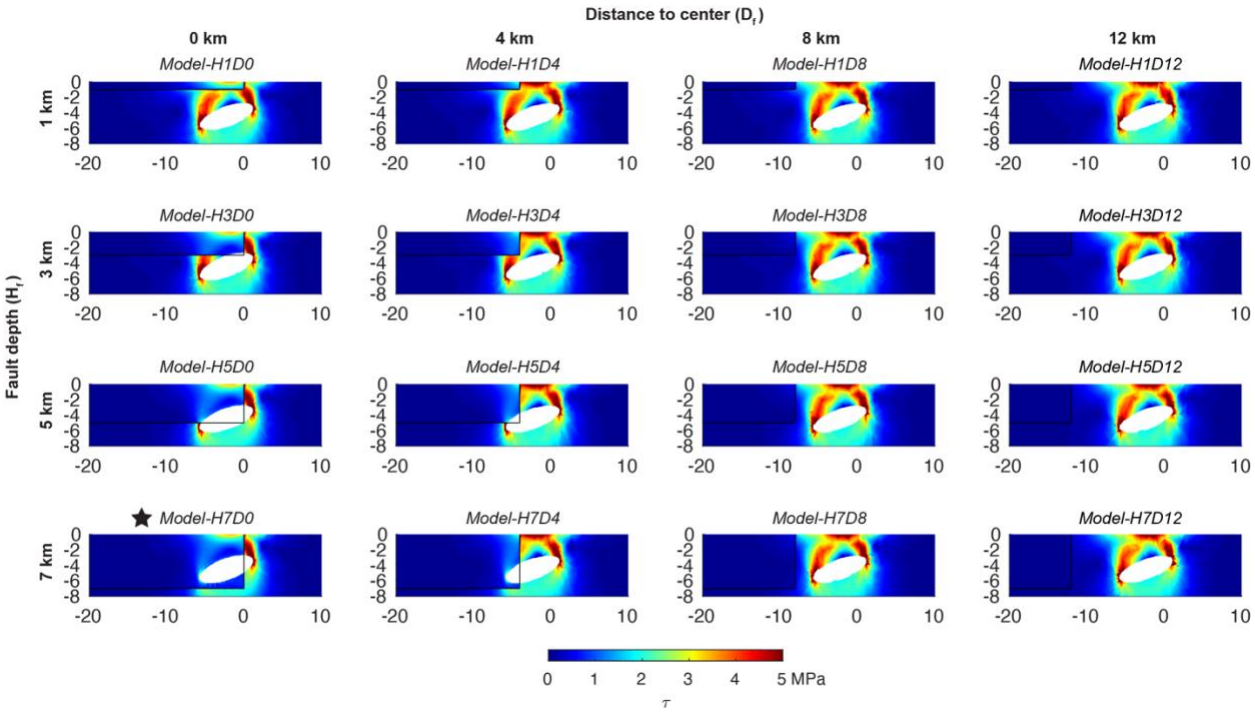

Figure B.6 Maximum shear stresses at the end of 2016 for the models with the fault. Young's modulus of the fault is 20% of the host rock. The width of the fault is 200 m. Model-H7D0 (label with a black star) is used for later calculation.

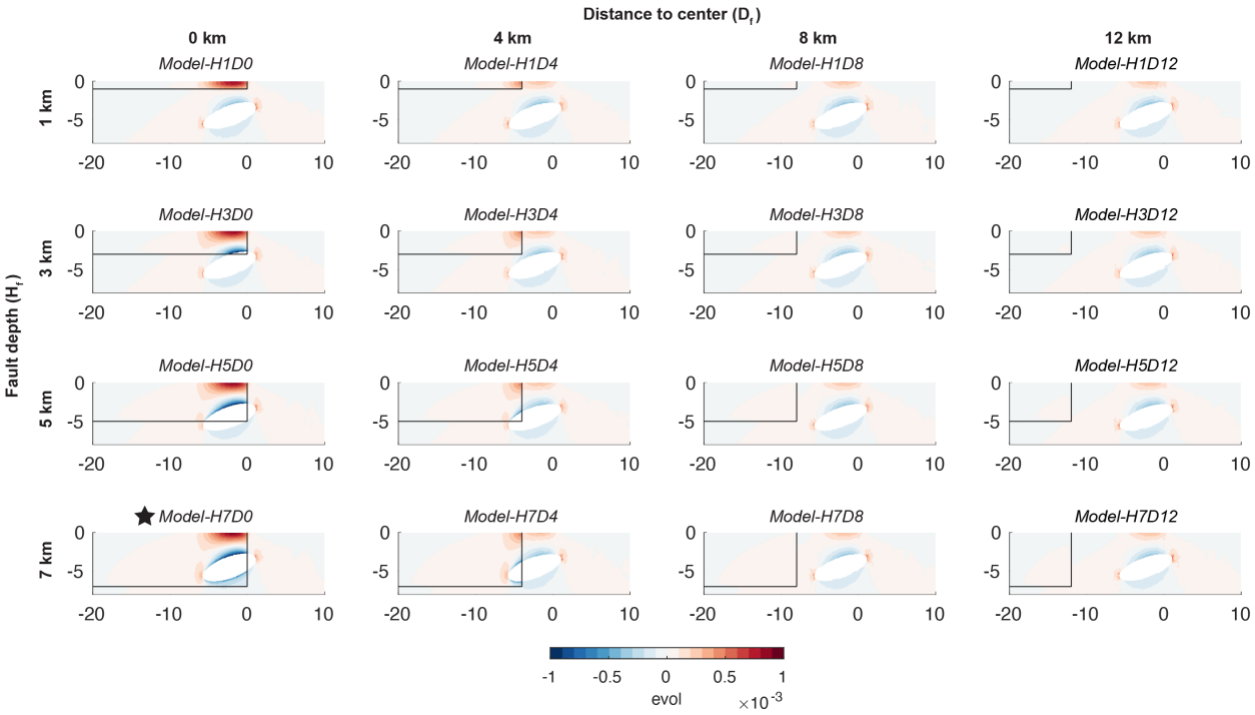

Figure B.7 Volumetric strain at the end of 2016 for the models with the fault. Young's modulus of the fault is 20% of the host rock. The width of the fault is 200 m. Model-H7D0 (label with a black star) is used for later calculation.

Table B.1 Model Parameters

Parameter	Description	Value	Unit
D_1	Constant in Eq. (5.2)	-0.0125	$GPa \cdot km^{-2}$
D_2	Constant in Eq. (5.2)	-1.025	$GPa \cdot km^{-1}$
D_3	Constant in Eq. (5.2)	40.25	GPa
T_0	Surface temperature	0	$°C$
T_c	Magma body temperature	850	$°C$
dT/dz	Geothermal gradient ($z < 0$)	-30	$°C$ / km
Kc	Thermal conductivity	3	$W \cdot m^{-1} \cdot K^{-1}$
C_p	Specific heat capacity	1.25	$kJ \cdot kg^{-1} \cdot K^{-1}$
ρ	Density	2.7×10^3	$kg \cdot m^{-3}$
ν	Poisson's ratio	0.25	1
ϕ_i	Internal friction angle	25	°

Table B.2 Variables

Variable	Description
Magma body parameters	
(X, Y, Z)	Location of the center of the magma body
R_1	Half height of the magma chamber
R_2	Half width of the magma chamber
A	Aspect ratio (R_2/R_1)
φ	Dip direction (clockwise angle from North)
θ	Dip angle
dP	Overpressure (excess to lithostatic pressure)
Fault zone parameters	
D_f	Distance of the end fault to the center (0, 0)
H_f	Fault depth
W_f	Fault thickness
$\frac{E_f}{E_r}$	Ratio of the Young's modulus between the fault and the host-rocks
Stress, strain and failure of the host-rock	
C_0	Cohesion
T_0	Tensile strength
σ_1	Maximum principal stresses
σ_3	Minimum principal stresses
σ_n	Normal stress ($(\sigma_1 + \sigma_3)/2$)
τ	Maximum shear stress ($(\sigma_1 - \sigma_3)/2$)

Reference

Bohm, M., Lüth, S., Echtler, H., Asch, G., Bataille, K., Bruhn, C., et al. (2002). The Southern Andes between 36° and 40°S latitude: seismicity and average seismic velocities. Tectonophysics, 356(4), 275–289. https://doi.org/10.1016/S0040-1951(02)00399-2

Cardona, C., Tassara, A., Gil-Cruz, F., Lara, L., Morales, S., Kohler, P., & Franco, L. (2018). Crustal seismicity associated to rpid surface uplift at Laguna del Maule Volcanic Complex, Southern Volcanic Zone of the Andes. Journal of Volcanology and Geothermal Research, 353, 83–94. **https://doi.org/10.1016/j.jvolgeores.2018.01.009**

Ciccotti, M., & Mulargia, F. (2004). Differences between static and dynamic elastic moduli of a typical seismogenic rock. Geophysical Journal International, 157(1), 474–477. https://doi.org/10.1111/j.1365-246X.2004.02213.x

Cordell, D., Unsworth, M. J., & Díaz, D. (2018). Imaging the Laguna del Maule Volcanic Field, central Chile using magnetotellurics: Evidence for crustal melt regions laterally-offset from surface vents and lava flows. Earth and Planetary Science Letters, 488, 168–180. **https://doi.org/10.1016/j.epsl.2018.01.007**

APPENDIX C: SUPPLEMENTARY FILE FOR CHAPTER 6

Enclosed are the Supplementary Figures C.1 to C.16, and Table C.1 and C.2 for "Modeling magma system evolution during 2006-2007 volcanic unrest of Atka volcanic center, Alaska".

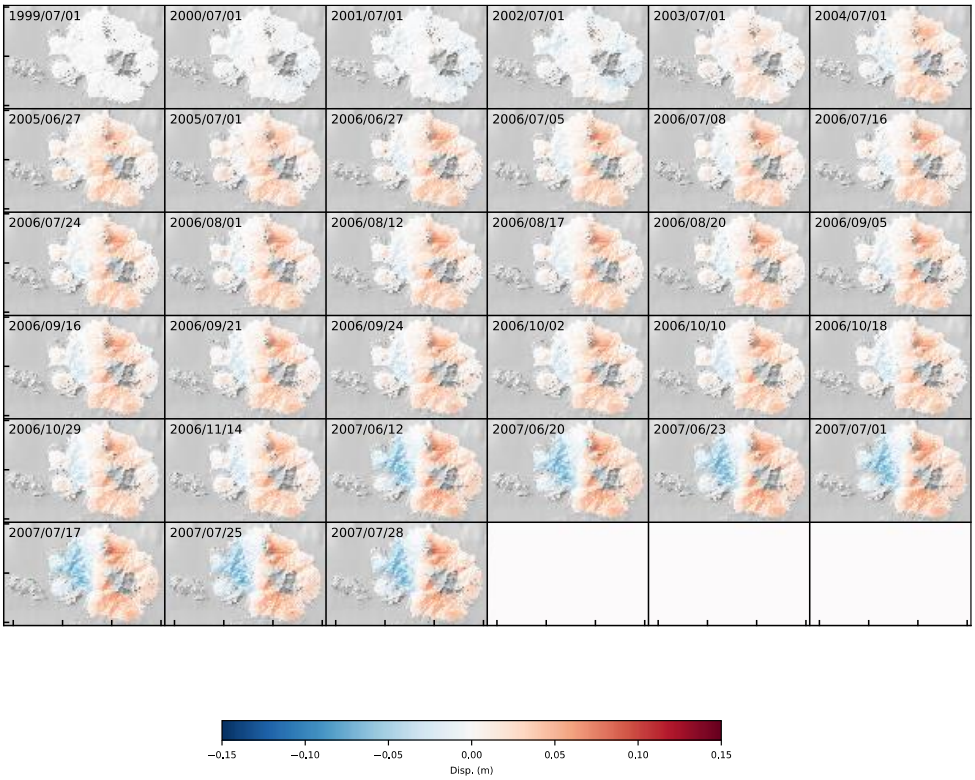

Figure C.1 Timeseries of the East-West component of surface displacement in the Atka volcanic center.

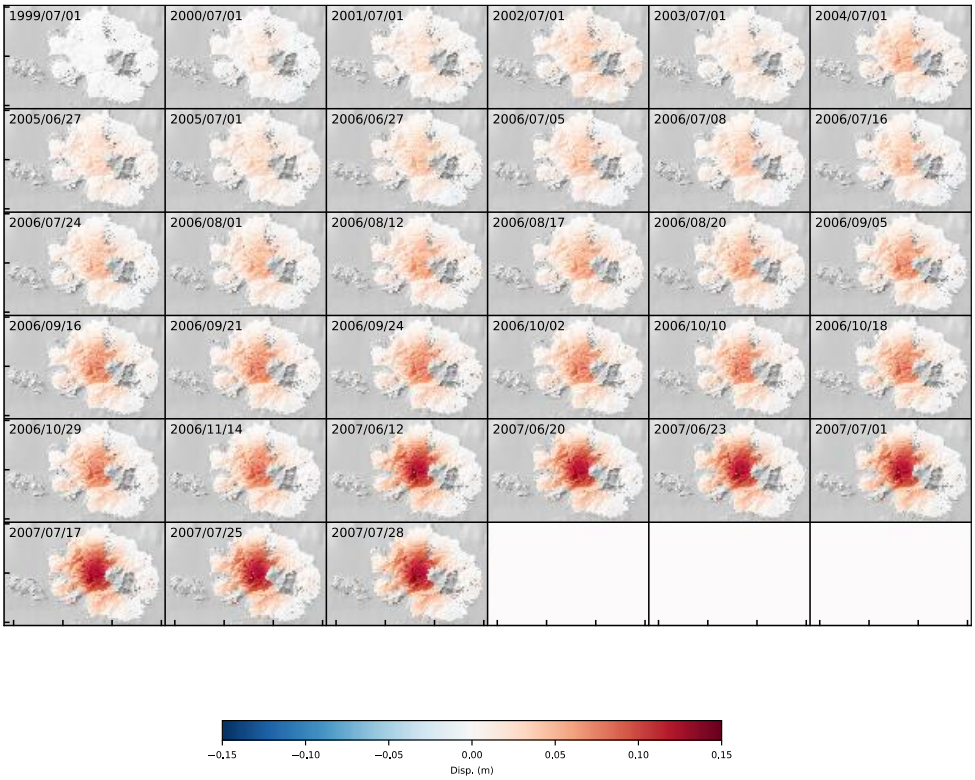

Figure C.2 Timeseries of the Up-Down component of surface displacement in the Atka volcanic center.

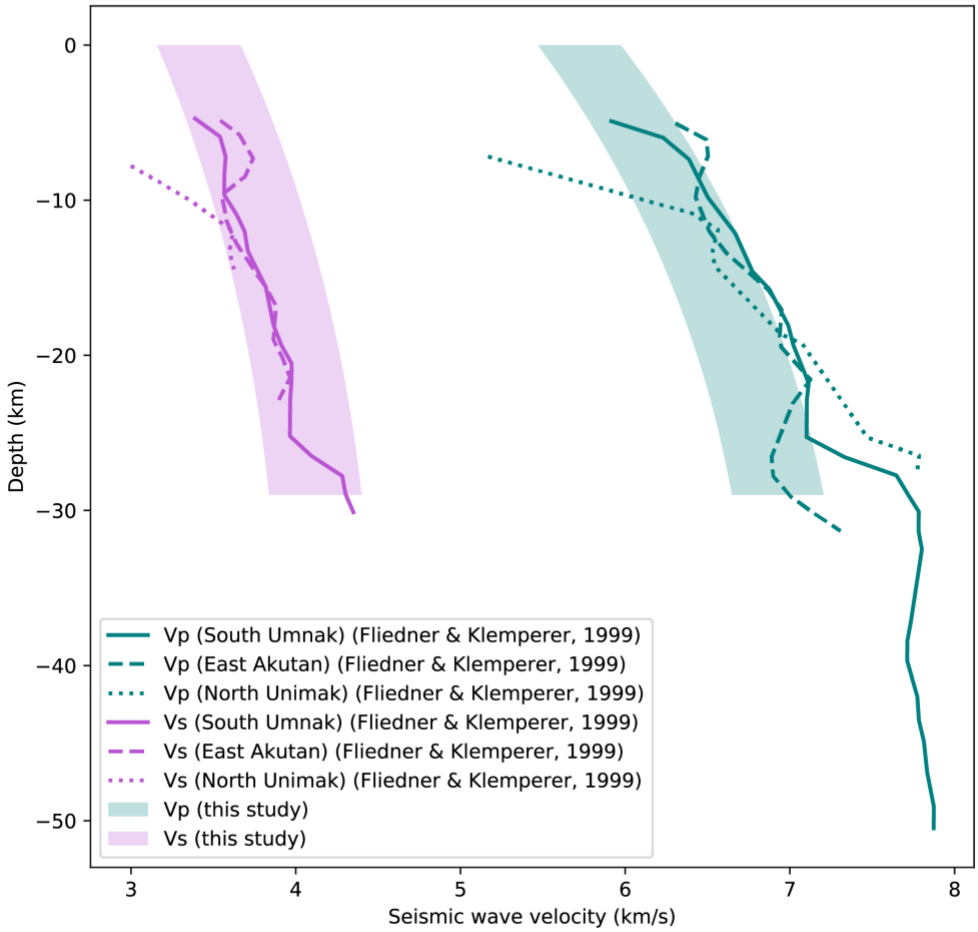

Figure C.3 Comparison of the seismic velocity model of this study and regional velocity models of Aleutian arc (Fliedner & Klemperer, 1999). Vp and Vs in this model are calculated by assuming the Poisson's ratio and density are constants (Table 1). The dynamic Young's modulus for calculating the seismic velocity is converted by the static far-field Young's modulus ($\boldsymbol{E_d}$ in Eq. 5.3) (Starzec, 1999; Ciccotti & Mulargia, 2004).

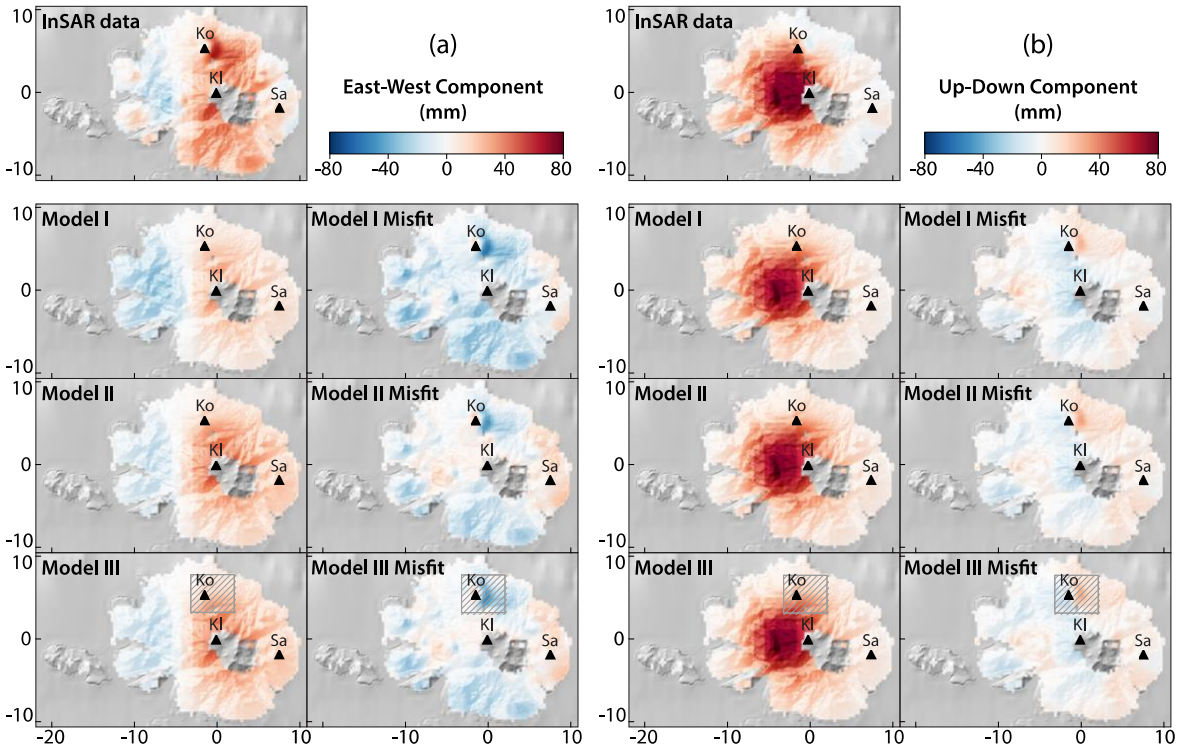

Figure C.4 Comparison between InSAR timeseries data and modeled surface displacement at 2006/11/14. (a) East-West component. (b) Up-down component. In Model I, the pressure source is an ellipsoid with a fixed dipping angle ($\theta = 90°$ in Fig. 6.3). In Model II, the dipping angle (θ) and direction (φ) are unfixed. Model III has the same setup as Model II but is constrained by masked InSAR data shown as the grey shaded rectangles. The black triangles represent volcanos, including Korovin (Ko), Kliuchef (Kl), and Sarichef (Sa).

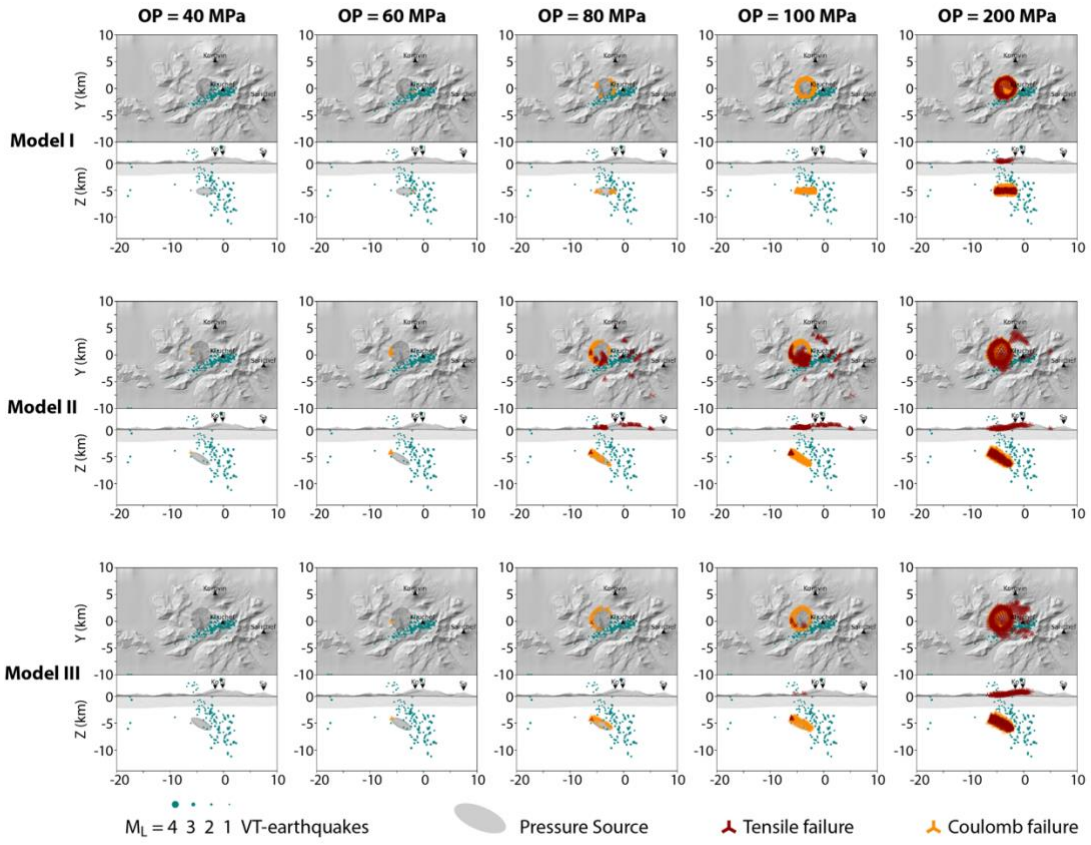

Figure C.5 Evolution of the host-rock failure at extrapolated overpressure from 40 MPa to 200 MPa. The geometry of the pressure is from the mean values of the parameter estimations at 2006/11/14 prior to the eruption. Red and orange triangles indicate tensile and Coulomb failure. Grey ellipse is the pressure source. Green dots show the location of the volcano tectonic (VTs) earthquakes occurring during 2006/10/30-2006/11/29. The setting of the models is same to Fig. C.4.

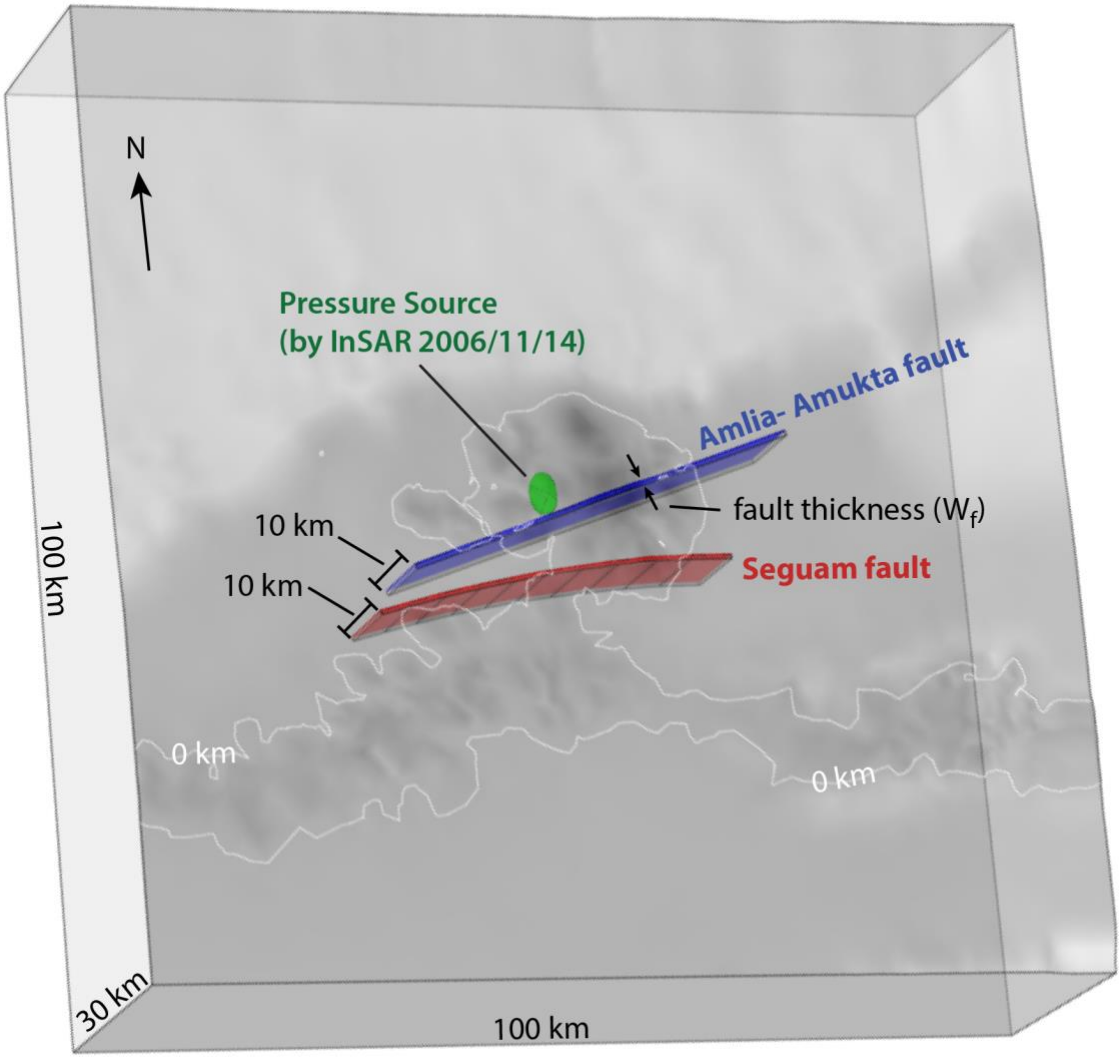

Figure C.6 The setup of the model with two pre-existing weak zones. The Amlia-Amukta and Seguam faults are modeled as vertical slates with a depth of 10 km. Young's modulus of the faults is lower than the surrounding host-rock. The pressure source at 2006/11/14 obtained by data assimilation with InSAR is shown as a green ellipsoid. Other settings of the model with the faults are same as the model without the faults.

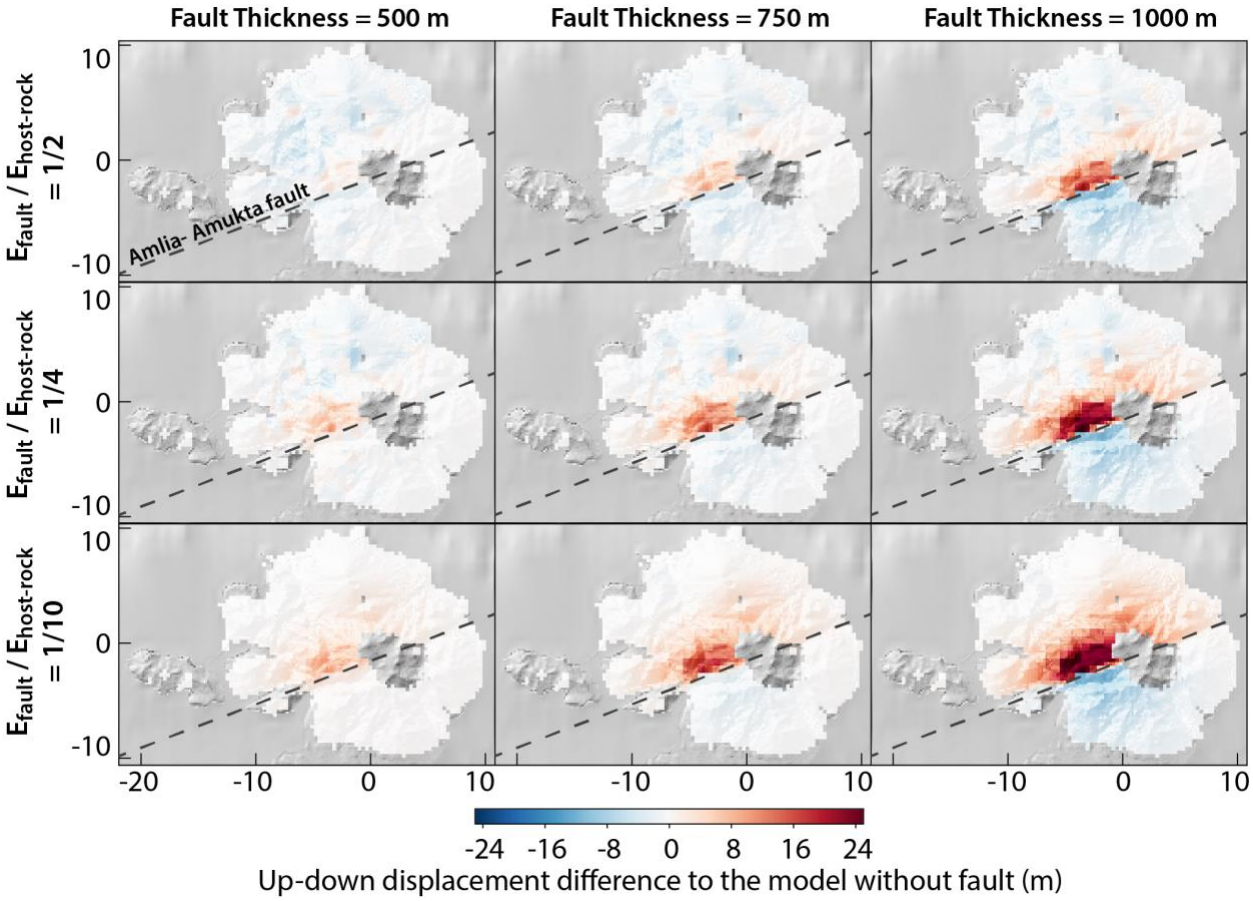

Figure C.7 The effect of the Amlia-Amukta (AA) fault on the surface deformation. The cool-warm colormap shows the difference in surface displacement between the models with the AA fault and the model without the fault (Model II) at 2006/11/24. Different fault thickness and weakness are tested to the impaction of the fault.

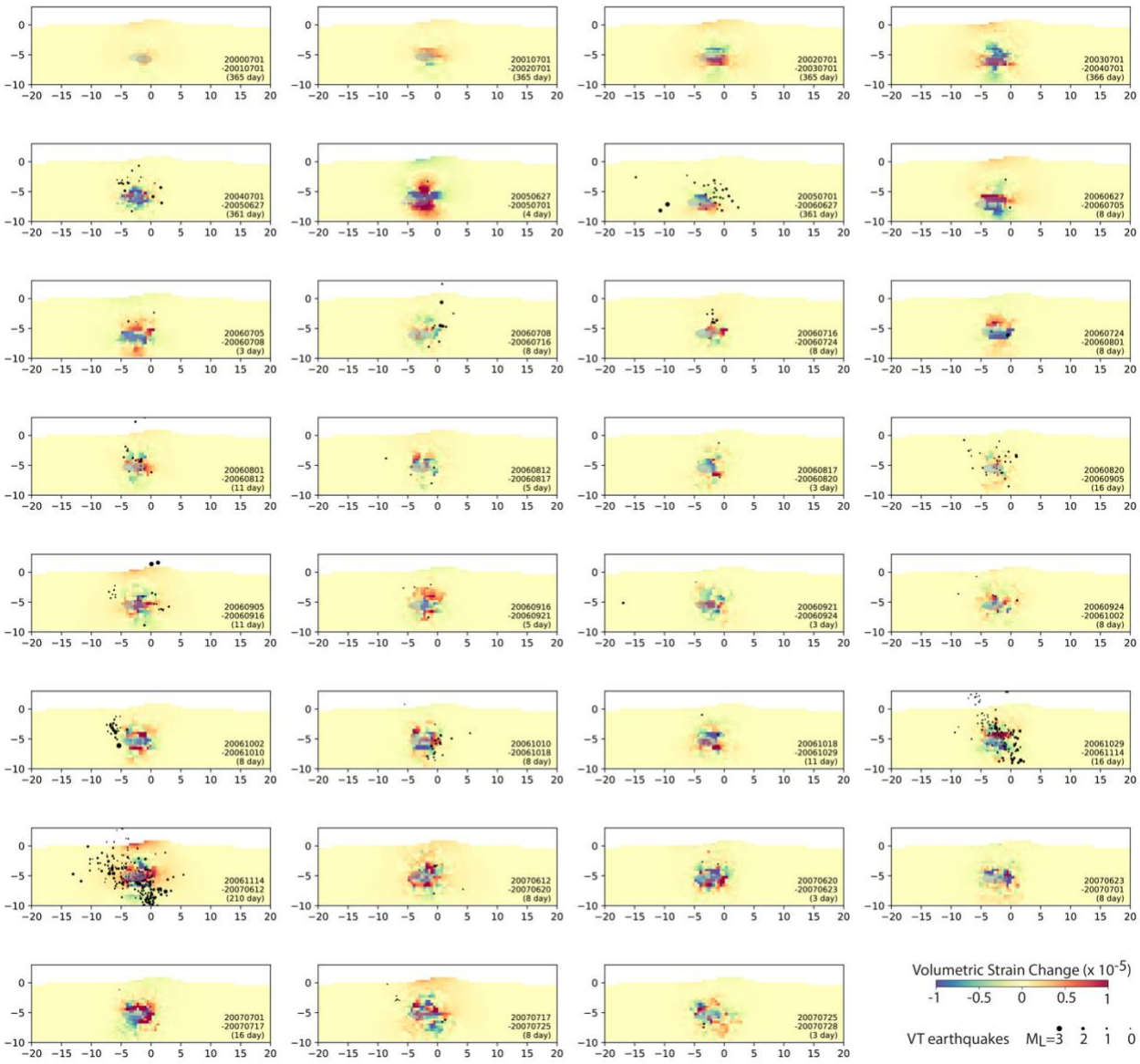

Figure C.8 Volumetric strain changes between two near InSAR acquisitions within the Amlia-Amukta fault by Model I (The mode with fixed dipping angles and directions). The warm color indicates the part of fault experiencing dilatancy during the period. Black dots are the volcano tectonic (VT) earthquakes occurring within a 2-km distance to the fault during the period. The light blue shadow is the projection of the pressure source at the end of the period on the fault.

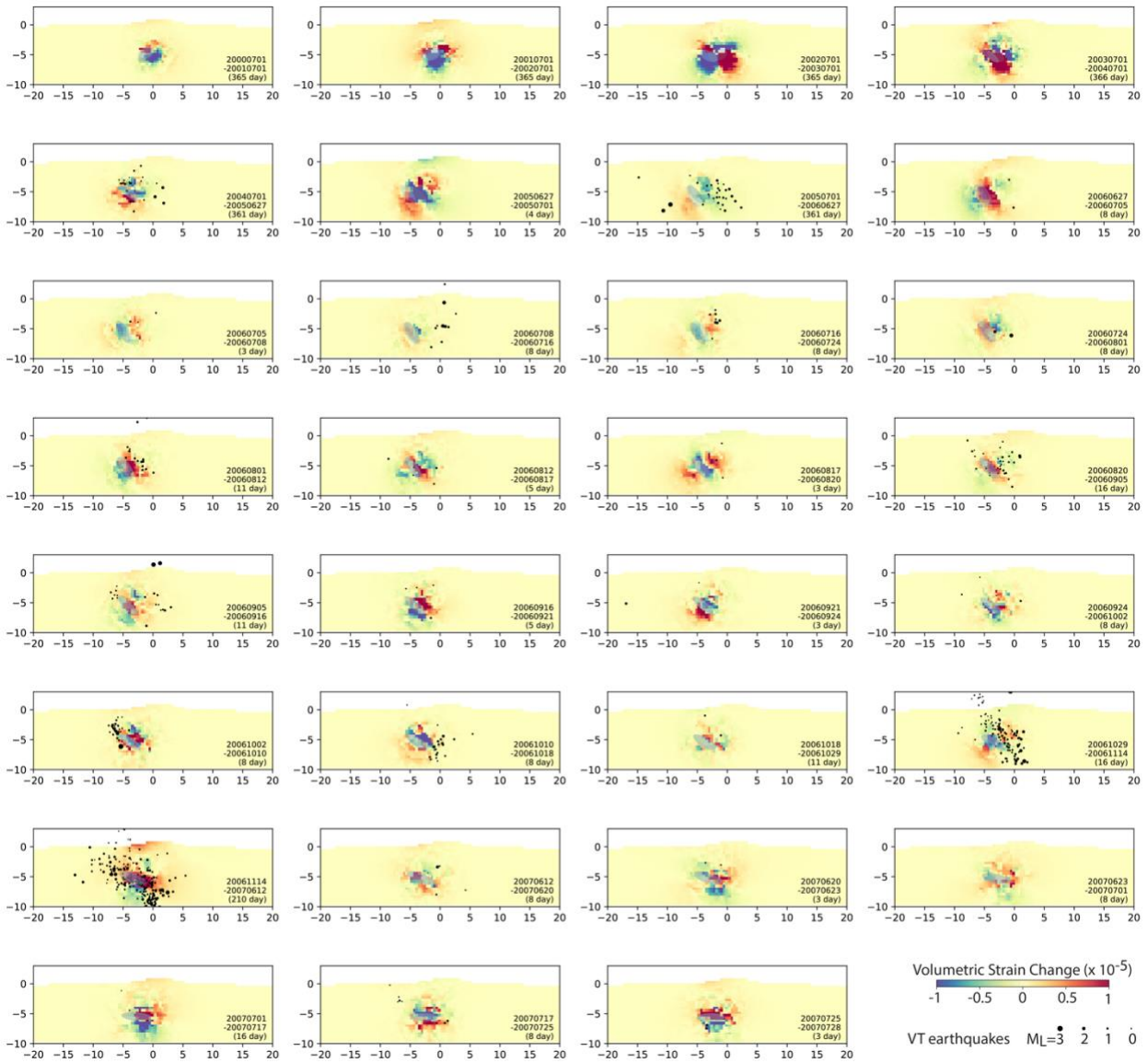

Figure C.9 Volumetric strain changes between two near InSAR acquisitions within the Amlia-Amukta fault by Model II (The mode with free dipping angles and directions). The warm color indicates the part of fault experiencing dilatancy during the period. Black dots are the volcano tectonic (VT) earthquakes occurring within a 2-km distance to the fault during the period. The light blue shadow is the projection of the pressure source at the end of the period on the fault.

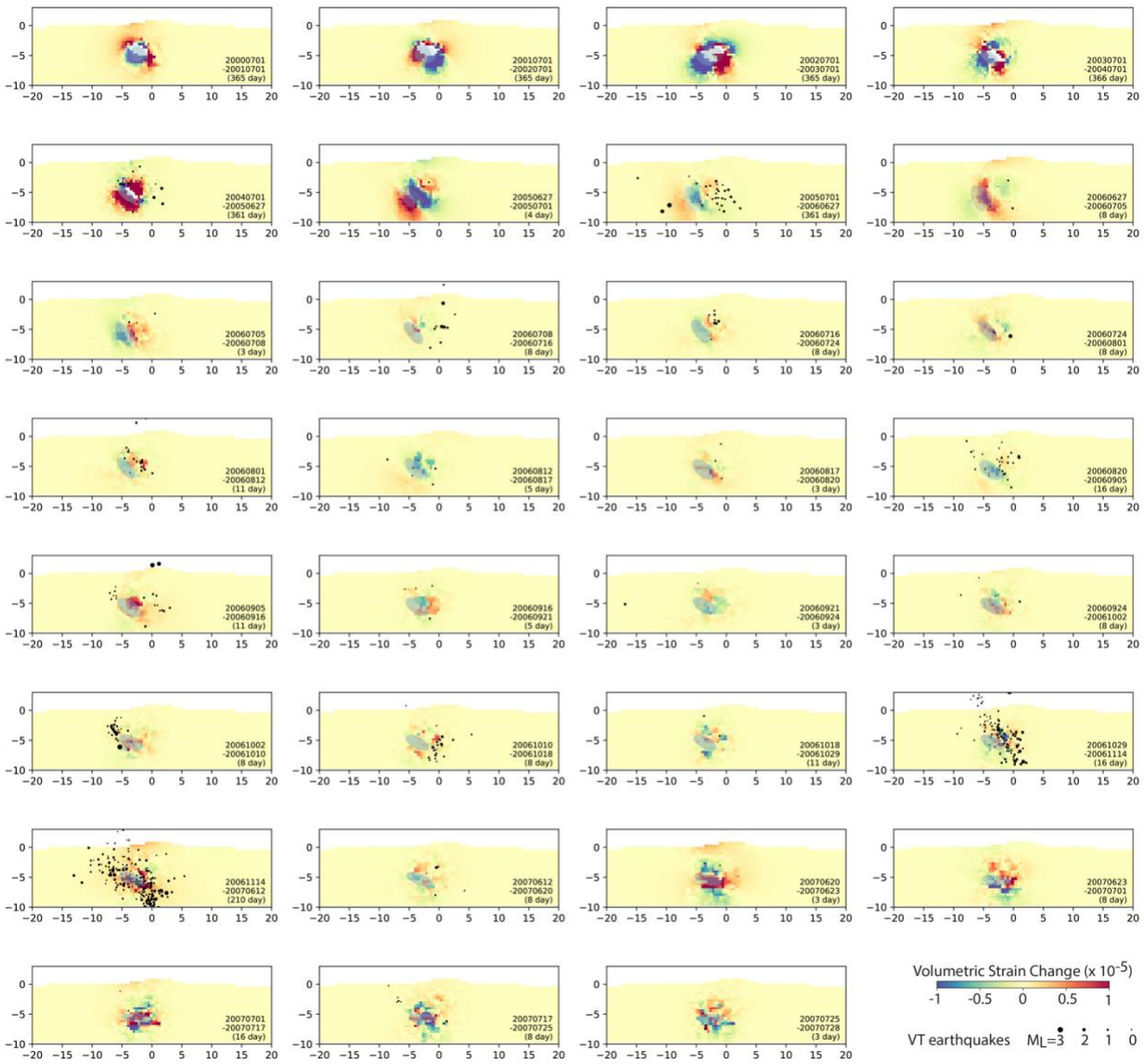

Figure C.10 Volumetric strain changes between two near InSAR acquisitions within the Amlia-Amukta fault by Model III (The mode with free dipping angles and directions, and masked InSAR data at Korovin). The warm color indicates the part of fault experiencing dilatancy during the period. Black dots are the volcano tectonic (VT) earthquakes occurring within a 2-km distance to the fault during the period. The light blue shadow is the projection of the pressure source at the end of the period on the fault.

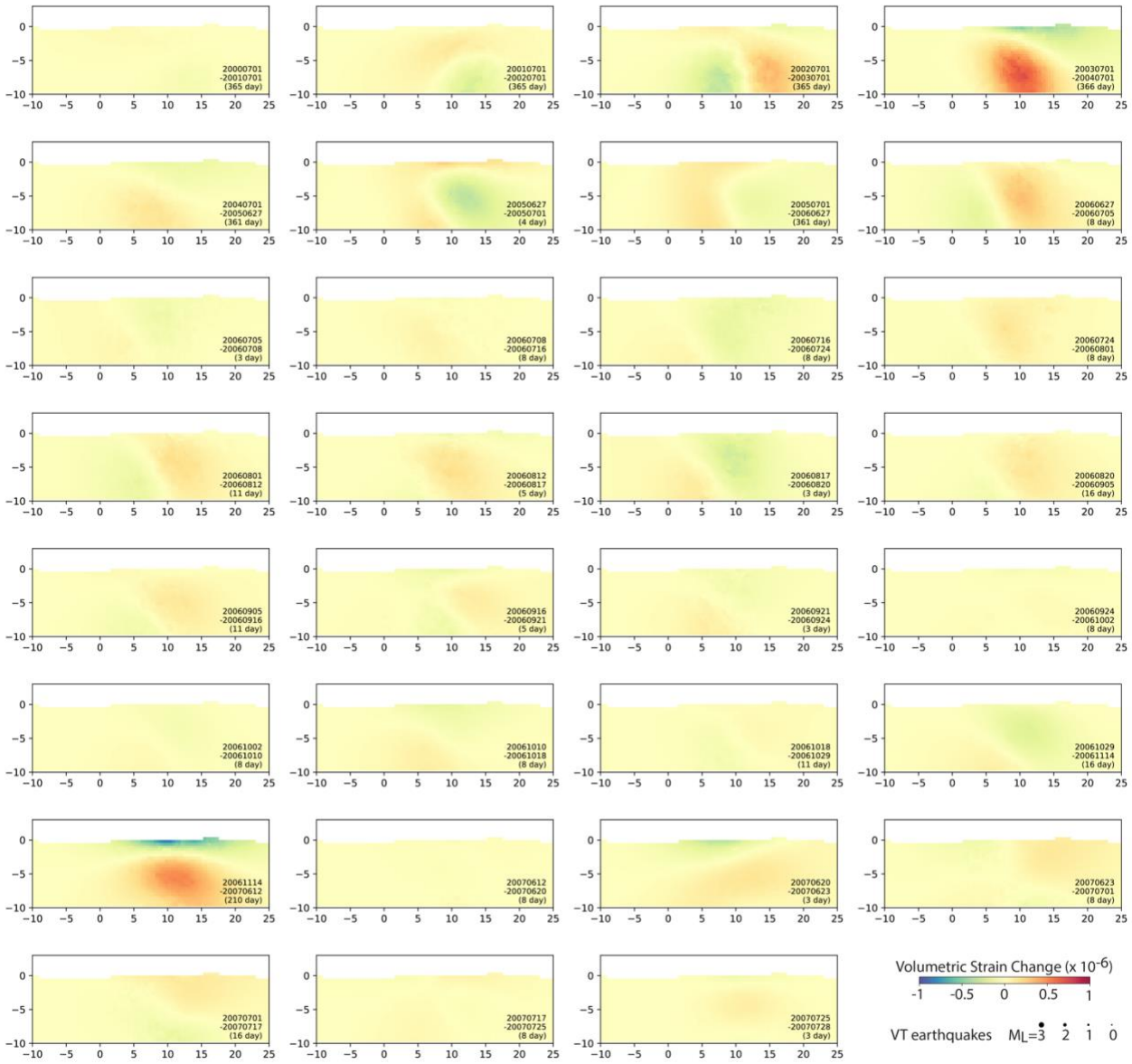

Figure C.11 Volumetric strain changes between two near InSAR acquisitions within the Seguam fault by Model II (The mode with free dipping angles and directions). The warm color indicates the part of fault experiencing dilatancy during the period.

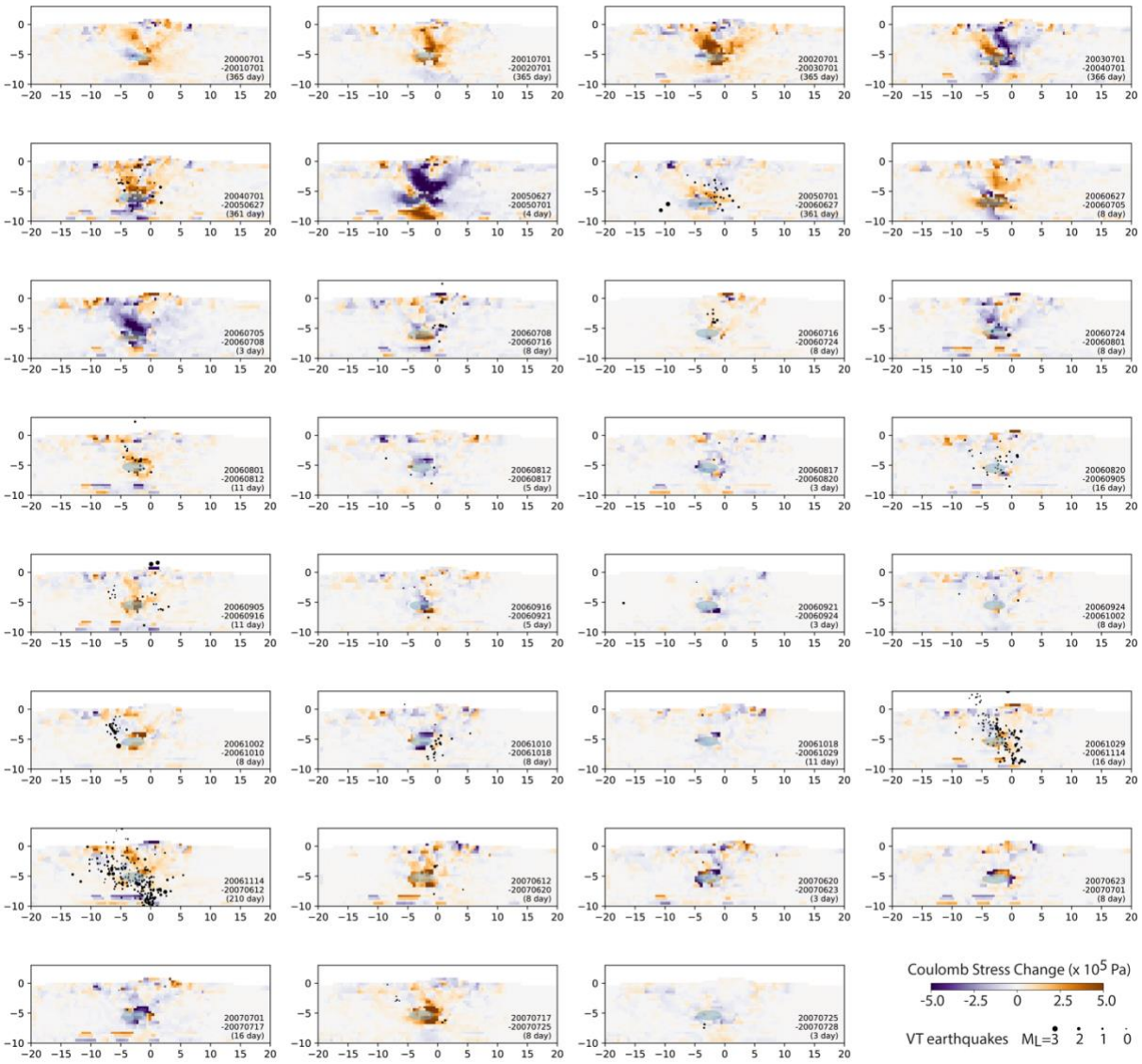

Figure C.12 Coulomb stress changes between two near InSAR acquisitions within the Amlia-Amukta fault by Model I (The mode with fixed dipping angles and directions). The warm color indicates the part of fault having a positive Coulomb stress change, which facilities the failure. Black dots are the volcano tectonic (VT) earthquakes occurring within a 2-km distance to the fault during the period. The light blue shadow is the projection of the pressure source at the end of the period on the fault.

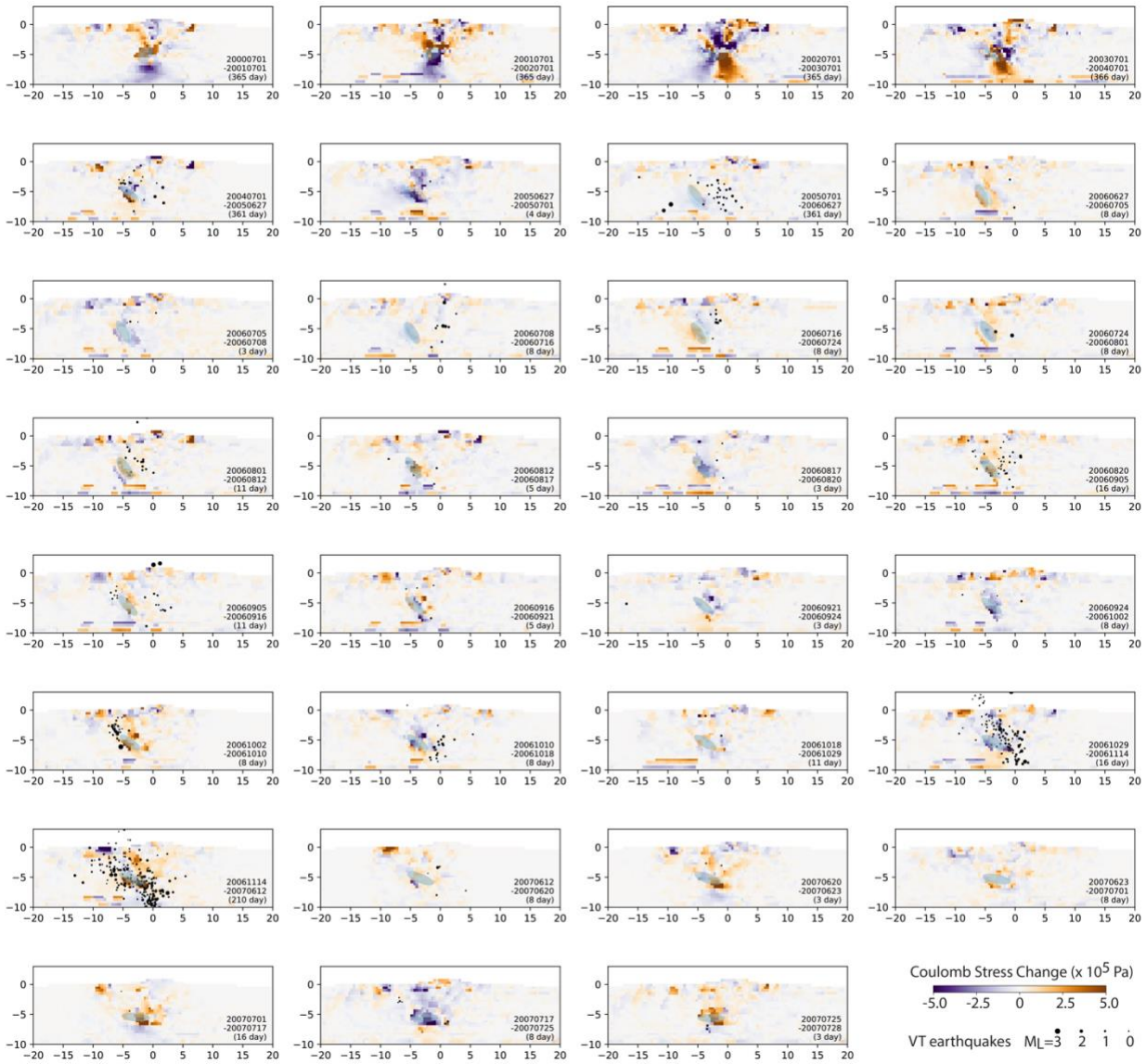

Figure C.13 Coulomb stress changes between two near InSAR acquisitions within the Amlia-Amukta fault by Model II (The mode with free dipping angles and directions). The warm color indicates the part of fault having a positive Coulomb stress change, which facilities the failure. Black dots are the volcano tectonic (VT) earthquakes occurring within a 2-km distance to the fault during the period. The light blue shadow is the projection of the pressure source at the end of the period on the fault.

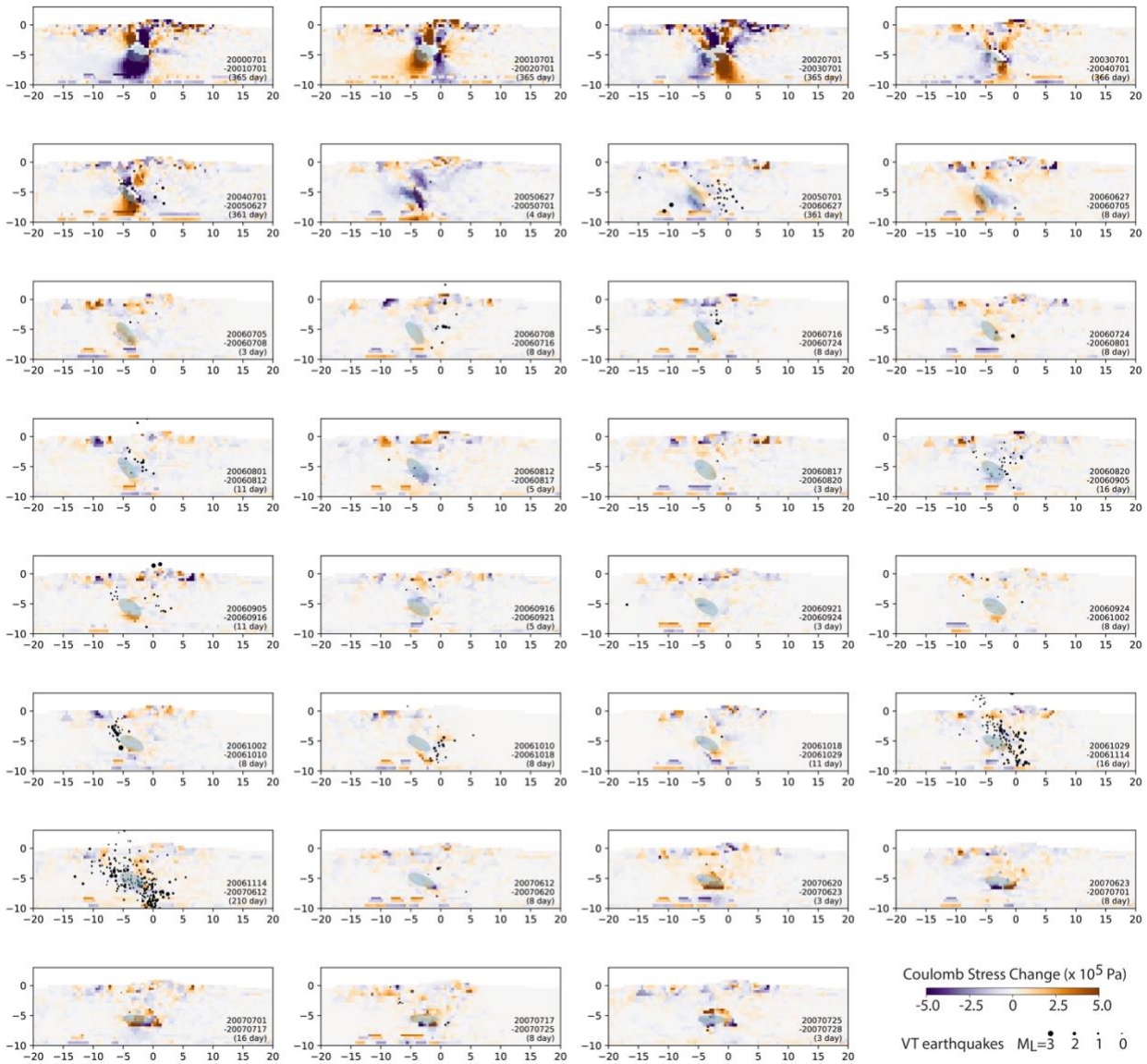

Figure C.14 Coulomb stress changes between two near InSAR acquisitions within the Amlia-Amukta fault by Model III (The mode with free dipping angles and directions, and masked InSAR data at Korovin). The warm color indicates the part of fault having a positive Coulomb stress change, which facilities the failure. Black dots are the volcano tectonic (VT) earthquakes occurring within a 2-km distance to the fault during the period. The light blue shadow is the projection of the pressure source at the end of the period on the fault.

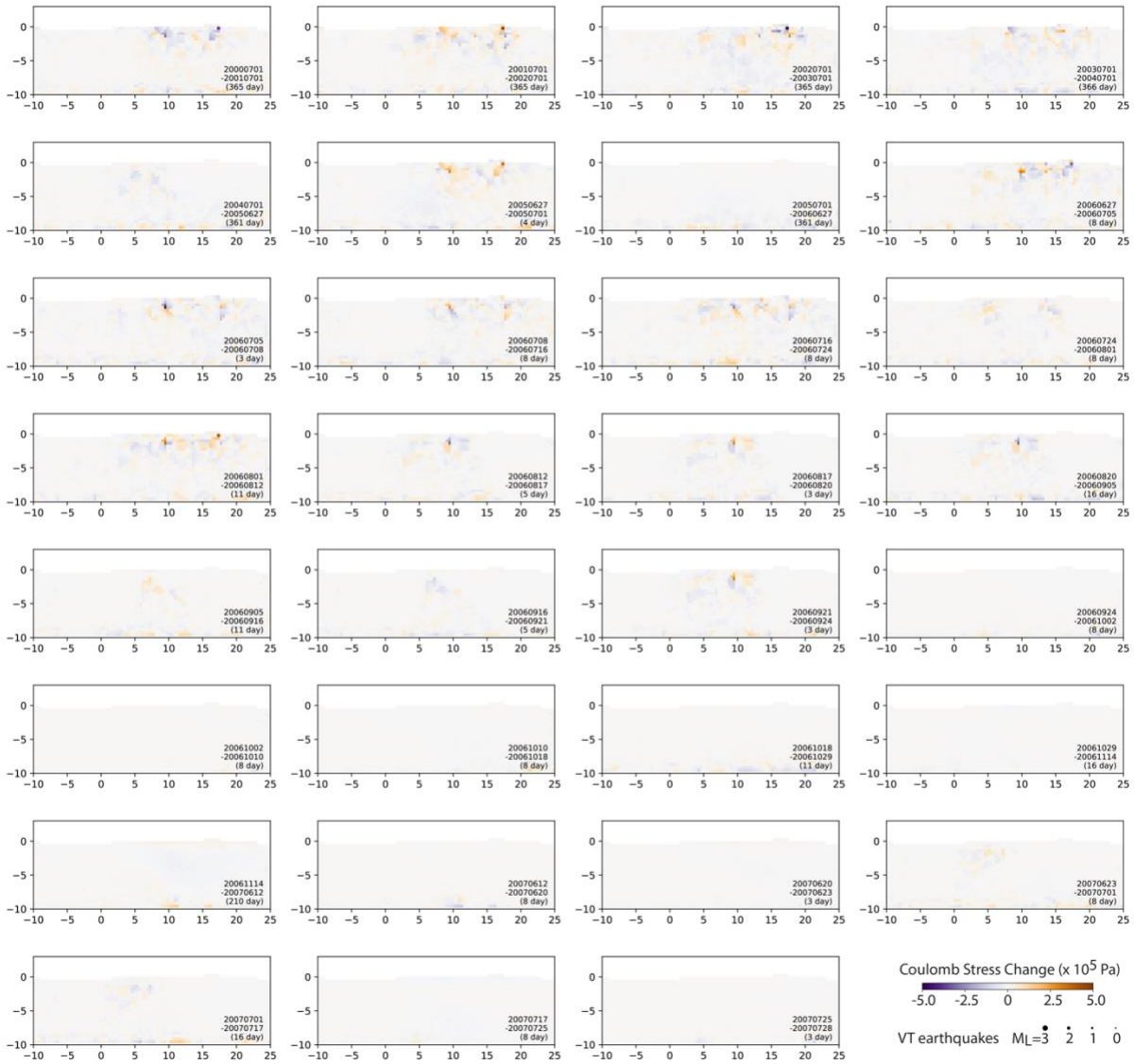

Figure C.15 Coulomb stress changes between two near InSAR acquisitions within the Seguam fault by Model II (The mode with free dipping angles and directions). The warm color indicates the part of fault having a positive Coulomb stress change, which facilities the failure.

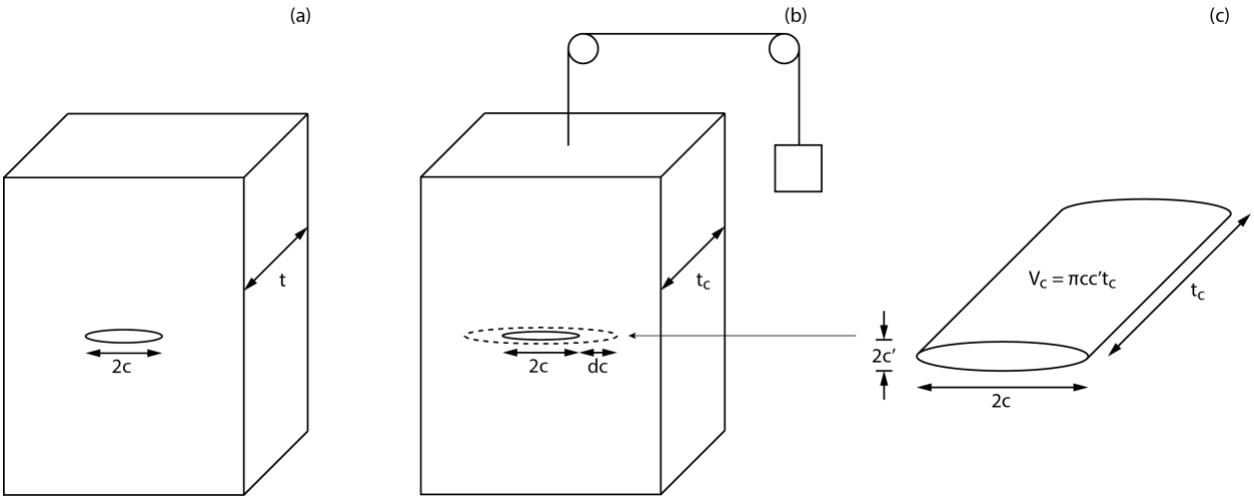

Figure C.16 A crack (a) extended under load (b) (after Jaeger et al., 2007). (c) Geometry of the crack.

Table C.1 Model Parameters

Parameter	Description	Value	Unit
T_0	Surface temperature	0	$°C$
T_c	Magma body temperature	850	$°C$
dT/dz	Geothermal gradient ($z < 0$)	-30	$°C\,/\,km$
Kc	Thermal conductivity	3	$W \cdot m^{-1} \cdot K^{-1}$
C_p	Specific heat capacity	1.25	$kJ \cdot kg^{-1} \cdot K^{-1}$
ρ	Density of rock	2.7×10^3	$kg \cdot m^{-3}$
ρ_w	Density of water	1.0×10^3	$kg \cdot m^{-3}$
ν	Poisson's ratio	0.25	1
ϕ_i	Internal friction angle of host-rocks	25	°
ϕ_f	Internal friction angle of faults	15	°

Table C.2 Variables

Variable	Description	Unit
(X, Y, Z)	Location of the center of the magma body ()	m
a	Half height of the magma chamber	m
b	Half width of the magma chamber	m
φ	Dip direction (clockwise angle from North)	°
θ	Dip angle	°
OP	Overpressure (excess to lithostatic pressure)	Pa
E_{Td}	Young's modulus of host-rock	Pa
E_d	Far-field Young's modulus	Pa
T	Temperature	$°C$
W_f	Fault thickness	m
$\frac{E_f}{E_r}$	Ratio of the Young's modulus between the fault and the host-rocks	1
C_0	Cohesion	Pa
σ_T	Tensile strength	Pa
σ_1	Maximum principal stresses	Pa
σ_3	Minimum principal stresses	Pa
σ_n	Normal stress $((\sigma_1 + \sigma_3)/2)$	Pa
τ	Maximum shear stress $((\sigma_1 - \sigma_3)/2)$	Pa
ϵ_V	Volumetric strain	1
ΔV^{tot}	Total volume change	m^3
E_{eq}	Earthquake energy release	J

References

Ciccotti, M., & Mulargia, F. (2004). Differences between static and dynamic elastic moduli of a typical seismogenic rock. Geophysical Journal International, 157(1), 474–477. https://doi.org/10.1111/j.1365-246X.2004.02213.x

Fliedner, M. M., & Klemperer, S. L. (1999). Structure of an island-arc: Wide-angle seismic studies in the eastern Aleutian Islands, Alaska. Journal of Geophysical Research: Solid Earth, 104(B5), 10667–10694. https://doi.org/10.1029/98JB01499

Starzec, P. (1999). Dynamic elastic properties of crystalline rocks from south-west Sweden. International Journal of Rock Mechanics and Mining Sciences, 36(2), 265–272. **https://doi.org/10.1016/S0148-9062(99)00011-X**